

**EXPERIMENTAL STUDY OF THE
NORMAL STATE AND THE
SUPERCONDUCTING PROPERTIES OF
THE Ti-V ALLOYS**

By

MD. MATIN

Enrolment No. PHYS03200904004

**Raja Ramanna Centre for Advanced Technology,
Indore**

*A thesis submitted to the
Board of Studies in Physical Sciences
In partial fulfilment of requirements*

for the Degree of

DOCTOR OF PHILOSOPHY

of

HOMI BHABHA NATIONAL INSTITUTE



August, 2014

Homi Bhabha National Institute

Recommendations of the Viva Voce Committee

As members of the Viva Voce Board, we certify that we have read the dissertation prepared by Shri Md. Matin entitled “**Experimental study of the normal state and the superconducting properties of the Ti-V alloys**” and recommend that it may be accepted as fulfilling the dissertation requirement for the Degree of Doctor of Philosophy.

Chairman – Dr. G. S. Lodha  Date: 11.3.15

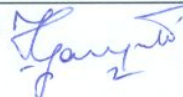
Guide/ Convener - Dr. S. B. Roy  Date: 16.3.15

Co-guide - Dr. M. K. Chattopadhyay  Date: 11/03/2015
 11-3-2015

External Examiner-Prof. S. Ramakrishnan Date:

Member 1 - Dr. S. M. Gupta  Date: 11/3/15

Member 2 - Dr. A. K. Tyagi  Date:

Co-opted Member - Dr. Tapas Ganguli  Date: 11/03/2015

Final approval and acceptance of this dissertation is contingent upon the candidate's submission of the final copies of the dissertation to HBNI.

We hereby certify that we have read this thesis prepared under our direction and recommend that it may be accepted as fulfilling the thesis requirement.


Co-guide


Guide

Date: 11-03-2015
Place: RRCAT, Indore

11.3.2015

STATEMENT BY AUTHOR

This dissertation has been submitted in partial fulfilment of requirements for an advanced degree at Homi Bhabha National Institute (HBNI) and is deposited in the Library to be made available to borrowers under rules of the HBNI.

Brief quotations from this dissertation are allowable without special permission, provided that accurate acknowledgement of source is made. Requests for permission for extended quotation from or reproduction of this manuscript in whole or in part may be granted by the Competent Authority of HBNI when in his or her judgement the proposed use of the material is in the interests of scholarship. In all other instances, however, permission must be obtained from the author.

M. Matin

Md. Matin

DECLARATION

I, hereby declare that the investigation presented in the thesis has been carried out by me. The work is original and has not been submitted earlier as a whole or in part for a degree / diploma at this or any other Institution / University.

M. Matin

Md. Matin

List of Publications arising from the thesis

Journal

1. “Magnetic irreversibility and pinning force density in the Ti-V alloys”, Md. Matin, L. S. Sharath Chandra, M. K. Chattopadhyay, R. K. Meena, Rakesh Kaul, M. N. Singh, A. K. Sinha, and S. B. Roy, *J. Appl. Phys.*, **2013**, 113, 163903-163913.
2. “High field paramagnetic effect in the superconducting state of $\text{Ti}_{0.8}\text{V}_{0.2}$ alloy”, Md. Matin, L. S. Sharath Chandra, M. K. Chattopadhyay, M. N. Singh, A. K. Sinha, and S. B. Roy, *Supercond. Sci. Technol.*, **2013**, *26*, 115005-115011.
3. “Spin-fluctuations in $\text{Ti}_{0.6}\text{V}_{0.4}$ alloy and its influence on the superconductivity”, Md. Matin, L. S. Sharath Chandra, Radhakishan Meena, M. K. Chattopadhyay, A. K. Sinha, M. N. Singh, and S. B. Roy, *Physica B*, **2014**, *436*, 20-25.
4. “The influence of electron-phonon coupling and spin fluctuations on the superconductivity of the Ti-V alloys”, Md. Matin, L. S. Sharath Chandra, S. K. Pandey, M. K. Chattopadhyay, and S. B. Roy, *Eur. Phys. J. B*, **2014**, *87*, 131-140.
5. “Critical current and flux pinning properties of the superconducting TiV alloys”, Md. Matin, L. S. Sharath Chandra, M. K. Chattopadhyay, R. K. Meena, Rakesh Kaul, M. N. Singh, A. K. Sinha, and S. B. Roy, *Physica C*, **2015**, 512, 32-41.

M. Matin

Md. Matin

TO MY PARENTS, WITH LOVE

Acknowledgement

I am thankful to my thesis guide **Dr. S. B. Roy**. His guidance, constant support, encouragement and motivation, and patience throughout the course of this work are valuable to me. His constructive criticism and valuable suggestions have helped me to present the scientific results in an efficient and effective manner in this thesis.

Dr. M. K. Chattopadhyay, my thesis co-guide, put his enthusiastic support in planning of experiments, analysis of the experimental data and scientific interpretation of the results, and in preparing manuscript for journals. He has taken care of me in every aspect of my life in Indore. I am thankful to him.

I felt lucky for working with **Dr. L. S. Sharath Chandra**. He has also supported me in many ways including planning of experiments, analysis of the experimental data and scientific interpretation of the results, and preparing manuscript for journals. I am thankful to him.

I am pleased to acknowledge the careful guidance of Dr. L. S. Sharath Chandra, Dr. M. K. Chattopadhyay and Dr. S. B. Roy in improving the presentation of this thesis. I am thankful to S. Sundar, Dr. V. K. Sharma, A. Chauhan, S. Rage, and R. K. Meena for their help at different stages of this work. I am also thankful to J. Chandra, S. Nath, P. Arora, and Dr. A. Khandelwal for providing me friendly environment in Magnetic and Superconducting Materials Section. I am grateful to Dr. K. J. S. Sokhey and also again to Dr. M. K. Chattopadhyay for their efforts to support me during my wifes illness. I am thankful to Dr. M. Manekar for his limited but useful scientific discussions with me. I would like to thank Dr. R. Kaul and Ram Nehal for optical metallography experiments, Dr. S. K. Pandey for doing band structure calculation, M. N. Singh and Dr. A. K. Sinha for

X-ray diffraction experiments. Thanks, as well, to the members of my Ph.D. advisory committee Dr. A. M. Gupta, Dr. G. S. Lodha, and Dr. A. K. Tyagi for their helpful discussions with me.

It is, of course, impossible to acknowledge all those friends who have encouraged and supported me during this work, but I should at least mention Lipika Nath and Sovana Khatun.

I am thankful to my wife Jannatun Nesa for her support and care for me. I thank my son **Md. Rayn**, my sister Amina Khatun, and my brother Md. Asique. Their love keeps me always warm.

I am also thankful to my other family members (Imam Sharif, Rukser Khatun, Izaz Ahamed, Riziya Sultana, Tuhina Khatun, Manoara Khatun, Sajjad Hossen, Sahajada Badsha, Ruhi Farhad, Runi Khatun, Khorshed Alam, Sk. Naim-ul Islam, Nur Farhad, Dr. Sk. Jahirul Islam, Habibur Rahaman, Ismile Sk., Luthfer Rahaman, Renija Bebum, Runa Begum, Rezaul Karim, (late) Rehana Akter Begum, (late) Jannatun Firdosh, (late) Zulekha Yesmin, my loving Budi Didi, Noorbanu Begum, Samsunnehar Begum, Morion Nesa, Kohinoor Begum, Abul Hassan, Abul Kashem (Mukta), Naimul Imam, Abdus Sabur, Abdus Sattar, Abul Kashem, Abdul Hakim, Golam Murshed Ali, (late) Halema Kathon, Mofizur Rahaman, Hosnera Begum, (late) Rokiya Begum, and (late) Prof. M. A. Roquib). Though it is impossible to mention their help and support during this work individually, I should at least mention the useful scientific discussions relating to this thesis with Nur Farhad and the valuable medical advices of Dr. Sk. Jahirul Islam when needed.

Last but not the least I would like to express my sincere gratitude to my parents for their care, love, and affection for me.

Contents

Synopsis	S1
List of figures	1
List of Tables	6
Chapter 1 Introduction	7
1.1 General introduction	7
1.2 Basics of superconductivity	9
1.2.1 A brief history of superconductivity	9
1.2.2 The critical temperature	12
1.2.3 The Ginzburg-Landau phenomenological theory	13
1.2.4 Type-I and type-II superconductors	16
1.2.5 The superconducting mixed state and the flux-line lattice	17
1.2.6 Field of first flux-line entry	19
1.2.7 Field for the nucleation of superconductivity	22
1.2.8 Reversible and irreversible type-II superconductors	23
1.2.9 The critical current	25
1.2.10 The field-temperature phase diagram; and the effect of thermal fluctuations and disorders on the supercon- ducting mixed state	28
1.3 Current status of research on the Ti-V alloy superconductors	30
1.3.1 Structural properties of the Ti-V alloys	31
1.3.2 Physical properties of the Ti-V alloys in their normal state	34
1.3.3 Superconducting properties of the Ti-V alloys	38
1.3.4 Fluctuation conductivity in the Ti-V alloys	44
1.4 Motivation of the present work	45

Chapter 2	Synthesis of the Ti-V alloys and experimental techniques	51
2.1	Introduction	51
2.2	Preparation of the samples	52
2.3	Structural characterization of Ti-V alloys	54
2.3.1	X-ray diffraction	54
2.3.2	Optical metallography	59
2.4	Measurement of the electrical resistivity	60
2.5	Measurement of the magnetization	61
2.6	Measurement of the heat capacity	65
2.7	Measurement of the strain	70
Chapter 3	Structural investigations of the Ti-V alloys	75
3.1	Introduction	75
3.2	Results and discussion	76
3.2.1	X-ray diffraction	76
3.2.2	Optical metallography	80
3.3	Conclusions	86
Chapter 4	Superconducting properties of the Ti-V alloys	89
4.1	Introduction	89
4.2	Results and discussion	90
4.2.1	The superconducting transition temperature of the Ti-V alloys	90
4.2.2	The upper critical field of the Ti-V alloys	97
4.2.3	The lower critical field of the Ti-V alloys	108
4.2.4	Thermodynamic critical field of the Ti-V alloys	114
4.2.5	Fundamental superconducting length scales in the Ti-V alloys	117
4.3	Summary and conclusions	121
Chapter 5	Fluctuation conductivity in the Ti-V alloys	125
5.1	Introduction	125
5.2	Results and discussion	128
5.2.1	The temperature dependence of electrical resistivity in the Ti-V alloys and the relevance of the superconducting fluctuations in these alloys	128

5.2.2	Theoretical models for the superconducting fluctuation induced conductivity	131
5.2.3	The temperature dependence of excess conductivity of the Ti-V alloys	133
5.2.4	Magneto-resistance of the Ti-V alloys	141
5.3	Summary and conclusions	143
Chapter 6 The normal state properties of the Ti-V alloys		145
6.1	Introduction	145
6.2	Results and discussion	147
6.2.1	The temperature dependence of heat capacity of the Ti-V alloys	147
6.2.2	The temperature dependence of magnetic susceptibility of the Ti-V alloys	151
6.2.3	Electrical resistivity of the Ti-V alloys	156
6.2.4	Validity of the Kadowaki-Woods scaling relation for the Ti-V alloys	166
6.2.5	Suppression of T_C due to spin fluctuations in the Ti-V alloys	167
6.3	Summary and conclusions	169
Chapter 7 Critical current and flux-line pinning in the Ti-V alloys		171
7.1	Introduction	171
7.2	Results and discussion	172
7.2.1	Magnetic field dependence of magnetization	172
7.2.2	Magnetic field dependence of the critical current densities in the Ti-V alloys	175
7.2.3	Peak-effect in the Ti-V alloys	195
7.3	Summary and conclusions	201
Chapter 8 Bose-glass to vortex-liquid phase transition in the vortex state of the annealed $\text{Ti}_{0.7}\text{V}_{0.3}$ alloy		203
8.1	Introduction	203
8.2	Results and discussion	207

8.2.1	Temperature dependence of electrical resistivity in different constant magnetic fields: Evidence of a glass to liquid phase transition in the flux-line system of the annealed $\text{Ti}_{0.7}\text{V}_{0.3}$ sample	207
8.2.2	The modified vortex-glass model	212
8.2.3	Temperature and field dependence of effective pinning energy	214
8.2.4	Scaling of the vortex-liquid resistivity	218
8.2.5	Vortex matter phase diagram	221
8.2.6	Crossover from individual flux-line pinning to collective pinning regime and its manifestations	222
8.3	Summary and conclusions	225
Chapter 9 High-field paramagnetic Meissner effect in the multi-phase Ti-V alloy superconductors		227
9.1	Introduction	227
9.2	Results and discussion	229
9.2.1	Temperature dependence of magnetization	229
9.2.2	Time dependence of magnetization	239
9.3	Summary and conclusions	248
Chapter 10 Summary, conclusions and future outlook of the study		251
10.1	Summary and conclusions	251
10.2	Future outlook	263
References		265



Homi Bhabha National Institute

Ph. D. PROGRAMME

- | | |
|---|--|
| 1. Name of the Student: | Md. Matin |
| 2. Name of the Constituent Institution: | Raja Ramanna Centre for Advanced Technology |
| 3. Enrolment No.: | PHYS03200904004 |
| 4. Title of the Thesis: | Experimental study of the normal state and superconducting properties of the Ti-V alloys |
| 5. Board of Studies: | Physical Sciences |

Synopsis

Superconductors are materials of choice for the production of high field magnets in thermo-nuclear reactors. There are, however, concerns that the Niobium-based materials and Ag sheathed high T_C superconducting materials are not good for such superconducting magnet applications where they may be subjected to long term neutron irradiation. This is because such neutron irradiation would transform them into radioactive materials with very long decay periods [1, 2]. Hence, there is a need for the development of newer superconducting materials with useful properties. In this direction, now the interest has been focused on other transition element alloy superconductors. One such system is the Ti-V alloys which were known to be superconducting for a long time [3]. Previous studies on Ti-V alloys indicate that these alloys are highly machinable and could be used as an alternative material for technological applications [4-6]. However, the usage of Ti-V alloys in the actual technological applications has been rather limited so far, because of the lack of in-depth studies of the superconducting and normal state properties in these materials.

The Ti-V alloys show a variety of structural phases across the complete compositional range [7]. The samples for the present study were chosen in such a way to cover the entire region of the body centered cubic phase of these alloys. It is reported in literature [8] that the superconducting transition temperature T_C increases with increase in the Vanadium concentration among the alloys considered for this study. It is well known that addition of a magnetic impurity in non-transition element based s-wave

superconductors suppress the superconductivity due to pair breaking. It is also reported in literature that even the addition of the non magnetic transition elements suppress the T_C [3, 9, 10] due to the formation of localized states. However, it has also been observed that the T_C of a dirty limit superconductor is not affected significantly by disorder [11]. In fact a very high level of disorder is required to change the T_C in such a system [12]. Surprisingly an enhancement in T_C is observed in spite of increased disorder when Ti and V are alloyed, as compared to the T_C of the constituent elements. Such behavior is observed in many transition metal alloys [3]. Apart from the enhanced T_C , these transition metal based disordered binary alloys are also observed to have strong fluctuation conductivity effects well above T_C and well above the upper critical field H_{C2} [13-15]. Moreover, these fluctuations have been found to be independent of the details of sample preparation, surface polishing, the size and shape of samples and the current density [13-15]. This could hint towards the fact that these alloys have the potential of exhibiting even higher values of T_C and H_{C2} than what are observed experimentally at present. However, the reason for the existence of such strong fluctuation conductivity effects well above T_C and well above H_{C2} is not clearly understood.

In the present thesis, the objective is to study in detail the structural, electrical, magnetic and thermal properties of binary Ti-V alloys so as to understand the normal state as well as the superconducting state properties, which might be helpful in resolving the points raised above. We found that the spin fluctuations play an important role in the superconducting and normal state properties [16]. Our studies reveal that the reduction in the electron-phonon interaction as well as the spin fluctuations with the increasing Ti concentration is responsible for the observed variation of the T_C as a function of composition [17]. Apart from this, the structural properties are also observed to influence the normal state and superconducting properties especially the critical current density of these alloys [18, 19]. In addition, several other interesting phenomena such as the high field paramagnetic effect [20], a vortex glass to vortex liquid phase transition [21] and a clear signature of a first order transition in the vortex matter (or the flux line lattice) leading to a peak effect observed in the field dependence of magnetization and the critical current density [22] were also observed in these alloys. The outline of the thesis, which includes the details of these studies are given below.

In **Chapter 1 (Introduction)**, an overview on the current status of the research on Ti-V alloys will be presented. The structural phase diagram of these alloys will be discussed in detail. A brief introduction will be given on the aspects of the superconductivity, which are needed to understand the physical properties addressed in the present work. The motivation of the present work will be given at the end of the chapter.

Chapter 2 (Preparation of samples and experimental techniques) will present the details of sample preparation and experimental techniques used in the present study. The samples of four Ti_xV_{1-x} alloys with $x = 0.8, 0.7, 0.6$ and 0.4 were prepared by arc-melting the constituent elements in Argon

atmosphere. The as-cast ingots were wrapped in Ta-foil and then sealed in quartz ampoules in an atmosphere of Argon. The samples were then annealed at 1300 °C for 10 hours. After that, the samples were cooled slowly to 1000 °C and then quenched rapidly into ice-water from 1000 °C. Details of the structural characterization techniques employed in the present study, such as, X-ray diffraction (XRD) experiments using the synchrotron radiation source, optical metallography, scanning electron microscopy (SEM), and energy dispersive analysis of X-ray (EDAX) will be given in this chapter. Basic principles of the measurements of resistivity, magnetization and heat capacity and the details of the experimental setups used will also be discussed.

A detailed structural characterization of the present alloys has been performed by XRD experiments using the synchrotron radiation source, optical metallography, SEM, and EDAX. The results of such studies will be presented in **Chapter 3 (Structural characterizations)**. The analysis of the XRD patterns performed using the Rietveld refinement technique [16, 18-20] reveals that the major phase in all the alloys is the body centered cubic (bcc) β phase (space group: $\text{Im}\bar{3}\text{m}$). It is also observed that in Ti rich $\text{Ti}_x\text{V}_{1-x}$ alloys ($x = 0.8$ and 0.7) contain secondary phases. The ω phase with a hexagonal crystallographic structure (space group: $\text{P6}/\text{mmm}$) is common to both these alloys. However, the α phase with a hexagonal-closed-packed (hcp) crystallographic structure is observed in annealed $\text{Ti}_{0.7}\text{V}_{0.3}$ alloy (space group: $\text{P6}_3/\text{mmc}$) whereas stress induced α' phase with an orthorhombic crystallographic structure is observed in $\text{Ti}_{0.8}\text{V}_{0.2}$ alloy (space group: Cmcm). The estimated lattice parameters corresponding to these phases are in agreement with the literature [23, 24]. SEM and optical metallography studies on the $\text{Ti}_x\text{V}_{1-x}$ alloys reveal that the major β phase of these alloys consists of well connected grains of varying grain size. The average size of the grains in these alloys ranges from few tens to few hundreds of μm . The signature of the α phase in the annealed $\text{Ti}_{0.7}\text{V}_{0.3}$ alloy and the stress induced α' phase in both the as-cast and annealed samples of the $\text{Ti}_{0.8}\text{V}_{0.2}$ alloy is also visible in both optical and electron micrographs. In all the $\text{Ti}_x\text{V}_{1-x}$ alloys, etch pits are also visible and these etched pits are distributed uniformly all over the sample. The results of the EDAX experiments show that the fluctuation in compositions of the investigated alloys over the entire sample surface is less than 2 % of the nominal compositions of the alloys.

In **Chapter 4 (Superconducting properties of $\text{Ti}_x\text{V}_{1-x}$ alloys)**, the details of the superconducting properties of the $\text{Ti}_x\text{V}_{1-x}$ alloys will be presented. The superconducting transition temperature T_C is estimated from the temperature dependence of resistivity, magnetization and heat capacity measurements. The estimated T_C values increase from 4.12 to 7.34 K as x is decreased from 0.8 to 0.4. These values are in agreement with the previously published results [8, 25]. The upper critical field H_{C2} and the lower critical field H_{C1} at different constant temperatures are determined from the isothermal M versus H curves obtained at various constant temperatures below the T_C of these alloys. The highest H_{C2}

value is obtained in the $\text{Ti}_{0.6}\text{V}_{0.4}$ alloy (H_{C2} is about 10 T at $T = 4.2$ K). The density of states at Fermi level $N(0)^{\text{HC2}}$ is estimated from the slope of the experimental $H_{C2}(T)$ curve near the T_C [26]. Electronic band structure calculations have been performed to estimate the density of states at the Fermi level $N(0)^{\text{BS}}$. The $N(0)^{\text{HC2}}$ is found to be considerably larger than the $N(0)^{\text{BS}}$ for all the $\text{Ti}_x\text{V}_{1-x}$ alloys. It is well known that the electron-phonon interaction leads to renormalization of the density of states at the Fermi level. The renormalization factor is $(1 + \lambda_{\text{ep}})$, where λ_{ep} is the electron-phonon coupling constant. The values of $N(0)^{\text{HC2}}$ and $N(0)^{\text{BS}}$ are used to estimate λ_{ep} from the relation: $N(0)^{\text{HC2}} = N(0)^{\text{BS}} (1 + \lambda_{\text{ep}})$ [26]. The estimated value of λ_{ep} increases from ~ 0.5 to ~ 1.0 as x is decreased from 0.8 to 0.4. The Maki parameter α_M estimated for these $\text{Ti}_x\text{V}_{1-x}$ alloys is higher than unity, implying that the Pauli paramagnetic pair breaking effect significantly influences the upper critical field in these alloys. Strong electron-phonon interactions, however, reduce the relative importance of Pauli paramagnetic pair breaking effect in V rich alloys. The experimental $H_{C2}(T)$ data are then analyzed with the formalism given by Orlando et al. [27], which considers both the Pauli paramagnetic pair breaking effect and the corrections for the electron-phonon interactions. The magnitude and the temperature dependence of H_{C1} are found to be nearly consistent with the predictions of the Ginzburg-Landau-Abrikosov-Gor'kov (GLAG) theory [28-31]. Two fundamental superconducting length scales namely the Ginzburg-Landau coherence length $\xi_{\text{GL}}(0)$ and the Ginzburg-Landau London penetration depth $\lambda_{\text{GL}}(0)$ at absolute zero temperature are estimated using the Ginzburg-Landau relations. The values of $\xi_{\text{GL}}(0)$ for these the $\text{Ti}_x\text{V}_{1-x}$ alloys come out to be in the range of $\sim 48-60$ Å, which are considerably larger than the estimated mean free path for the electron conduction (l_e) in these alloys. This indicates that the $\text{Ti}_x\text{V}_{1-x}$ alloys are dirty limit superconductors. It is found that the $\text{Ti}_x\text{V}_{1-x}$ alloys are characterized with very high values of Ginzburg-Landau parameter $\kappa = \lambda_{\text{GL}}(0) / \xi_{\text{GL}}(0)$ and the κ value increases with the increase in x . For example, the value of κ is as high as ~ 60 for the $\text{Ti}_{0.7}\text{V}_{0.3}$ alloy. Hence, these alloys are extreme type-II superconductors. The thermodynamic critical field H_C is deduced from the measured electronic heat capacity in the superconducting state [32]. The experimental $H_C(T)$ curves are fitted with the empirical relation $H_C(T) = H_C(0) [1 - (T/T_C)^2]$ to obtain the value of $H_C(0)$. The obtained value of $H_C(0)$ in the $\text{Ti}_x\text{V}_{1-x}$ alloys increases with decreasing x . Furthermore, we have estimated the Ginzburg number G_i [33] for the present $\text{Ti}_x\text{V}_{1-x}$ alloys. The G_i number increases with increasing x and their values are in the range $\sim 10^{-6} - 10^{-5}$ [19]. Although these values are lower than those for the high- T_C Cuprate superconductors ($G_i \sim 10^{-2}$), they are considerably higher than those for typical low- T_C superconductors ($G_i \sim 10^{-8} - 10^{-9}$). Thus, significant thermal fluctuation effect is expected in these crystalline $\text{Ti}_x\text{V}_{1-x}$ alloys in spite of their low values of T_C .

The studies on the effect of superconducting fluctuations in the $\text{Ti}_x\text{V}_{1-x}$ alloys above the T_C will be presented in **Chapter 5 (Fluctuation conductivity in $\text{Ti}_x\text{V}_{1-x}$ alloys)**. The strong rounding-off behavior of $\rho(T)$ curve observed above T_C as well as the relatively high positive magneto-resistance observed in

the temperature regime between T_C and $\sim 2T_C$ for the present Ti_xV_{1-x} alloys are due to the superconducting fluctuations. Experimentally obtained excess conductivity is then analyzed with the help of the existing theoretical models of Aslamazov-Larkin [34] and Maki-Thompson [35-37]. For all the Ti_xV_{1-x} alloys except $Ti_{0.8}V_{0.2}$, the magnitude and the temperature dependence of the excess conductivity at low reduced temperatures ($\varepsilon \leq 0.1$) are found to be well explained by the Aslamazov-Larkin theory for 3D superconducting fluctuations. The roles of different pair-breaking mechanisms, such as, thermal phonons, magnetic impurities and spin fluctuations in the complete suppression of the Maki-Thompson type contribution to superconducting fluctuations in Ti_xV_{1-x} alloys will be discussed. It is observed that thermal phonons may not be strong enough for the complete suppression of the Maki-Thompson type superconducting fluctuations in these alloys. A linear field dependence of magnetization is observed in the normal state of these alloys up to magnetic fields of 80 kOe, which suggests that these alloys may not contain any magnetic impurities. Hence, the only probable pair breaking mechanism that leads to the suppression of Maki-Thompson type superconducting fluctuations in Ti_xV_{1-x} alloys is the spin fluctuations. Therefore, motivated by the fact that the spin fluctuations might be important in the Ti_xV_{1-x} alloys we have performed a detailed study of the normal state properties of these alloys.

Chapter 6 (Normal state properties of Ti_xV_{1-x} alloys) will present the study on thermal, electric transport and magnetic properties of the Ti_xV_{1-x} alloys in their normal state. The heat capacity measured at low temperatures above T_C is fitted with the function $C(T) = \gamma T + \beta T^3$ to obtain the Sommerfeld coefficient of electronic heat capacity γ and the Debye temperature θ_D . The electron-phonon coupling constant λ_{ep} is also estimated using the experimental γ value and the density of states at Fermi level $N(0)^{BS}$ determined from the band structure calculations. The electrical resistivity in the Ti_xV_{1-x} alloys with $x = 0.7$ and 0.8 increases with decreasing temperature over a wide range of temperatures. For the Ti_xV_{1-x} alloys with $x = 0.4$ and 0.6 , the electrical resistivity in the normal state increases with increasing temperature at all measured temperatures up to room temperature. At low temperatures ($15 < T < 40$ K), the temperature dependence of electrical resistivity observed for these two alloys is found to be described well with the function: $\rho(T) = \rho_0 + AT^2 + BT^5$. The T^5 term represents the phononic contribution to the resistivity at low temperatures. The coefficient of the T^5 term is found to be unusually small and it is positive for the $x = 0.4$ alloy and negative for the $x = 0.6$ alloy. This behavior and the quadratic temperature dependence of low-temperature resistivity are characteristic feature of the spin fluctuations [38]. In the normal state, the Ti_xV_{1-x} alloys exhibit temperature induced dc magnetic susceptibility $\chi(T) \propto -T^2 \ln T$, which also indicates the presence of the spin fluctuations [39, 40]. We have also estimated the Stoner factor S for the Ti_xV_{1-x} alloys. The S is observed to be about ~ 2 for the x

= 0.6 and 0.4 alloys. Such high value of S is generally observed in materials with spin fluctuations [41, 42]. Kadowaki-Woods scaling relation [43] between γ^2 and the coefficient A of the quadratic term of the low-temperature electrical resistivity is also observed to be valid for the $\text{Ti}_x\text{V}_{1-x}$ alloys (for $x = 0.6$ and 0.4). The above experimental evidences clearly suggest the presence of spin fluctuations in the $\text{Ti}_x\text{V}_{1-x}$ alloys. Our study also reveals that the spin fluctuations present in these alloys are itinerant in nature.

We have further studied the influence of spin fluctuations on the superconductivity in $\text{Ti}_x\text{V}_{1-x}$ alloys. When spin fluctuation interactions are not important, the superconducting transition temperature T_C of a superconductor is governed by three important parameters, namely, θ_D , λ_{ep} and the coulomb interaction parameter μ^* [44]. The calculated T_{C0} values using the McMillan formula for V rich $\text{Ti}_x\text{V}_{1-x}$ alloys are found to be significantly higher than the experimentally observed values (T_C). The disagreement between T_{C0} and T_C increases with decreasing x . This observed disagreement arises mainly due to the electron-spin fluctuation interactions [45-48]. In the other words, we can say that the spin fluctuations in $\text{Ti}_x\text{V}_{1-x}$ substantially reduce the superconducting transition temperature from the theoretically predicted value (T_{C0}) to the one observed experimentally (T_C). We have also provided an explanation based on the distribution of the electron-spin fluctuation interaction for the observed fluctuation conductivity above T_C .

The commercial application of a superconductor depends on its capability of carrying dissipation-less current in the presence of high magnetic fields. This aspect will be discussed for the $\text{Ti}_x\text{V}_{1-x}$ alloys in **Chapter 7 (Critical current and flux-line pinning in $\text{Ti}_x\text{V}_{1-x}$ alloys)**. This chapter will be divided in two parts. The first part will cover a detailed study on the field dependence the critical current density J_C and the pinning force density F_P in both the as-cast and annealed samples of the $\text{Ti}_x\text{V}_{1-x}$ alloys. The peak effect (PE) observed in the field dependence of magnetization curves [$M(H)$ curves] in high fields near H_{C2} will be discussed in the second part of chapter 7. Isothermal $M(H)$ curves obtained for both the as-cast and annealed samples of the $\text{Ti}_x\text{V}_{1-x}$ alloys at various constant temperatures below their respective T_C 's are distinctly irreversible. The observed irreversibility is caused by the pinning of flux lines within the superconductors. We have estimated the J_C from the irreversible $M(H)$ curves with the help of the Bean's critical state model [49]. The as-cast $\text{Ti}_{0.7}\text{V}_{0.3}$ alloy has the highest J_C value among all the investigated alloys. In zero fields and at 2 K temperature, the J_C value estimated for this alloy is $\sim 6 \times 10^8 \text{ A/m}^2$. In order to understand the pinning mechanisms operating in these superconducting $\text{Ti}_x\text{V}_{1-x}$ alloys, a detailed analysis of the field dependence of pinning force density $F_P = J_C \times H$ is done using the Dew-Hughes model [50]. Except in the as-cast and annealed samples of the $\text{Ti}_{0.8}\text{V}_{0.2}$ alloy, the pinning force in all the $\text{Ti}_x\text{V}_{1-x}$ alloys (both the as-cast and annealed) in the field regime of the main magnetic irreversibility arises primarily from the flux-line pinning by normal surface pins [19, 20]. The grain boundaries, edge dislocations and martensitic α phase boundaries (in annealed $\text{Ti}_{0.7}\text{V}_{0.3}$ alloy) constitute

the sources of such normal surface pinning centers in these alloys [19, 20]. In the as-cast and annealed samples of the $\text{Ti}_{0.8}\text{V}_{0.2}$ alloy, flux-line pinning occurs predominantly at normal point pins while the role of normal surface pins is prominent at relatively lower fields [19]. Substantial amount of ω phase available in the as-cast and annealed samples of these alloys functions as normal point pinning centers [19]. We will then present the effect of thermal fluctuations on the high field critical current density in these alloys. The peak effect is observed in the isothermal $M(H)$ curves in high-field regime near H_{C2} in all the present alloys except annealed $\text{Ti}_{0.7}\text{V}_{0.3}$. The peak effect in various superconductors occurs due to a field induced transition in the flux-line lattice from a phase of low to high flux pinning characteristic [51]. The nature of this phase transition has been investigated by using a minor hysteresis loop (MHL) technique [51] which revealed various characteristic features i. e., metastability, and superheating/supercooling associated with a first order phase transition. Moreover, we have estimated the equilibrium magnetization (M_{eq}), which exhibits a clear jump in the PE regime. This was used for the estimation of the latent heat with the help of the Clausius-Clapeyron relation. At 2 K, latent heat comes out to be $L \sim 35.7 \mu\text{J/g}$ for the annealed $\text{Ti}_{0.8}\text{V}_{0.2}$ alloy whereas $L \sim 70 \mu\text{J/g}$ at 4 K for annealed $\text{Ti}_{0.4}\text{V}_{0.6}$ alloy. These results provide further support that the PE in the $\text{Ti}_x\text{V}_{1-x}$ alloys is associated with a first order phase transition in the vortex matter.

In **Chapter 8 (Vortex-glass to vortex-liquid transition in annealed $\text{Ti}_{0.7}\text{V}_{0.3}$ alloy)**, we will present the experimental study of vortex-solid to vortex-liquid phase transition [52-54] in the $\text{Ti}_{0.7}\text{V}_{0.3}$ alloy through the measurement of electrical resistivity in presence of various constant magnetic fields up to 50 kOe. We found that both the width of the normal to superconducting phase transition in the alloy, and the tail in the electrical resistivity observed before achieving the zero resistivity state increase with increasing magnetic field. Using the Arrhenius relation, we have identified a vortex-glass to vortex-liquid phase transition in this low T_C superconductor. We have also identified a critical region corresponding to this phase transition and obtained the critical exponent for the same. We have used a modified vortex-glass model to separate out the temperature and field dependent parts of the effective pinning energy. The field dependent part of the effective pinning energy exhibits power law dependence on the applied magnetic field, and both the temperature and field dependent parts of the effective pinning energy indicate a crossover of behavior close to the vortex-glass to vortex-liquid phase transition in the alloy. This change of behavior might be because of a crossover from a regime of single vortex pinning dominate to a regime of collective vortex pinning tends to dominate.

In **Chapter 9 (High-field paramagnetic Meissner effect in $\text{Ti}_x\text{V}_{1-x}$ alloys)**, we will present the study related to an anomalous feature in the samples of annealed $\text{Ti}_{0.7}\text{V}_{0.3}$ and as-cast as well as annealed $\text{Ti}_{0.8}\text{V}_{0.2}$ alloys. In contrast to conventional type-II superconductor, the magnetization in these samples is observed to increase when temperature is decreased below the T_C in presence of high magnetic fields beyond a certain critical value. In this field and temperature regime, it is observed that the

magnetization values in the field cooled cooling (FCC) protocol have a smaller magnitude as compared to that in the field cooled warming (FCW) protocol. We have also observed that the magnetization at a constant temperature well below T_C when cooled in the presence of high magnetic fields increases with time. These observed features are characteristics of the high-field paramagnetic Meissner effect (HFPME) [55-58]. We argue that the HFPME is observed in these alloys due to the non-uniform flux-line pinning at the boundary of the inhomogeneously distributed α' or α phases [20]. As stated in Chapter 2, the α' phase in both the as-cast and annealed samples of $Ti_{0.8}V_{0.2}$ alloy is a stress induced phase which forms during the mechanical processing such as cutting of the sample. We therefore remove the α' phase from the annealed sample of $Ti_{0.8}V_{0.2}$ alloy, which shows the signature of HFPME, by carrying out a second stage annealing following the same protocol employed during the first annealing [20]. HFPME becomes completely suppressed in this re-annealed sample suggesting that the non-uniform flux density promoted by pinning at α' or α phase is indeed the reason for the occurrence of HFPME in $Ti_{0.8}V_{0.2}$ and $Ti_{0.7}V_{0.3}$ alloys. Our studies suggest that the observation of HFPME in these alloys is due to the inhomogeneous flux pinning and the trapping of the flux lines at the α' or α phase boundary, which creep from rest of the sample volume.

In **Chapter 10 (Summary, Conclusion and Future work)**, we will present the summary and the conclusions drawn from the study and the scope for the further studies. The important conclusions are listed below:

- (1) The superconducting transition temperature T_C of the present alloys is higher than the constituent elements Ti and V. The experimentally observed T_C , however, is much less than that estimated by considering the electron-phonon interaction alone.
- (2) The Ginzburg number G_i for these Ti_xV_{1-x} alloys are estimated to be about $10^{-6} - 10^{-5}$ indicating the significant influence of the thermal fluctuations in these alloys. Such thermal fluctuations contribute to the observation of fluctuation conductivity well above T_C .
- (3) The presence of spin fluctuations in V rich Ti_xV_{1-x} alloys is inferred from the normal state properties. We have shown that the spin fluctuations present in these alloys are itinerant in nature.
- (4) The variation of T_C with composition in the Ti_xV_{1-x} alloys is explained by considering the electron-phonon interaction and spin fluctuations. We also provide an explanation based on the distribution of the electron-spin fluctuation interaction for the observed fluctuation conductivity above T_C .
- (5) Grain boundaries, edge dislocations, ω phase, and α (or α') phase boundaries seem to be the sources of the flux-line pinning mechanisms in these superconducting alloys. The irreversibility field H_{irr} particularly in Ti rich Ti_xV_{1-x} alloys is observed to be lower than H_{C2} due to the increased role of thermal fluctuations which ultimately resulted in the suppression of the high-field J_C in these alloys.

(6) The relatively strong flux line pinning along with thermal fluctuation effects in annealed $\text{Ti}_{0.7}\text{V}_{0.3}$ alloy resulted in the formation of the Bose Glass phase in the mixed state of this superconductor. A difference is observed between the observed properties at high and low field regime when the data is analyzed with the existing scaling law. A new scaling law is proposed to resolve this difference.

(7) We have observed the high field paramagnetic effect in $\text{Ti}_{0.8}\text{V}_{0.2}$ alloy and annealed $\text{Ti}_{0.7}\text{V}_{0.3}$ alloy. We have shown that this effect results from the inhomogeneous flux pinning due to the presence of stress induced martensitic α' phase in $\text{Ti}_{0.8}\text{V}_{0.2}$ alloy, whereas it is resulted from the inhomogeneous flux pinning due to the presence of α phase in $\text{Ti}_{0.7}\text{V}_{0.3}$ alloy. We have shown that the high field paramagnetic effect is related with the flux pinning and can result wherever the inhomogeneous pinning centers are present.

References:

- [1] T. Noda, T. Takeuchi, and M. Fujita, *J. Nucl. Mat.* 329-333, 1590-1593 (2004)
- [2] T. Noda, K. Maki, T. Takeuchi, H. Suzuki, H. Araki, and W. Yang, *Fusion Eng. and Des.* 81, 1033-1037 (2006)
- [3] See, e.g., S. V. Vonsovsky, Yu. A. Izyumov and E. Z. Kurmaev in *Superconductivity of Transition Metals: Their Alloys and compounds* (Translated by E. H. Brandt and A. P. Zavaritsyn) (Springer Verlag, Berlin, 1982) and the references therein.
- [4] J. B. Vetrano, G. L. Guthrie, H. E. Kissinger, J. L. Brimhall, and B. Mastel, *J. Appl. Phys.* 39, 2524 (1968)
- [5] M. Tai, K. Inoue, A. Kikuchi, T. Takeuchi, T. Kiyoshi, and Y. Hishinuma, *IEEE Trans. Appl. Supercond.* 17, 2542 (2007), and references therein.
- [6] T. Takeuchi, H. Takigawa, M. Nakagawa, N. Banno, K. Inoue, Y. Iijima, and A. Kikuchi, *Supercond. Sci. Technol.* 21, 025004 (2008)
- [7] E. W. Collings in *Applied Superconductivity, Metallurgy, And Physics Of Titanium Alloys Vol. 1 & 2*, (Plenum Press, New York, 1986)
- [8] E. W. Collings, P. E. Upton, J. C. Ho, *J. Less-Comm. Metals*, 42, 285 (1975)
- [9] R. Aoki and T. Ohtsuka, *J. Phys. Soc. Japan*, 23, 955 (1967)
- [10] R. Aoki and T. Ohtsuka, *J. Phys. Soc. Japan*, 26, 651 (1969)
- [11] P. W. Anderson, *J. Phys. Chem. Solids* 11, 26 (1959)
- [12] B. Sacepe, T. Dubouchet, C. Chapelier, M. Sanquer, M. Ovadia, D. Shahar, M. Feigelman, L. Ioffe, *Nature Phys.* 7, 239 (2011) and the references therein.
- [13] R. R. Hake, *Phys. Rev. Lett.* 23, 1105 (1969)
- [14] R. R. Hake, *Phys. Lett.* 32A, 143 (1970)
- [15] J. W. Lue, A. G. Montgomery, R. R. Hake, *Phys. Rev. B* 11, 3393 (1975)

- [16] Md. Matin, L. S. Sharath Chandra, Radhakishan Meena, M. K. Chattopadhyay, M. N. Singh, A. K. Sinha and S. B. Roy, *Physica B* 436, 20 (2014)
- [17] Md. Matin, L. S. Sharath Chandra, S. K. Pandey, M. K. Chattopadhyay, and S. B. Roy, (Communicated)
- [18] Md. Matin, L. S. Sharath Chandra, M. K. Chattopadhyay, R. K. Meena, Rakesh Kaul, M. N. Singh, A. K. Sinha and S. B. Roy, *J. Appl. Phys.* 113, 163903 (2013)
- [19] Md. Matin, L. S. Sharath Chandra, M. K. Chattopadhyay, R. K. Meena, Rakesh Kaul, M. N. Singh, A. K. Sinha, and S. B. Roy, (Communicated)
- [20] Md. Matin, L. S. Sharath Chandra, M. K. Chattopadhyay, M. N. Singh, A. K. Sinha and S. B. Roy, *Supercond. Sci. Technol.* 26, 115005 (2013)
- [21] Md. Matin, L. S. Sharath Chandra, M. K. Chattopadhyay, and S. B. Roy, (Communicated)
- [22] Md. Matin, L. S. Sharath Chandra, M. K. Chattopadhyay, and S. B. Roy (unpublished)
- [23] Ch. Leibovitch, A. Rabinkin, and M. Talianker, *Metall. Trans. A* 12, 1513 (1981)
- [24] G. Aurelio, A. F. Guillermet, G. J. Cuello, and J. Campo, *Metall. Mater. Trans. A* 33, 1307 (2002)
- [25] C. H. Cheng, K. P. Gupta, E. C. Van Reuth, and Paul. A. Beck, *Phys. Rev.* 126, 2030 (1962)
- [26] G. Bergmann, *Phys. Rev. B* 7, 4850 (1973)
- [27] T. P. Orlando, E. J. McNiff, Jr. and S. Foner, and M. R. Beasley, *Phys. Rev. B* 19, 4545 (1979)
- [28] V. L. Ginzburg and L. D. Landau, *Zh. Eksperim. i Theo. Fiz.* 20, 1064 (1950)
- [29] A. A. Abrikosov, *Zh. Eksperim. i Theo. Fiz.* 32, 1442 (1957) [*Soviet Phys. –JETP* 5, 1174 (1957)]
- [30] L. P. Gor'kov, *Zh. Eksperim. i Theo. Fiz.* 36, 1918 (1959) [*Soviet Phys. –JETP* 9, 1364 (1959)]
- [31] L. P. Gor'kov, *Zh. Eksperim. i Theo. Fiz.* 37, 835 (1959) [*Soviet Phys. –JETP* 10, 593 (1960)]
- [32] K. J. Song, C. Park, S. S. Oh, Y. K. Kwon, J. R. Thompson, D. G. Mandrus, D. McK. Paul, and C. V. Tomy, *Physica C* **398**, 107 (2003)
- [33] A. D. Hernandez, B. J. Baelus, D. Dominguez, and F. M. Peeters, *Phys. Rev. B* 71, 214524 (2005)
- [34] L. G. Aslamazov and A. I. Larkin, *Phys. Lett. A* 26, 238 (1968)
- [35] K. Maki, *Prog. Theor. Phys.* 40, 193 (1968)
- [36] R. S. Thompson, *Phys. Rev. B* 1, 327 (1970)
- [37] W. L. Johnson and C. C. Tsuei, *Phys. Rev. B* 13, 4827 (1976)
- [38] A. I. Schindler and B. R. Coles (1968) *J. Appl. Phys.* 39, 956 (1968)
- [39] S. Misawa and K. Kanematsu, *J. Phys. F: Met. Phys.* 6, 2119 (1976)
- [40] G. Barnea, *J. Phys. C: Solid State Phys.* 8, L216 (1975)
- [41] H. Rietschel and H. Winter, *Phys. Rev. Lett.* 43, 1256 (1979)

- [42] C. Candolfi, B. Lenoir, A. Dauscher, C. Bellouard, J. Hejtmanek, E. Santava, and J. Tobola, Phys. Rev. Lett. 99, 037006 (2007)
- [43] K. Kadowaki and S. B. Woods, Solid State Commun. 58, 507 (1986)
- [44] W. L. McMillan, Phys. Rev. 167, 331 (1968)
- [45] J. M. Daams, B. Mitrovic, and J. P. Carbotte, Phys. Rev. Lett. 46, 65 (1981)
- [46] Z. Altounian and J. O. Strom-Olsen, Phys. Rev. B 27, 4149 (1983)
- [47] A. Junod, T. Jarlborg, and J. Muller, Phys. Rev. B 27, 1568 (1983)
- [48] G. Riblet, Phys. Rev. B 3, 91 (1971)
- [49] C. P. Bean, Rev. Mod. Phys. 36, 31 (1964)
- [50] D. Dew-Hughes, Phil. Mag. 30, 293 (1974)
- [51] S. B. Roy, P. Chaddah, and S. Chaudhary, Phys. Rev. B 62, 9191 (2000); and references therein.
- [52] H. Safar, P. L. Gammel, D. J. Bishop, D. B. Mitzi, and A. Kapitulnik, Phys. Rev. Lett. 68, 2672 (1992).
- [53] P. Wagner, U. Frey, F. Hillmer, and H. Adrian, Phys. Rev. B 51, 1206 (1995)
- [54] B. Lundqvist, J. Larsson, A. Herting, O. Rapp, M. Andersson, Z. G. Ivanov, and L.-G. Johansson, Phys. Rev. B 58, 6580 (1998)
- [55] A. Terentiev, D. B. Watkins, L. E. De Long, D. J. Morgan, and J. B. Ketterson, Phys. Rev. B 60, R761 (1999)
- [56] W. A. C. Passos, P. N. Lisboa-Filho, G. L. Fraga, F. W. Fabris, P. Pureur, and W. A. Ortiz, Brazillian Journal of Physics 32, 777 (2002)
- [57] F. T. Dias, P. Pureur, Jr. P. Rodrigues, and X. Obradors, Phys. Rev. B 70, 224519 (2004)
- [58] C. Z. Chen, C. B. Cai, L. Peng, Z. Y. Liu, Y. M. Lu, H. W. Wang, and X. M. Xie, Europhys. Lett. 89, 37005 (2010)

List of Figures

1.1	Temperature dependence of resistivity of mercury as measured by Kamerlingh Onnes in 1911.	9
1.2	(Schematic) Demonstration of the Meissner-Ochsenfeld effect.	10
1.3	Reversible magnetization curves as a function of applied field for ideal type-I and type-II superconductors (schematic). . . .	16
1.4	The variation of the order parameter and the magnetic field profile inside an isolated superconducting flux line; and the Abrikosov flux-line lattice in the mixed state of a type-II superconductor (schematic).	18
1.5	Flux-line lattice in $\text{Ba}_{0.6}\text{K}_{0.4}\text{Fe}_2\text{As}_2$ and 2H-NbSe_2 superconductors observed by the scanning tunnelling microscopy experiments.	19
1.6	(Schematic) The field dependence of magnetization for type-II superconductor.	23
1.7	Voltage-current ($V - I$) characteristic curves of a type-II superconductor (schematic).	25
1.8	The magnetic field penetration profile and the associated critical current density inside a superconducting sample at various stage of applied magnetic fields (schematic).	26
1.9	A schematic field-temperature ($H - T$) phase diagram of type-II superconductors.	29
1.10	Equilibrium and non-equilibrium phase diagram of the binary Ti-V alloy system.	31
1.11	Optical and electron micrographs of the Ti-V samples to show the ω and the stress-induced α' phases in these samples. . . .	33
1.12	Residual resistivity ρ_0 and the temperature dependence of resistivity of various Ti-V alloys.	35

1.13	Debye temperature and Sommerfeld coefficient of the Ti-V alloys; and the temperature dependence of magnetic susceptibility χ of various Ti-V alloys.	36
1.14	Superconducting transition temperature T_C and upper critical field H_{C2} of the Ti-V alloys.	39
1.15	$V - I$ characteristic curves and critical current density for the $\text{Ti}_{0.8}\text{V}_{0.2}$ alloy at 4.2 K.	43
1.16	Temperature and magnetic field dependence of the resistivity of the Ti-V alloys	45
2.1	Arc melting furnace used for the preparation of the Ti-V samples.	53
2.2	Schematic of the X-ray diffraction from lattice planes.	55
2.3	XRD pattern of annealed $\text{Ti}_{0.8}\text{V}_{0.2}$ alloy obtained using X-ray from laboratory source and synchrotron radiation source.	57
2.4	Optical micrographs showing the grain structures in the annealed $\text{Ti}_{0.6}\text{V}_{0.4}$ alloy and the presence of martensite α phase in the main β phase matrix of the $\text{Ti}_{0.7}\text{V}_{0.3}$ alloy.	58
2.5	Schematic diagram of different components of a vibrating sample magnetometer.	61
2.6	A schematic presentation of the experimental configuration in the Quantum Design MPMS SQUID magnetometer used to measure the magnetization.	63
2.7	Schematic diagram of the calorimeter used in the PPMS Heat Capacity option.	66
3.1	XRD patterns of the Ti-V alloys.	77
3.2	Rietveld refinement of X-ray diffraction pattern of the annealed $\text{Ti}_{0.8}\text{V}_{0.2}$ sample.	78
3.3	Optical micrographs showing of the Ti-V samples	81
3.4	Optical micrographs showing of the Ti-V samples	82
3.5	Optical micrographs showing the formation of the martensite α phase in the annealed samples of $\text{Ti}_{0.7}\text{V}_{0.3}$ and $\text{Ti}_{0.4}\text{V}_{0.6}$ alloys, and the stress induced martensite α' phase in both annealed and as cast $\text{Ti}_{0.8}\text{V}_{0.2}$ samples.	85
4.1	Temperature dependence of resistivity, magnetization, and heat capacity of the $\text{Ti}_x\text{V}_{1-x}$ alloys at low temperatures; and the T_C values of these alloys as a function Ti concentration	91

4.2	Temperature dependence of heat capacity for the Ti-V alloys (plotted as C/T versus T^2); and the Sommerfeld coefficient γ and the Debye temperature θ_D of the Ti-V alloys.	93
4.3	Electronic density of state for the β phase Ti-V alloys.	96
4.4	Magnetic field dependence of magnetization for the $\text{Ti}_{0.7}\text{V}_{0.3}$ alloy at various constant temperatures below T_C	98
4.5	Temperature dependence of H_{C2} of the Ti-V alloys; and the fitting of the $H_{C2}(T)$ data based on the model given by Orlando <i>et al.</i>	100
4.6	Magnetic field dependence of magnetization at different constant temperatures below T_C ; and the deviation from linearity δM as a function of effective magnetic field H_e for the $\text{Ti}_{0.6}\text{V}_{0.4}$ alloy.	109
4.7	The temperature dependence of H_{C1} of the Ti-V alloys.	111
4.8	Temperature dependence of the thermodynamic critical field H_C for the Ti-V alloys.	115
4.9	M versus $\ln(H)$ curves for the $\text{Ti}_{0.6}\text{V}_{0.4}$ alloy at different constant temperatures; and the temperature dependence of the penetration depth λ for the $\text{Ti}_{0.6}\text{V}_{0.4}$ alloy.	118
5.1	Temperature dependence of resistivity for the Ti-V alloys showing the rounding-off behaviour of the resistive transition above T_C	129
5.2	Plots of $G_i T_C$ and the temperature window where the rounding-off behaviour of the resistive transition is observed in the Ti-V alloys to show the correlation between the enhanced conductivity above T_C and the thermal fluctuations.	130
5.3	Experimental excess conductivity for the Ti-V alloys as a function of reduced temperature $\varepsilon = (T - T_C)/T_C$ in <i>log-log</i> scales.	135
5.4	$\Delta\sigma(\varepsilon)$ curves for the $\text{Ti}_{0.6}\text{V}_{0.4}$ alloy plotted in <i>log-log</i> scales using different choice of T_C	137
5.5	The temperature dependence of the electrical resistivity and heat capacity of the $\text{Ti}_{0.8}\text{V}_{0.2}$ alloy to show the presence of T_C distribution in this alloy.	138
5.6	Magneto-resistance data of the Ti-V alloys, and the fittings of the magneto-resistance data with the theoretical model of Usadel.	141

6.1	Temperature dependence of heat capacity of the Ti-V alloys. .	146
6.2	The plots of $C_L T^{-3}$ against $\ln(4.928T)$; and $(4/5)R\pi^2\omega^{-2}F(\omega)$ as a function of $\ln(\omega)$ for the Ti-V alloys.	149
6.3	Temperature dependence of dc magnetic susceptibility for the Ti-V alloys.	152
6.4	Temperature dependence of resistivity of the Ti-V alloys in temperature range 10-300 K.	156
6.5	Temperature dependence of electrical resistivity of the Ti-V alloys to show the T^2 dependence of resistivity ρ at low temperatures in $\text{Ti}_{0.6}\text{V}_{0.4}$ and $\text{Ti}_{0.4}\text{V}_{0.6}$ alloys and a $-\ln T$ dependence of resistivity in $\text{Ti}_{0.7}\text{V}_{0.3}$ alloy.	157
6.6	Temperature dependence of resistivity of the $\text{Ti}_{0.8}\text{V}_{0.2}$ alloy. .	164
6.7	Kadowaki-Woods scaling for the $\text{Ti}_{0.6}\text{V}_{0.4}$ and $\text{Ti}_{0.4}\text{V}_{0.6}$ alloys. .	166
7.1	Magnetic field dependence of magnetization curves for few selected Ti-V alloys at various constant temperatures below their respective T_C	172
7.2	Temperature dependence of H_{C2} and H_{Irr} for the Ti-V alloys. .	174
7.3	Magnetic field dependence of critical current density for the Ti-V alloys at various constant temperatures below their T_C . .	176
7.4	Magnetic field dependence of the pinning force density for the Ti-V alloys at various constant temperatures below their T_C . .	179
7.5	Estimation of the scaling field H^* from $J_C(H)$ data.	183
7.6	Normalized pinning force curves for the annealed $\text{Ti}_{0.8}\text{V}_{0.2}$ alloy. .	183
7.7	Normalized pinning force curves for the as cast $\text{Ti}_{0.8}\text{V}_{0.2}$ alloy. .	185
7.8	Normalized pinning force curves for both the annealed and as cast $\text{Ti}_{0.7}\text{V}_{0.3}$ alloys.	186
7.9	Normalized pinning force curves for the annealed $\text{Ti}_{0.6}\text{V}_{0.4}$ alloy. .	187
7.10	Normalized pinning force curves for the as cast $\text{Ti}_{0.6}\text{V}_{0.4}$ alloy. .	189
7.11	Normalized pinning force curves for both the annealed and as cast $\text{Ti}_{0.4}\text{V}_{0.6}$ alloys.	189
7.12	$M(H)$ curves to show the peak-effect in $\text{Ti}_{0.8}\text{V}_{0.2}$ alloy. . . .	195
7.13	Construction of minor hysteresis loops within the peak-effect regime of the annealed $\text{Ti}_{0.8}\text{V}_{0.2}$ alloy.	196
8.1	Temperature dependence of electrical resistivity of annealed $\text{Ti}_{0.7}\text{V}_{0.3}$ alloy at low temperatures and in different magnetic fields.	206

8.2	Arrhenius plots for the annealed $\text{Ti}_{0.7}\text{V}_{0.3}$ alloy.	209
8.3	The plots of $[d(\ln\rho)/dT]^{-1}$ against temperature for the annealed $\text{Ti}_{0.7}\text{V}_{0.3}$ sample for 5 and 0.5 T magnetic fields.	210
8.4	Critical exponent s for the annealed $\text{Ti}_{0.7}\text{V}_{0.3}$ alloy as a function of magnetic field; and optical micrograph and SEM images of the same alloy	211
8.5	Effective pinning energy U_0 for the annealed $\text{Ti}_{0.7}\text{V}_{0.3}$ alloy.	215
8.6	Scaling behaviour of the vortex-liquid resistivity of annealed $\text{Ti}_{0.7}\text{V}_{0.3}$ alloy following the modified vortex-glass model.	219
8.7	The field-temperature ($H-T$) phase diagram for the annealed $\text{Ti}_{0.7}\text{V}_{0.3}$ sample	222
9.1	Evolution of the temperature dependence of the FCC and FCW magnetization with increasing magnetic field up to 3 T for the annealed $\text{Ti}_{0.8}\text{V}_{0.2}$ sample.	230
9.2	The evolution of the temperature dependence of the FCC and FCW magnetization with increasing magnetic field in the as cast $\text{Ti}_{0.8}\text{V}_{0.2}$ and annealed $\text{Ti}_{0.7}\text{V}_{0.3}$ samples.	232
9.3	Optical micrographs showing the spatial distribution of α phase in the annealed $\text{Ti}_{0.7}\text{V}_{0.3}$ and α' phase in the annealed and as cast $\text{Ti}_{0.8}\text{V}_{0.2}$ samples.	235
9.4	Temperature dependence of the FCC and FCW magnetization to show the disappearance of the HFPME in the annealed $\text{Ti}_{0.8}\text{V}_{0.2}$ sample after removing the α' phase from this sample.	237
9.5	Optical micrograph and the temperature dependence of the ZFC, FCC and FCW magnetization of the of annealed $\text{Ti}_{0.4}\text{V}_{0.6}$ sample.	238
9.6	Time dependence of the FCC magnetization for few selected samples of the Ti-V alloys.	241
9.7	Temperature dependence of FCC magnetization for the as cast and annealed $\text{Ti}_{0.8}\text{V}_{0.2}$ samples in two different temperature sweep rate.	244

List of Tables

3.1	Volume fraction and lattice parameters of different constituent phases present in the as cast and annealed samples of Ti-V alloys.	79
3.2	Average grain size in the Ti-V alloys.	83
4.1	Comparison of the experimentally measured T_C values of the Ti-V alloys with those estimated from the McMillan formula. .	98
4.2	Few important parameters in the superconducting and normal state of the Ti-V alloys.	102
4.3	Various fundamental parameters in the superconducting state of the Ti-V alloys.	119
5.1	The superconducting transition temperature and the coherence length of the Ti-V alloys.	139
6.1	T_C of the Ti-V alloys estimated with the help of the Allen-Dynes form of the McMillan formula using $\mu^*=0.12$ and, $\bar{\omega}_{log}$ and λ_{ep} obtained from the heat capacity data.	151
6.2	Various parameters estimated from the temperature dependence of dc magnetic susceptibility of the Ti-V alloys in their normal state.	155
6.3	The electron-phonon coupling constant λ_{ep} and the electron-spin fluctuation coupling constant λ_{sf} for the Ti-V alloys. . . .	169

Chapter 1

Introduction

1.1 General introduction

The thermonuclear reactors are potential sources of green and safe energy [1]. Superconducting Tokamak is an essential component of such thermonuclear reactors, which magnetically confines the hydrogen plasma that is used to generate electrical power [2]. The radiation and high energy particles generated in thermonuclear reactors can induce radioactivity in the materials that are used to construct the reactor. Thus, the superconducting material used to construct the magnet for the thermonuclear reactors might become radioactive in long run. The superconducting materials currently being used in the superconducting Tokamak are the Nb-based alloys such as Nb-Ti [2]. Some of the radioactive Nb isotopes, however, have very long half-life (few hundreds to few thousands of years). In fact, some of the artificially created

radioactive isotopes of Nb may have the half-life period as long as about 35 million years [3, 4]. Therefore, the nuclear waste management of the Nb-based alloys used in the thermonuclear reactors is an important issue, which could lead to hazardous consequences [5]. Thus, there is a need for newer superconducting materials with useful properties from radioactivity points of view. In this direction, a significant interest is now focused on other transition element alloy superconductors. One such system is the Ti-V alloys, which were known to be superconductors for a long time [6]. The longest half-life of artificially created radioactive vanadium is known to be around 330 days [3, 4]. Therefore V-based alloys, especially V-Ti alloys are considered to be one of the suitable candidates for superconducting magnet applications in thermonuclear reactors [5]. Previous studies on the Ti-V alloys indicate that these alloys are highly machinable and could be an alternative material for technological applications [5, 7, 8]. However, the usage of the Ti-V alloys in the actual technological applications has been rather limited so far because of the lack of in-depth studies of the superconducting and normal state properties of these materials.

In this thesis a detailed study of the superconducting as well as normal state properties of the Ti-V alloys are presented. In the current chapter, we present a brief discussion on the basics of superconductivity, which is followed by a discussion on the experimental results on the superconducting and normal state properties of the Ti-V alloys available in the literature. The motivation for the present studies is given at the end of this chapter.

1.2 Basics of superconductivity

1.2.1 A brief history of superconductivity

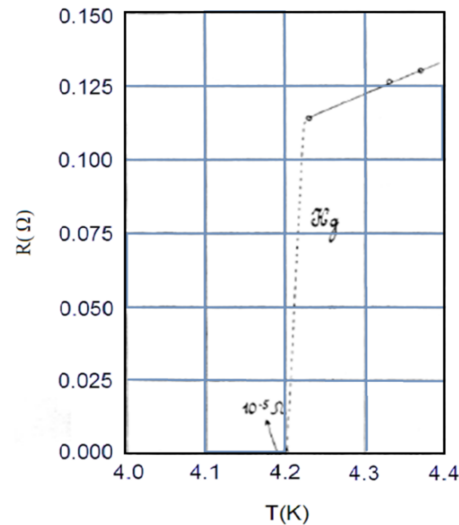


Figure 1.1: Temperature dependence of resistivity of mercury as measured by Kamerlingh Onnes in 1911. The figure is taken from Ref. [11].

The discovery of superconductivity in mercury by H. Kamerlingh Onnes [9] in the year of 1911 is an important milestone of low temperature physics. In the course of his experiments on the electric conductivity of mercury at low temperatures, he had observed that the dc electrical resistance of mercury drops abruptly to zero below a critical temperature $T_C = 4.19$ K [9]. Following the discovery of superconductivity in mercury, H. Kamerlingh Onnes had observed that other elements such as tin, lead etc. also exhibit zero resistance below a certain T_C (specific to each metal) [10]. The exhibition of zero resistance is a characteristic feature of a superconductor.

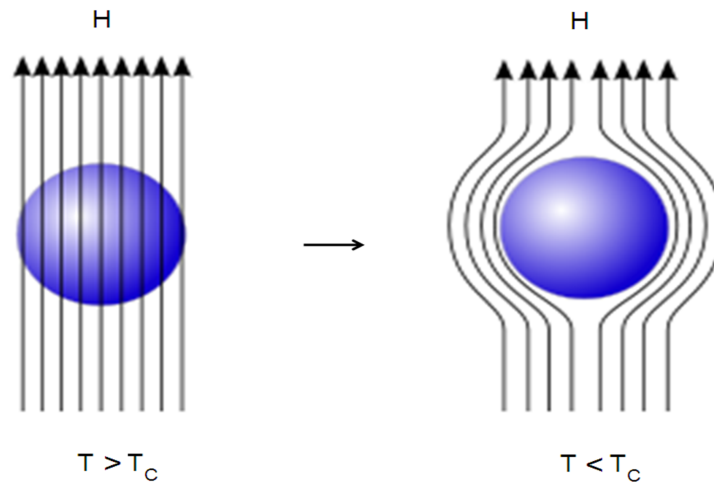


Figure 1.2: (Schematic) Demonstration of the Meissner-Ochsenfeld effect. When the sample is cooled below T_C in the presence of a magnetic field lower than H_C , the magnetic flux is expelled from the interior of the superconductor. The figure is taken from Ref. [11].

Twenty two years later, Meissner and Ochsenfeld [12] discovered that these superconductors expel magnetic flux from their interiors and exhibit perfect diamagnetism. This phenomenon is known as Meissner-Ochsenfeld effect, and is shown schematically in Fig. 1.2. F. London and H. London [13] were first able to explain the Meissner-Ochsenfeld effect based on a semi-phenomenological approach. They had argued that the magnetic field penetrates only through a thin layer at the sample surface. The characteristic length scale over which the magnetic field can penetrate the sample is known as the London penetration depth λ_L . A superconductor, however, exhibits Meissner-Ochsenfeld effect only in the presence of an applied magnetic field less than a critical field H_C (typically few hundreds of mT for most of the

elemental superconductors). As the applied field is increased to the critical field H_C , the superconducting sample reverts to its normal conducting state, and the magnetic field penetrates throughout the sample.

In the year of 1950, Maxwell [14] and Reynolds *et al.* [15] had discovered that the T_C varies with the mass of the atom for different isotopes as $T_C \propto M^{-n}$, where M is the ionic mass and n is equal to 0.5 for most of the metals. This is known as the *isotope effect*. The isotope effect provides a strong support to the view-point that the electron-phonon interaction is important for the occurrence of superconductivity. However, the understanding of the phenomenon of superconductivity became clear only 46 years after the discovery of the phenomenon, when Bardeen, Cooper, and Schrieffer [16] had put forward their microscopic theory (the *BCS theory*) in the year of 1957. According to the BCS theory, the interaction between the conduction electrons and the quantized excitation of the lattice (phonons) can give rise to an additional interaction between the electrons themselves. In certain circumstances this interaction between the electrons can be attractive. A very similar attractive interaction between the electrons mediated by phonons was also shown by Frohlich [17] prior to the formulation of the BCS theory. However, the major triumph of the BCS theory lies in the fact that this theory describes the formation of electron pairs and their subsequent condensation in a coherent superconducting state, which is represented by a single superconducting wave function. The attractive interaction between the electrons leads to the formation of electron pairs known as the Cooper

pairs, and opens up a gap in the electronic density of states around the Fermi energy. The BCS theory successfully explains most of the observed features of superconductivity such as zero resistivity, the Meissner-Ochsenfeld effect, the isotope effect, existence of superconducting energy gap etc.

1.2.2 The critical temperature

The temperature at which a superconducting material undergoes a transition from normal to superconducting state upon cooling is called the critical temperature or the superconducting transition temperature T_C of the superconducting material. According to the BCS theory, the critical temperature T_C of a superconductor can be expressed as [16]

$$k_B T_C = 1.14 \langle \hbar\omega \rangle_{av} \exp \left[-\frac{1}{N(E_F)V} \right]. \quad (1.1)$$

Where, $\langle \hbar\omega \rangle_{av}$ is the average phonon energy, $N(E_F)$ is the electronic density of states at Fermi energy, and V is the interaction potential between the Cooper pairs. By substituting $(3/4)k_B\theta_D$ for $\langle \hbar\omega \rangle_{av}$, as suggested by Goodman *et al.* [18], we have

$$T_C = 0.855\theta_D \exp \left[-\frac{1}{N(E_F)V} \right]. \quad (1.2)$$

Here, θ_D is the Debye temperature. The above expression for T_C is, however, valid in the weak-coupling limit. McMillan [19] had derived a strong-coupling

expression for T_C based on the Eliashberg theory. The McMillan expression for T_C is given as [19]

$$T_C = \frac{\theta_D}{1.45} \exp \left[\frac{-1.04(1 + \lambda_{ep})}{\lambda_{ep} - \mu^*(1 + 0.62\lambda_{ep})} \right]. \quad (1.3)$$

where, $\lambda_{ep} = N(E_F)V$ is the electron-phonon coupling constant and μ^* is the Coulomb interaction parameter.

1.2.3 The Ginzburg-Landau phenomenological theory

Ginzburg and Landau had developed a phenomenological theory for the phase transition from normal to superconducting state based on Landau's original theory for the second-order phase transitions [20]. Landau had argued that the transition from normal to superconducting state occurs because the free energy of the superconducting phase is lower than that of the normal phase. The Landau theory introduces the concept of an order parameter associated with a second order phase transition [20]. The order parameter vanishes in the high-temperature phase at $T > T_C$, but acquires a non-zero value at the low-temperature phase at $T < T_C$. Here, T_C is the critical temperature for the second order phase transition. In the phenomenological Ginzburg-Landau theory for superconductivity, the existence of a wave function Ψ for the coherent superconducting state is assumed, and this wave function was taken as the order parameter associated with the phase transition from normal to superconducting state. Since the order parameter evolves contin-

uously from zero value at T_C , the free energy is expanded in the temperature regime close to T_C as a power series in this order parameter as [21]

$$F = F_0 + \int [a|\Psi(\vec{r})|^2 + \frac{1}{2}b|\Psi(\vec{r})|^4 + \frac{\hbar^2}{2m^*}|\vec{\nabla}\Psi(\vec{r}) - \frac{ie^*}{\hbar c}\vec{A}(\vec{r})\Psi(\vec{r})|^2 + \frac{1}{2}\mu_0 H^2(\vec{r})]dV. \quad (1.4)$$

Here, the integration is performed over the sample volume. In the above expression, F_0 is the free energy of the sample in its normal state, H is the internal magnetic field, the parameters a and b are functions of temperature, \hbar is the reduced planck's constant, μ_0 is the permeability of the free space, and c is the speed of light. The parameters e^* and m^* are chosen as respectively the mass and the charge of the superconducting entities so that the third term in the square bracket mimics the quantum mechanical kinetic energy term. The increase in the energy due to the spatial variation of order parameter caused by the sample inhomogeneity is taken into account by the gradient term in the above free energy expression. The minimization of the free energy given in the above expression (1.4) with respect to small changes in Ψ^* yields the first Ginzburg-Landau equation as

$$-\frac{\hbar^2}{2m^*} \left[\vec{\nabla} - \frac{ie^*}{\hbar c}\vec{A}(\vec{r}) \right]^2 \Psi(\vec{r}) + a\Psi(\vec{r}) + b|\Psi(\vec{r})|^2\Psi(\vec{r}) = 0. \quad (1.5)$$

The minimization of the free energy given in the expression (1.4) with respect to small changes in \vec{A} yields the second Ginzburg-Landau equation.

This second Ginzburg-Landau equation describes the super-current density flowing in a superconductor, and is given as

$$\vec{J}(\vec{r}) = -\frac{ie^*\hbar}{2m^*}[\Psi^*(\vec{r})\vec{\nabla}\Psi(\vec{r}) - \Psi(\vec{r})\vec{\nabla}\Psi^*(\vec{r})] - \frac{e^{*2}}{m^*c}|\Psi(\vec{r})|^2A(\vec{r}) \quad (1.6)$$

The Ginzburg-Landau equations [Eqns. (1.5) and (1.6)] provide two characteristic length scales for a superconductor, namely the Ginzburg-Landau penetration depth

$$\lambda = \sqrt{\frac{m^*c^2b}{4\pi e^{*2}|a|}}, \quad (1.7)$$

and, the Ginzburg-Landau coherence length

$$\xi = \sqrt{\frac{\hbar^2}{2m^*|a|}}. \quad (1.8)$$

The Ginzburg-Landau penetration depth λ is, like the London magnetic field penetration depth, a characteristic length scale for the decay of magnetic field in a superconductor while the Ginzburg-Landau coherence length ξ is a characteristic length scale for the decay of the superconducting order parameter. The parameter $\kappa = \lambda/\xi$ is known as the Ginzburg-Landau parameter. The κ value determines the magnetic behaviour a superconductor, and is useful to distinguish between two different classes of superconductors, namely, type-I and type-II superconductors. It is to be noted that the Ginzburg-Landau equations are derived from the series expansion of the free energy around T_C , and therefore, they are valid only in the close vicinity of T_C .

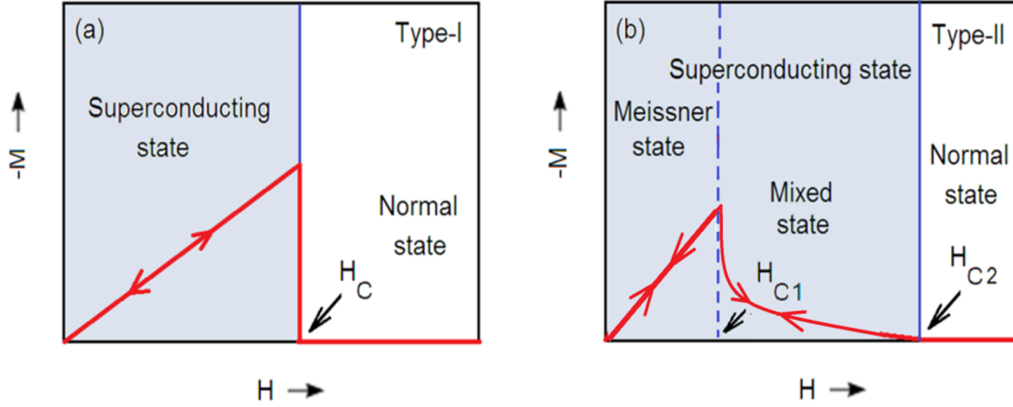


Figure 1.3: Reversible magnetization curves as a function of applied field for ideal type-I (a) and type-II (b) superconductors (schematic).

1.2.4 Type-I and type-II superconductors

Based on the value of the Ginzburg-Landau parameter κ , superconductors are categorized into two different classes. Superconductors with $\kappa < \frac{1}{\sqrt{2}}$ are categorized as the type-I superconductors. These superconductors exhibit perfect diamagnetism for magnetic fields up to the critical field H_C . The magnetic response exhibited by a type-I superconductor is shown schematically in Fig. 1.3(a). Most of the elemental superconductors are type-I in nature. Superconductors with $\kappa \geq \frac{1}{\sqrt{2}}$ are known as type-II superconductors. This class of superconductor exhibits perfect diamagnetism until a lower critical field H_{C1} is reached. For magnetic fields higher than H_{C1} , it is energetically more favourable for the superconductor to enter into a state called the mixed state where the magnetic flux lines (vortices) are first formed at the surface of the superconductor within a thickness of the order of

λ , and then penetrate into the interior of the superconductor. Each normal core of the flux-line carries one magnetic flux quantum $\Phi_0 (= 2.07 \times 10^{-7} \text{ G-cm}^2)$. Consequently, when the magnetic field is increased above H_{C1} , the flux lines penetrate the superconductor, and the diamagnetic magnetization starts to decrease suddenly. Flux penetration grows further until an upper critical field H_{C2} is reached. Eventually, the normal conducting state of the specimen is achieved at and above H_{C2} . The magnetic response of a type-II superconductor is presented in Fig. 1.3(b). All the alloys and inter-metallic compounds that exhibit superconductivity are of type-II category.

1.2.5 The superconducting mixed state and the flux-line lattice

The surface energy of the interface between a normal and a superconducting region is negative for a type-II superconductor. Hence, in the superconducting mixed state, the normal cores of the flux lines threading a superconducting material should be such that the surface to volume ratio of the normal cores is maximized. An energetically favourable configuration of the flux lines is one in which the superconducting material is threaded by cylinders of normal material lying parallel to the direction of applied magnetic field. The order parameter would vanish inside the normal cores over the length scale of the order of coherence length ξ . Therefore, the diameter of the normal cores will be $\sim 2\xi$. On the other hand, the magnetic field associated with the vortex current persists over the length scale of the order of the penetration

depth λ . The variation of the order parameter as well as the magnetic field profile inside an isolated flux line is schematically shown in Fig. 1.4(a).

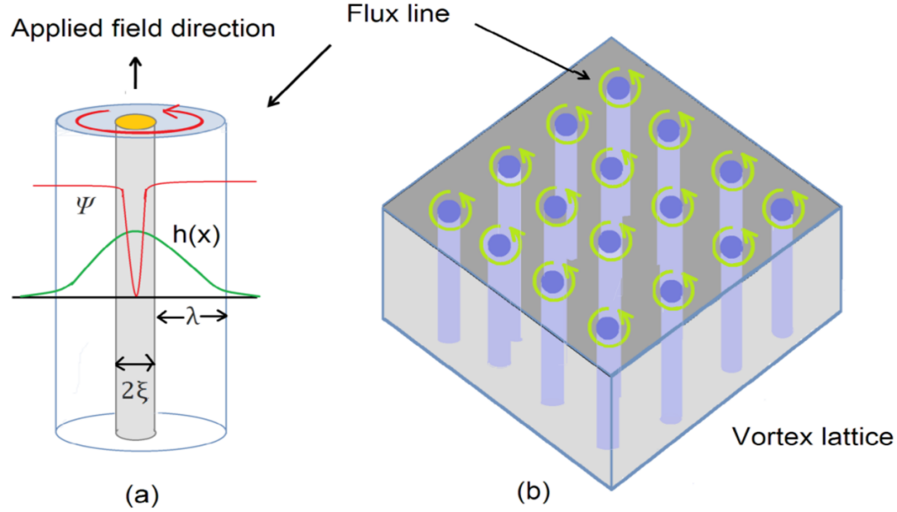


Figure 1.4: (a) The variation of the order parameter and the magnetic field profile inside an isolated superconducting flux line (schematic). (b) Abrikosov flux-line lattice in the mixed state of a type-II superconductor (schematic).

In the mixed state, mutual repulsive interaction among the flux lines tends to arrange them in a regular periodic hexagonal or triangular array with a long range order. This regular periodic array of flux lines is called the *Abrikosov flux-line lattice* (AFL) [22]. Such a flux-line lattice structure is schematically shown in Fig. 1.4 (b). The existence of AFL in the mixed state of type-II superconductors has been confirmed by Bitter decoration, neutron scattering and scanning tunnelling microscopy (STM) experiments. Fig. 1.5 shows the flux-line lattice in the mixed state of $\text{Ba}_{0.6}\text{K}_{0.4}\text{Fe}_2\text{As}_2$ [23] and 2H-NbSe_2 [24] superconductors obtained using STM experiments.

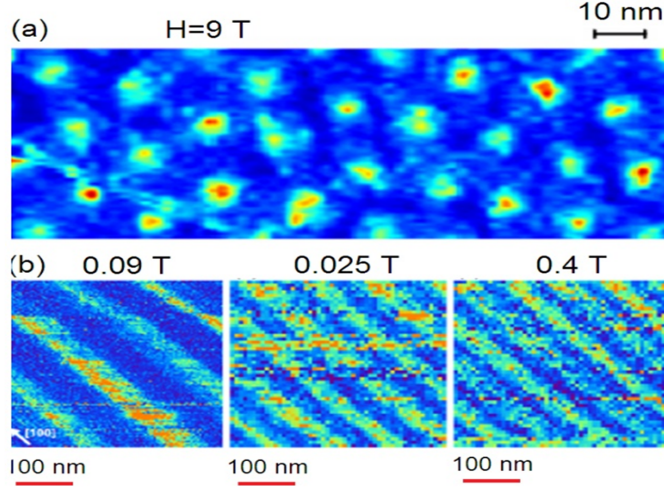


Figure 1.5: (a) Flux-line lattice observed in $\text{Ba}_{0.6}\text{K}_{0.4}\text{Fe}_2\text{As}_2$ superconductor at 2 K and in 9 T applied magnetic field. (b) Lateral view of the flux-line lattice in 2H-NbSe_2 superconductor at 300 mK and in various applied magnetic fields. These results are obtained from the STM experiments.

1.2.6 Field of first flux-line entry

The flux lines start penetrating a type-II superconductor at H_{C1} . For magnetic fields slightly above H_{C1} , the flux lines are few in number and they are far apart. Hence, the interaction between the flux lines can be assumed to be negligible. In such case the Gibbs free energy per unit volume may be written as [25]

$$G(H) = G(H = 0) - \frac{BH}{4\pi} + n_L E_L. \quad (1.9)$$

Here, the second term in the r.h.s. of the above equation is the energy term which relates the Gibbs and Helmholtz free energies. The third term represents the line energy of the flux lines with n_L being the number density

of the flux lines and E_L being the energy per unit length of the flux line. In presence of uniform array of the flux lines, the magnetic induction B can be written as $B = \Phi_0 n_L$, where Φ_0 is the magnetic flux quantum. Hence, Eqn. (1.9) can be rewritten as

$$G(H) = G(H = 0) + n_L \left[E_L - \frac{\Phi_0 H}{4\pi} \right]. \quad (1.10)$$

It is evident from Eqn. (1.10) that for magnetic fields $H < 4\pi E_L/\Phi_0$, the minimization of the Gibbs free energy can be obtained by setting $n_L = 0$. In other words, no flux lines will penetrate the superconductor for magnetic fields $H < 4\pi E_L/\Phi_0$. However, for magnetic fields $H > 4\pi E_L/\Phi_0$, the minimization of the Gibbs free energy can be obtained if the superconductor is penetrated by flux lines. Hence, we can identify H_{C1} as

$$H_{C1} = \frac{4\pi E_L}{\Phi_0}. \quad (1.11)$$

The energy per unit length of the flux line E_L is given as [21]

$$E_L = \left[\frac{\Phi_0}{4\pi\lambda} \right]^2 \ln \left(\frac{\lambda}{\xi} \right). \quad (1.12)$$

When Eqn. (1.12) is substituted in Eqn. (1.11), we obtain the expression for H_{C1} as

$$H_{C1} = \frac{\Phi_0}{4\pi\lambda^2} \ln \left(\frac{\lambda}{\xi} \right). \quad (1.13)$$

It is to be noted in Eqn. (1.10) that the superconductor can lower its energy by creating more and more number of flux lines. This will lead to a negative divergence of the Gibbs free energy. However, this negative divergence of the Gibbs free energy can be eliminated if we consider the interaction among the flux lines, which gives a positive contribution in the expression of the Gibbs free energy given in Eqn. (1.10).

When a flux line penetrates inside a superconductor, not very far from the surface of the superconductor on the length scale of the magnetic field penetration depth λ , the vortex current associated with the flux line has a component normal to the surface of the superconductor. In order to satisfy the boundary condition that no current flows normal to the surface of the superconductor, one need to consider an image flux line with associated vortex current flowing in the sense opposite to that of the flux line located inside the superconductor [25]. If the flux line is located at a distance $x = r$ (inside the superconductor) from the edge (at $x=0$) of the superconductor such that $r < \lambda$, then the image flux line will be located at $x = -r$ [25]. This image flux line will then exert an attractive force on the flux line located inside the superconductor. Bean and Livingston [26] suggested that this attractive force can prevent the penetration of the flux line inside a superconductor up to a certain value of the applied magnetic field $H_P > H_{C1}$. For magnetic field $H_{C1} < H < H_P$, the Meissner state persists as a metastable state. The existence of such a barrier for the penetration of the flux lines inside a superconductor is known as the *Bean-Livingston surface barrier*.

1.2.7 Field for the nucleation of superconductivity

As the magnetic field is increased above H_{C1} , the density of the flux lines increases and the normal cores of the flux lines eventually touch each other at H_{C2} . The H_{C2} can be thought as the magnetic field value at which superconductivity first nucleates in the interior of a sample upon decreasing the magnetic field from a value higher than H_{C2} . The order parameter is vanishingly small in the magnetic field regime just below H_{C2} . In such case the first Ginzburg-Landau equation [Eqn. (1.5)] can be linearized by neglecting the higher order term in Ψ as [21, 25]

$$-\frac{\hbar^2}{2m^*} \left[\vec{\nabla} - \frac{ie^*}{\hbar c} \vec{A}(\vec{r}) \right]^2 \Psi(\vec{r}) = -a\Psi(\vec{r}). \quad (1.14)$$

Eqn. (1.14) is the same as the Schrödinger equation for a particle with mass m^* and charge e^* placed in a uniform magnetic field \vec{H} with an associated vector potential \vec{A} . Only the lowest eigen value solution is meaningful here because the linearized Ginzburg-Landau equation is valid only to describe the onset of the superconductivity. The solution for the lowest energy (equal to $-a$) corresponds to a circular motion of that particle in a plane perpendicular to the applied magnetic field with a cyclotron frequency $\omega_c = e^*H/m^*c$, and is given as: $-a = (\hbar\omega_c/2)$ or $-a = (\hbar e^*H/2m^*c)$ [21, 25]. Since the lowest eigen value solution corresponds to the highest magnetic field up to which the nucleation of the superconductivity occurs in the interior of the sample, we can write $-a = (\hbar e^*H_{C2}/2m^*c)$ [21, 25]. Using Eqn. (1.8), we can then

write the expression for H_{C2} in term of coherence length ξ as

$$H_{C2} = \frac{\Phi_0}{2\pi\xi^2}. \quad (1.15)$$

Hence, for a type-II superconductor, the bulk superconductivity persists up to H_{C2} , beyond which surface superconductivity can persist up to the third critical field H_{C3} . The two characteristic critical fields H_{C2} and H_{C3} are related with each other through the relation $H_{C3} = 1.7H_{C2}$ [21].

1.2.8 Reversible and irreversible type-II superconductors

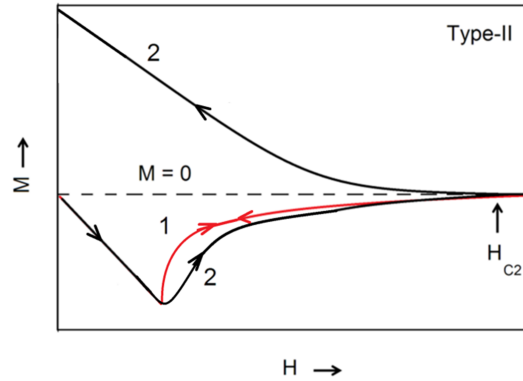


Figure 1.6: (Schematic) The field dependence of magnetization for an ideal type-II superconductor free from any structural defects (curve 1) and non-ideal type-II superconductors with structural defects (curve 2).

If a type-II superconductor is completely free from any crystal imperfections or defects, its magnetization is reversible i.e. the $M(H)$ curves are the same whether the applied magnetic field is increased from zero or de-

creased from a value greater than H_{C2} . This is schematically shown by the curve 1 in Fig. 1.6. But a real sample usually possesses many kinds of crystal imperfections, such as, voids, impurities, dislocations, grain boundaries, precipitates of non-superconducting or weaker superconducting phases etc. The flux lines can be pinned to these crystal imperfections. The pinning of a flux line is energetically favourable because it effectively reduces the loss of the condensation energy in the normal core of the flux line. Any kind of crystal imperfection having dimension comparable to the diameter of the normal core is capable of pinning the flux line. These crystal imperfections are known as pinning centres. Consequently, on increasing the magnetic field from zero, magnetic field does not penetrate the material in the form of flux lines suddenly at H_{C1} because the flux lines formed at the surface of the superconductor are hindered from moving freely into the interior of the superconductor due to pinning of the flux lines at the pinning centres. Similarly, on decreasing the magnetic field from a value greater than H_{C2} , some of the flux lines may be pinned to the pinning centres and cannot escape from the interior of the superconductor. Consequently, the field dependence of the magnetization curve [$M(H)$ curve] obtained in field increasing and the subsequent decreasing branches become distinctly different. This is schematically shown by the curve 2 in Fig. 1.6. The observed irreversibility in the field dependence of magnetization of a superconducting sample is a measure of flux-line pinning inside the superconducting sample, and it increases with the increase in the density of the pinning centres in the sample.

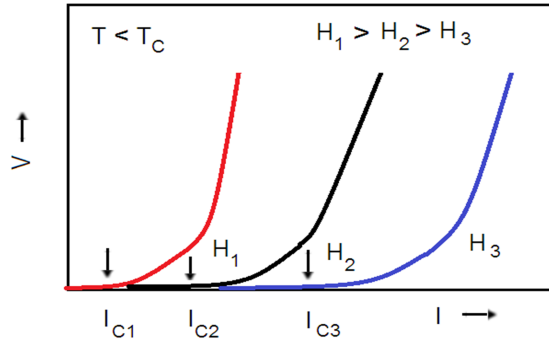


Figure 1.7: Voltage-current ($V - I$) characteristic curves of a type-II superconductor at a temperature less than T_C and in different values of applied magnetic field (schematic)

1.2.9 The critical current

When a type-II superconductor carries a transport current in its mixed state, the flux lines experience Lorentz force in the direction perpendicular to both the applied magnetic field and the current. If the superconductor is absolutely free from any kind of structural imperfections or defects, the flux lines would set into motion at an infinitely small Lorentz force. The motions of the flux lines lead to a dissipation of energy, and hence the development of a finite resistance. Hence, the perfect conducting state of the superconductor is lost. In type-II superconductors containing various types of structural defects, the pinning of the flux lines at these structural defects impedes the motions of the flux lines. A finite transport current is then required to set these flux lines into motion such that the Lorentz force produced by it is large enough to tear the flux lines off the structural defects. The current

density required for de-pinning the flux-lines from the structural defects is called the critical current density J_C . The critical current density of a superconductor, therefore, depends strongly on the presence of structural defects in the superconductor. Hence, the mixed state of a type-II superconductor is therefore perfect conducting only in the presence of the structural defects, which can pinned down the flux-lines and prevent their dissipative motions. Apart from the high values of T_C and H_{C2} , an appreciably large value of J_C of a superconductor is therefore desirable for the development of superconducting magnets. Because of very large values of these critical parameters (T_C , H_{C2} and J_C) in Nb-Ti, Nb₃Sn, and Nb₃Ge, these materials are used for the fabrication of the high-field magnets.

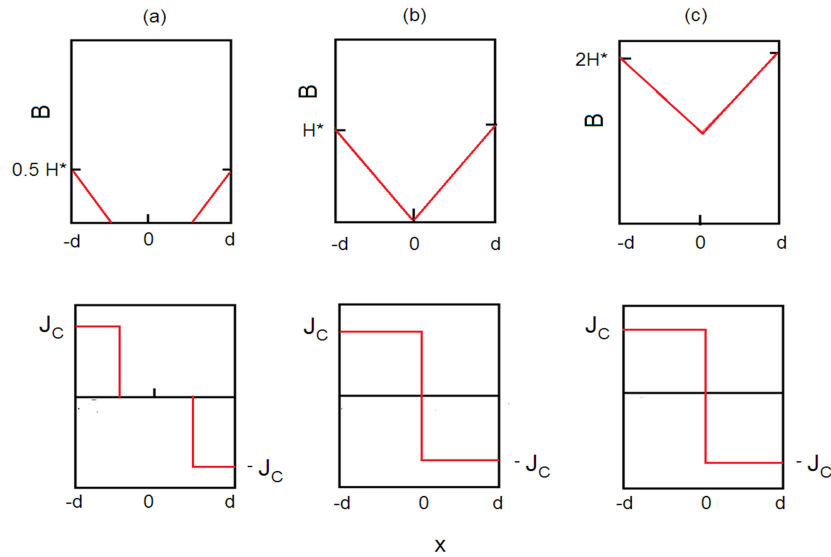


Figure 1.8: The magnetic field penetration profile and the associated critical current density inside a superconducting sample at various applied magnetic fields, after starting from a zero-field-cooled state (schematic) [21].

The critical current density of a superconductor can be directly obtained from the measurement of voltage-current (V - I) characteristic curves. Fig. 1.7 illustrates schematically the V - I characteristic curves of a type-II superconductor. The current value for which a measurable voltage first appears in the V - I curve is taken as the critical current I_C (indicated by arrow heads in Fig. 1.7). The critical current density J_C is related to I_C as $J_C = I_C/A$, where A is the cross sectional area of the specimen in the direction perpendicular to the direction of the current flow. The critical current density can also be inferred from the irreversible $M(H)$ curves using Bean's critical state model [27] and its various extensions [28-31]. This critical state model assumes that, when a low magnetic field is applied to a superconducting sample, a macroscopic super-current is induced on the surface of the sample while the interior of the sample is shielded from the magnetic field and current. The super-current flows where the magnetic field is present in accordance with the Maxwell equation: $\vec{\nabla} \times \vec{H} = \vec{J}_C$ (\vec{H} being the internal magnetic field). As the applied magnetic field is increased, the magnetic field and the associated super-current penetrate deeper into the sample. The field and current are present throughout the sample for a characteristic field H^* . The penetration of magnetic field and the associated current density inside a superconducting sample at various stages of the applied magnetic field is shown schematically in Fig. 1.8. In the critical state model, the super-current always flows at the level of the current critical current density J_C [21]. According to the Bean's critical state model [27], for applied magnetic fields greater than H^* , the

critical current density is directly proportional to the difference between the magnetization measured in the increasing- and the decreasing-field branches [21]. Hence, J_C can be inferred from the irreversible $M(H)$ curves using the Bean's critical state model.

1.2.10 The field-temperature phase diagram; and the effect of thermal fluctuations and disorders on the superconducting mixed state

According to the discussion on the type-II superconductors presented so far, the magnetic field-temperature ($H - T$) phase diagram of a type-II superconductor will be somewhat like that shown schematically in Fig. 1.9(a). The superconducting state consists of two distinct regions in the $H - T$ phase diagram. The Meissner state occupies the low-field portion of the $H - T$ phase diagram and persists up to the $H_{C1}(T)$ -line, above which the superconductor enters into the mixed state. The mixed state persists until the $H_{C2}(T)$ -line, above which the normal conducting state of the sample emerges. Such a $H - T$ phase diagram is usually observed in the case of conventional low- T_C superconductors, for which the effect of thermal fluctuations is insignificant. However, thermal fluctuations become significant in high- T_C cuprate, Chevrel-phases, Fe-pnictides, MgB₂ superconductors etc. The flux-line lattice or the vortex lattice in these superconductors is less rigid as compared to that in the conventional low- T_C superconductors. Consequently, the flux-line lattice in these superconductors undergoes a transition into a vortex-liquid state well below the $H_{C2}(T)$ -line. The $H - T$ phase diagram for

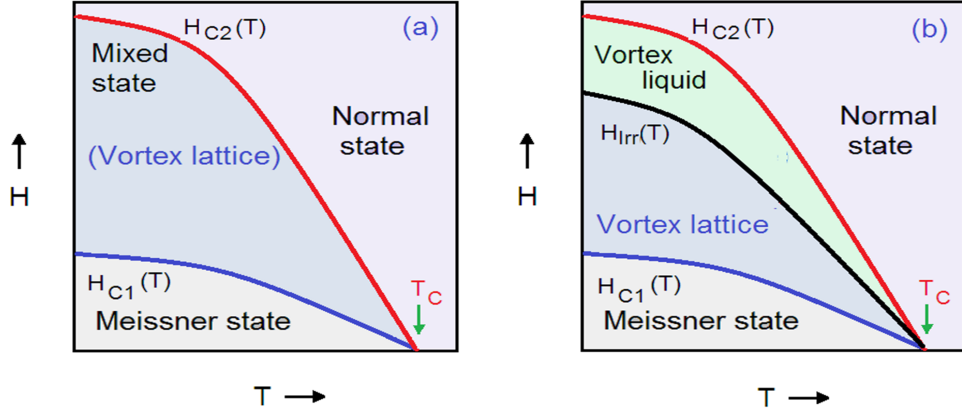


Figure 1.9: (a) A schematic field-temperature ($H - T$) phase diagram of low- T_C superconductors where the superconducting state is subdivided into Meissner state and the superconducting mixed state. (b) $H - T$ phase diagram of the high- T_C superconductors showing that the mixed state is subdivided into vortex lattice and vortex liquid in these superconductors.

these superconductors is therefore more complex than that observed for the conventional low- T_C superconductors. In Fig. 1.9(b), we show schematically the $H - T$ phase diagram for a typical high- T_C superconductor, where the flux-line lattice arrangement with a long range order is persevered only up to the irreversibility line or the $H_{Irr}(T)$ -line. In a type-II superconductor with flux-line pinning a finite dissipation-less current can flow only below this $H_{Irr}(T)$ -line. Hence, from the technological application point of view, H_{Irr} is more relevant than the H_{C2} .

We have discussed above that in a defect free type-II superconductor, the repulsive interactions among the flux lines tend to drive these flux lines to get arranged in the hexagonal array of flux lines called Abrikosov flux line

lattice. However, flux-line pinning at structural disorders may deform the Abrikosov flux line lattice and prevent the emergence of long-range order of the later [32]. In presence of weak random pinning, a quasi-ordered Bragg-glass phase is observed in the mixed state of type-II superconductors [33-37]. On the other hand, the presence of very large number of strong quench disorders in a superconductor leads to the formation of a disordered solid vortex phase. Depending on the nature of the quenched disorders present in the superconductor, the disordered vortex solid phase may be either the vortex-glass or the Bose-glass. A vortex-glass phase [38, 39] is observed in a superconductor where point defects act as the major pinning centres for the flux lines. On the other hand, a Bose-glass phase [40, 41] exists in a superconductor involving correlated defects like twin boundaries or ion-induced columnar tracks.

1.3 Current status of research on the Ti-V alloy superconductors

Since the discovery of high field superconductors, ductile Ti-V alloys are being studied as an alternative to the Nb based alloys for high field applications. It is well known that the structural as well as the physical properties in the normal state of a material influence its superconducting properties. Hence, experimental studies were done over several decades to understand the structural as well as the physical properties of the Ti-V alloys in their normal state. In the normal state, studies on the physical properties such as

the electrical resistivity [42-48], heat capacity [49-51], and dc magnetic susceptibility [43, 52] of the Ti-V alloys are available in the literature. We will first outline the present status on the structural and the physical properties of the Ti-V alloys and then we will give a summary of the studies on the superconducting properties of the Ti-V alloys.

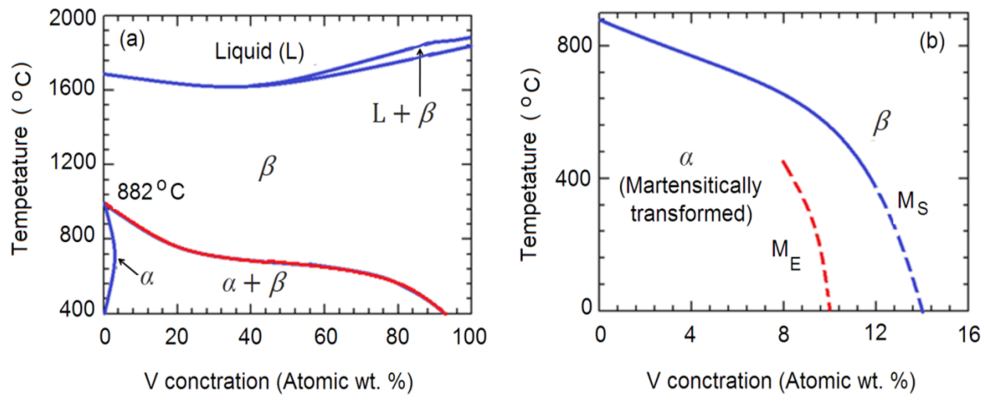


Figure 1.10: (a) Equilibrium phase diagram of the binary Ti-V alloy system. (b) Non-equilibrium phase diagram of the quenched Ti-V alloys— data P. Duwez [54] as modified by the results of the studies by Collings *et al.* [42, 51]. M^S indicates the onset of the martensitic transition and M^E , its end.

1.3.1 Structural properties of the Ti-V alloys

The equilibrium phase diagram (temperature versus concentration) for the binary Ti-V alloy system is shown in Fig. 1.10(a). This figure is taken from Ref. [53]. According to this phase diagram, elemental Ti undergoes a structural phase transformation at 882 °C, where it transforms martensitically from the high-temperature body-centered-cubic (bcc) β phase into α phase

having a hexagonal-close-packed (hcp) crystal structure. Addition of V into Ti pushes the β -transus temperature toward lower temperatures. The β -transus temperature is the limiting temperature down to which the stable β can exist in the Ti-V alloys [indicated by red solid line in Fig. 1.10(a)] [42, 55]. Below the β -transus temperature, the stable metallurgical phase of the Ti-V alloys is an admixture of β and α phase. The high-temperature β phase of the Ti-V alloys can be retained at room temperature by quenching these alloys into ice water from a temperature higher than the β -transus temperature. The non-equilibrium phase diagram [42, 51] for the quenched Ti-V alloys is shown in Fig. 1.10(b). According to this non-equilibrium phase diagram, the crystallographic structure of the quenched Ti-V alloys at room-temperature is predominantly the β phase down to about 12 atomic weight percent of V [42, 51]. The β phase is unstable for V concentration less than ~ 10.5 atomic percent and exhibits a martensitic phase transformation from β to hcp-based α phase [42, 51].

An additional α' phase can also be formed upon quenching the Ti-V alloys having higher Ti concentrations [56]. The α' phase has an orthorhombic crystal structure and is formed due to a stress induced martensitic phase transformation of the β phase matrix [56-58]. The main panel of Fig. 1.11(a) shows the formation of the stress-induced α' phase within the main β phase matrix of a quenched $\text{Ti}_{0.8}\text{V}_{0.2}$ alloy whereas the internal structure of such stress-induced α' phase is illustrated in its inset. These results are taken from Ref. [58]. Quenched Ti-V alloys also form submicroscopic precipitation

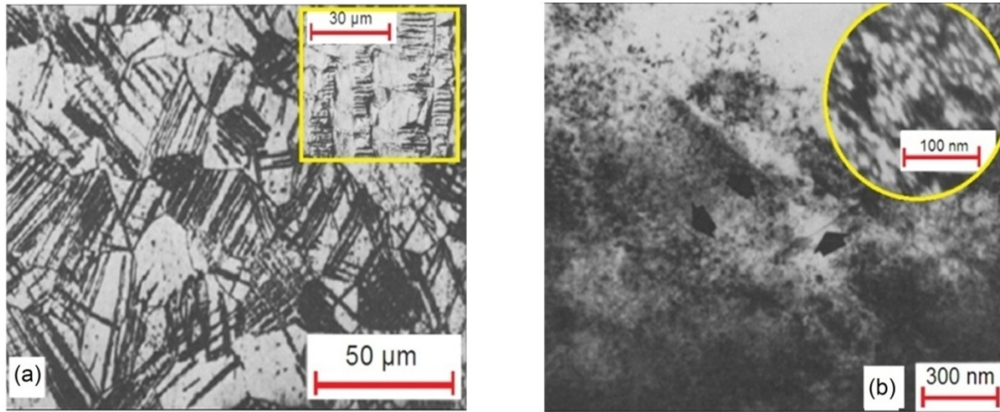


Figure 1.11: (a) Optical micrograph showing the typical formation of the stress-induced martensitic α' phase in a $\text{Ti}_{0.8}\text{V}_{0.2}$ alloy. The inset to figure (a) illustrates the internal features associated with the stress-induced martensitic phase [58]. [(b) and its inset] Bright field electron micrographs for a quenched $\text{Ti}_{0.86}\text{V}_{0.14}$ alloy showing the formation of ω phase precipitates within the β phase matrix [62].

of ω phase within the β phase matrix of these alloys having V concentration in the range 13-25 atomic weight % [59, 60]. The formation of the ω phase in the quenched Ti-V alloys had been studied previously using the transmission electron microscopy (TEM) experiment [61-64] and by neutron and X-ray diffraction experiments performed after a high-pressure treatment of the samples [65, 66]. The ω phase has a hexagonal crystal structure, and is formed by a displacive transformation involving the collapse of the (111) planes of the bcc β phase crystal structure [67-69]. Fig. 1.11(b) shows the morphology of the submicroscopic ω phase in a quenched $\text{Ti}_{0.86}\text{V}_{0.14}$ alloy obtained by the transmission electron microscopy experiment. These results are taken from Ref. [62].

1.3.2 Physical properties of the Ti-V alloys in their normal state

I. Electrical resistivity of the Ti-V alloys:

Previous studies had shown that the electrical resistivity in the normal state of the Ti-V alloys depends strongly on the alloy concentration [42-45]. Fig. 1.12(a) shows the residual resistivity ρ_0 of various $\text{Ti}_x\text{V}_{1-x}$ alloys measured at 1.2 K and in magnetic field higher than the upper critical field of these alloys. These data are taken from Ref. [70]. It is observed that ρ_0 increases with increasing Ti concentration and reaches the maximum for Ti concentration $x \sim 0.8$. On increasing the Ti concentration further, ρ_0 shows a decrease towards that of the pure Ti. Within the Ti concentration range $0.7 \geq x \geq 0.8$, Ti-V alloys have very high values of ρ_0 ($>120 \mu\Omega\text{-cm}$). Such high values of the residual resistivity of the Ti-V alloys indicate that the mean free path for the electron conduction is very short in these alloys. For the Ti-V alloys, the mean free path for the electron conduction estimated using the free electron model lies in the range of 2-8 Å[48].

Fig. 1.12(b) shows the temperature dependence of electrical resistivity of various $\text{Ti}_x\text{V}_{1-x}$ alloys. These data are taken from the Ref. [44]. As can be seen in this figure the temperature coefficient of resistance (TCR) of the $\text{Ti}_x\text{V}_{1-x}$ alloys is negative within the Ti concentration range $0.7 \geq x \geq 0.8$. Various mechanisms have been proposed in order to interpret the negative TCR observed in the Ti-V alloys. The negative TCR is observed in the Ti-V

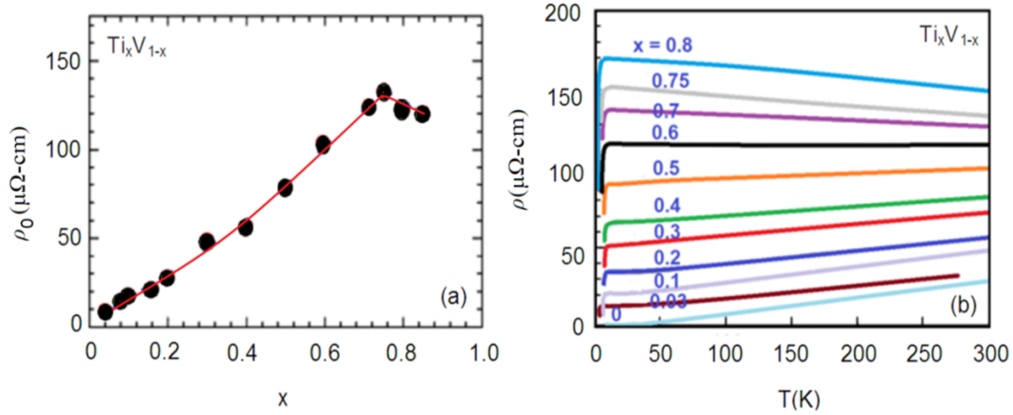


Figure 1.12: (a) Residual resistivity ρ_0 of various Ti-V alloys as a function of Ti concentration x —after reference [70]. The solid line is the guide to the eyes. (b) Temperature dependence of electrical resistivity of various Ti-V alloys. This figure is taken from the Ref. [44]. The figure is reconstructed for better clarity.

alloys where the formation of the ω phase precipitates is favourable. It was initially suggested that the negative TCR exhibited by these Ti-rich Ti-V alloys is related to the phenomenon of the formation of the ω phase precipitates in the β phase matrix of these alloys in a reversible manner during temperature cycling [42, 43]. Ho *et al.* [71] had suggested that the negative TCR in the Ti-Mo alloys (Ti-V and Ti-Mo alloys exhibit qualitatively similar variation of resistivity with temperature and also with the Ti concentration in these alloy systems) is caused by the enhanced scattering of the conduction electrons by the crystalline ω phase precipitates present in the β phase matrix of these alloys. On the other hand, E. W. Collings had suggested that the soft phonons associated with the formation of the ω phase

precipitation are responsible for the negative TCR in the Ti-V alloys rather than the crystalline ω precipitation itself [42]. Later, the problem of negative TCR of the Ti-V alloys was revisited by many other groups [46, 47]. These studies suggest that the observed temperature behaviour of resistivity of the $\text{Ti}_x\text{V}_{1-x}$ alloys in the concentration range $0.7 \geq x \geq 0.8$, can be explained fairly well with the help of the theoretical models of structural Kondo effect [72] and weak localization [73].

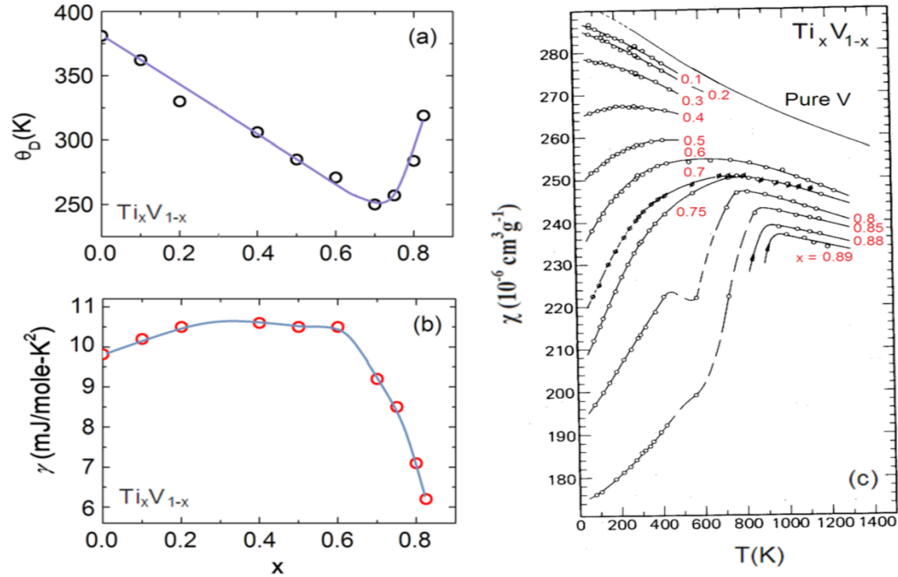


Figure 1.13: (a), (b) Variation of the Debye temperature θ_D and the Sommerfeld coefficient γ as functions of Ti concentration x in the $\text{Ti}_x\text{V}_{1-x}$ alloys. Data are taken from Ref. [51]. The solid lines are the guide to the eyes. (c) Temperature dependence of the dc magnetic susceptibility of various $\text{Ti}_x\text{V}_{1-x}$ alloys. This figure is taken from the Ref. [52].

II. Heat capacity of the Ti-V alloys: Chen *et al.* [49, 50] and Collings *et al.* [1.51] had measured the heat capacity of the Ti-V alloys at temperatures

below and above the T_C of these alloys. They had estimated the Sommerfeld coefficient γ and the Debye temperature θ_D from the low-temperature heat capacity data taken just above T_C . The values of θ_D and γ for various $\text{Ti}_x\text{V}_{1-x}$ alloys are shown as a function of Ti concentration x in Fig. 1.13(a) and (b) respectively. The magnitude as well as the nature of variation of γ with Ti concentration in the Ti-V alloy system is almost similar to that observed in the Nb-Ti alloy system [74]. For the Ti-V alloy system, the plots of γ and θ_D as functions of Ti concentration x show inverse scaling behaviour over the entire range of concentration. However, this inverse scaling behaviour observed between $\gamma(x)$ and $\theta_D(x)$ plots is much stronger near the Ti-rich end of the Ti-V alloy system, where the formation of ω phase precipitates is favourable. It is observed that the addition of Ti into V increases γ up to the Ti concentration $x \sim 0.4$. With further addition of Ti, γ decreases strongly, and thereby gives rise to a peak in $\gamma(x)$ curve near $x \sim 0.4$.

III. Magnetic susceptibility of the Ti-V alloys: Magnetic susceptibility χ of various $\text{Ti}_x\text{V}_{1-x}$ alloys was measured in the temperature range 77-1200 K by E. W. Collings [43, 52]. The temperature dependence of magnetic susceptibility of few selected Ti-V alloys is shown in Fig.1.13(c). It is observed that the magnetic susceptibility of the Ti-V alloys depends strongly on temperature as well as the concentration of the alloys. For Ti concentration $x \geq 0.4$, magnetic susceptibility initially increases with the increase in temperature, and then exhibits a broad peak at temperatures much higher than the room temperature. However, the peak position in $\chi(T)$ curve shifts progressively

towards lower temperature side with decreasing Ti concentration in the Ti-V alloys. After the peak, magnetic susceptibility shows weak decrement with further increase in temperature. For further lower Ti concentration ($x < 0.4$), magnetic susceptibility decreases with increasing temperature up to 1200 K (which was the highest temperature used for performing the measurements). E. W. Collings had interpreted that in the Ti-V alloys with Ti concentration $x \geq 0.4$, the observed decreasing trend of the magnetic susceptibility with decreasing temperature is related to the formation of the ω phase precipitation in the β phase matrix [43]. He had suggested that the magnetic susceptibility of the ω phase is lower than that of the β phase. Hence, the formation of the ω phase during cooling of the sample effectively decreases the overall magnetic susceptibility of the sample [43].

1.3.3 Superconducting properties of the Ti-V alloys

I. The superconducting transition temperature of the Ti-V alloys:

Both the elemental Ti and V are known to be superconducting at 0.4 K and 5.4 K respectively [75]. Their alloys are, however, superconducting at temperatures higher than the superconducting transition temperature T_C 's of the constituent elements. Fig. 1.14(a) shows the variation of T_C of the Ti-V alloys as a function of Ti concentration. These values of T_C are obtained from the low-temperature heat capacity data measured by Collings *et al.* [51]. It is evident from Fig. 1.14(a) that the variation of T_C with the alloy concentration has the trend almost similar to that of the Sommerfeld

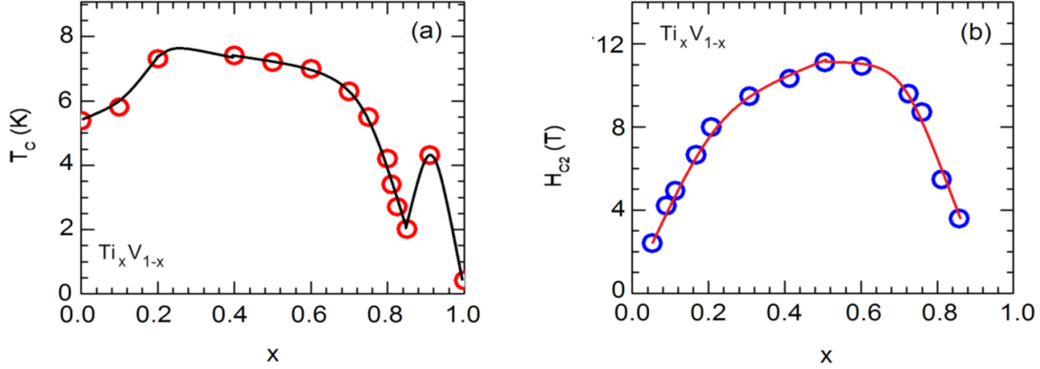


Figure 1.14: (a) Superconducting transition temperature T_C of the $\text{Ti}_x\text{V}_{1-x}$ alloys as a function of the Ti concentration x . The data are taken from Ref. [51]. T_C values for the elemental Ti and V are taken from Ref. [75]. (b) Upper critical field H_{C2} of various $\text{Ti}_x\text{V}_{1-x}$ alloys —after Ref. [76]. The solid lines in both the figures are the guide to the eyes.

coefficient γ shown in Fig. 1.13(b). Both T_C and γ of the Ti-V alloys increase weakly with the addition of Ti into V up to Ti concentration $x \sim 0.4$. With further increase in Ti concentration, both T_C and γ decrease strongly. This observation is in consonance with the BCS theory which predicts a parallelism between the variation of T_C and γ (both are related to the electronic density of states at the Fermi energy). Consequently, studies were attempted for quantitative comparison of T_C of the Ti-V alloys with the BCS theory [6, 50]. Hulm and Blaugher [6] had found that for the Ti-V alloys, particularly those having higher V concentration, T_C value calculated using the BCS theory is significantly higher than the experimental value. For the estimation of T_C , they had used the θ_D values obtained from the linear interpolation between pure metals, and the γ values obtained from the heat capacity data

of reference [49]. The T_C problem in the Ti-V alloys was revisited by Cheng *et al.* [50]. Using the values of γ and θ_D obtained from their heat capacity data, they had found a reasonably good agreement between the T_C values obtained from experiments and the BCS theory. Cheng *et al.* [50] had concluded that the discrepancy found by Hulm and Blaugher [6] between the T_C values obtained from experiments and the BCS theory is most likely due to the incorrect values of γ and θ_D used by Hulm and Blaugher.

II. The upper critical field of the Ti-V alloys: The upper critical field H_{C2} for various $\text{Ti}_x\text{V}_{1-x}$ alloys was measured by Berlincourt and Hake [70, 76] and Bellin *et al.* [8] from the electrical resistivity measurements in presence of magnetic field. The H_{C2} values for the $\text{Ti}_x\text{V}_{1-x}$ alloys measured at 1.2 K by Berlincourt and Hake are shown in Fig. 1.14(b) as a function of Ti concentration x . The concentration dependence of H_{C2} of the $\text{Ti}_x\text{V}_{1-x}$ alloys exhibits a broad peak at $x \sim 0.6$. For the $\text{Ti}_x\text{V}_{1-x}$ alloys, an optimum value of H_{C2} is obtained for $x \sim 0.6$. For this optimum alloy concentration, $H_{C2} \sim 9$ T at 4.2 K [8, 77], which is slightly lower than the highest H_{C2} value observed in the Nb-Ti alloy system [76]. For the V-rich Ti-V alloys, experimental H_{C2} values are in agreement with the H_{C2} values calculated based on the Ginzburg-Landau-Abrikosov-Gorkov (GLAG) theory [70, 76]. On the other hand, experimental H_{C2} value in Ti-rich Ti-V alloys falls below the H_{C2} value predicted by the GLAG theory [70, 76]. This discrepancy is supposed to be due to the Pauli paramagnetic pair-breaking effect which

becomes important for the Ti-rich Ti-V alloys [70, 76, 78].

III. The characteristic superconducting parameters of the Ti-V alloys: The superconducting transition temperature T_C and also the normal state parameters such as the residual resistivity ρ_0 and the Sommerfeld coefficient γ are related to the various important parameters for the superconducting state. Several groups [50, 70, 76, 78, 79] have estimated the fundamental superconducting parameters of the Ti-V alloys using the values of T_C and the normal state parameters ρ_0 and γ of these alloys. For this purpose, the values of γ were taken from the reference [50], while the ρ_0 values were taken from the reference [70]. We will present here the most important results of these studies, which are needed for the characterization of the superconducting state properties of the Ti-V alloys.

The thermodynamic critical field H_C was estimated for the Ti-V alloys [78, 79] using the BCS relation $H_C(T) = 2.42\gamma^{\frac{1}{2}}T_C(1 - t^2)$, where $t = T/T_C$ [16]. The results of Blaugher [79] show that in the Ti concentration range $0.3 \geq x \geq 0.7$, the H_C values of the Ti-V alloys at 4.2 K lie in the range of 0.15-0.16 T, and these values increase weakly with decreasing Ti concentration in the Ti-V alloys. The Ginzburg-Landau coherence length $\xi(0)$ was estimated for few selected Ti-rich Ti-V alloys [78] with the help of the relation [80, 81]

$$\xi(0) = 1.0 \times 10^{-6}(\rho_0\gamma T_C)^{-\frac{1}{2}}. \quad (1.16)$$

In the above relation, γ is in $\text{erg}/\text{cm}^3\text{-K}^{-2}$ and ρ_0 is in $\Omega\text{-cm}$. The estimated values of $\xi(0)$ lie in the range of 4-6 nm for these Ti-rich Ti-V alloys [78]. These values are much larger than the mean free path for the electron conduction [48], indicating that these Ti-V alloys are dirty limit superconductors. The Ginzburg-Landau parameter κ was estimated for the Ti-V alloys [76, 79] using the Gorkov relation [82] as approximated by Goodman [83]

$$\kappa = \kappa_0 + \kappa_l = \kappa_0 + 7.53 \times 10^3 \rho_0 \gamma^{\frac{1}{2}}. \quad (1.17)$$

Here, γ is in $\text{erg}\text{-cm}^{-3}\text{-K}^2$ and ρ_0 is in $\mu\Omega\text{-cm}$. The term κ_0 involves only the electronic structure of a material and is independent of the electron scattering mechanisms while the term κ_l involves the electron scattering mechanisms [76, 82]. The normal state parameters ρ_0 and γ were used to calculate the values of κ_0 and κ_l for the Ti-V alloys. It is observed that for Ti-V alloys $\kappa_0 \ll \kappa_l$, i.e., $\kappa \sim \kappa_l$, and the calculated values of κ were found to be very high for these Ti-V alloys [76, 79]. For an example, the calculated value of κ for the $\text{Ti}_{0.6}\text{V}_{0.4}$ alloy is ~ 80 [76]. The high values of κ estimated for the Ti-V alloys indicate that these alloys are extreme type-II superconductors.

IV. The critical current density of the Ti-V alloys: Vetrano *et al.* [84] had studied the effect of heat treatment on the critical current density J_C in a $\text{Ti}_{0.8}\text{V}_{0.2}$ alloy. Their study shows that the appropriate heat treatment produces precipitation of α and ω phases in the $\text{Ti}_{0.8}\text{V}_{0.2}$. These precipitates act as efficient flux-line pinning centres because of their appropriate sizes.

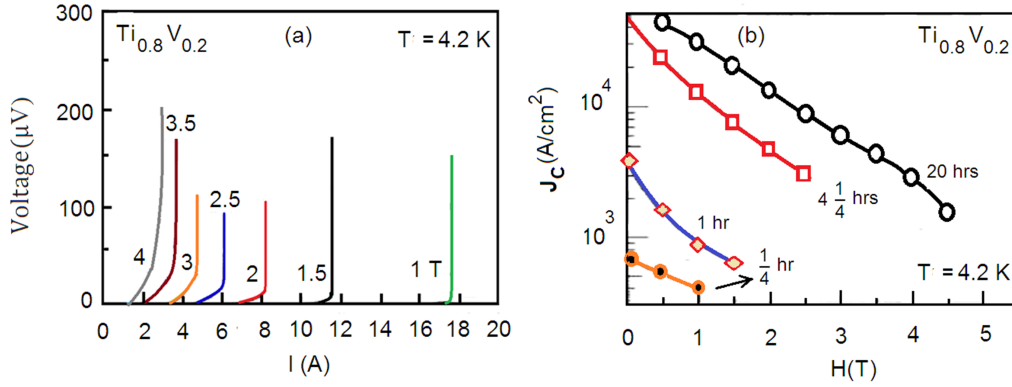


Figure 1.15: (a) Voltage-current ($V - I$) characteristic curves for a $\text{Ti}_{0.8}\text{V}_{0.2}$ alloy at 4.2 K in the presence of different magnetic fields. (b) Critical current density J_C of the same alloy at different stage of heat treatment. Figures are taken from the Ref. [84]. These figures are reconstructed for better clarity.

Consequently, the formation of both α and ω phase precipitates by heat treatment causes the enhancement of J_C by almost one order of magnitude [84]. At liquid helium temperature and in the absence of any magnetic field, the maximum value of J_C achieved in this $\text{Ti}_{0.8}\text{V}_{0.2}$ alloy is $\sim 3 \times 10^8$ A/m², and J_C is observed to be measurable for magnetic fields up to only ~ 5 T [84]. However, recent studies [5, 7] have shown that the Ti-V alloys rich enough in V are capable of carrying high dissipation-less currents in the presence of relatively high magnetic field. With proper heat treatment, J_C in the V-rich Ti-V alloys can be increased up to $\sim 3 \times 10^8$ A/m² in the presence of 6 T magnetic field. This study also suggests that the formation of α phase precipitates by heat treatment is the reason for such J_C enhancement in these V-rich Ti-V alloys [5]. However, the obtained values of J_C for the Ti-V alloys do not reach to a level desired for the technological applications.

1.3.4 Fluctuation conductivity in the Ti-V alloys

The temperature dependence of the electrical resistivity curve of the Ti-V alloys exhibits a strong rounding-off behaviour above the T_C , and the behaviour spreads up to temperatures $\sim(2-3)T_C$ [44, 85, 86]. Rassokhin *et al.* [44] had investigated this rounding-off behaviour of the $\rho(T)$ curve in a series of Ti-V alloys. Their results are shown in Fig. 1.16(a). The observed rounding-off behaviour of the $\rho(T)$ curve in the Ti-V alloys is not markedly influenced by the presence of disorders and/or preparation-sensitive secondary phases in the samples [85, 86]. This suggests that the observed phenomenon is intrinsic to the Ti-V alloys. These alloys also exhibit a temperature dependent large positive magneto-resistance in the temperature regime where the rounding-off behaviour in the $\rho(T)$ curve is observed [85-87]. This is shown in Fig. 1.16(b). These data are taken from the reference [86]. Hake and co-workers had explained both the intrinsically wide resistive transition and the positive magneto-resistance observed in the Ti-V alloys at temperatures above T_C in term of thermodynamic fluctuations of the order parameter, as is the case for the high- T_C superconductors [85-87]. Rassokhin *et al.* [44] had pointed out that for the conventional low- T_C superconductors like Ti-V alloys, the additional conductivity caused by the superconducting fluctuation effect is generally limited only in the close vicinity of T_C . Rassokhin *et al.* [44] had concluded that the rounding-off behaviour of the $\rho(T)$ curve observed in the Ti-V alloys is caused by the pair breaking mechanism of the localized spin fluctuations, which were supposed to be important in these alloys. Prior to

Rassokhin *et al.* [44], the possible influence of localized spin fluctuations on the superconductivity of the Ti-V alloys had been inferred by Prekul *et al.* [88].

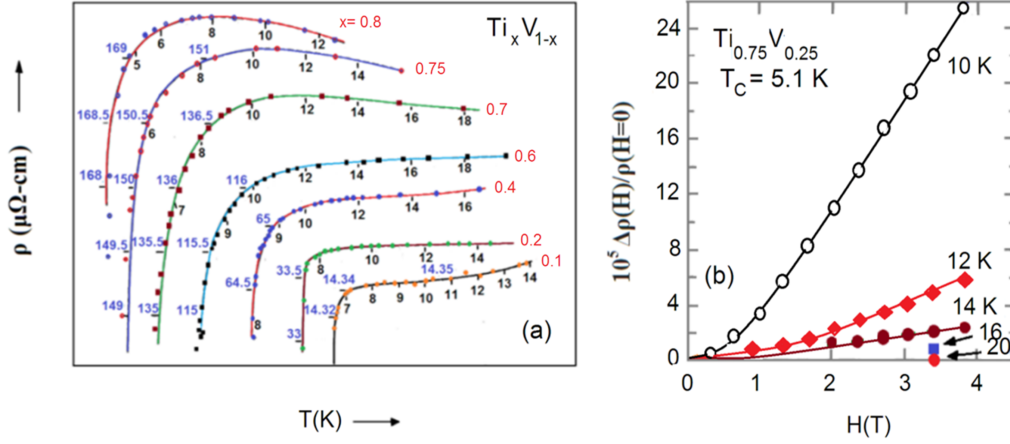


Figure 1.16: (a) Temperature dependence of electrical resistivity of various $\text{Ti}_x\text{V}_{1-x}$ alloys at low temperatures showing strong rounding-off behaviour of the resistivity just above the T_C . The figure is taken from Ref. [44]. The numbers appearing in blue colour represent the resistivity in $\mu\Omega\text{-cm}$ whereas the numbers appearing in black colour represent the temperature in K. (b) Magneto-resistance as a function of magnetic field in a $\text{Ti}_{0.75}\text{V}_{0.25}$ alloy at different constant temperatures above T_C . The figure is taken from Ref. [86]. These figures are reconstructed for better clarity.

1.4 Motivation of the present work

The Bardeen-Cooper-Schrieffer (BCS) theory [16] predicts that the superconducting transition temperature T_C is proportional to the electronic density of states at the Fermi energy. At the same time, a large density of states

at the Fermi energy is the reason behind the magnetic behaviour of Fe, Co and Ni etc. In spite of large density of states at the Fermi energy, most of the transition elements are found to be non-superconducting or have very low values of T_C , even though they are not magnetic. It has been pointed out that the presence of spin fluctuations is the reason behind the variation of T_C among the transition elements [89]. Later on, the effects of localized spin-fluctuations on the properties of dilute superconducting alloys were studied by Zuckermann [90]. He showed that the superconducting transition shifted to lower temperatures than that expected from the band structure calculations performed without considering the spin-fluctuations [90]. Previous studies indicate that the spin fluctuations are important in the elements such as V and Nb, and are the reason behind the suppression of T_C in these elements [91-93]. On the other hand, spin fluctuations are considered to be unimportant in Ti [92, 93].

When we look at the variation of T_C with the e/a (electrons per atom) among the transition element binary alloys, we find a common trend [75]. For certain combination of elements, the T_C enhances quite significantly. This is true for the Ti-V alloys as well. When the transition element Ti is added into another transition element V, the resulting Ti-V alloys have T_C values higher than the constituent elements. Earlier studies have been focused to explain the T_C of the Ti-V alloys. However, the inferences of these studies contradict with each other. Therefore, a consistent description of the T_C in the Ti-V alloys system is indeed necessary.

Another important observation in the Ti-V alloys is the rounding-off behaviour of the temperature dependence of resistivity curve in the temperature regime between T_C and $\sim 2T_C$. Hake and co-workers [85, 86, 87] had suggested that the observed phenomenon is intrinsic to the Ti-V alloys because it is not influenced by the presence of any preparation sensitive secondary phases in the sample. They had inferred that the superconducting fluctuation induced conductivity is the reason behind the observed phenomenon. Prekul *et al.* [94, 95], on the other hand, invoked the idea of the localized spin fluctuations to understand the same phenomenon. Therefore, a precise reason behind the observed phenomenon is yet to be made.

Moreover, it has been recognized in the recent times that the Ti-V alloys can be promising candidates for the fabrication of superconducting magnets for fusion reactors due to their good mechanical, thermal, superconducting properties, and better immunity in the environment of nuclear radiation [5, 56]. However, their use in technological application is limited, mainly due to the lack of complete understanding of the physical properties of these alloys. A better understanding of the properties of the Ti-V alloys in their normal as well as the superconducting state could lead to the possibility of enhancing their superconducting properties (e.g., increasing the T_C and H_{C2} towards the theoretical limits) and enhancing other functional properties like critical current density by suitable engineering techniques.

With this motivation, we present in this thesis, the studies on the structural, electrical, magnetic and thermal properties of the binary Ti-V alloys.

Applicability of various possible mechanisms is tested to understand the normal state properties of these Ti-V alloys. The results of the study of the normal state properties of the Ti-V alloys indicates the presence of itinerant spin fluctuation in these alloys. The spin fluctuations are observed to be playing an important role in the properties of the Ti-V alloys in their normal as well as superconducting state. We also investigate the factors that govern the critical current density in the as cast and annealed samples of the Ti-V alloys. Moreover, we find some novel features such as signatures of high-field paramagnetic Meissner effect and vortex-glass to vortex-liquid phase transition in the superconducting mixed state that have not been reported so far for the Ti-V alloys. In the next few chapters we systematically present our study on the annealed and as cast samples of the $\text{Ti}_x\text{V}_{1-x}$ alloys of four different compositions ($x = 0.8, 0.7, 0.6$ and 0.4). Chapter 2 describes the detail of the sample preparation and the experimental methods used in this study. In chapter 3, a detail of the structural and the metallographical characterization of the Ti-V alloys is given. The properties of the Ti-V alloys in their superconducting state are extensively studied in chapter 4. In this chapter, we discuss on the superconducting transition temperature T_C and various critical fields (H_C , H_{C1} , and H_{C2}) of the Ti-V alloys. The superconducting length scales, namely the coherence length ξ and the magnetic field penetration depth λ are also estimated for these Ti-V alloys. Various important physical properties such as electric resistivity, magnetization, and heat capacity of the Ti-V alloys are also studied in the normal state of these

alloys, and this study is summarized in chapter 5. This chapter also includes a detail study to understand the superconductivity in Ti-V alloys utilizing the outcomes of the study of the normal state properties of these alloys. The study of the superconducting fluctuations induced conductivity in the Ti-V alloys at temperatures above the T_C of these alloys is presented in chapter 6. For the purpose of practical applications, particularly in the field of high-field magnet technology, the critical current density of Ti-V superconductors is studied in detail in chapter 7. In chapter 8, high-field paramagnetic Meissner effect observed in multiphase Ti-rich Ti-V alloys is study to understand the origin of this effect. In chapter 9, Bose-glass to vortex-liquid phase transition in the annealed $\text{Ti}_{0.7}\text{V}_{0.3}$ sample is studied through the resistive transition in presence of magnetic field. A summary and conclusions of our study is presented in chapter 10.

—This page is intentionally kept blank—

Chapter 2

Synthesis of the Ti-V alloys and experimental techniques

2.1 Introduction

In this chapter, we describe the methods of preparation and structural characterization of the Ti-V alloys, and other experimental techniques used in the present study of the Ti-V alloys. X-ray diffraction (XRD) and optical metallography experiments were used for the structural characterization of the present Ti-V alloys. In order to investigate the physical properties of the Ti-V alloys in their superconducting and normal states, we have measured electrical resistivity, magnetization, heat capacity, and strain of these alloys as functions of temperature and magnetic field. The experimental techniques and equipments used for these measurements are discussed in this chapter.

2.2 Preparation of the samples

The samples of four $\text{Ti}_x\text{V}_{1-x}$ alloys having compositions $x = 0.8, 0.7, 0.6$ and 0.4 were prepared for the present study by melting the constituent elements Ti (99.99 %, Alfa Aesar) and V (99.9+ %, Aldrich) taken in stoichiometric ratio. The melting was done in a tri-arc furnace (model 5TA from Centorr Vacuum Industries). Before melting the ingredients, the surfaces of the ingredients were polished using emery paper in order to remove the oxide layer if any. The ingredients were then cleaned using ethyl alcohol, dried and weighed in the ratio of their atomic weight percent. The estimated masses of the ingredients were taken and loaded in the chilled-water cooled copper hearth and then melted in pure argon atmosphere. Tungsten was used as an arc producing tip of the electrode in the tri-arc furnace. The operating current for producing the arc was about 120-150 A. A pure Ti ball was used as a getter element. This pure Ti ball was melted before melting the ingredients of the sample (to be prepared) in order to absorb the residual trace of the reactive gases present inside the furnace. Hemispherical-shaped as cast ingots were obtained after melting the ingredient elements. The ingots were flipped and re-melted four times to ensure homogeneity. Then the as cast ingots were weighed in order to check the weight loss of the samples during the process of their preparation. No perceptible weight loss was observed for any of the present samples.

Each as cast ingot thus obtained was cut into two halves with the help

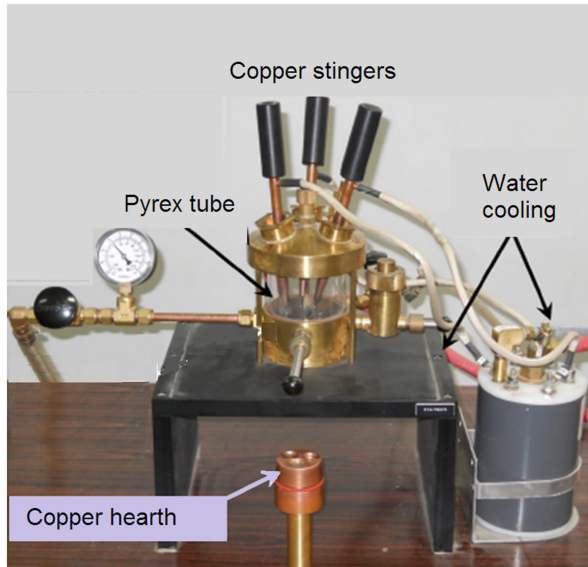


Figure 2.1: Arc melting furnace (model 5TA from Centorr Vacuum Industries) used for the preparation of the samples of the Ti-V alloys.

of a low-speed diamond blade (Buehler, USA). One half of the ingots of each alloy composition was annealed at 1300 °C, which is appreciably higher than the β -transus temperature for the present alloy compositions (refer to Fig. 1.10 of chapter 1). Before placing in the annealing furnace, the as cast samples were first wrapped in Ta-foil and then sealed in quartz ampoules in argon atmosphere to avoid the direct contact between the samples and the quartz ampoule. The samples were annealed at 1300 °C for 10 hours and then cooled down slowly to 1000 °C before quenching them into ice water. Both the as cast and annealed half-ingots were cut into smaller pieces with suitable shapes and sizes using the low-speed diamond blade for doing various measurements as well as structural characterization experiments.

2.3 Structural characterization of Ti-V alloys

2.3.1 X-ray diffraction

Powder X-ray diffraction experiment was used to determine the crystal structure and phase purity of the as cast and annealed samples of the Ti-V alloys. This experimental method is based on the fact that the X-rays, when incident on a crystalline material, get diffracted from the regular arrangement of atoms of the crystalline material. The relation between the distance d from one atomic plane to the next and the angle θ in which the constructive interference of the diffracted X-ray beam occurs (Fig. 2.1) is given by the Bragg's law: $2d\sin\theta = n\lambda$, where λ is the wavelength of the X-ray beam and n assumes different positive integer values depending on the order of diffraction [96]. A monochromatic X-ray beam is used for the powder X-ray diffraction measurements, and a scanning in 2θ (which is the angle between the incident and the diffracted beam) is performed to obtain a diffraction pattern. The position of the peaks in the diffraction pattern is related to the inter-planar spacing between the atomic planes in the crystalline material, and hence gives information about the parameters of the unit cell [96] while the intensity of the diffraction peaks gives the information about the internal structure of the unit cell [96].

X-rays are generally produced in laboratories with sealed tubes where accelerated electrons collide with an anode. Upon decelerating, the electrons emit electromagnetic waves (Bremsstrahlung), which have a continuous en-

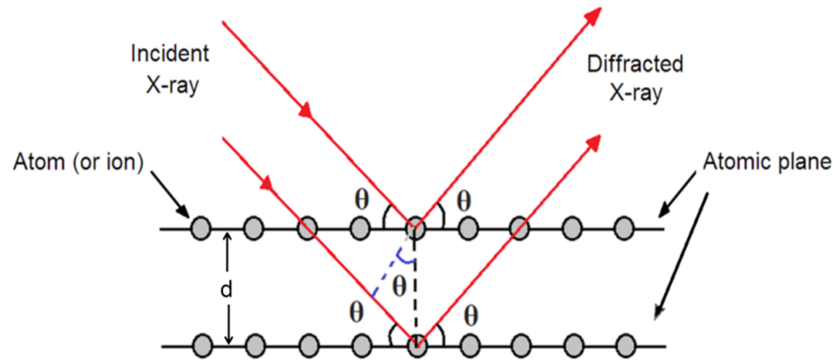


Figure 2.2: X-ray diffraction from the lattice planes with spacing d (schematic). The diffraction maximum occurs at an angle θ whenever the path difference $2d \sin \theta$ between the X-rays diffracted from consecutive lattice planes is an integral multiple of the wavelength of the X-ray.

ergy distribution up to the total kinetic energy of the electrons. In addition, the fast moving electrons knock out electrons from the inner shells of the atoms of the constituent material of the anode. When an electron from higher energy level fills this vacancy, an energy, which is equal to the difference in energy between these two electronic levels participating in this process, is released in the form of electromagnetic radiation. For the innermost K levels, the energy of the emitted electromagnetic radiation lies in the X-ray range with characteristic wavelengths depending on the constituent material of the anode. If a certain wavelength is chosen using a monochromator crystal, it has to be one of these characteristic lines; otherwise a very low intensity of X-ray will be obtained. Consequently, the wavelengths of X-rays generated by sealed tubes are restricted to certain characteristic values (most common are 1.54 \AA and 0.71 \AA with Cu and Mo anodes respectively

[97]). A serious limitation with the laboratory based sources (sealed tubes) is that they have low brilliance of the order of 10^5 photons/(Sec-mm²-mrad²-0.1 %BW) of the emitted X-rays. After the major improvement of the sealed tube by introducing the rotating anode, a brilliance up to of the order of 10^8 photons/(Sec-mm²-mrad²-0.1 %BW) may be reached in the laboratory based sources of X-rays [98]. The synchrotron radiation sources, on the other hand, are much more versatile and stronger. X-rays photons with a wide range of wavelengths and high level of brilliance [$\sim 10^{10} - 10^{12}$ photons/(Sec-mm²-mrad²-0.1 %BW)] can be produced in the synchrotron.

The angle dispersive X-ray diffraction (XRD) experiments on the present Ti-V alloys were performed on powdered samples using the X-rays from INDUS-2 synchrotron radiation source at the Raja Ramanna Centre for Advanced Technology, India. Fast moving electrons in the storage ring of INDUS-2 emit photons upon changing direction at the bending magnet. The emitted photons are not affected by the bending magnet and leave the storage ring tangentially. These emitted photons are used for different experiments conducted at different experimental end stations known as beamline. The present experiments were performed at beamline BL-12. A Si (311) double crystal monochromator was used to choose the certain wavelength of the X-rays, and adaptive focusing optics was used to focus the photon beam. The experiments were performed using an area detector (Image Plate, MAR-345 dtb) for fast recording of the XRD data obtained from the powdered samples. The parameters of the photon beam used in the angle dispersive X-ray

diffraction experiments in Beamline-12 are:

Spectral range: 5–20 keV
Spectral resolution: 1.5 eV at 10 keV
Flux: 10^9 – 10^{10} photons/sec/100 mA at 10 keV
Beam Size: 0.6 mm (Horizontal) \times 0.5 mm (Vertical)

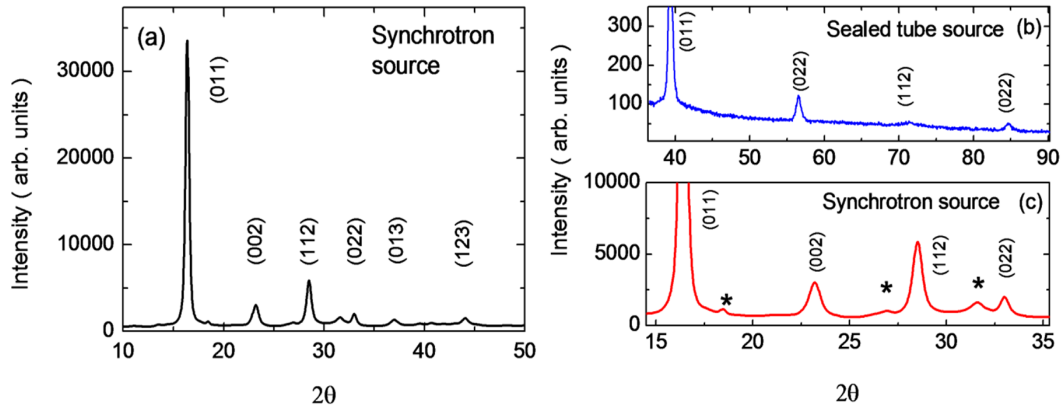


Figure 2.3: (a) XRD pattern of the annealed $\text{Ti}_{0.8}\text{V}_{0.2}$ alloy obtained using X-ray from synchrotron radiation source. The peaks corresponding to a body-center-cubic β phase structure are indexed. (b), (c) XRD patterns of the same alloy obtained using X-rays from laboratory source and synchrotron radiation source, showing the advantage of the later over the former. Few additional peaks (indicated by asterisks) become visible only in the XRD pattern obtained using the synchrotron radiation source.

In the present work, the energy of the X-ray beam used in the experiments was 19 keV ($\lambda \sim 0.65 \text{ \AA}$), and an NIST-LaB₆ standard was used for the wavelength calibration. Two dimensional XRD pattern of powder sample obtained on the image plate was reduced to the 1D (intensity versus 2θ)

pattern using the Fit2D software [99]. Such a XRD pattern (intensity versus 2θ pattern) is shown in Fig. 2.3(a) for the annealed $\text{Ti}_{0.8}\text{V}_{0.2}$ alloy. In Fig. 2.3(b) and (c), we show for comparison the XRD patterns of the annealed $\text{Ti}_{0.8}\text{V}_{0.2}$ sample obtained from the XRD experiments using a conventional laboratory based source equipped with $\text{Cu-K}\alpha$ radiation and the synchrotron radiation source. Due to the low signal-to-noise ratio of the laboratory based source, the peaks in the XRD pattern are weak and only a few peaks are visible. On the other hand, the XRD pattern obtained using the synchrotron radiation source not only has peaks with high intensity but also shows the presence of few additional peaks indicated by the symbol (*) due to the very high signal-to-noise ratio of the synchrotron radiation source. These clearly show the advantages of synchrotron radiation sources over laboratory based sources of X-ray for the structural investigations in our samples.

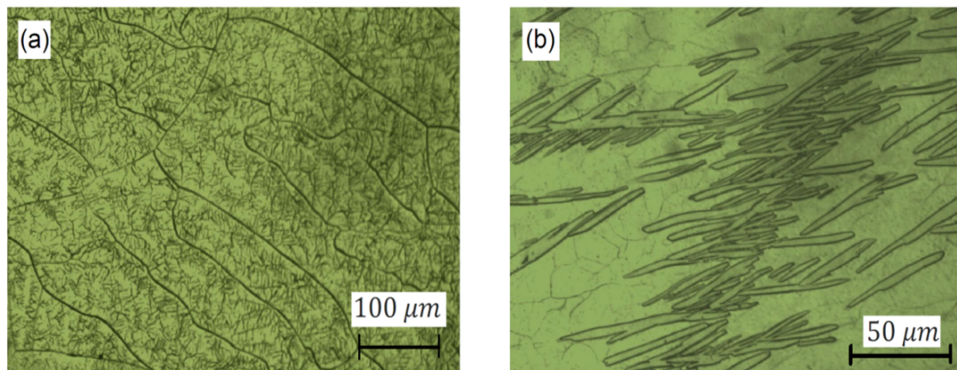


Figure 2.4: Optical micrographs showing (a) the grain structures in the annealed $\text{Ti}_{0.6}\text{V}_{0.4}$ alloy and (b) the presence of martensite α phase in the main β phase matrix of the annealed $\text{Ti}_{0.7}\text{V}_{0.3}$ alloy.

2.3.2 Optical metallography

Optical metallography is an efficient experimental technique to investigate the microstructural properties of a sample. It provides direct visualization of the microstructures of a sample. The presence of grain boundaries, edge dislocations, secondary phases etc. with sizes of the order of few micrometers can be detected through optical metallography experiments. The knowledge about these microstructures is very essential particularly for a superconducting sample because their presence in the sample determines the critical current density of the same. For obtaining optical micrographs, the samples having typical surface area $\sim 3 \times 3 \text{ mm}^2$ were first embedded in moulds prepared by liquid resin and its hardener taken in the volume ratio of 2:1. The moulds were then allowed to become solid by leaving them for 24 hours. When the mould becomes solid, it holds the sample firmly onto it. The samples were first grinded to make their surface flat. After the finest possible grinding, the surface of the samples was successively polished using 6, 3, 1 and 1/2 micron diamond paste respectively, in a polishing machine (Buehler, model: Minimet 1000). The polished samples were then etched using a solution of 2 ml HF and 2 ml HNO₃ in 1000 ml of water. The optical micrographs of these etched samples were taken using a high power optical microscope (Olympus, PME-3). This optical microscope is capable of taking images of the sample with magnifications up to 100 times of the actual size of the sample. Two selected optical micrographs obtained from the optical metallography experiments on the present Ti-V alloys are shown in Fig. 2.4.

2.4 Measurement of the electrical resistivity

All the samples under present study have resistances of the order of few $\text{m}\Omega$, which is comparable with the resistances of the lead wires used in a typical experimental set-up for the resistance measurement. Moreover, the Ti-V alloys undergo superconducting transition at low temperatures, and the resistance of the samples reaches very low values in the superconducting transition region. Therefore, we have used the four-probe configuration for the measurement of electrical resistance of the present Ti-V samples. Once the resistance R_S of a sample is measured, the resistivity ρ of the sample is obtained using the relation ρ ($\Omega\text{-cm}$) = R_S (Ω) \times A (cm^2)/ ℓ (cm), where A is the cross-sectional area of the sample and ℓ is the separation distance between the voltage leads across the sample. The resistivity of the present Ti-V samples was measured as a function of temperature (4.2-300 K) and magnetic field (0-5 T) with the help of a home-made set-up using a commercial liquid helium cryostat (AMI, USA). The measurement probe consists of a copper block with a manganin heater and a Cernox (CX-1030) temperature sensor mounted onto it. The heater and the thermometer are connected to a temperature controller (Lakeshore, Model 340). This arrangement measures and controls the temperature of the sample. The sample was fixed onto the measurement probe with the help of GE-7031 varnish near to the heater and the temperature sensor in order to ensure good thermal contact among them. The measurement of the resistance was accomplished with the help of a high

precision nano-voltmeter (Keithley, model 2182) and a current source (Keithley, model 6220). The data acquisition was done with the help of a computer program written in Visual basic language. The present experimental set-up for the measurement of resistance has a background noise level of the order of 25 nV, and is sensitive to measure a change of resistance $\sim 10^{-7} \Omega$.

2.5 Measurement of the magnetization

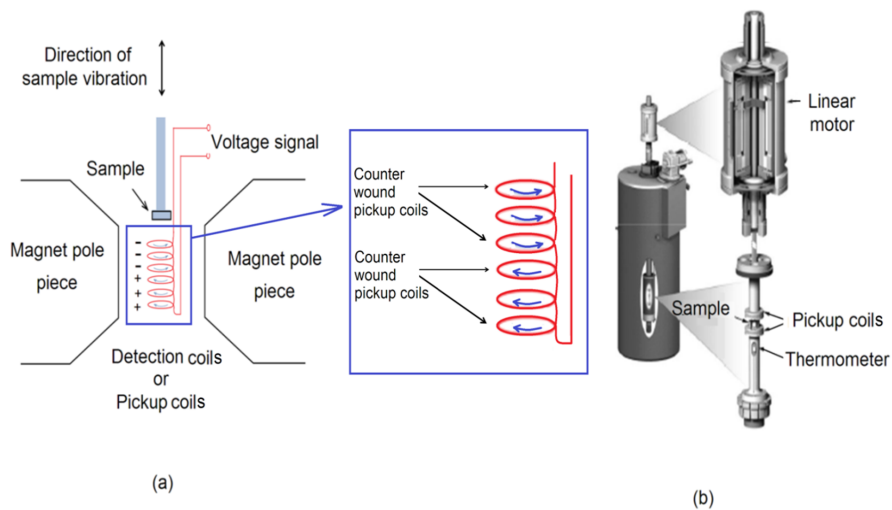


Figure 2.5: Schematic diagram of different components of a vibrating sample magnetometer (VSM Quantum Design, USA). The inset shows the schematic diagram of the detection coil assembly which is wound in a second-order gradiometer configuration with oppositely wound detection coils.

The measurement of magnetization of the present samples were performed using a 9 T vibrating sample magnetometer (VSM, Quantum Design, USA)

and a 7 T Superconducting Quantum Interference Device (SQUID) magnetometer (MPMS XL, Quantum Design, USA). The principle of measurement of magnetization in these systems is based on the Faraday's law of electromagnetic induction, according to which a voltage is induced in a conductor under a time-varying magnetic field. In a VSM, the sample vibrates in presence of a homogeneous magnetic field with small fixed amplitude and a constant frequency with respect to the stationary detection coils of the VSM. The motion of the sample induces voltage in the detection coils. The magnitude of the voltage signal induced in the detection coils depends on the magnetic moment of the sample, the amplitude and frequency of vibration of the sample, and the distance of the sample from the detection coils [100]. The use of the lock-in technique provides accurate measurement of this voltage signal induced in the detection coils. A schematic diagram of the components in a VSM is shown in Fig. 2.5.

The SQUID magnetometer is used for the measurement of the magnetization with higher sensitivity. A SQUID is basically a superconducting ring where one (in an rf-SQUID) or two (in a dc-SQUID) Josephson junctions are inserted. The SQUID works in the principle that the magnetic flux linked with it is periodic in the units of magnetic flux quantum $\Phi_0 = h/2e$, where h is the Planck's constant and e is the electronic charge [101]. For the measurement of magnetization, the sample is moved in a detection coil assembly made of a superconducting material. As shown in Fig. 2.6(a) the detection coil assembly is wound in a second-order gradiometer configuration with

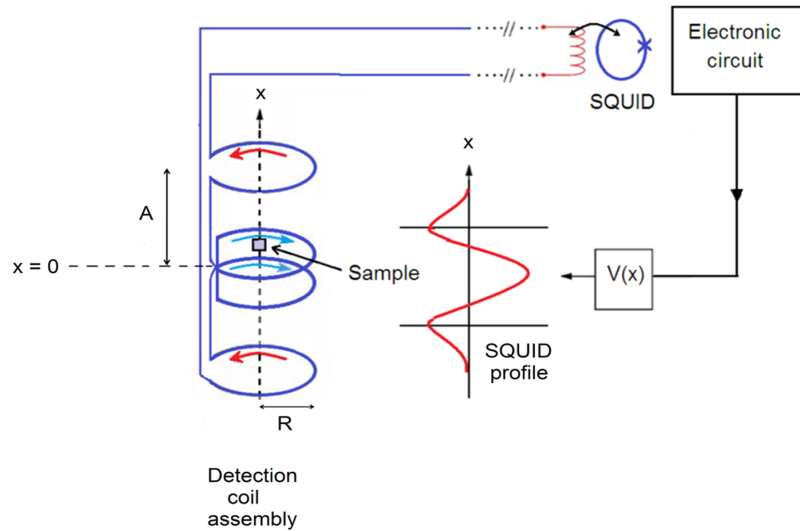


Figure 2.6: A schematic presentation of the experimental configuration in the Quantum Design MPMS SQUID magnetometer used to measure the magnetization.

oppositely wound detection coils in order to reject the contributions other than those coming from the sample. The detection coils are connected to the SQUID-input coil. The detection coils, the SQUID-input coil and the connecting wires are the parts of a closed superconducting loop acting as a flux transformer. The SQUID-input coil is inductively coupled to the SQUID sensor. A superconducting magnet provides the magnetic field required for the measurements. The motion of the sample through the detection coil assembly changes the flux linked with the detection coil assembly. Any change of flux linked with the detection coil assembly will result in a persistent current to flow through the closed superconducting loop to keep the total flux constant. The persistent current is proportional to the change in flux linked

with the detection coil assembly due to the motion of the sample. This persistent current produces a change in flux linked with the SQUID sensor. The voltage signal across the SQUID sensor varies in accordance with the persistent current in the closed superconducting loop. In a SQUID magnetometer, one does not measure the current but rather the voltage across the SQUID output. The Quantum Design MPMS XL is an rf-SQUID based magnetometer where the voltage signal at the SQUID output is used to fit the response of an ideal magnetic dipole. The response function G of an ideal magnetic dipole in a second-order gradiometer coil assembly (or the detection coil assembly) is given by [102]

$$G(x) = -[R^2 + (x - A)^2]^{-\frac{3}{2}} + 2(R^2 + x^2)^{-\frac{3}{2}} - [R^2 + (x + A)^2]^{-\frac{3}{2}}, \quad (2.1)$$

where x is the position of the magnetic dipole, A is the distance of the outer coil from the centre of the detection coil assembly and R is the radius of the coils (see Fig. 2.6). Additionally, the response of an actual sample placed inside the detection coils is also associated with a constant background signal as well as a drift which is linear in x . Therefore, the total output signal of the SQUID in the case of actual magnetization measurement of a sample is represented as [102]

$$S(x) = a_1 + a_2x + G_T(x). \quad (2.2)$$

The software of the Quantum Design (MPMS) magnetometer generates the values of the parameters a_1 and a_2 through curve fitting so that $G_T(x)$ ap-

proximates $a_3G(x)$, where the parameter a_3 is directly proportional to the magnetic moment of the sample. The function $G_T(x)$ is displayed as the SQUID profile instead of the raw data $S(x)$, and the best fit value of the parameter a_3 is quoted as the magnetic moment of the sample. The temporal drift in the electronics is accounted for by the parameter a_2 , and this parameter is chosen to make $G_T(x)$ symmetric about $x = 0$. That is why a usual scan collects data on either sides of $x = 0$.

2.6 Measurement of the heat capacity

The relaxation technique is an appropriate experimental method used for the measurement of heat capacity of small size samples [103]. In this method, the sample is heated to raise its temperature by a small amount ΔT above a constant reference temperature T_0 ($\Delta T/T_0 \sim 1\%$). When the heat is turned-off, the temperature of the sample decays exponentially [103]. The time constant τ of this heat relaxation process (assuming one dimension heat flow) is related to the heat capacity C of the sample and the thermal conductance of the connecting wires K_W as: $\tau = C/K_W$ [103]. Therefore, the heat capacity of the sample can be obtained by knowing the temperature response of the sample and the thermal conductance of the connecting wires. This relaxation method has an advantage that it is easy for signal averaging (at a given T_0 , numerous decay can be used to improve the signal to noise ratio). This method can be used when the sample's thermal conductivity is very poor.

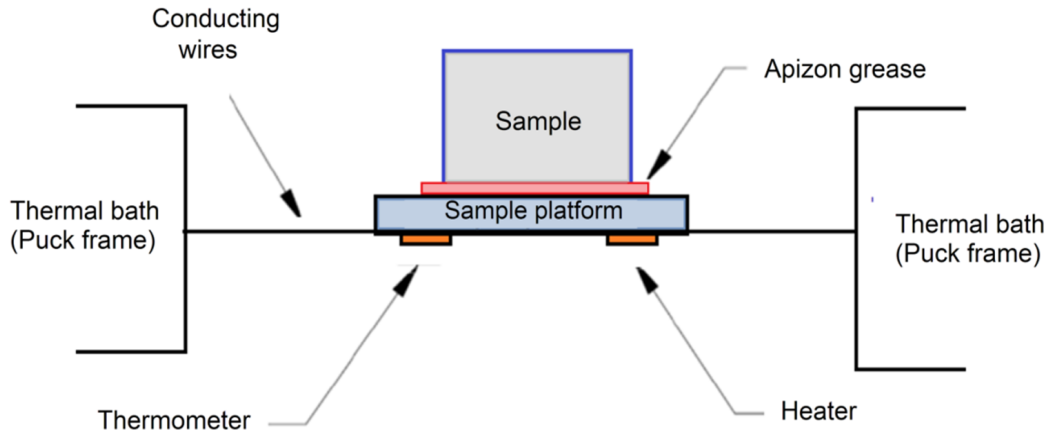


Figure 2.7: Schematic diagram of the calorimeter used in the PPMS Heat Capacity option -from Ref. [104].

The heat capacity measurements of the present samples were performed with the help of a Physical Properties Measurement System (PPMS) manufactured by Quantum design, USA. The PPMS uses the relaxation technique for the measurement of heat capacity. The system works down to 2 K with liquid ^4He employing the evaporation technique. The maximum achievable magnetic field in this set-up is 9 T. The schematic diagram of the calorimeter used in the PPMS Heat Capacity option is shown in Fig. 2.7. The sample was mounted on a sample-platform by thermally conducting grease [104]. A thermometer and a heater are embedded onto the platform. The thermometer provides the measurement of the temperature of the platform while the heater provides the necessary heating power to the platform. The platform is supported by thin gold-wires which provide electrical connections for the thermometer and the heater embedded onto the platform. These wires also

provide thermal anchoring between the platform and the puck. The puck serves as calorimetric thermal bath. An additional thermometer embedded in the puck provides the measurement of the temperature of this thermal bath. A thermal shield covers the whole assembly in order to prevent unwanted loss or inflow of heat through radiation. The measurements were performed in high vacuum so that the conduction of heat from the platform to puck occurs dominantly through the connecting wires.

The measurement of heat capacity of a sample involves a number of steps. The first step of the heat capacity measurement involves the calibration of the resistance of the puck thermometer and the platform thermometer. Starting from the highest temperature and moving downward, the system stabilizes the temperature which is within the calibration temperature range, and measures the resistance of the puck thermometer and the platform thermometer at that temperature. Consequently, a table of resistance values at various temperatures is obtained. After this, the calibration of the thermal conductance of the connecting wires and the electrical resistance of the heater embedded on the platform are performed. Again, starting from the highest temperature and moving downward, the temperature stabilizes at each temperature that is in the calibration temperature range. When the temperature stabilizes, the resistance of the heater R_H is measured at that temperature. To measure the thermal conductance K_W of the connecting wires at the same temperature, some amount of heating power $P_W(t)$ is given to the platform by the heater. In doing so, the temperature of the platform T_P will be in-

creased to some value higher than the puck temperature T_B . In such case, the heat balance equation will be

$$C_P \frac{dT_P}{dt} = P_W(t) - K_W[T_P(t) - T_B]. \quad (2.3)$$

Here, C_P is the heat capacity of the platform. In the steady state condition, $(dT_P/dt) = 0$, giving $K_W = P_W(t)/(T_P - T_B) = I^2 R_H/(T_P - T_B)$. In this way, the thermal conductance K_W of the connecting wires is determined from the known value of the heater resistance R_H and the temperature difference between the platform and the puck. The actual values of the thermal conductance K_W of the connecting wires and the electric resistance of the heater R_L at different temperatures within the calibration temperature range are then saved in the appropriate calibration table.

In the next step, the heat capacity measurement is performed without sample in order to determine the heat capacity of the addenda C_A . For accurate heat capacity measurement of a sample, a small amount of grease, which is just enough to hold the sample, is first applied to the sample platform, and then the heat capacity of the platform and the grease is measured. Solving the differential equation given in Eqn. (2.3), the temperature of the platform at a time t during the heating and the cooling cycles will be obtained as

Heating cycle:

$$T_P(t) = T_B + [T_P(t) - T_B][1 - \exp(-\frac{t}{\tau})], \quad (2.4)$$

Cooling cycle:

$$T_P(t) = T_B + [T_P(t) - T_B][1 - \exp(-\frac{t}{\tau})]. \quad (2.5)$$

Here, $\tau = C_A/K_W$ is the relaxation time of the platform. Hence, the experimentally obtained temperature response of the platform during both the heating and the cooling cycles is fitted with the above equations. The best fit value of the parameter τ determines the value of C_A using the initially determined K_W value.

Finally, the heat capacity measurement of the platform is performed with the sample, using the so called *two-tau* model. In the *two-tau* model, it is assumed that the thermal contact between the sample and the sample platform is not good and there exists a finite temperature difference between them. In such a case, the heat balance equations are obtained as

$$C_P \frac{dT_P}{dt} = P_W(t) - K_W[T_P(t) - T_B] + K_G[T_S(t) - T_P(t)], \quad (2.6)$$

and

$$C_S \frac{dT_S}{dt} = -K_G[T_S(t) - T_P(t)]. \quad (2.7)$$

Here, C_S is the heat capacity of the sample and K_G is the thermal conductance of the grease. Since the *two-tau* model considers both the thermal relaxation between the platform and the puck, and the thermal relaxation between the platform and the sample, there are two time-constants involved

in the thermal relaxation process. They are given by $\tau_1 = 1/(\alpha + \beta)$ and $\tau_2 = 1/(\alpha - \beta)$, where

$$\alpha = \frac{1}{2} \left[\frac{K_W}{C_P} + \frac{K_G}{C_P} + \frac{K_G}{C_S} \right],$$

and

$$\beta = \sqrt{\frac{K_G^2 C_S^2 + K_G^2 C_S C_P + K_G^2 C_P^2 + K_W^2 C_S^2 + 2K_W K_G C_S^2 - 2K_W C_S K_G C_P}{2C_S C_P}}.$$

The experimentally obtained temperature response of the composite system of sample and platform is fitted considering K_G and C_S as fitting parameters; while for K_W and C_A , the values obtained in the previous (calibration) steps are used. The values of the fitting parameters, which give the smallest deviation of the experimentally obtained temperature response of the composite system of sample and platform from the fit, provide the estimate of C_S . If the thermal contact between the sample and the platform is very good (which would mean that the grease has nearly infinite thermal conductivity), then a *single-tau* model may also be used for the measurements.

2.7 Measurement of the strain

There are a number of experimental techniques developed for the measurement of strain of a sample. These include the resistance strain gauge, the capacitance strain gauge, the inductance method, and the interferometric

methods etc. Among these experimental techniques, the resistance strain gauge technique is the simplest and an extensively used experimental technique for the measurement of strain. We have used this technique for the measurement of the temperature dependence of strain in our samples. A resistance strain gauge is constructed by bonding a fine electrical wire or photographically etched metallic resistance foil to an electrical insulation base using an appropriate bonding material. Electrical leads are attached to the gauge for the measurement of resistance of the gauge. A change in strain ε in the gauge causes a change in its resistance R as [105]

$$\frac{\Delta R}{R_0} = \frac{R - R_0}{R_0} = F\varepsilon, \quad (2.8)$$

where, R_0 is the resistance of the strain gauge in the strain free condition and F is the gauge factor which qualifies the strain sensitivity of the strain gauge and can have temperature dependence. For strain measurement, the gauge is attached to the sample with an adhesive so that the gauge becomes an integral part of the sample. The thermal strain experienced by the sample transfers to the gauge, causing a change in the gauge resistance. The relative change in gauge resistance is used to estimate the thermal strain of the sample by using Eqn. (2.9) as:

$$\varepsilon = \frac{\Delta L}{L_0} = \frac{1}{F} \frac{R - R_0}{R_0} = \frac{1}{F} \frac{\Delta R}{R_0}. \quad (2.9)$$

A variation in temperature will cause change in the gauge resistance due to (i) the inherent temperature dependence of the gauge resistance, (ii) the thermal expansion of the gauge, and (iii) the thermal expansion of the sample (as the gauge is mounted on the sample). When temperature is varied from T to $(T + \Delta T)$, the resistance of the gauge will change due to its inherent temperature dependence as

$$\left(\frac{\Delta R}{R_{T0}}\right)_{G,Thermal} = \frac{R_{T0+\Delta T} - R_{T0}}{R_{T0}} = \beta_G \Delta T. \quad (2.10)$$

Here β_G is the temperature coefficient of the gauge resistance and R_{T0} is the resistance of the strain gauge at temperature T in the strain free condition. On the other hand, the change of gauge resistance caused by the thermal expansion of both the gauge and the sample can be expressed as

$$\left(\frac{\Delta R}{R_0}\right)_{G,Strain} = F \left[\left(\frac{\Delta L}{L_0}\right)_{Sample} - \left(\frac{\Delta L}{L_0}\right)_{Gauge} \right]. \quad (2.11)$$

Here $(\Delta L/L_0)_{Sample}$ and $(\Delta L/L_0)_{Gauge}$ are the thermal strain of the gauge and the sample respectively. Therefore, the overall change of gauge resistance can be obtained by combining Eqns. (2.11) and (2.12) as

$$\left(\frac{\Delta R}{R_0}\right)_{G/Sample} = \beta_G \Delta T + F \left[\left(\frac{\Delta L}{L_0}\right)_{Sample} - \left(\frac{\Delta L}{L_0}\right)_{Gauge} \right]. \quad (2.12)$$

Since we are interested in measuring strain of the sample, we need to get rid of the term $(\Delta L/L_0)_{Gauge}$ as well as $\beta_G \Delta T$ appearing in Eqn. (2.13) so that

the strain of the sample can be obtained by measuring only the change of resistance of the gauge. This is done by mounting an identical gauge on a reference material. In this case the overall change of gauge resistance due to a change in temperature from T to $T + \Delta T$ will be

$$\left(\frac{\Delta R}{R_0}\right)_{G/Ref} = \beta_G \Delta T + F \left[\left(\frac{\Delta L}{L_0}\right)_{Ref} - \left(\frac{\Delta L}{L_0}\right)_{Gauge} \right]. \quad (2.13)$$

Here $(\Delta L/L_0)_{Ref}$ is the thermal strain of the reference material. Taking the difference of Eqns. (2.13) and (2.14), the strain of the sample will be obtained as

$$\left(\frac{\Delta L}{L_0}\right)_{Sample} = \frac{1}{F} \left[\left(\frac{\Delta R}{R_0}\right)_{G/Sample} - \left(\frac{\Delta R}{R_0}\right)_{G/Ref} \right] + \left(\frac{\Delta L}{L_0}\right)_{Ref}. \quad (2.14)$$

The quantities appearing in the square bracket in the Eqn. (2.15) are measured either in a bridge configuration or from separate measurements performed on the sample and the reference material. The measured values of these quantities at different temperatures along with the temperature dependence of the strain of the reference material and the gauge factor F are used to estimate the strain of the sample at different temperatures. We have used copper as the reference material. The temperature dependence of the strain data are available in the reference [106]. On the other hand, temperature dependence of the gauge factor F is provided by the manufacturer of the strain gauge. The temperature dependence of strain of the samples of the present

Ti-V alloys was measured with reference to the length at 293 K. For the measurement of strain we have used CFLA-1-350-11 strain gauges (Tokyo Sokki, Tokyo). The experimental set-up for the measurement of strain is capable of measuring both the temperature as well as the magnetic field dependence of strain in the temperature range 30-300 K and in magnetic fields up to 5 T.

Chapter 3

Structural investigations of the Ti-V alloys

3.1 Introduction

The quenched Ti-V alloys retain their high temperature β phase structure in a metastable state down to the room temperature when the V concentration in these alloys is higher than 14 at. wt. % [42, 51, 107]. The β phase has a body-centered-cubic (bcc) crystal structure (space group $Im\bar{3}m$). For still lower V concentration, precipitations of α phase take place through a martensitic phase transformation of the β phase [42, 51, 107]. The martensite α phase has a hexagonal-closed-packed (hcp) crystal structure (space group: $P6_3/mmc$). The β phase of Ti-rich Ti-V alloys may also undergo a stress induced athermal transition (martensite) to form an orthorhombic α' phase with a space group $Cmcm$ [58, 107, 108]. This stress induced α' phase is formed in the sample depending on where and how the stress is applied to the sample. The quenched Ti-V alloys having higher Ti concentration may

also exhibit the formation of a hexagonal ω phase (space group: $P6/mmm$) within the main β phase of these alloys [61-64, 66, 109]. The presence of the secondary phases (α , α' and ω) phases influences the properties of Ti-V alloys in their normal as well as superconducting state [42, 43, 51, 107]. Hence, the knowledge of the structural properties of the Ti-V alloys is very crucial for understanding both the normal and the superconducting state of these alloys. For example, the presence of these secondary phases has strong influence on the current carrying properties of the Ti-V superconductors in their superconducting state. We have performed detailed structural characterization of as cast and annealed samples of four $\text{Ti}_x\text{V}_{1-x}$ alloys ($x = 0.8, 0.7, 0.6,$ and 0.4) with X-ray diffraction (XRD) and optical metallography experiments. The results of these structural investigations are presented in this chapter.

3.2 Results and discussion

3.2.1 X-ray diffraction

Fig. 3.1 shows the XRD patterns of the as cast and annealed Ti-V samples. The XRD experiments are performed using X-ray from synchrotron radiation source (Beam line-12 of Indus-II synchrotron radiation source at the Raja Ramanna Centre for Advanced Technology, Indore). The position of the peaks in the XRD patterns indicates that the present samples are formed mainly in the bcc β phase structure, and the peaks corresponding to

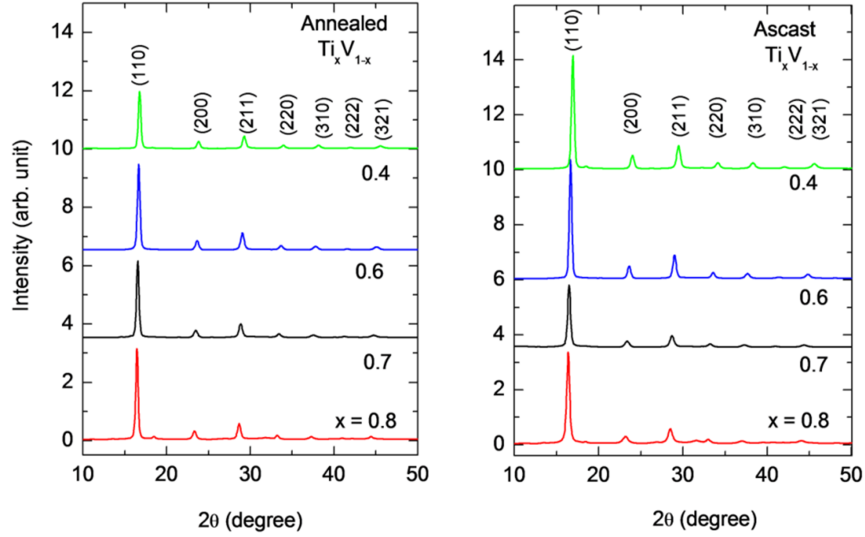


Figure 3.1: XRD patterns of the as cast and annealed samples of Ti-V alloys. The peaks corresponding to the β phase are indexed in these figures

this phase are indexed in Fig. 3.1. Apart from these β phase peaks, additional peaks are also present in the XRD patterns of all the samples except annealed $\text{Ti}_{0.6}\text{V}_{0.4}$ and as cast $\text{Ti}_{0.4}\text{V}_{0.6}$ samples, and their presence indicates the formation of secondary phases in these samples. These additional peaks are quite weak as compared to the peaks corresponding to the β phase, and are not visible very distinctly in Fig. 3.1. In order to know the crystal structures as well as the volume fractions of these secondary phases present in these Ti-V samples, the XRD patterns of these samples are analysed using the Rietveld refinement technique.

The Rietveld refinement of the XRD pattern of the annealed $\text{Ti}_{0.8}\text{V}_{0.2}$ sample is shown in Fig. 3.2. The red and black solid lines respectively

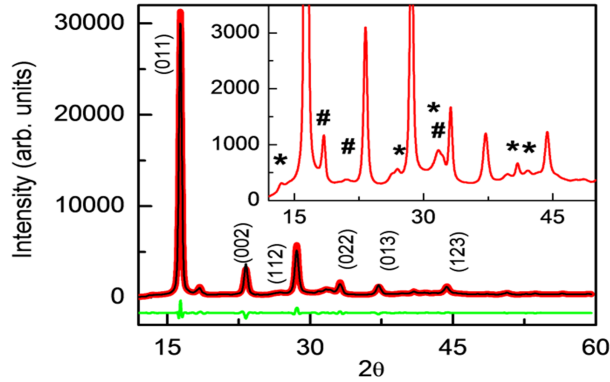


Figure 3.2: The main panel shows the Rietveld refinement of the XRD pattern of the annealed $\text{Ti}_{0.8}\text{V}_{0.2}$ sample. The red solid line is the experimental data, the black solid line is the fitted curve and the green solid line is the difference between the experimental and fitted curve. The inset show the additional peaks corresponding to the hexagonal ω (indicated by symbol $*$) and stress induced α' (indicated by symbol $\#$) phases present in this sample.

represent the experimental data and the fitted curve. The green solid line indicates the difference between the experimental data and the fitting. Similar analysis has been performed for all the samples, but not shown here. The analysis of the XRD patterns indicates that the present Ti-V samples, depending on the concentration, contain α , α' and ω phases within the main β phase matrix. The phase fractions of the α , α' , ω , and β phases and the lattice parameters corresponding to these phases are obtained from the analysis of the XRD patterns, and these values are given in Table 3.1. The obtained lattice parameters corresponding to the constituent phases of the present Ti-V samples are in agreement with the previous results [62,66].

The analysis of the XRD peaks reveals the presence of a large amount

of α phase ($\sim 28\%$) in annealed $\text{Ti}_{0.7}\text{V}_{0.3}$ sample. The presence of a small amount ($\sim 2\%$) of this phase is also inferred in annealed $\text{Ti}_{0.4}\text{V}_{0.6}$ sample. On the other hand, the presence of α' phase is inferred for both the annealed and as cast $\text{Ti}_{0.8}\text{V}_{0.2}$ samples. The ω phase is present mostly in annealed and as cast $\text{Ti}_{0.8}\text{V}_{0.2}$ and $\text{Ti}_{0.7}\text{V}_{0.3}$ samples. The formation of α , α' and ω phases in the Ti-V alloys has been reported previously [58, 62, 66, 107, 108].

Table 3.1: Volume fraction and lattice parameters of different constituent phases present in the as cast and annealed samples of Ti-V alloys.

Metallurgical phases						
	β phase		α or α' phase		ω phase	
	Phase fraction (%)	Lattice parameter (\AA)	Phase fraction (%)	Lattice parameter (\AA)	Phase fraction (%)	Lattice parameter (\AA)
As cast $\text{Ti}_{0.8}\text{V}_{0.2}$	77	3.2583	3(α')	$a=2.4732$ $b=4.7002$ $c=5.6075$	20	$a=4.6018$ $c=2.8183$
Annealed $\text{Ti}_{0.8}\text{V}_{0.2}$	71	3.2350	4(α')	$a=2.6000$ $b=5.7400$ $c=4.0680$	25	$a=4.5750$ $c=2.8080$
As cast $\text{Ti}_{0.7}\text{V}_{0.3}$	>98	3.2373	---	---	<2	$a=4.5900$ $c=2.6438$
Annealed $\text{Ti}_{0.7}\text{V}_{0.3}$	~ 70	3.2150	$\sim 28(\alpha)$	$a=2.9776$ $c=4.5307$	~ 2	$a=4.6711$ $c=2.5950$
As cast $\text{Ti}_{0.6}\text{V}_{0.4}$	>98	3.2053	---	---	<2	$a=4.2646$ $c=2.6545$
Annealed $\text{Ti}_{0.6}\text{V}_{0.4}$	100	3.1879	---	---	---	---
As cast $\text{Ti}_{0.4}\text{V}_{0.6}$	>98	3.1575	$<2(\alpha)$	$a=2.7478$ $c=4.0876$	---	---
Annealed $\text{Ti}_{0.4}\text{V}_{0.6}$	98	3.1511	2(α)	$a=2.6946$ $c=4.0850$	---	---

3.2.2 Optical metallography

Fig. 3.3 and 3.4 shows the optical micrographs for the as cast and annealed Ti-V samples. These optical micrographs evidence that the grain structure is mostly equiaxed for these Ti-V samples. Apart from these equiaxed grains, columnar grains are also observed to form in some portions of the annealed $\text{Ti}_{0.6}\text{V}_{0.4}$ sample. This is shown in the panel (b) of the Fig. 3.4. The grain size in the present Ti-V samples is found to be quite large, which is a characteristic of the ductile Ti-V alloys [107]. The average grain size varies from few tens to few hundreds of μm in these Ti-V samples. No correlation is found to exist between the grain size and the alloy concentration. However, we find that the heat treatment performed on the present Ti-V alloys has an influence on the grain size. The annealed samples, in general, have relatively smaller grain size as compared to their as cast counterparts. It is observed that the grain size in the as cast $\text{Ti}_{0.6}\text{V}_{0.4}$ sample is the largest among all the present Ti-V samples. While a very few smaller grains with an approximate size of $100 \mu\text{m}$ are observed in this sample, most of the grains are very large, and the average size of some of these larger grains exceeds almost $1000 \mu\text{m}$. On the other hand, the grain are smallest in size in annealed $\text{Ti}_{0.7}\text{V}_{0.3}$ sample. The average size of the grains in this sample is $40 \mu\text{m}$ approximately. For a comparison, the average grain sizes observed in all the present Ti-V samples are given Table 3.2.

Apart from the signature of the grain boundaries, uniformly distributed dots are also visible in the main β phase matrix of few samples of the present

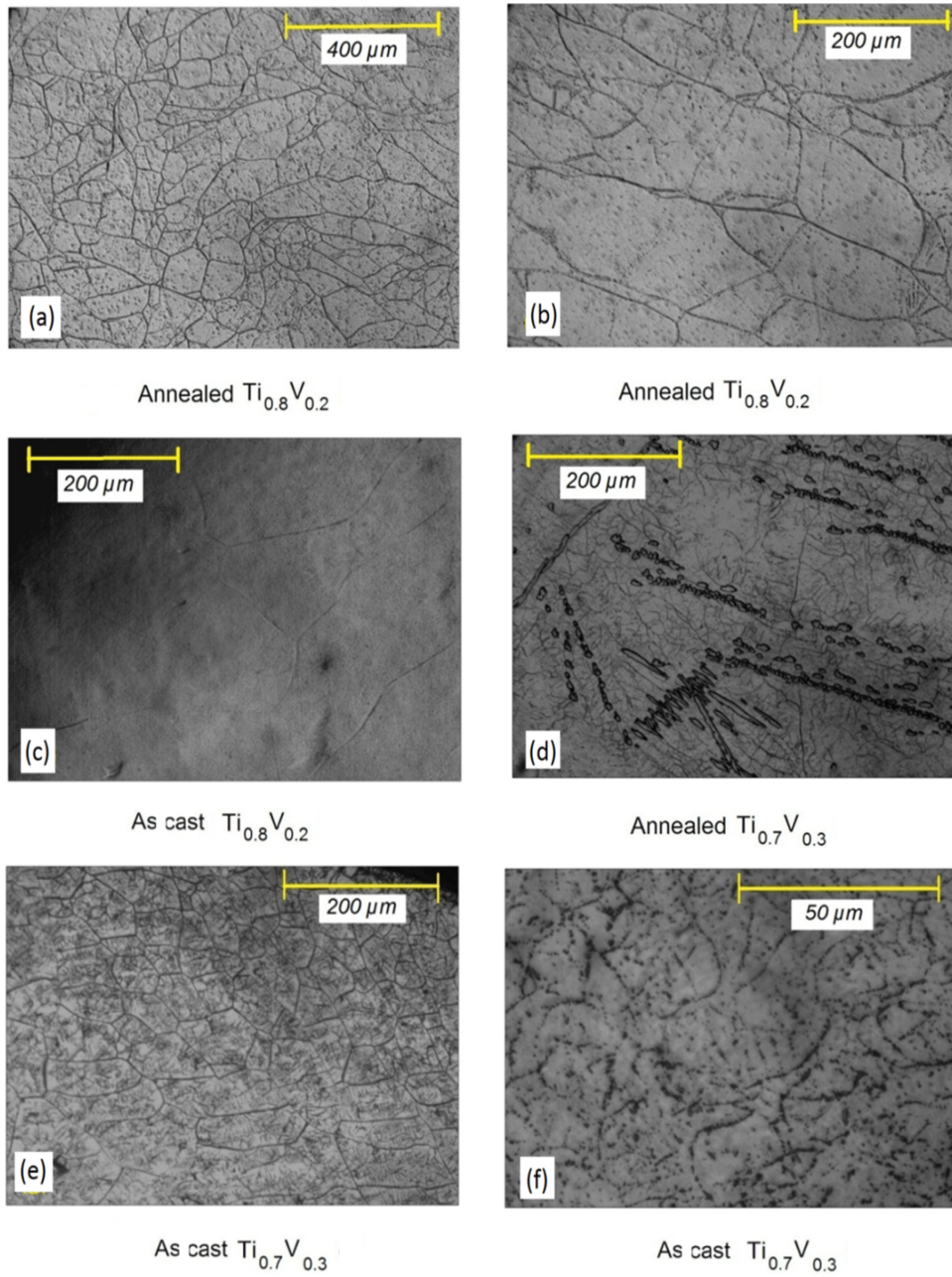


Figure 3.3: Optical micrographs showing the grain structure in the Ti-V samples. A dotted microstructure is also visible within the major β phase matrix of few samples of the Ti-V alloys.

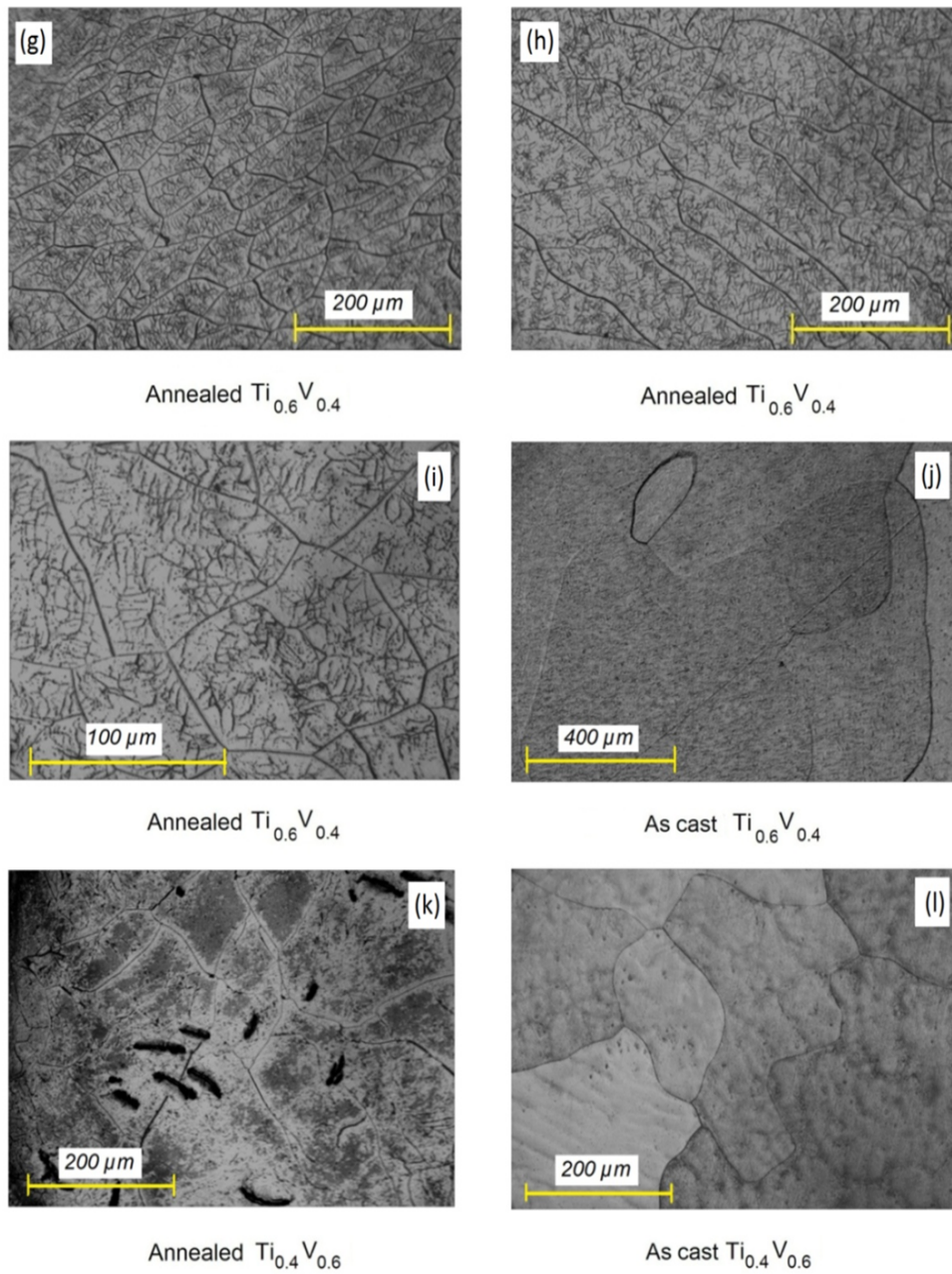


Figure 3.4: Optical micrographs showing the grain structure in the Ti-V samples. A dotted microstructure is also visible within the major β phase matrix of few samples of the Ti-V alloys.

Ti-V alloys. The presence of such dotted microstructures is more prominently observed in annealed $\text{Ti}_{0.6}\text{V}_{0.4}$ sample and as cast $\text{Ti}_{0.7}\text{V}_{0.3}$ samples. In many places these dots are found to line-up forming a network of a dotted line microstructure. This is more clearly visible in Fig. 3.3 (f) and 3.4 (c), where optical micrographs having higher magnification are shown. The dotted microstructures mentioned above are also observed in annealed $\text{Ti}_{0.8}\text{V}_{0.2}$ sample though they are present in this sample with low density. The dots appear to be etched pits forming on the sample surface, as has been observed earlier in scanning electron microscopy experiments on Ti-V alloy [37], and their lining-up is reported to indicate the presence of edge dislocations and low angle grain boundaries inside the β phase domains [37]. We recall that our

Table 3.2: Average grain size in the Ti-V alloys.

	Average grain size(μm)
As cast $\text{Ti}_{0.8}\text{V}_{0.2}$	300
Annealed $\text{Ti}_{0.8}\text{V}_{0.2}$	200
As cast $\text{Ti}_{0.7}\text{V}_{0.3}$	90
Annealed $\text{Ti}_{0.7}\text{V}_{0.3}$	40
As cast $\text{Ti}_{0.6}\text{V}_{0.4}$	400
Annealed $\text{Ti}_{0.6}\text{V}_{0.4}$	175
As cast $\text{Ti}_{0.4}\text{V}_{0.6}$	250
Annealed $\text{Ti}_{0.4}\text{V}_{0.6}$	200

XRD analysis indicates the presence of the hcp α phase in annealed samples of the $\text{Ti}_{0.7}\text{V}_{0.3}$ and $\text{Ti}_{0.4}\text{V}_{0.6}$ alloys and the orthorhombic α' phase in both annealed and as cast $\text{Ti}_{0.8}\text{V}_{0.2}$ samples. The optical micrographs shown in

Fig. 3.5 also depict the formation of the secondary phase(s) within the major β phase matrix of these samples, and these secondary phases are very similar to those formed in a martensitic phase transformation in many transition metal alloys. In annealed $\text{Ti}_{0.7}\text{V}_{0.3}$ sample, regions of needle-like as well as disc shaped α phase are observed to be inhomogeneously distributed over the β phase matrix of this sample. However, the martensitic phase pattern is not very well-formed in many parts of this sample, and in such parts the dotted microstructures and the grain boundaries of the main β phase are observed more clearly. In annealed $\text{Ti}_{0.4}\text{V}_{0.6}$ sample, few martensitic needles are also found to be inhomogeneously distributed over the main β phase matrix of this sample.

It has been reported in the literature that the α phase in Ti-V alloys is formed through a martensitic phase transformation from the β phase when these alloys are heat treated at temperatures below the β -transus temperature [62, 107]. According to the phase diagram of the Ti-V alloy system [53], the β -transus temperature depends on the V content in the alloy. For $\text{Ti}_{0.7}\text{V}_{0.3}$ and $\text{Ti}_{0.4}\text{V}_{0.6}$ alloys, the β -transus temperatures are 720 °C and 640 °C respectively [37, 53]. Since the present alloys were quenched into ice water from 1000 °C, the formation of α phase is not really expected in the $\text{Ti}_{0.7}\text{V}_{0.3}$ and $\text{Ti}_{0.4}\text{V}_{0.6}$ alloys. However, the disordered Ti-V alloys are known to have compositional variation within their major β phase matrix [37, 62, 107]. Consequently, if some portions of the β phase in as cast samples of the $\text{Ti}_{0.7}\text{V}_{0.3}$ and $\text{Ti}_{0.4}\text{V}_{0.6}$ alloys become richer in Ti content than the nominal compo-

sitions, then these regions with elevated Ti content could act as nucleation centres for the β to α phase transformation during the quenching of these samples.

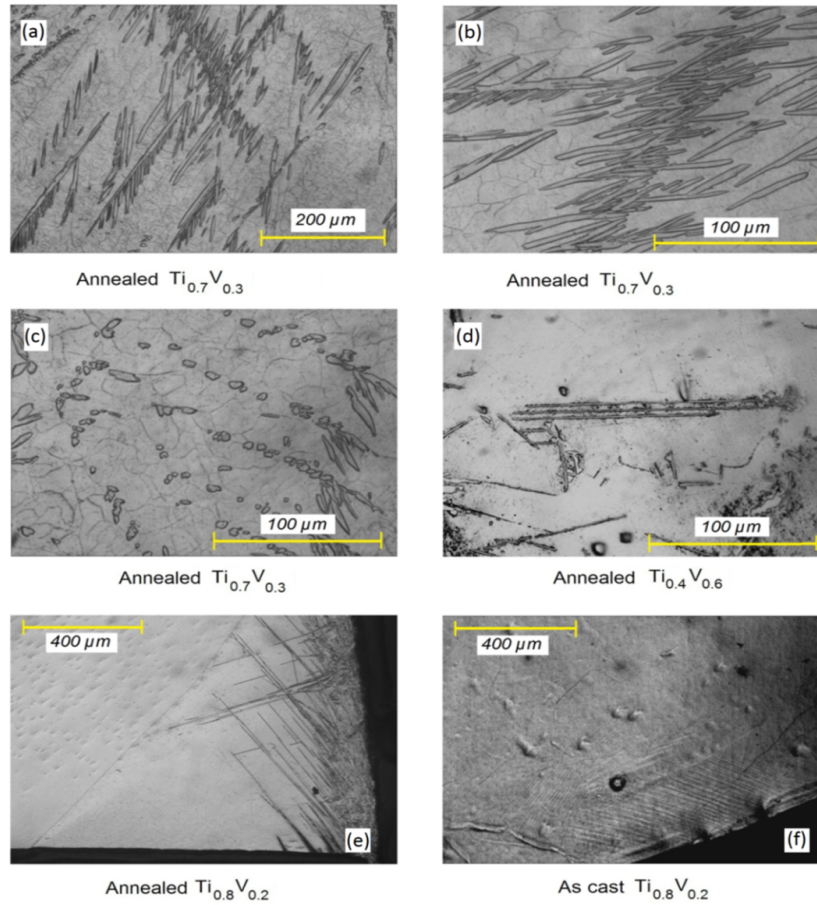


Figure 3.5: Optical micrographs showing the formation of the martensite α phase in the annealed samples of $\text{Ti}_{0.7}\text{V}_{0.3}$ and $\text{Ti}_{0.4}\text{V}_{0.6}$ alloys, and the stress induced martensite α' phase in both annealed and as cast $\text{Ti}_{0.8}\text{V}_{0.2}$ samples.

On the other hand, in both annealed and as cast $\text{Ti}_{0.8}\text{V}_{0.2}$ samples, the martensitic α' phase needles are formed only near the edge of these samples.

Since the α' phase is a stress induced phase, any mechanical processing of the samples such as cutting of the sample may induce the formation of this phase in Ti-rich Ti-V alloys. While cutting the samples, a weight equivalent to 0.010.1 kg is placed on the rotating diamond wheel. Ti-V alloys being ductile, a shear stress is applied at the edge of the sample at the end of the cutting process due to the tearing-off of the material. This applied stress might be the reason for the formation of the α' phase near the edges of the as cast and annealed $\text{Ti}_{0.8}\text{V}_{0.2}$ samples [110]. It should be noted that the amount of the stress induced α' phase present in both as cast and annealed $\text{Ti}_{0.8}\text{V}_{0.2}$ samples estimated from the XRD experiments may not be the same as that present in the samples used in optical metallography experiments because of the different mechanical routes followed for the preparation of the samples for these experiments [110].

3.3 Conclusions

Our XRD results indicate that the present Ti-V alloys have been formed predominantly in the body-centre-cubic β phase crystal structure. Apart from the major β phase matrix of these alloys, the Ti-V alloys rich enough in Ti also contain hexagonal ω phase as well as martensite α and α' phases. The α phase has a hexagonal-closed-packed crystal structure while the α' phase has an orthorhombic crystal structure and this phase is inferred to be formed due to a stress induced athermal phase transformation from the β phase.

The present Ti-V alloys are polycrystalline in nature, where the β phase has very large grain size ranging from few tens to few hundreds of micron. The presence of the dotted line microstructure is also revealed in some of the present Ti-V samples through the optical metallography experiments. Such lining-up of this dotted microstructure is reported [37] to indicate the presence of edge dislocations and low angle grain boundaries within the β phase matrix of these samples.

—This page is intentionally kept blank—

Chapter 4

Superconducting properties of the Ti-V alloys

4.1 Introduction

The properties of a material in its superconducting state are characterized by certain parameters, such as the superconducting transition temperature T_C , the coherence length ξ , the magnetic field penetration depth λ , the Ginzburg-Landau parameter κ , and various critical magnetic fields (the upper critical field H_{C2} , the lower critical field H_{C1} , and the thermodynamic critical field H_C). These parameters are of great importance for understanding the charge-pairing mechanism in the superconductor. These parameters also govern the properties of superconducting mixed state of a type-II superconductor. Although superconductivity in Ti-V alloys had been discovered long ago, in the 1960's, only few studies [70, 76, 78] are available in the literature, which are being focused for characterizing the properties of the Ti-V alloys in their superconducting state. However, a detail study of the

superconducting properties of the Ti-V alloy is still lacking. In this chapter we estimate the fundamental superconducting parameters for the annealed samples of the Ti-V alloys. The temperature dependence of electrical resistivity, magnetization, and heat capacity are used to estimate the T_C of these alloys. The lower and upper critical fields are estimated from the field dependence of magnetization. The thermodynamic critical field is estimated from the temperature dependence of heat capacity. These critical fields then are used for the estimation of κ and the fundamental superconducting length scales ξ and λ . These fundamental superconducting parameters are then used to understand the superconducting properties, in general, and also the superconducting mixed-state properties of the Ti-V alloys.

4.2 Results and discussion

4.2.1 The superconducting transition temperature of the Ti-V alloys

Fig. 4.1(a) shows the temperature dependence of electrical resistivity (ρ) for the Ti-V alloys at temperatures below 10 K and in zero magnetic field. On decreasing temperature, the resistivity of these Ti-V alloys drops abruptly to zero, indicating a transition from normal to superconducting state occurs in these alloys. These Ti-V alloys have very high value of residual resistivity ρ_0 which is taken as the resistivity value measured at 10 K. The residual resistivity increases with increasing Ti concentration in the Ti-V alloys. Fig. 4.1(b) shows the temperature dependence of magnetization (M) measured

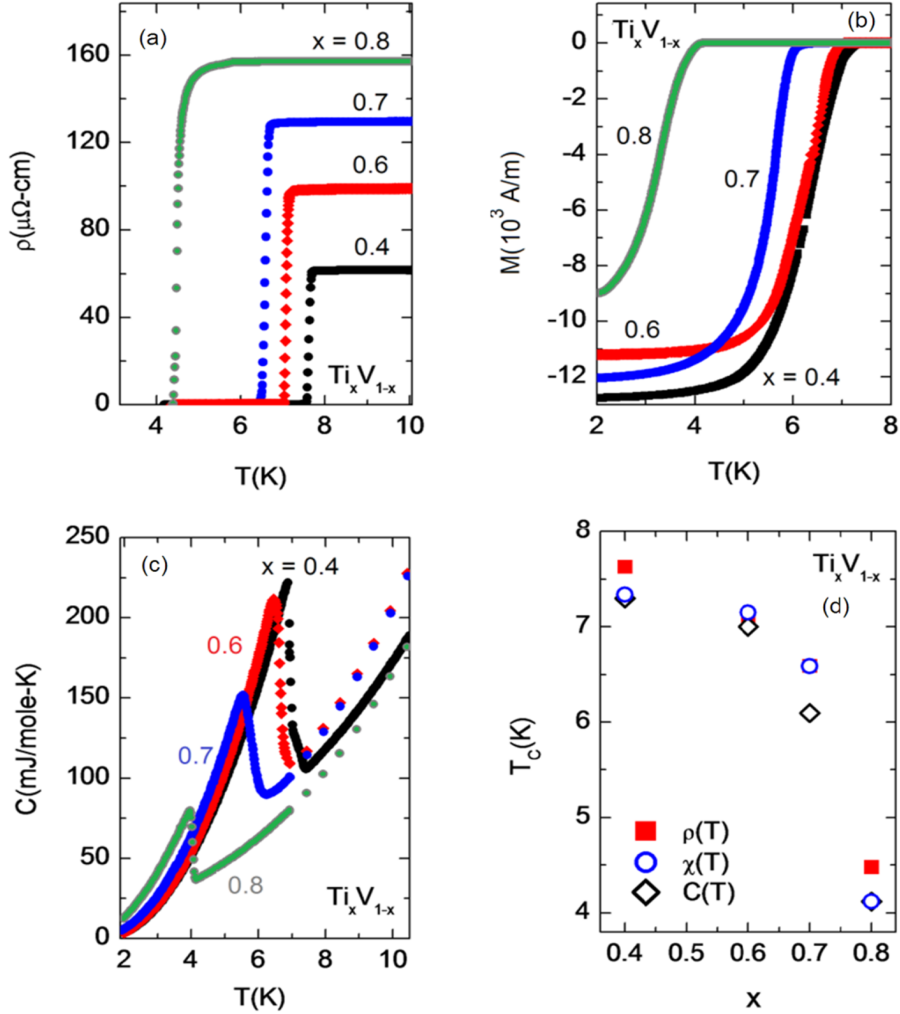


Figure 4.1: Temperature dependence of (a) electrical resistivity, (b) magnetization, and (c) heat capacity of the $\text{Ti}_x\text{V}_{1-x}$ alloys at low temperatures to show the superconducting transition in these alloys. The electrical resistivity and heat capacity measurements are performed in zero magnetic field while the magnetization measurements are performed in the presence of 10 mT magnetic field. (d) The T_C values (estimated from the temperature dependences of resistivity, magnetization, and heat capacity) of the $\text{Ti}_x\text{V}_{1-x}$ alloys presented as a function of the Ti concentration x .

in the zero-field-cooled (ZFC) warming protocol in the presence of 10 mT applied magnetic field. In this protocol, the sample is first cooled to 2 K in the absence of any field, and then a 10 mT magnetic field is applied before performing the measurements while warming up the sample. All the present Ti-V alloys exhibit diamagnetic behaviour in superconducting state. Fig. 4.1(c) shows the temperature dependence of heat capacity (C) in absence of any magnetic field for the Ti-V alloys. A steep jump in heat capacity across the superconducting transition is observed for all the Ti-V alloys, indicating the bulk nature of the superconductivity in these Ti-V alloys. The temperature dependences of electrical resistivity, magnetization, and heat capacity data are used to estimate the superconducting transition temperature T_C for the Ti-V alloys. The T_C is estimated from the $\rho(T)$ curve as the temperature at which the temperature derivative of the resistivity becomes the maximum. On the other hand, T_C is estimated from the $M(T)$ data by finding the temperature at which M approaches towards a negative value from its normal state paramagnetic value. For the estimation of T_C from the $C(T)$ data, we take T_C as the temperature at which the steep jump in the heat capacity occurs. As shown in Fig. 4.1(d), the T_C values of the present Ti-V alloys estimated from the temperature dependences of resistivity, magnetization, and heat capacity are roughly same. These values are in agreement with the previously published results [50, 51]. It is observed that T_C decreases with increasing Ti concentration in the Ti-V alloys. The values of T_C of the present Ti-V alloys are, however, lower as compared to those observed in

the technologically important Ti-Nb alloy system which is widely used in the fabrication of superconducting magnets [74, 111, 112].

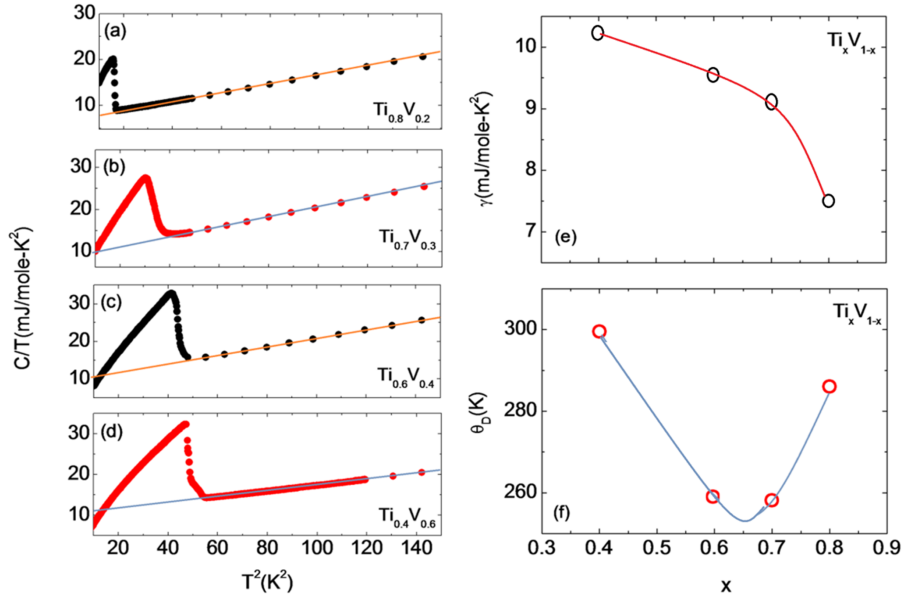


Figure 4.2: (a)-(d) Temperature dependence of heat capacity for the Ti-V alloys (plotted as C/T versus T^2 fashion). The solid lines represent the fits based on the relation (4.2). (e) The Sommerfeld coefficient γ and (f) the Debye temperature θ_D for the Ti-V alloys obtained from the heat capacity data. The solid lines in (e) and (f) are the guides to the eyes.

We can also estimate T_C using the McMillan formula given as [19]

$$T_C = \frac{\theta_D}{1.45} \exp \left[\frac{-1.04(1 + \lambda_{ep})}{\lambda_{ep} - \mu^*(1 + 0.62\lambda_{ep})} \right]. \quad (4.1)$$

Here, λ_{ep} is the electron-phonon coupling constant, θ_D is the Debye temperature, and μ^* is the Coulomb interaction parameter. The parameters λ_{ep} and θ_D for the present Ti-V alloys are estimated using the heat capacity data.

At low temperatures, the heat capacity of a metallic system is expressed as:

$$C(T) = \gamma T + \beta T^3. \quad (4.2)$$

The first term in the above expression represents the electronic contribution to the heat capacity whereas the second term represents the lattice contribution. The parameter γ is the Sommerfeld coefficient, which is related to the electronic density of states at the Fermi energy, and the parameter β is related to the Debye temperature θ_D of a material as $\theta_D = (1944/\beta)^{\frac{1}{3}}$, where β is in J/mole-K⁴ [113, 114]. Following Eqn. (4.2), the plot of C/T as a function of T^2 will be a straight line. Therefore, the interception of this linear C/T versus T^2 curve on the C/T axis will provide an estimation of θ_D while the slope will give an estimation of γ . Fig. 4.2(a)-(d) shows that the C/T versus T^2 curves for the Ti-V alloys are linear in a wide temperature regime above T_C , where a straight line is fitted (indicated by the solid line) to obtain the values of γ and θ_D for these Ti-V alloys. These values of γ and θ_D are given in Table 4.1. These values are in agreement with the literature [50, 51].

In the absence of spin fluctuations, the Sommerfeld coefficient γ is expressed as

$$\gamma = \frac{1}{3}\pi^2 k_B^2 N(0)(1 + \lambda_{ep}), \quad (4.3)$$

where, k_B is the Boltzmann constant and $N(0)$ is the bare value of the electronic density of states at the Fermi energy [114]. The bare density of state at

the Fermi energy $N(0)$ for the present Ti-V alloys is estimated from the electronic structure calculations performed in collaboration with S. K. Pandey of Indian Institute of Technology, Mandi. The *ab initio* electronic structure calculations were carried out using the spin polarized Korringa-Kohn-Rostoker method [115]. The effect of doping was considered under the coherent potential approximation (CPA). The exchange correlation functional developed by Vosko Wilk and Nusair was used for the calculation [116]. The number of k -points used in the irreducible part of the Brillouin zone is 104. For the angular momentum expansion, $\ell_{max}=2$ was considered for each atom. The potential convergence criterion was set to 10^{-6} . The results of these electronic structure calculations are shown in Fig. 4.3. Then the $N(0)$ values along with the experimental γ values are used to estimate λ_{ep} for the present Ti-V alloys, and these values are given in Table 4.1. We can infer from these values of λ_{ep} that the Ti-rich Ti-V alloys are weak-coupling superconductors. As the Ti concentration is decreased, λ_{ep} increases and becomes ~ 1 for the $\text{Ti}_{0.4}\text{V}_{0.6}$ alloy, indicating the moderate to strong coupling nature of superconductivity in the V-rich Ti-V alloys.

The Coulomb interaction parameter μ^* that appears in the McMillan formula given in Eqn. (4.1) can be estimated from $N(0)$ as [117]

$$\mu^* = \left[1 + \frac{1}{N(0)} \right]^{-1}. \quad (4.4)$$

In the above relation, $N(0)$ is expressed in the unit of states/eV-f.u. The

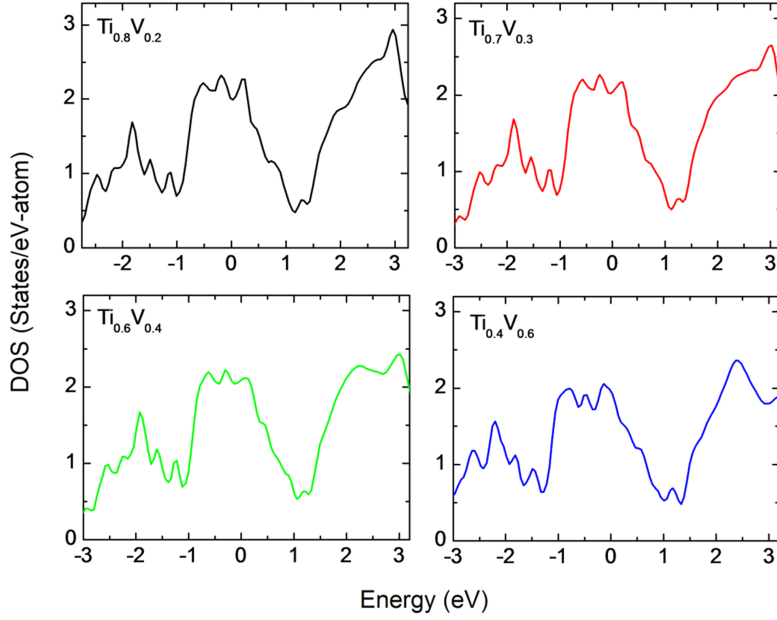


Figure 4.3: Electronic density of state (DOS) for the β phase Ti-V alloys

value of μ^* for all the present Ti-V alloys turns out to be about 0.175(2). The estimated values of λ_{ep} , θ_D , and μ^* are used to estimate the T_C of the Ti-V alloys with the help of the McMillan formula. The T_C value thus estimated for the $\text{Ti}_x\text{V}_{1-x}$ alloys having compositions $x = 0.4, 0.6$ and 0.7 is found to be much higher than the experimentally measured value, whereas for $x = 0.8$ alloy, it is significantly lower than the experimental value. Though a higher value of estimated T_C than the experimental value as observed for the $\text{Ti}_x\text{V}_{1-x}$ alloys with $x = 0.4, 0.6$ and 0.7 is physically accepted, the lower value of estimated T_C for the $\text{Ti}_{0.8}\text{V}_{0.2}$ alloy as compared to that observed experimentally is non-physical, and thereby suggesting that the value of μ^* used for the estimation of T_C is not correct. Therefore, we rather estimate

μ^* from the experimentally determined T_C value of $\text{Ti}_{0.8}\text{V}_{0.2}$. The value of μ^* comes out to be ~ 0.12 . The reduction in μ^* from its value estimated from $N(0)$ may be due to the screening effect [92]. It is also to be noted here that the value of $\mu^* \sim 0.12$ is a standard value that is taken for the analysis of superconductivity in the transition elements [75]. Therefore, we use $\mu^* \sim 0.12$ for all the present Ti-V alloys. However, the experimental T_C value for the $\text{Ti}_x\text{V}_{1-x}$ alloys with $x = 0.4, 0.6$ and 0.7 is still found to be significantly smaller as compared to that estimated from McMillan formula by considering $\mu^* \sim 0.12$ (the estimated T_C values are given in Table 4.1). This discrepancy may arise due to the presence of soft phonons [118] or spin fluctuations [119, 120] in the $\text{Ti}_x\text{V}_{1-x}$ alloys with $x \leq 0.4$. The relevance of the soft-phonons and/or spin fluctuations in the Ti-V alloy and their probable influences on T_C of these alloys will be addressed in chapter 6.

4.2.2 The upper critical field of the Ti-V alloys

In Fig. 4.4(a), we present the magnetic field dependence of magnetization (M) for the $\text{Ti}_{0.7}\text{V}_{0.3}$ alloy obtained at various constant temperatures less than the T_C . Similar curves exist for all the other Ti-V alloys but are not shown here for the sake of conciseness. The $M(H)$ curves for these Ti-V alloys are distinctly irreversible over a large magnetic field regime. The observed irreversibility in the $M(H)$ curves is due to the flux-line pinning at the structural defects present in the alloys. The upper critical field H_{C2} is estimated from the magnetic field dependence of magnetization as the

Table 4.1: Comparison of the experimentally measured T_C values of the Ti-V alloys with those estimated from the McMillan formula. Experimental T_C 's are obtained from the $M(T)$ data. Magnetization of the annealed $\text{Ti}_{0.7}\text{V}_{0.3}$ sample exhibit very weak drop-off below 7 K. However, an appreciable change in magnetization occurs only below 6.6 K, which we taken as T_C to make consistent the T_C values obtained from resistivity and heat capacity data. The values of γ , θ_D and λ_{ep} obtained from the heat capacity data are also given.

	$\text{Ti}_{0.8}\text{V}_{0.2}$	$\text{Ti}_{0.7}\text{V}_{0.3}$	$\text{Ti}_{0.6}\text{V}_{0.4}$	$\text{Ti}_{0.4}\text{V}_{0.6}$
Experimental T_C (K)	4.15 ± 0.03	6.67 ± 0.03	7.15 ± 0.02	7.46 ± 0.02
γ (mJ/mole-K ²)	7.43 ± 0.014	9.09 ± 0.018	9.51 ± 0.019	10.33 ± 0.02
θ_D (K)	286 ± 5	257 ± 4	260 ± 2	304 ± 2
$N(0)$ (state/eV-atom)	1.98	2.05	2.12	2.00
λ_{ep}	0.59 ± 0.003	0.88 ± 0.004	0.91 ± 0.004	1.19 ± 0.004
T_C (K)	4.1	10.6 ± 0.2	11.4 ± 0.2	21.0 ± 0.4
from McMillan formula				

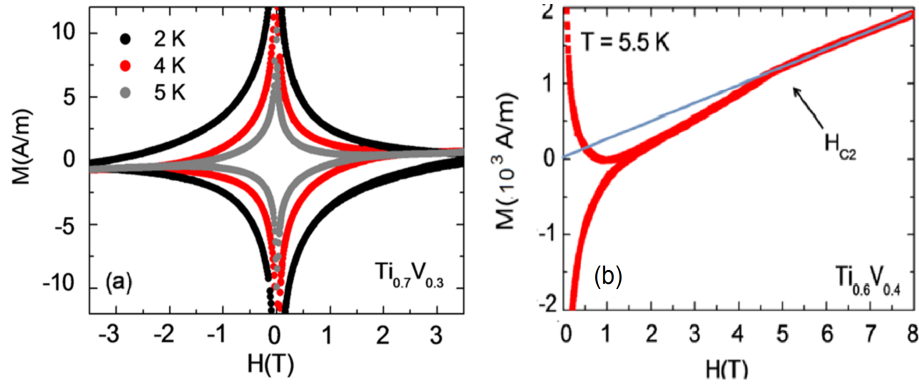


Figure 4.4: (a) Magnetic field dependence of magnetization for the $\text{Ti}_{0.7}\text{V}_{0.3}$ alloy at various constant temperatures below T_C . (b) Determination of H_{C2} from the $M - H$ curve.

magnetic field at which a distinct deviation from the linear magnetic field dependence of the normal state magnetization is observed. For this, we first fit a straight line to the normal state magnetization, which is shown in Fig. 4.4(b). The value of H_{C2} is taken as that point at which the difference between the experimental curve and the fitted line exceeds the standard deviation of the experimental points from the fitted line. Figs. 4.5(a) and (b) present the temperature dependence of H_{C2} for the Ti-V alloys. The H_{C2} values obtained by the extrapolation of the $H_{C2}(T)$ data to 2 K (with the help of the model given by Orlando *et al.* [121] and equation 4.10 given below) are shown as a function of Ti concentration x in Fig. 4.5(c). A peak is observed in the $H_{C2}(x)$ curve around $x \sim 0.6$, which is in agreement with the previously reported results [8, 76]. For the $\text{Ti}_{0.6}\text{V}_{0.4}$ alloy, H_{C2} is about 9 T at 4.2 K, which is slightly lower compared to the $H_{C2}(T = 4.2 \text{ K})$ of Nb-Ti alloys [122, 123].

The Ginzburg-Landau-Abrikosov-Gor'kov (GLAG) theory [20, 22, 124, 125] was formulated in order to describe the temperature dependence of H_{C2} of type-II superconductors. The effect of the normal state paramagnetic energy, the spin-orbit coupling, and the details of the scattering mechanism were not taken into consideration in the GLAG theory. However, the added complications due to the normal state paramagnetic energy, the spin-orbit coupling, and the details of the scattering mechanism may be neglected in the close vicinity of T_C [126]. Therefore, the comparison of the experimental $H_{C2}(T)$ data with the GLAG theory may be done in the close vicinity of T_C .

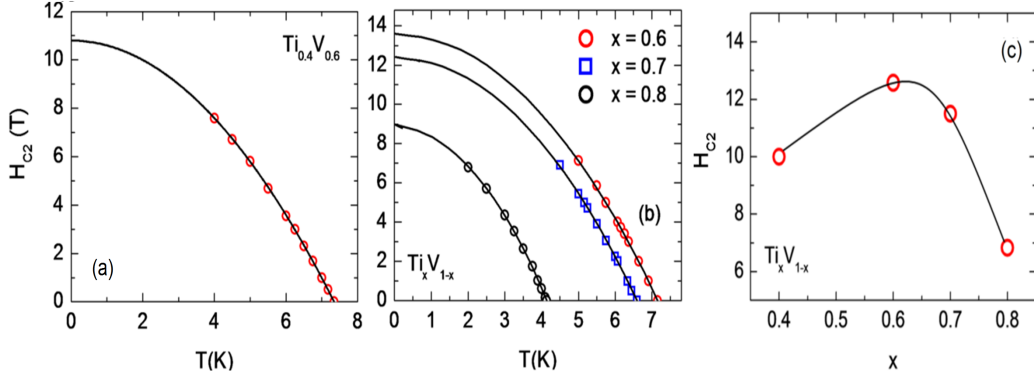


Figure 4.5: (a), (b) Temperature dependence of H_{C2} of the Ti-V alloys (open symbols). The solid line in panel (a) represents the function given in relation (4.10) whereas the solid lines in panel (b) represent the fits to the experimental $H_{C2}(T)$ data based on the model given by Orlando *et al.* [121].(d) The H_{C2} values at 2 K for the Ti-V alloys obtained by the extrapolation of the $H_{C2}(T)$ data. The solid line is the guide to the eyes.

According to the GLAG theory, the slope of the experimental $H_{C2}(T)$ data at T_C is related to important normal state parameters, such as the Sommerfeld coefficient γ and the residual resistivity ρ_0 as [20, 22, 124-126]

$$\left[\frac{dH_{C2}}{dT} \right]_{T=T_C} = -\frac{12e\gamma\rho_0}{\pi^3 k_B}. \quad (4.5)$$

Here, e is the electronic charge. Since γ is related to the electronic density of state at the Fermi energy $N(0)^*$ as $\gamma = \frac{1}{3}\pi^2 k_B^2 N(0)^*$, the density of states at the Fermi energy $N(0)^*$ can be obtained from the experimentally measured quantities as [121]

$$N(0)^* = -9.451 \times 10^{-10} \left(\frac{M_W}{d\rho_0} \right) \left[\frac{dH_{C2}}{dT} \right]_{T=T_C}. \quad (4.6)$$

In the above relation, the pre-factor is chosen so that $N(0)^*$ comes out in states/eV-atom, provided the density d is in gram/cm³, the molecular weight M_W is in gram, ρ_0 is in Ω -cm, and (dH_{C2}/dT) is in Oe/K. The values of $N(0)^*$ estimated for the present Ti-V alloys are given in Table 4.2. It is observed that $N(0)^*$ increases progressively with the increasing V concentration in the Ti-V alloys. It is also observed that for the present Ti-V alloys, the bare density of states $N(0)$ is significantly lower than $N(0)^*$, and the difference between these two values increases with the increase of the V concentration. The observed disagreement arises mainly due to the electron-phonon interactions. The electron-phonon interactions change the energy of the conduction electrons, and thereby causing an enhancement in the density of states from its bare value $N(0)$ by a factor of $(1+\lambda_{ep})$. Accordingly, the values of $N(0)^*$ and $N(0)$ can be used to estimate λ_{ep} employing the relation: $(1+\lambda_{ep})=N(0)^*/N(0)$. The values of λ_{ep} estimated in this procedure agree with those estimated from the heat capacity data. These values of λ_{ep} are given in table-4.2.

The application of magnetic field destroys the superconductivity in a type-II superconductor by two distinct pair-breaking effects. These are the orbital and the Pauli paramagnetic pair-breaking effects. The kinetic energy of the Cooper-pairs circulating around the normal core of the superconducting vortices reduces the superconducting condensation energy, and thereby imposes a limitation on the value of H_{C2} at which the phase transition from the su-

Table 4.2: Few important parameters in the superconducting and normal state of the Ti-V alloys. The numbers inside the brackets are the Maki parameter obtained by considering the strong-coupling theory.

	ρ_0	$-\left[\frac{dH_{C2}}{dT}\right]_{T=T_C}$	$N(0)^*$	λ_{ep}	α_M
	($\mu\Omega\text{-cm}$)	(T/K)	(state/eV-atom)		
Ti _{0.8} V _{0.2}	157.21±0.01	4.43±0.03	2.80±0.03	~0.46	2.42 (2.00)
Ti _{0.7} V _{0.3}	129.63±0.01	3.87±0.05	2.92±0.03	~0.67	2.16 (1.67)
Ti _{0.6} V _{0.4}	98.94±0.02	3.94±0.03	3.71±0.04	~0.74	2.01 (1.52)
Ti _{0.4} V _{0.6}	61.63±0.01	2.90±0.04	4.06±0.04	~1.05	1.55 (1.00)

perconducting to normal state occurs. The orbital limiting field at absolute zero temperature is commonly derived from the slope of the experimental $H_{C2}(T)$ -line at T_C as [127]

$$H_{C2}^{orb}(0) = -0.693T_C \left[\frac{dH_{C2}}{dT}\right]_{T=T_C}. \quad (4.7)$$

On the other hand, the Pauli paramagnetic pair-breaking effect [128, 129] originates from the Zeeman splitting of the energy levels of a single electron. A spin-up electron parallel to an applied magnetic field H raises its energy by an amount of $\mu_B H$ whereas a spin-down electron anti-parallel to the applied field lowers its energy by the same amount (μ_B being the Bohr magneton). Hence, an energy difference of $2\mu_B H$ arises between spin-up and spin-down

electrons in the presence of a magnetic field H . Consequently, a reduction in energy by an amount of $2\mu_B H$ can be achieved by flipping an electron spin to the energetically favourable direction. In the superconducting state, the spins of the two electrons in a spin-singlet Cooper-pair has anti-parallel spin configuration. Then, these spin-singlet Cooper-pairs must be broken in order to polarize condensed electrons along the energetically favourable direction. The paramagnetic pair breaking effect leads to the destruction of the superconductivity when the Pauli paramagnetic energy $E_P = \chi_P H^2/2$ becomes equal to the superconducting condensation energy $E_C = N(0)^* \Delta^2/2$, where χ_P is the spin susceptibility in the normal state of the material, Δ is the superconducting energy gap, and $N(0)^*$ is the electronic density of states at the Fermi energy [128, 129]. The Pauli limiting upper critical field at zero temperature is obtained from the experimental value of T_C as [70, 128, 130]

$$H_{C_2}^P(0) = 1.86 T_C \quad [T]. \quad (4.8)$$

The relative importance of the orbital and the Pauli paramagnetic pair-breaking effect in determining the upper limit of the H_{C_2} of a superconductor is described by the Maki parameter given by [127]

$$\alpha_M = \sqrt{2} \frac{H_{C_2}^{orb}(0)}{H_{C_2}^P(0)}. \quad (4.9)$$

A value of the Maki parameter α_M larger than unity implies that the Pauli paramagnetic pair-breaking effect dominates over the orbital pair-breaking

effect in determining the H_{C2} of a superconductor. We estimate α_M for the present Ti-V alloys from the experimental T_C and the slope of the $H_{C2}(T)$ -line at T_C using the relations (4.7)-(4.9). These values are given in Table 4.2. For the present Ti-V alloys, the value of α_M is found to be significantly larger than unity, and it increases progressively with increasing Ti concentration in the Ti-V alloys. Electron-phonon interaction, however, significantly alters the picture of the Pauli paramagnetic pair breaking effect [121]. The re-normalization of the normal state parameters due to electron-phonon interactions augments the Pauli limited upper critical field as: $H_{C2}^P = 1.86T_C\eta_{H_C(0)}(1 + \lambda_{ep})^{\frac{1}{2}}$ [121]. Here, $\eta_{H_C(0)}$ is a correction factor. We will see below that this correction factor does not alter the value of H_{C2}^P significantly. However, the correction factor $(1 + \lambda_{ep})^{\frac{1}{2}}$ does alter H_{C2}^P and hence α_M drastically even for a weak-coupled superconductor. The values of α_M for the present Ti-V alloys are estimated after considering the re-normalization effect due to electron-phonon interactions, and these values are also included in Table 4.2. We have found that even after considering the effect of electron-phonon interactions, the value of α_M for all the Ti-V alloys except the $\text{Ti}_{0.4}\text{V}_{0.6}$ alloy remains larger than unity. This implies that the Pauli paramagnetic pair breaking effect strongly influences the H_{C2} of the Ti-rich Ti-V alloys. The probable influence of the Pauli paramagnetic pair-breaking effect on the experimental H_{C2} in the Ti-rich Ti-V alloys had already been suggested earlier [70, 76, 78]. On the other hand, α_M becomes of the order of unity for the $\text{Ti}_{0.4}\text{V}_{0.6}$ alloy, suggesting that the Pauli

paramagnetic pair-breaking effect is less important in this alloy. Hence, the experimental $H_{C2}(T)$ data for the $\text{Ti}_{0.4}\text{V}_{0.6}$ alloy is expected to exhibit good agreement with the GLAG theory because this theory does not take the influences of the normal state Pauli paramagnetism into account. According to the GLAG theory, the temperature dependence of H_{C2} is given as [20, 22, 124, 125, 131]

$$H_{C2}(T) = H_{C2}(0)(1 - t^2). \quad (4.10)$$

Here, $t = T/T_C$ and $H_{C2}(0)$ is the upper critical field at zero temperature. As can be seen from Fig. 4.5(a), the relation (4.10) fits the experimental $H_{C2}(T)$ data of the $\text{Ti}_{0.4}\text{V}_{0.6}$ alloy quite well. The fit gives the value of $H_{C2}(0) \sim 11$ T for this alloy.

Since the Pauli paramagnetic pair-breaking effect is found to be important for the $\text{Ti}_x\text{V}_{1-x}$ alloys having composition $x > 0.4$, we analyse the experimental $H_{C2}(T)$ data of these Ti-V alloys based on the theoretical model given by Orlando *et al.* [121]. This theoretical model is a revised version of the Werthamer-Helfand-Hohenberg (WHH) theory [132] proposed to analyse the temperature dependence of H_{C2} . This revised model considers both the Pauli paramagnetic pair breaking effect as well as the corrections for the electron-phonon interactions. In the original WHH theory, which includes the Pauli paramagnetic limitation, the H_{C2} of a bulk type-II superconductor can be written as an implicit function of temperature as [132]

$$\begin{aligned} \ln t = \varphi \left[\frac{1}{2} \right] - \frac{1}{2} \left[1 + \frac{\lambda_{so}}{4X} \right] \varphi \left[\frac{1}{2} + \frac{Y + (\lambda_{so}/4) - X}{t} \right] \\ - \frac{1}{2} \left[1 - \frac{\lambda_{so}}{4X} \right] \varphi \left[\frac{1}{2} + \frac{Y + (\lambda_{so}/4) + X}{t} \right]. \end{aligned} \quad (4.11)$$

Where, φ is the digamma function;

$$t = T/T_C;$$

$$X = \left[\left(\frac{\lambda_{so}}{4} \right)^2 - \frac{4h^2 \alpha_M^2}{\pi^4} \right]^{\frac{1}{2}};$$

$$Y = \left[\frac{2h}{\pi^2} \right];$$

$$h = H_{C2}(T)T_C \left[\frac{dH_{C2}}{dT} \right]_{T=T_C};$$

λ_{so} is the spin-orbit scattering parameter; and α_M is the Maki parameter given by the relations (4.7)-(4.9). For the fitting of the experimental $H_{C2}(T)$ data of the $\text{Ti}_x\text{V}_{1-x}$ alloys having composition $x > 0.4$, we have considered the re-normalization of the normal state parameters due to the electron-phonon interactions by using $H_{C2}^P(0) = 1.86T_C\eta_{H_C(0)}(1 + \lambda_{ep})^{\frac{1}{2}}$ instead of the BCS expression $H_{C2}^P(0) = 1.86T_C$. Hence, the fitting of the experimental $H_{C2}(T)$ data involves the estimation of the correction factor $\eta_{H_C(0)}$ as well. According to Rainer and Bergman [133], any particular experimentally measured physical quantity Z [e.g. $H_C(T)$, $\Delta(T)$, $H_{C2}(T)$ etc.] is related to its weak-coupled BCS expression Z^{BCS} as [121]

$$Z(T) = \eta_Z(T)Z^{BCS}(X^*). \quad (4.12)$$

Here, $\eta_Z(T)$ is the correction factor reflecting the additional correction due to the strong-coupling theory, X^* stands for the normal-state parameters, the asterisk denotes that for evaluating Z^{BCS} one uses normal-state parameters renormalized by the presence of electron-phonon interactions [121]. Therefore, for the superconducting energy gap, we can write

$$\frac{2\Delta(0)}{k_b T_C} = \eta_{\Delta}(0) \left[\frac{2\Delta(0)}{k_b T_C} \right]^{BCS} = 3.53\eta_{\Delta}(0). \quad (4.13)$$

Using the results of references [134, 135] we have the expressions for the correction factors $\eta_{H_C}(0)$ and $\eta_{\Delta}(0)$ given by [121]

$$\eta_{H_C}(0) = 1 + 2.3 \left[\frac{T_C}{\omega_0} \right]^2 \ln \left[\frac{\omega_0}{T_C} \right], \quad (4.14)$$

$$\eta_{\Delta}(0) = 1 + 5.3 \left[\frac{T_C}{\omega_0} \right]^2 \ln \left[\frac{\omega_0}{T_C} \right], \quad (4.15)$$

where, ω_0 is the characteristic frequency (equivalent Einstein frequency). Combining Eqns. (4.13)-(4.15), we obtain $\eta_{H_C}(0) = 0.56604 + 0.12294n$, where $n = 2\Delta(0)/k_B T_C$ is the experimentally measured quantity. For the present Ti-V alloys, n is estimated from the temperature dependence of the heat capacity data taken in the superconducting state of these Ti-V alloys. It is found that $n \sim 3.6$ for the $\text{Ti}_{0.8}\text{V}_{0.2}$ alloy while it is ~ 4 for the rest of the Ti-V alloys. Such values of n imply that the correction factor $\eta_{H_C}(0) \sim 1-1.05$ is not very significant for the present Ti-V alloys. Once the correction factor $\eta_{H_C}(0)$ is obtained, we perform a two-parameter fitting of the experimen-

tal $H_{C2}(T)$ data. The electron-phonon coupling constant λ_{ep} and spin-orbit scattering parameter λ_{so} are taken as the fitting parameters. For the other parameters appearing in the fitting function, the experimentally obtained values are used. We obtain a reasonably good fitting of the experimental $H_{C2}(T)$ data for the $\text{Ti}_x\text{V}_{1-x}$ alloys with compositions $x > 0.4$ [Fig. 4.5(b)]. The fitting provides the value of $H_{C2}(0)$ for the Ti-V alloys (see Table 4.3). The values of λ_{ep} obtained from the fitting are almost identical to one obtained from the heat capacity data (Tables 4.1 and 4.2). We also compare the value of λ_{so} for the present $\text{Ti}_x\text{V}_{1-x}$ alloys with the literature. For an example, the fitting of the $H_{C2}(T)$ data provides the value of $\lambda_{so}=0.5\pm 0.1$ for the present $\text{Ti}_{0.8}\text{V}_{0.2}$ alloy. On the other hand, a value of λ_{so} in the range of 0.6-0.1 is reported for a $\text{Ti}_x\text{V}_{1-x}$ alloy having nearby composition ($x=0.775$) in Ref. [78]. The observed slight difference between these values of λ_{so} may be due to the fact that the $H_{C2}(T)$ data in Ref. [78] was fitted without considering the re-normalization effect due to the electron-phonon interactions.

4.2.3 The lower critical field of the Ti-V alloys

In Fig. 4.6(a), we present the magnetic field dependence of magnetization [$M(H)$ curves] obtained at various constant temperatures $T < T_C$ for the $\text{Ti}_{0.6}\text{V}_{0.4}$ alloy in low magnetic field regime. The magnetization measurements were performed after zero-field-cooling the sample down to the temperature of measurement. Similar curves exist for all the other Ti-V alloys

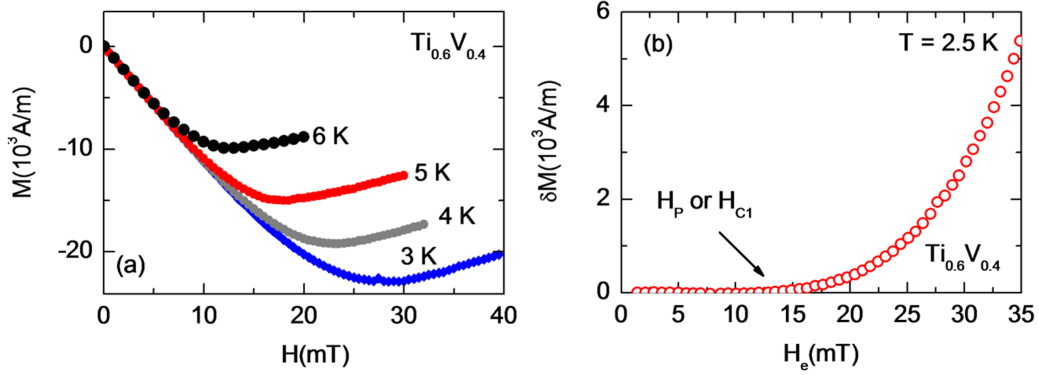


Figure 4.6: (a) Field dependence of magnetization at various constant temperatures below T_C of the $\text{Ti}_{0.6}\text{V}_{0.4}$ alloy. (b) The deviation from linearity δM against the effective magnetic field H_e for the $\text{Ti}_{0.6}\text{V}_{0.4}$ alloy at 2.5 K.

but are not shown here for the sake of conciseness. These $M(H)$ curves are linear at low magnetic fields, and a deviation from showing such linear behaviour is observed at different values of field for different temperatures. The lower critical field H_{C1} is usually determined by finding the point of deviation of the $M(H)$ curve from showing such linear behaviour. It is well known that a demagnetizing field is associated with the irregular geometry of the sample, and the effective magnetic field H_e inside the sample is related to the externally applied magnetic field H as $H_e = (H - 4\pi DM)$ (in CGS unit), where D is the demagnetization factor. Hence, the effective magnetic field H_e inside a sample may differ considerably from the field H applied. This effect becomes particularly important for magnetic fields close to H_{C1} because the superconductors exhibit strong diamagnetism at such low magnetic fields. We have determined D for the Ti-V alloys by assuming complete

flux expulsion at the lowest measuring field (1 mT in the present case).

For the estimation of H_{C1} , we first fit a straight line to the low-field part of the $M(H_e)$ curve. Then, we quantify the deviation δM from the initial linear magnetization by subtracting the fitted curve from the experimental $M(H_e)$ data. The plot of δM as a function of effective magnetic field is shown in Fig. 4.6(b). The value of H_{C1} is taken as the field value at which a non-zero value of δM appears first. This procedure actually gives the value of the field for the first flux-line penetration H_P which may or may not be equal to H_{C1} . It is well known that the edge effect [136] and/or the Bean-Livingston (BL) surface barrier [26, 137] delays the penetration of flux lines in a superconductor, and hence the characteristic field H_P can be different from the true value of H_{C1} of the sample. In such situations, H_{C1} estimated from the deviation of linearity of the $M(H_e)$ curve becomes ill defined. This problem was observed earlier in the determination of H_{C1} of various high- T_C cuprate superconductors [136, 137-139].

According to the Bean's critical state model [140-142], the deviation from the linearity δM in the magnetic field regime $H_{C1} \ll H \ll H^*$ has a field dependence of the form $\delta M \propto (H - H_{C1})^2$. Here, the characteristic field H^* is related to the critical current density J_C of the sample [137, 138]. Hence, the $\delta M^{1/2}$ versus H_e plot should be a straight line. Such plots are shown for the $\text{Ti}_{0.7}\text{V}_{0.3}$ and $\text{Ti}_{0.6}\text{V}_{0.4}$ alloys in Fig. 4.7(a). These plots are indeed linear in the high-field regime. However, a distinct deviation from linearity is observed in these curves in the magnetic field regime just above H_P , and the observed

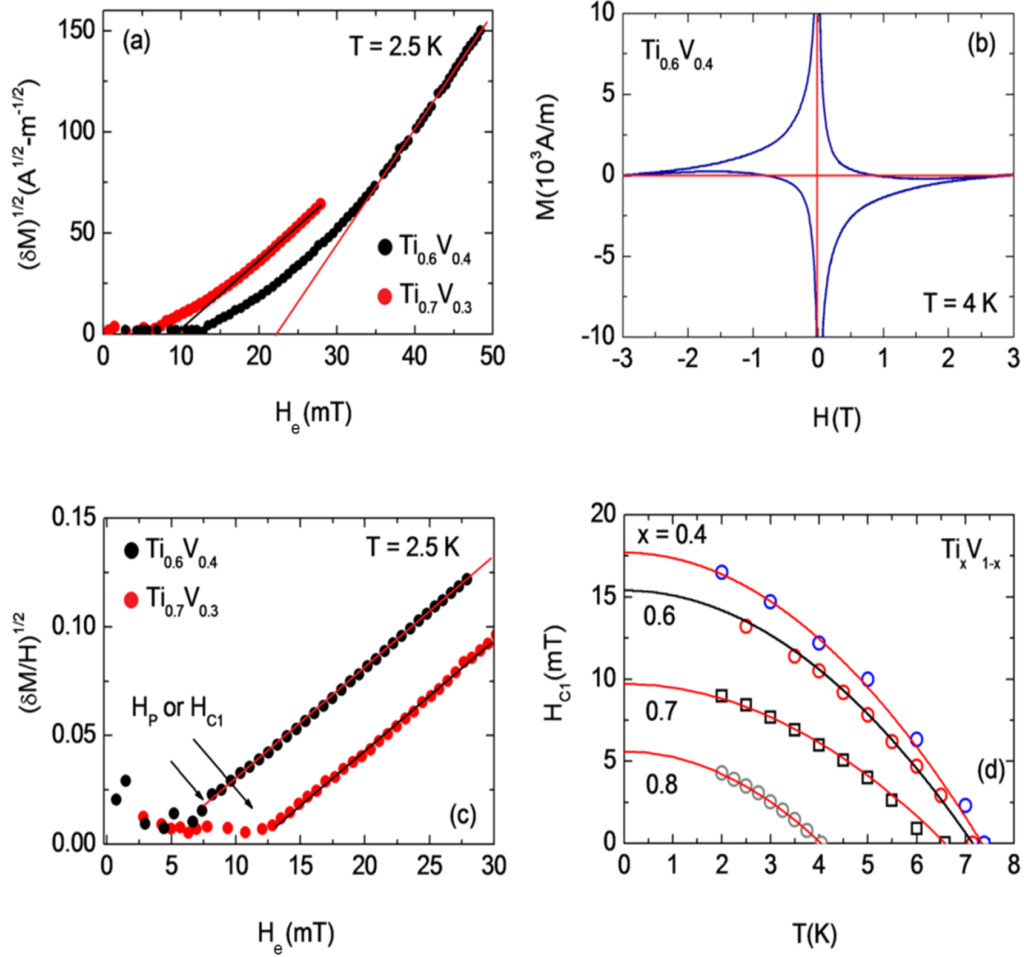


Figure 4.7: (a) The plots of $\delta M^{\frac{1}{2}}$ as a function of internal magnetic field H_e for the $\text{Ti}_{0.6}\text{V}_{0.4}$ and $\text{Ti}_{0.7}\text{V}_{0.3}$ alloys at 2.5 K. (b) The field dependence of magnetization for the $\text{Ti}_{0.6}\text{V}_{0.4}$ alloys at 4 K to illustrate the signature of the existence of the Bean-Livingston surface barrier in this alloy. (c) The plots of $(\delta M/H)^{\frac{1}{2}}$ against H_e for the $\text{Ti}_{0.6}\text{V}_{0.4}$ and $\text{Ti}_{0.7}\text{V}_{0.3}$ alloys. (d) The temperature dependence of H_{C1} of the Ti-V alloys (open symbols). The solid lines are the fittings to the experimental $H_{C1}(T)$ data points based on the empirical relation $H_{C1}(T) = H_{C1}(0)[1 - t^2]$, where $t = T/T_C$.

deviation is particularly significant in the case of $\text{Ti}_{0.6}\text{V}_{0.4}$ alloy. Similar behaviour was observed previously in many other superconductors, such as La-Sr-Cu-Co [136], Y-Ba-Cu-O [137], and Nb [143], where the observation has been attributed due to either the edge effect [136] or the existence of the Bean-Livingston surface barrier effect in the samples [137, 143].

In Fig. 4.7(b), we show the $M(H)$ curve for the $\text{Ti}_{0.6}\text{V}_{0.4}$ alloy at 4 K and in the high magnetic field regime. This $M(H)$ curve appears to be markedly asymmetric around the field axis. Moreover, the magnetization measured in the field-decreasing branch exhibit a tendency to saturate near the $M = 0$ line. Similar characteristics are also observed in the $M(H)$ curves of the $\text{Ti}_{0.4}\text{V}_{0.6}$ and $\text{Ti}_{0.8}\text{V}_{0.2}$ alloys (these curves are not shown here). These observations give clear indication for the existence of the Bean-Livingston surface barrier in these Ti-V alloy superconductors [26, 144]. As can be seen from Fig. 4.4(a), the $M(H)$ curves for the $\text{Ti}_{0.7}\text{V}_{0.3}$ alloy are almost symmetric around the field axis. Hence, the relevance of the Bean-Livingston surface barrier is expected to be less significant in this alloy. Interestingly, the deviation of the $\delta M^{\frac{1}{2}}$ versus H_e plot from showing the linear behaviour is also observed to be minimal for the $\text{Ti}_{0.7}\text{V}_{0.3}$ alloy. Hence, the straightforward method for the determination of H_{C1} by finding the deviation of linearity of the $M(H_e)$ curve cannot be used for the present Ti-V alloys. Burlachkov *et al.* [139] had proposed a generalized Bean's critical state model, which considers the effect of the Bean-Livingston surface barrier. They assumed that flux lines start penetrating into the sample at some distinct points at

the surface of the sample where the barrier is suppressed by the presence of defects, and obtained [137]

$$\begin{aligned}\delta M &= A \left[(1-m)H_{C1} \frac{(H_e - H_{C1})^2}{2} + \frac{(H_e - H_{C1})^3}{6} \right] \\ &= \frac{A(H_e - H_{C1})^2 [H_e - (3m-2)H_{C1}]}{6}.\end{aligned}\quad (4.16)$$

In the above relation, A is a constant related to critical current density and also to the shape of the sample. The parameter m is the ratio of equilibrium magnetization M to the maximum negative magnetization $M(H_{C1})$, and depends only on the Ginzburg-Landau parameter κ . Burlachkov *et al.* [139] had estimated $m \approx 0.7$ for the high- κ (~ 100) $\text{YBa}_2\text{Cu}_3\text{O}_{7-\delta}$ superconductor. Putting $m=0.7$ in the relation (4.16), one obtains $(\delta M/H_e)^{\frac{1}{2}} \propto (H_e - H_{C1})$ [137]. Consequently, the plot of $(\delta M/H_e)^{\frac{1}{2}}$ as a function of H_e will be a straight line with a threshold at H_{C1} . Such a plot is often used to check the influence of the Bean-Livingston surface barrier in many superconductors [137]. In Fig. 4.7(c), we present the $(\delta M/H_e)^{\frac{1}{2}}$ versus H_e plots for the $\text{Ti}_{0.7}\text{V}_{0.3}$ and $\text{Ti}_{0.6}\text{V}_{0.4}$ alloys. These plots are indeed linear in the magnetic field regime above H_P . We estimate H_{C1} from the threshold of the $(\delta M/H_e)^{\frac{1}{2}}$ versus H_e plots. It is to be noted that the H_{C1} value thus estimated almost coincides with the value of H_P . This is also found to be true for the $\text{Ti}_{0.4}\text{V}_{0.6}$ and $\text{Ti}_{0.8}\text{V}_{0.2}$ alloys. These observations suggest that the existence of the Bean-Livingston surface barrier in the present Ti-V alloys does not rise H_P above the H_{C1} , but just lower the rate of flux line penetration into the sample.

Similar result has also been found previously in Nb sample [143]. Fig. 4.7(d) summarizes the temperature dependence of H_{C1} for the Ti-V alloys after considering the correction for demagnetization effect. The experimentally determined values of $H_{C1}(T)$ are found to follow the empirical relation [145]

$$H_{C1}(T) = H_{C1}(0) \left[1 - \left(\frac{T}{T_C} \right)^2 \right], \quad (4.17)$$

where, $H_{C1}(0)$ is the lower critical field at absolute zero temperature. We obtain the values of $H_{C1}(0)$ for the Ti-V alloys by fitting the experimental $H_{C1}(T)$ data based on the above relation. These values are given in Table 4.3. For the Ti-V alloys, $H_{C1}(0)$ is found to have relatively low value and it increases with the decrease in Ti concentration in the Ti-V alloys.

4.2.4 Thermodynamic critical field of the Ti-V alloys

The thermodynamic critical field H_C can be obtained from the heat capacity data in the superconducting state using the relation [146]

$$H_C(T)^2 = \int_T^{T_C} dT' \int_{T'}^{T_C} \frac{[C_{es}(T'') - C_{ns}(T'')]}{T''} dT''. \quad (4.18)$$

Here, C_{es} and C_{en} respectively represent the electronic heat capacities in the superconducting and normal states. In order to obtain C_{en} , we first fit the temperature dependence of the experimental heat capacity data in the temperature range from the T_C to 12 K based on the relation (4.2). In

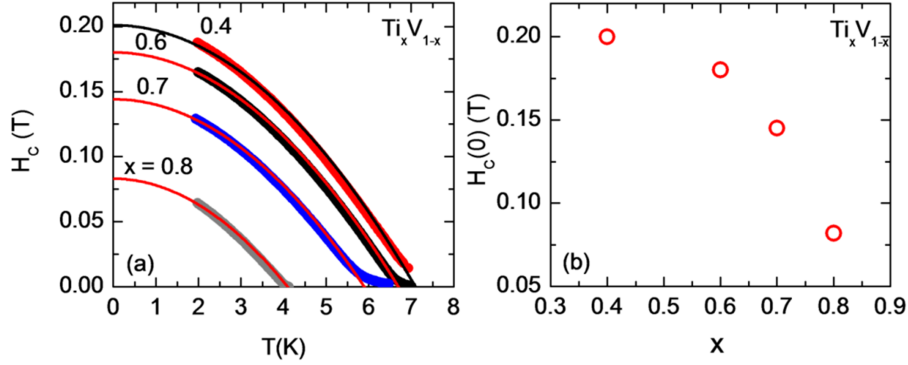


Figure 4.8: (a) Temperature dependence of the thermodynamic critical field H_C for the $\text{Ti}_x\text{V}_{1-x}$ alloys estimated from the heat capacity data. The solid lines are the fits to the experimental data points based on the empirical relation: $H_C(T) = H_C(0)(1 - t^2)$, where $t = T/T_C$. (b) $H_C(0)$ values of the $\text{Ti}_x\text{V}_{1-x}$ alloys obtained from the fittings are shown as a function Ti concentration x .

this relation, the first term represents the electronic heat capacity (C_{en}) and the second term represents the lattice heat capacity (C_L). The temperature behaviour of the lattice heat capacity is not altered when the material undergoes a phase transition from normal to superconducting state. This allows us to obtain the lattice heat capacity in the superconducting state by the low temperature extrapolation of the normal state lattice heat capacity $C_L(T) = \beta T^3$. Then the electronic heat capacity in the superconducting state (C_{es}) is obtained by subtracting the lattice heat capacity (C_L) from the experimental heat capacity data taken at temperatures $T \leq T_C$. We then estimate $H_C(T)$ for the Ti-V alloys based on the relation (4.18). These results are shown in Fig. 4.8(a). The $H_C(T)$ curves follow the empirical relation $H_C(T) = H_C(0)(1 - t^2)$, where $t = T/T_C$ and $H_C(0)$ is the thermodynamic

critical field at zero temperature. The fitting of the $H_C(T)$ curves with this empirical relation is shown in Fig. 4.8(a) with the help of solid lines. The values of $H_C(0)$ obtained as fitting parameter are presented in Table 4.3. The value of $H_C(0)$ can also be obtained from the phenomenological Ginzburg-Landau theory. According to this phenomenological theory, the critical fields $H_{C1}(0)$ and $H_{C2}(0)$ are related to $H_C(0)$ as [147]

$$H_{C1}(0) = \frac{\ln\kappa}{\sqrt{2\kappa}} H_C(0) \quad (4.19)$$

and

$$H_{C2}(0) = \sqrt{2\kappa} H_C(0). \quad (4.20)$$

Here κ is the Ginzburg-Landau parameter. Therefore, the above two expressions provide the estimation of both $H_C(0)$ and κ from the knowledge of $H_{C1}(0)$ and $H_{C2}(0)$. We have estimated $H_C(0)$ values for the present set of Ti-V alloys using the values of $H_{C1}(0)$ and $H_{C2}(0)$. The estimated values of $H_C(0)$ using this procedure match very well with the values obtained from the heat capacity data. It is found that the $H_C(0)$ values for the Ti-V alloys increases with the decrease in the Ti concentration. This is in agreement with the BCS relation, according to which, $H_C(0)$ depends on both the T_C and the Sommerfeld coefficient γ as: $H_C(0) \propto \gamma^{\frac{1}{2}} T_C$ [70, 121]. We have observed above that both the T_C and γ increase with decreasing Ti concentration in the Ti-V alloys. Consequently, $H_C(0)$ increases with decreasing Ti concentration in the Ti-V alloys [Fig. 4.8(b)].

4.2.5 Fundamental superconducting length scales in the Ti-V alloys

In the phenomenological Ginzburg-Landau theory, the upper critical field H_{C2} is the magnetic field value at which flux-line cores of radius ξ overlap with each other. Therefore, $H_{C2}(0)$ is related to the Ginzburg-Landau coherence length $\xi(0)$ as

$$H_{C2}(0) = \frac{\Phi_0}{2\pi\xi(0)^2}. \quad (4.21)$$

We estimate $\xi(0)$ for the Ti-V alloys from the $H_{C2}(0)$ values using relation (4.21). The estimated values of $\xi(0)$ are given in Table 4.3. For the Ti-V alloys, the coherence length is found to be much larger than the mean free path of the conduction electrons (l_e) estimated for these alloys in the Ref. [148], suggesting that these alloys are dirty limit superconductors. The Ginzburg-Landau penetration depth at zero temperature $\lambda(0)$ can be obtained from the values of $H_{C1}(0)$ and $\xi(0)$ using the Ginzburg-Landau relation given as

$$H_{C1}(0) = \left[\frac{\Phi_0}{4\pi\lambda(0)^2} \right] \ln\kappa, \quad (4.22)$$

where, the Ginzburg-Landau parameter $\kappa = \lambda(0)/\xi(0)$. The above relation is employed to estimate the value of $\lambda(0)$ for the Ti-V alloys using the known values of $H_{C1}(0)$ and $\xi(0)$. The estimated values of $\lambda(0)$ for the Ti-V alloys are presented in Table 4.3.

According to the London model, the reversible magnetization M in the

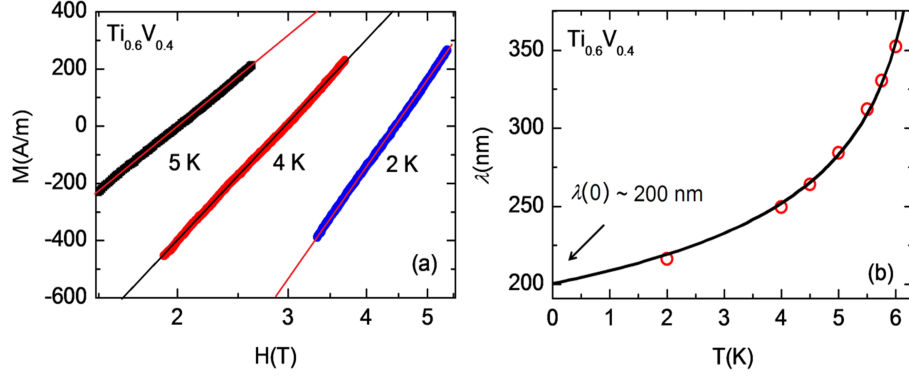


Figure 4.9: (a) M versus $\ln(H)$ curves for the $\text{Ti}_{0.6}\text{V}_{0.4}$ alloy at different constant temperatures. (b) Temperature dependence of the penetration depth λ for the $\text{Ti}_{0.6}\text{V}_{0.4}$ alloy obtained from the slope of the M versus $\ln(H)$ curves of Fig. (a) (open symbols). The solid lines are the fits to the experimental data points with the empirical relation $\lambda(T) = \lambda(0)/(1 - t)^{\frac{1}{4}}$, where $t = T/T_C$.

intermediate magnetic field regime $H_{C1} \ll H \ll H_{C2}$ may be written as

$$-4\pi M = \frac{\Phi_0}{8\pi\lambda^2} \ln \left[\eta \frac{H_{C2}(T)}{H} \right], \quad (4.23)$$

where, η is a constant of the order of unity [149]. Therefore, the plot of magnetization as a function of $\ln(H)$ should be linear in the intermediate magnetic field regime, and its slope will provide the value of λ . In Fig. 4.9(a), we show few selected $M(H)$ curves for the $\text{Ti}_{0.6}\text{V}_{0.4}$ alloy plotted in M versus $\ln(H)$ fashion. At temperatures much lower than the T_C , these M versus $\ln(H)$ curves are linear over a considerably large magnetic field regime. However, the linear region in the M versus $\ln(H)$ curves becomes gradually narrower as the temperature approaches T_C . This is found to be

true for the other Ti-V alloys as well (not shown here). We then estimate λ at various constant temperatures from the slopes of these M versus $\ln(H)$ curves, and these results for the $\text{Ti}_{0.6}\text{V}_{0.4}$ alloy are shown in Fig. 4.9(b). In the entire temperature regime, the $\lambda(T)$ data follow the empirical relation $\lambda(T) = \lambda(0)/(1 - t)^{\frac{1}{4}}$, where $t = T/T_C$ [150]. The fitting of the $\lambda(T)$ data with this empirical relation is shown in Fig. 4.9(b) by the solid lines. For performing the fitting we take T_C and $\lambda(0)$ as the fitting parameters. The curve-fitting gives a value of $\lambda(0) \sim 200$ nm which is close to $\lambda(0) \sim 190$ nm obtained from the values of $H_{C1}(0)$ and $\xi(0)$ using the Ginzburg-Landau relation. We estimate $\lambda(0)$ for all Ti-V alloys from the $M(H)$ curves, which are found to be almost identical to the values given in Table 4.3.

Table 4.3: Various fundamental parameters in the superconducting state of the Ti-V alloys.

	$H_{C2}(0)$	$H_{C1}(0)$	$\xi(0)$	$\lambda(0)$	κ	$H_C(0)$
	(T)	(mT)	(nm)	(nm)		(mT)
$\text{Ti}_{0.8}\text{V}_{0.2}$	8.7 ± 0.4	5.7 ± 0.25	6.15 ± 0.14	330 ± 16	~ 55	80 ± 2
$\text{Ti}_{0.7}\text{V}_{0.3}$	11.6 ± 0.4	9.7 ± 0.4	5.33 ± 0.09	246 ± 10	~ 50	148 ± 5
$\text{Ti}_{0.6}\text{V}_{0.4}$	13.5 ± 0.5	15.4 ± 0.25	4.94 ± 0.09	190 ± 15	~ 40	178 ± 3
$\text{Ti}_{0.4}\text{V}_{0.6}$	10.6 ± 0.1	17.8 ± 0.3	5.57 ± 0.03	172 ± 13	~ 32	200 ± 5

The estimated values of $\xi(0)$ and $\lambda(0)$ is used for the estimation of the Ginzburg-Landau parameter κ for the Ti-V alloys, and these values are given in Table 4.3. The present Ti-V alloys are found to have very large values of

κ , indicating that these Ti-V alloys are extreme type-II superconductors. As discussed in the chapter 1, the Ginzburg-Landau parameter κ is obtained by using the Gorkov relation [82] as approximated by Goodman [83] as

$$\kappa = \kappa_0 + \kappa_\ell = \kappa_0 + 7.53 \times 10^3 \rho_0 \gamma^{\frac{1}{2}}. \quad (4.24)$$

The physical meaning of each term appearing in the above relation is discussed in chapter 1. When the mean free path for the conduction electrons l_e is much less than the Bardeen-Cooper-Schrieffer (BCS) coherence length ξ_0 , then we can approximate [70, 76]

$$\kappa \approx \kappa_\ell \approx 7.53 \times 10^3 \rho_0 \gamma^{\frac{1}{2}}. \quad (4.25)$$

We have already found that the present Ti-V alloys are dirty limit superconductors. In a dirty superconductor, the Ginzburg-Landau coherence length $\xi(0)$ is related to the BCS coherence length ξ_0 as: $\xi(0) = 0.85(l_e \xi_0)^{\frac{1}{2}}$ [151]. Hence, we find that $l_0 \ll \xi(0) \ll \xi_0$ for the dirty limit Ti-V superconducting alloys, which implying that the approximation given in Eqn. (4.25) is valid for the Ti-V alloys. It then appears from Eqn. (4.25) that the large value of κ in these Ti-V alloys is due to the high values of ρ_0 and γ of these alloys. Since the variation of κ with γ is slower than the variation of κ with ρ_0 , the increase in the value of κ in the $\text{Ti}_x\text{V}_{1-x}$ alloys with the increase in the Ti concentration x can therefore be ascribed to the increase of the ρ_0 with x .

4.3 Summary and conclusions

- (i) The superconducting transition temperature T_C of the present set of Ti-V alloys increase from 4.48 K to 7.64 K as the Ti concentration is decreased from 0.8 to 0.4. For the $\text{Ti}_x\text{V}_{1-x}$ alloys with compositions $x \leq 0.7$, the T_C estimated using the McMillan formula is found to be much larger than the experimentally obtained T_C value. A detailed study probing the possible reasons (viz. soft-phonons or spin fluctuations) for this observed disagreement will be presented in chapter 6.
- (ii) Our estimation of the electron-phonon coupling constant λ_{ep} indicates that the Ti-rich Ti-V alloys are weak-coupling superconductors. The value of λ_{ep} increases with decreasing Ti concentration in the Ti-V alloys. In the V-rich Ti-V alloys, λ_{ep} is close to unity, indicating the moderate to strong coupling nature of superconductivity in the V-rich Ti-V alloys.
- (iii) For the Ti-V alloys, the upper critical field H_{C2} depends strongly on the alloy concentration. The maximum value of H_{C2} is obtained for the $\text{Ti}_{0.6}\text{V}_{0.4}$ alloy. A value of $H_{C2} \sim 9$ T is estimated for this alloy at 4.2 K. The Pauli paramagnetic pair breaking effect significantly influences the H_{C2} of the Ti-V alloys. Electron-phonon interactions, however, reduce the influence of the Pauli paramagnetic pair breaking effect in the V-rich Ti-V alloys.

(iv) The magnetic field dependence of magnetization indicates that the Bean-Livingston surface barrier effect might be present in the superconducting Ti-V samples. Generally, the experimental observation of the Bean-Livingston surface barrier effect in the conventional superconductors requires highly polished surfaces of the sample because the strong local fields caused by the surface roughness can overcome the surface barrier. However, Ti-V alloys have very large value of the Ginzburg-Landau parameter κ . Therefore, the magnetic field limit ($\sim H_C/\sqrt{2}$) up to which the Bean-Livingston surface barrier can exist is much larger than the H_{C1} of these Ti-V alloys [137]. Then the local fields caused by the surface roughness may not be strong enough to completely destroy the surface barrier in these Ti-V alloys. However, the Bean-Livingston surface barrier is also known to become suppressed by the presence of defects on the sample surfaces, which act as gates for the penetration of the flux lines into the sample [137]. The grain boundary is one such defect structure present in the Ti-V alloys. Due to the smallest grain size and hence the highest defect density in the $\text{Ti}_{0.7}\text{V}_{0.3}$ alloy, the Bean-Livingston surface barrier appears to be less significant in this alloy. For the present Ti-V alloys, we have found that the estimation of H_{C1} from the low-field $M(H)$ data is not affected by the presence of the Bean-Livingston surface barrier, though the presence of such surface barrier lowers the rate of flux line penetration into the sample. The presence of defects on the surface along with the surface roughness

seems to be successful in nullifying the effect of the surface barrier at some regions of the sample surfaces allowing the penetration of flux lines into the sample at H_{C1} .

- (v) The coherence length ξ estimated for the present Ti-V alloys is found to be much larger than the mean free path l_e for the electron conduction in these alloys, suggesting that these Ti-V alloys are dirty limit superconductors. The very large values of Ginzburg-Landau parameter κ estimated for the Ti-V alloys make them extreme type-II superconductors. However, the κ values estimated here are notably smaller than those estimated using the normal state parameters in Refs. [70, 76, 79]. For the Ti-V alloys, the magnetic field penetration depth λ increases with increasing Ti concentration. Since λ is related to the line tension energy of the flux line as $E_L = (\Phi_0/4\pi\lambda)^2 \ln\kappa$, the flux line lattice in the V-rich Ti-V alloys is expected to be more rigid as compared to that in the Ti-rich Ti-V alloys. This is an important information because soft flux line lattice is generally detrimental for the lossless current carrying aspect of a superconductor. Moreover, the T_C of the V-rich Ti-V alloys is also higher than the liquid helium temperature. One of the major problems with the V-rich Ti-V alloys is that the H_{C2} values decrease as the Ti concentration decreases below $x = 0.6$. However, for the V-rich Ti-V alloys, the value of the electronic mean free path l_e is much larger than the inter-atomic spacing [148]. Consequently, l_e can be further reduced by introducing defects in these Ti-V alloys. In doing

so, the Ginzburg-Landau coherence length $\xi [\propto (\xi_0 l_e)^{\frac{1}{2}}$, where the BCS coherence length ξ_0 is an intrinsic property of a superconductor which remains unchanged when disorder is introduced in the system] can be reduced, which in turn will result an enhancement of the H_{C2} . On the other hand, the value of l_e is comparable to the inter-atomic spacing for the Ti-rich Ti-V alloys [148]. Consequently, l_e cannot be reduced further by introducing defects. Therefore, such H_{C2} enhancement is not possible for the Ti-rich Ti-V alloys. Based on these arguments it appears that the V-rich Ti-V alloys are more relevant from the technological application points of view.

Chapter 5

Fluctuation conductivity in the Ti-V alloys

5.1 Introduction

Previous studies [44, 85, 86] on the bulk Ti-V alloys reported that the temperature dependence of the electrical resistivity (ρ) of these alloys exhibited strong rounding-off behaviour above the superconducting transition temperature T_C , as is the case for the many high- T_C superconductors. The trace of such a rounding-off behaviour of the $\rho(T)$ curve persists up to a temperature $\sim 2T_C$. This phenomenon is also observed in the thin film samples of the Ti-V alloys [152]. It is also found that this phenomenon is not markedly influenced by the presence of disorders and/or preparation-sensitive secondary phases in the samples [85]. Thus the phenomenon appears to be intrinsic to the Ti-V alloys. Hake [85] had found that the theories of superconducting fluctuations induced conductivity well describe the $\rho(T)$ curve in the wide temperature regime where the rounding-off behaviour is observed. Accordingly, Hake had

inferred that the intrinsic rounding-off behaviour of the $\rho(T)$ curve observed in the Ti-V alloys was a consequence of the superconducting fluctuation effect [85, 86]. However, the theories Hake had used to analyze the results [85, 86], were derived based on the time-dependent Ginzburg-Landau theory [85, 86, 153, 154], which is valid only in the close vicinity of T_C . Therefore, the legitimacy of his approach for analysing the experimental data in the large temperature regime above T_C is rather questionable. Later, Rassokhin *et al.* [44] had suspected the superconducting fluctuations scenario by arguing that the superconducting fluctuation effect is expected to be limited only in the close vicinity of T_C for bulk low- T_C superconductors like Ti-V alloys. In the work of Rassokhin *et al.* [44] and also in few concurrent works led by Prekul *et al.* [88, 94], it was suggested that the rounding-off behaviour of the $\rho(T)$ curve exhibited by the Ti-V alloys arises due to an interplay between the (Cooper-pair) pair-breaking mechanism by the localized spin fluctuations and a high temperature superconductivity of the Ti-V alloys (if localized spin fluctuations were absent, these Ti-V alloys would show superconductivity at temperature almost twice of the experimentally observed T_C value). In fact, a significant suppression of the T_C by the presence of spin fluctuations in the Ti-V alloys had been inferred previously by Pictet *et al.* [93] and recently by us [155, 156]. These results put strength to the view point of Rassokhin *et al.* and Prekul *et al.*. Therefore, the question whether the observed rounding-off behaviour of the $\rho(T)$ curve of the Ti-V alloys is due to the superconducting fluctuation effect or due to the non-trivial role of the spin fluctuations in

these alloys is still remained imprecise.

This chapter is motivated to find a precise answer to the question raised above. For this, we have study four annealed $\text{Ti}_x\text{V}_{1-x}$ alloys having compositions $x = 0.8, 0.7, 0.6$ and 0.4 . In these Ti-V alloys, $\rho(T)$ curve becomes strongly rounded-off at temperatures ranging from T_C up to $\sim 2T_C$. Moreover, these Ti-V alloys exhibit strong positive magneto-resistance for temperatures $T \leq 2T_C$. To check whether the superconducting fluctuation effect is behind these observed phenomena, we have analysed the excess conductivity data of these Ti-V alloys based on the Aslamazov-Larkin (AL) theoretical model [157] and its extended version [158]. We have also invoked the theoretical model of Usadel [159], which considers the magneto-resistance associated with the AL contribution to the excess conductivity. These theoretical models consistently describe the experimental data of the present Ti-V alloys, suggesting that the superconducting fluctuation effect is behind the observed rounding-off behaviour of the resistive transition of the Ti-V alloys.

5.2 Results and discussion

5.2.1 The temperature dependence of electrical resistivity in the Ti-V alloys and the relevance of the superconducting fluctuations in these alloys

Fig. 5.1 shows the temperature dependence of resistivity (ρ) for the Ti-V alloys in zero magnetic field. The $\rho(T)$ curve for all these Ti-V alloys appears to be strongly rounded-off before a sharp drop of resistivity occurs at the onset superconducting transition temperature T_C . The trace of this rounding-off behaviour of the $\rho(T)$ curve persists up to a temperature $T^* \sim 2T_C$. Such a behaviour of the $\rho(T)$ curve is common in high- T_C materials, where superconducting fluctuation effect is attributed for the observed behaviour. The effectiveness of the superconducting fluctuation is quantified by the Ginzburg number G_i , which for an isotropic superconductor is expressed as [160]

$$G_i = \frac{1}{2} \left[\frac{k_B T_C}{H_C(0)^2 \xi(0)^3} \right]^2, \quad (5.1)$$

where $H_C(0)$ and $\xi(0)$ are respectively the thermodynamic critical field and the coherence length at zero temperature, and k_B is the Boltzmann constant. For the high- T_C superconductors, $G_i \sim 10^{-2}$, making the superconducting fluctuations significant in an experimentally accessible temperature window $\sim G_i T_C$ [161], though the experimental results indicate that the actual temperature window for observing the superconducting fluctuation effect is still larger than this estimate. On the other hand, experimental observation of

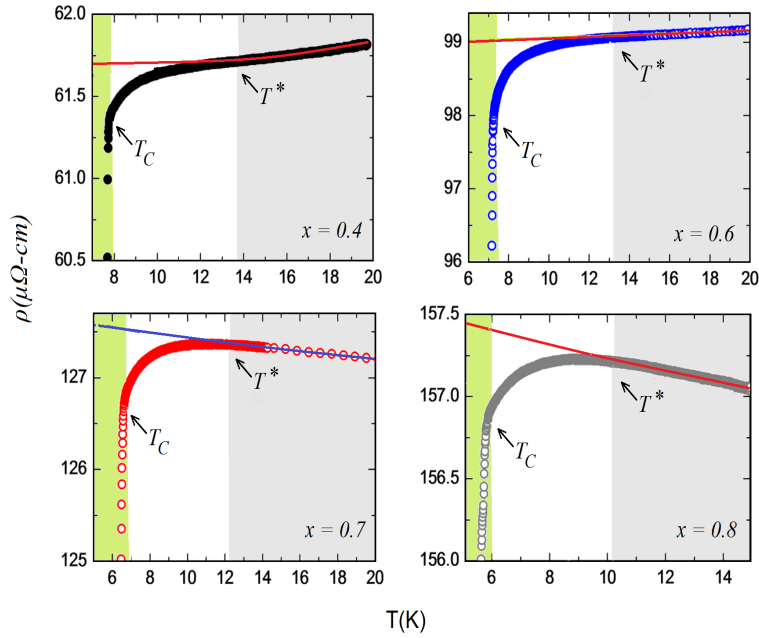


Figure 5.1: The temperature dependence of resistivity curves for the $\text{Ti}_x\text{V}_{1-x}$ alloys. These curves show a strong rounding-off behaviour before a sharp drop in the resistivity is observed at the onset temperature of the superconducting transition, T_C . The trace of this effect persists up to a characteristic temperature $T^* \sim 2T_C$. The solid lines shown are extrapolations of the normal-state resistivity. The temperature at which the extrapolated curve bifurcates from the experimental $\rho(T)$ curve is taken as T^* .

the superconducting fluctuation effect becomes extremely difficult in the conventional low- T_C superconductors due to their very small values of $G_i \sim 10^{-8}$. We have estimated the G_i number for the present Ti-V alloys using the values of $H_C(0)$ and $\xi(0)$ obtained for these alloys in chapter 4. The G_i number is estimated to be $G_i \sim 10^{-6}$ - 10^{-5} for the Ti-V alloys, which is intermediate between those for the high- T_C and the low- T_C superconductors. A comparable magnitude of the G_i number is found for MgB_2 [162, 163] and YNi_2B_2 [164] superconductors, for which the superconducting fluctuations induced conductivity above T_C is well documented [164-166]. Therefore, strong effect of the superconducting fluctuations may also be expected for the Ti-V alloys in an experimentally accessible temperature window.

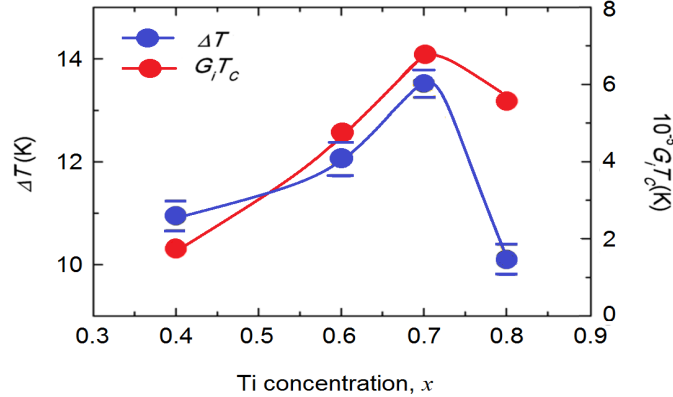


Figure 5.2: The plots of temperature window $\Delta T = (T^* - T_C)$ where the excess conductivity can be measured experimentally in the present $\text{Ti}_x\text{V}_{1-x}$ alloys, and the parameter $G_i T_C$ for these $\text{Ti}_x\text{V}_{1-x}$ alloys as a function of Ti concentration x . The observed parallelism between these plots indicates the correlation of superconducting fluctuations with the observed rounding-off behaviour of the $\rho(T)$ curve shown in Fig. 5.1.

To get a deeper insight into this, the temperature window $\Delta T(=T^* - T_C)$, where the rounding-off behaviour of the $\rho(T)$ curve of the Ti-V alloys is observed, is plotted against the Ti concentration in Fig. 5.2. Since the temperature window, where the experimental observation of the superconducting fluctuations induced conductivity is possible, can be correlated with the parameter $G_i T_C$ [161], we also plot $G_i T_C$ against the Ti concentration in Fig. 5.2. The observed parallelism between these plots indicates that superconducting fluctuations might be the probable reason behind the rounding-off behaviour of the $\rho(T)$ curve of the present Ti-V alloys. This observation motivates us to analyse the experimentally measured excess conductivity data of the present Ti-V alloy in the temperature regime above T_C based on the theoretical models for the superconducting fluctuation induced conductivity.

5.2.2 Theoretical models for the superconducting fluctuation induced conductivity

In a superconductor, both the formation of the Cooper-pairs and their condensation into a coherent state of zero resistivity occur simultaneously at T_C . However, superconducting fluctuations can lead to the formation of the short-lived Cooper-pairs at temperature above T_C (a consequence of the superconducting order parameter fluctuations). The presence of such short-lived Cooper-pairs has a consequence to increase the conductivity of the material, and thereby forming the rounding-off feature in the $\rho(T)$ curve above T_C . On theoretical ground, Aslamazov and Larkin [157] had proposed

a direct contribution to the conductivity caused by the acceleration of the short-lived Cooper-pairs. The Aslamazov-Larkin (AL) theory was derived on the basis of the mean field approximation of the GinzburgLandau theory. According to this theory, the excess conductivity above T_C is given by $\Delta\sigma_{AL}(\varepsilon) = A_0\varepsilon^{-\lambda}$, where $\varepsilon = (T - T_C)/T_C$ is the reduced temperature, A_0 is a temperature independent amplitude of the excess conductivity, and λ is the critical exponent of the excess conductivity or fluctuation conductivity [167]. The critical exponent λ depends on the dimensionality D of the superconducting fluctuations as $\lambda = (2 - D/2)$. The AL contribution to the excess conductivity for isotropic superconductors in different dimensions (indicated by super-index) is expressed as [161, 167, 168]

$$\Delta\sigma_{AL}^{3D}(\varepsilon) = \frac{e^2}{32\hbar\xi(0)}\varepsilon^{-0.5}, \quad (5.2)$$

and

$$\Delta\sigma_{AL}^{2D}(\varepsilon) = \frac{e^2}{16\hbar d}\varepsilon^{-1}, [\xi(T) \gg d]. \quad (5.3)$$

Here, e is the electronic charge, \hbar is the reduced Planck's constant, $\xi(T)$ is the coherence length at temperature T , and d is the characteristic length of a two-dimensional system (usually denotes the thickness of the thin film). Later, Maki [169] and Thompson [5.22] had proposed that the short-lived Cooper-pairs formed above T_C can also indirectly increase the conductivity of a material. The Maki-Thompson (MT) contribution arises due to the change in normal current in presence of superconducting fluctuations [168].

In contrast to the direct AL contribution to the excess conductivity which results from the acceleration of the short-lived Cooper-pairs, the indirect MT contribution depends strongly on the presence of pair breaking mechanisms in the material. The indirect MT contribution to the excess conductivity is given by [168, 170]

$$\Delta\sigma_{MT}^{3D}(\varepsilon) = \frac{e^2}{8\hbar\xi(0)}\varepsilon^{-\alpha} \left[1 + \left(\frac{\delta}{\varepsilon} \right)^{\frac{1}{2}} \right]^{-1}, \quad (5.4)$$

and

$$\Delta\sigma_{MT}^{2D}(\varepsilon) = \frac{e^2}{8\hbar d} \left[\frac{1}{\varepsilon - \delta} \right] \ln \left[\frac{\varepsilon}{\delta} \right]. \quad (5.5)$$

In the above expression, δ is the pair breaking parameter which varies between zero and unity depending on the strength of the pair breaking mechanisms present in a material. The sources of pair breaking mechanism may be intrinsic to a material such as phonons, and/or magnetic impurities, and/or spin fluctuations.

5.2.3 The temperature dependence of excess conductivity of the Ti-V alloys

The excess conductivity resulted from the formation of the short-lived Cooper-pairs can be obtained from the resistivity data as

$$\Delta\sigma(T) = \frac{1}{\rho_{exp}(T)} - \frac{1}{\rho_{fit}(T)}. \quad (5.6)$$

Here, $\rho_{exp}(T)$ is the experimentally measured resistivity and $\rho_{fit}(T)$ is the background resistivity. Hence, the accuracy in the estimation of the excess conductivity depends strongly on the way of determination of the background resistivity. For obtaining the background resistivity, $\rho_{exp}(T)$ data of the Ti-V alloys are fitted with suitable function forms of resistivity in the temperature regime $3T_C \geq T \geq 40$ K, and then the fitted curve is extrapolated through the T_C . For the Ti_xV_{1-x} alloys with compositions $x= 0.4$ and 0.6 , $\rho_{exp}(T)$ data are fitted based on the relation $\rho_{exp}(T) = \rho_0 + AT^2 + BT^5$, where ρ_0 , A , and B are constants. On the other hand, $\rho_{exp}(T)$ data of the $Ti_{0.7}V_{0.3}$ and $Ti_{0.8}V_{0.2}$ alloys are fitted using the relations $\rho_{exp}(T) = \rho_0 - A' \ln T$ and $\rho_{exp}(T) = \rho_0 - B' \sqrt{T}$ respectively. Here A' and B' are constants. These functional forms well describe the $\rho_{exp}(T)$ data of the present Ti-V alloys. The temperature dependence of resistivity of the Ti-V alloys will be discussed in detail in chapter 6. The background resistivity of the present Ti-V alloys obtained in this procedure are shown by the solid lines in Fig. 5.1.

The excess conductivity $\Delta\sigma$ for the present Ti-V alloys is estimated following the procedure described above, and plotted against the reduced temperature $\varepsilon = (T - T_C^{mf})/T_C^{mf}$ in *log-log* scales in Fig. 5.3. Here T_C^{mf} is the mean field transition temperature which is taken as the temperature at which the temperature derivative of the resistivity across the superconducting transition becomes the maximum. The T_C^{mf} values for the present Ti-V alloys are given in Table 5.1. The $\Delta\sigma(\varepsilon)$ curves for all the Ti-V alloys except $Ti_{0.8}V_{0.2}$ exhibit some common features. A rapid upturn is observed in these curves

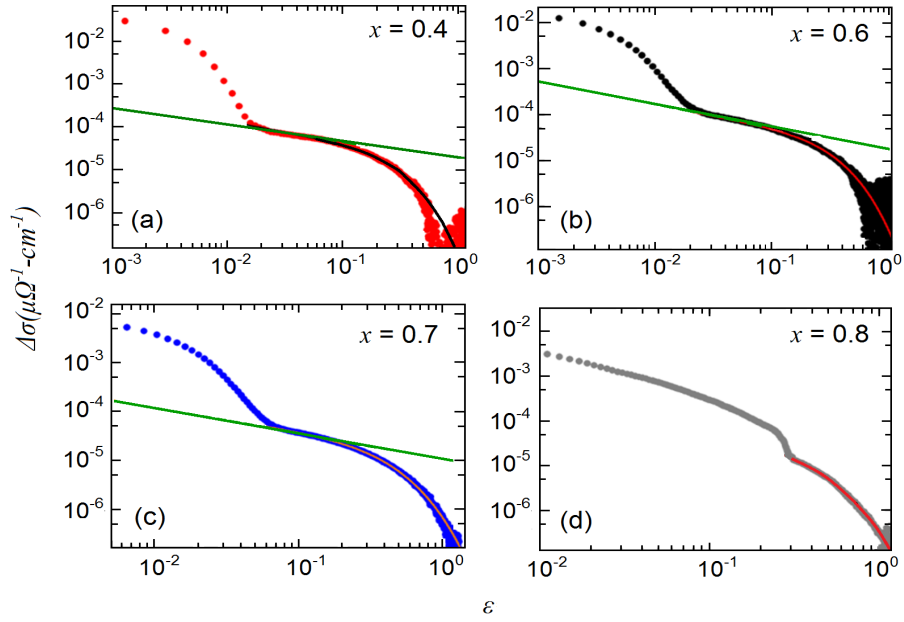


Figure 5.3: Experimentally measured excess conductivity $\Delta\sigma$ for the $\text{Ti}_x\text{V}_{1-x}$ alloys as a function of reduced temperature $\varepsilon = (T - T_C^{mf})/T_C^{mf}$ in *log-log* scales (solid symbols). The solid straight lines are the fits to the experimental data base on the relation: $\Delta\sigma(\varepsilon) = A_0\varepsilon^{-\lambda}$. On the other hand, the non-linear solid lines are the fits to the experimental data based on the function given in Eqn. (5.7).

in the close vicinity of T_C^{mf} , i.e. near to $\varepsilon = 0$. Such a rapid upturn in $\Delta\sigma(\varepsilon)$ curve is quite common, and is known to arise due to the overestimation of the excess conductivity in the broadened superconducting transition caused by the presence of inhomogeneities in the sample [161, 171, 172]. In such case, the rapid upturn observed in the $\Delta\sigma(\varepsilon)$ curve is expected to depend on the criterion to define T_C [161, 171, 172]. In agreement with this the rapid upturn in the $\Delta\sigma(\varepsilon)$ curves of the Ti-V alloy is observed to depend strongly on the specific criterion to define T_C . This is illustrated in Fig. 5.4 for the $\text{Ti}_{0.6}\text{V}_{0.4}$ alloy. We also observe in Fig. 5.4 that the rapid upturn in the $\Delta\sigma(\varepsilon)$ curve is gradually washed out as the chosen T_C approaches towards the onset temperature of the superconducting transition. These observations clearly indicate that the observed feature indeed arises due to the overestimation of the excess conductivity in the broadened superconducting transition. Therefore, we will not focus our attention to analyse the excess conductivity data in the temperature regime where this rapid upturn is observed.

After the rapid upturn, the $\Delta\sigma(\varepsilon)$ curves plotted in *log-log* scales become linear with a negative slope within a narrow reduced temperature regime up to $\varepsilon \sim 0.1$. The observed temperature dependence of the excess conductivity is in agreement with the AL theoretical model. We have determined the critical exponent λ by fitting the linear portion of the $\Delta\sigma(\varepsilon)$ curve shown in Fig. 5.3 with the function $\Delta\sigma_{AL}(\varepsilon) = A_0\varepsilon^{-\lambda}$. The fittings are shown by the solid straight lines in Fig. 5.3. For the present Ti-V alloys, λ values are estimated out to be $\sim(0.5\pm 0.05)$. These values of λ correspond to $D \sim 3$, indicating

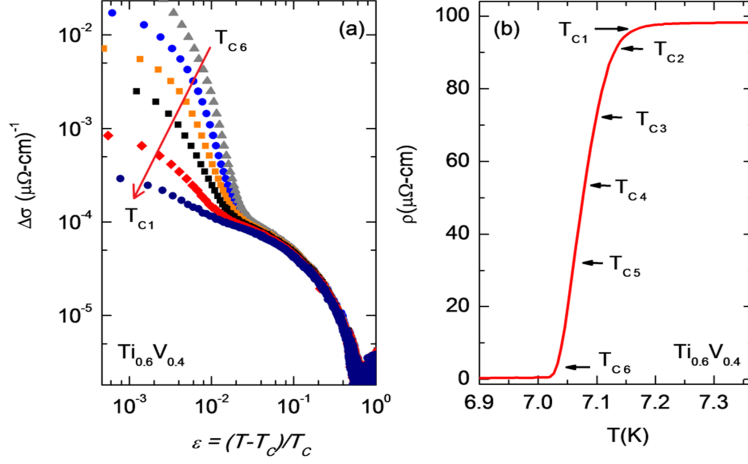


Figure 5.4: (a) $\Delta\sigma(\varepsilon)$ curves for the $\text{Ti}_{0.6}\text{V}_{0.4}$ alloy plotted in *log-log* scales using different choice of T_C . (b) The $\rho(T)$ curve for the same alloy showing the temperature points which are used as T_C in panel (a).

the 3D character of the superconducting fluctuations as is expected for these bulk Ti-V alloys. In the AL theoretical model, the temperature independent amplitude of the excess conductivity for 3D superconducting fluctuations is given by $A_0 = e^2/32\hbar\xi(0)$ (refer to Eqn. 5.3). Then the A_0 value obtained from the $\Delta\sigma(\varepsilon)$ data will provide an estimation of the coherence length at zero temperature $\xi(0)$. The $\xi(0)$ values thus estimated for the present Ti-V alloys are given in Table 5.1. The values of $\xi(0)$ estimated from the knowledge of $H_{C2}(0)$ are also given in Table 5.1 for a comparison. We find that the values of $\xi(0)$ estimated for the $\text{Ti}_x\text{V}_{1-x}$ alloys with compositions $x=0.4, 0.6,$ and 0.7 using two different approaches agree with each other. These observations suggest that (i) the AL theory consistently describes both the magnitude as well as the temperature dependence of measured excess conduc-

tivity in these Ti-V alloys and (ii) the indirect Maki-Thompson contribution, which was originally proposed particularly for the low- T_C superconductors, is negligible in the present Ti-V alloys.

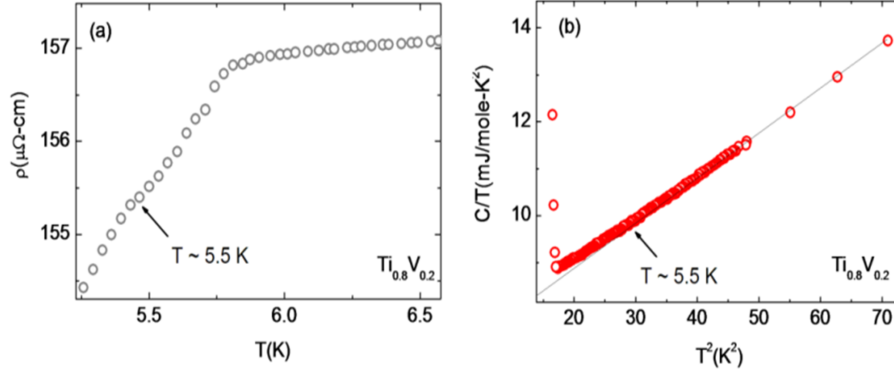


Figure 5.5: The temperature dependence of the electrical resistivity and heat capacity of the $\text{Ti}_{0.8}\text{V}_{0.2}$ alloy. The temperature dependence of heat capacity is (C) plotted in C/T versus T^2 fashion. These curves exhibit a change of slope at $T \sim 5.5$ K, which is above the T_C of this alloy.

The $\Delta\sigma(\varepsilon)$ curve of the $\text{Ti}_{0.8}\text{V}_{0.2}$ alloy exhibits an abrupt jump at $\varepsilon \sim 0.3$ [Fig. 5.3(d)]. Qualitatively very similar behaviour has been observed previously in $\text{YBa}_2\text{Cu}_3\text{O}_7$ [173], $\text{Bi}_2\text{Sr}_2\text{Ca}_2\text{Cu}_3\text{O}_x$ [174] and $\text{Tl}_2\text{Ba}_2\text{CaCu}_2\text{O}_x$ thin films [175], where the observed effect is inferred to occur due to a distribution of T_C within these samples [176]. For $\text{Ti}_{0.8}\text{V}_{0.2}$ alloy, the resistive transition from the normal to the superconducting state is observed to be significantly broadened, and such a broadened resistive transition is an indication of the presence of T_C distribution in this sample. Moreover, for this alloy, both the temperature dependence of resistivity [Fig. 5.5(a)] as well as the temperature dependence of heat capacity (C) plotted in C/T versus T^2 fashion [Fig.

5.5(b)] exhibit change of slope at $T \sim 5.5$ K ($\varepsilon \sim 0.3$) which is clearly larger than the T_C of this alloy. The change of slope in the $\rho(T)$ and C/T versus T^2 curves occurring at a temperature well above the T_C further indicates the presence of some superconducting regions with T_C values relatively higher than that of the main superconducting matrix. As a result of this the measured excess conductivity is strongly affected by the distribution of T_C within this sample at temperatures $\varepsilon < 0.3$, and thereby preventing us to compare the experimental $\Delta\sigma(\varepsilon)$ data with the AL theoretical model.

Table 5.1: The superconducting transition temperature and the coherence length of the Ti-V alloys.

	Ti _{0.4} V _{0.6}	Ti _{0.6} V _{0.4}	Ti _{0.7} V _{0.3}	Ti _{0.8} V _{0.2}
T_C^{mf} (K)	7.4	7.0	6.6	4.6
$\xi(0)$ from AL theory (nm)	5.4	4.5	5.5	—
$\xi(0)$ from $H_{C2}(0)$ (nm)	5.5	4.9	5.3	6.1
$\xi(0)$ from extended AL theory (nm)	5.5	4.6	5.0	5.7

In the present Ti-V alloys, the AL behaviour of the measured excess conductivity persists up to $\varepsilon \sim 0.1$. At further higher temperature, the excess conductivity falls much more rapidly than predicted from the AL theory, and is observed to be measurable only up to the temperature $\sim 2T_C$. The disagreement between the AL theory and the experimentally measured excess conductivity data at high temperature regime is commonly observed in various superconducting samples [158, 161, 171, 172, 177, 178]. This dis-

agreement is attributed to the short-wavelength fluctuations which become increasingly important at high temperature regime [179]. However, an extended AL model is proposed recently by Leridon *et al.* [158], which suggests that the low-temperature ($\varepsilon \leq 0.1$) 3D AL behaviour as well as the high-temperature ($\varepsilon > 0.1$) rapid collapse of the excess conductivity data can be modelled by the same interpolating function given by

$$\Delta\sigma(\varepsilon) = \left[\frac{e^2}{16\hbar\xi(0)} \right] \left[2\varepsilon_0 \sinh\left(\frac{2\varepsilon}{\varepsilon_0}\right) \right]^{-\frac{1}{2}}, \quad (5.7)$$

where, ε_0 is the only adjustable parameter which along with $\xi(0)$ governs the collapse of the excess conductivity data at high temperature regime. The above function well describes the excess conductivity data of Fe-based [178] and high- T_C cuprate superconductors [158] in both low as well as high-temperature regimes. The excess conductivity data of all the Ti-V alloys are fitted based on the function given in Eqn. (5.7) in the entire temperature range of the fluctuation spectrum except at very low temperature regime where the rapid upturn in the excess conductivity data is observed. The fittings are shown by the non-linear solid lines in Fig. 5.3. The agreement of our data with this purely heuristic function is extremely good. The $\xi(0)$ values obtained from the fittings are given in Table 5.1. These values are found to be almost identical with those deduced from the $H_{C2}(0)$ values, indicating that in the Ti-V alloys, the AL contribution is the only contribution giving rise to the excess conductivity in the entire temperature range of the

fluctuation spectrum of the present alloys.

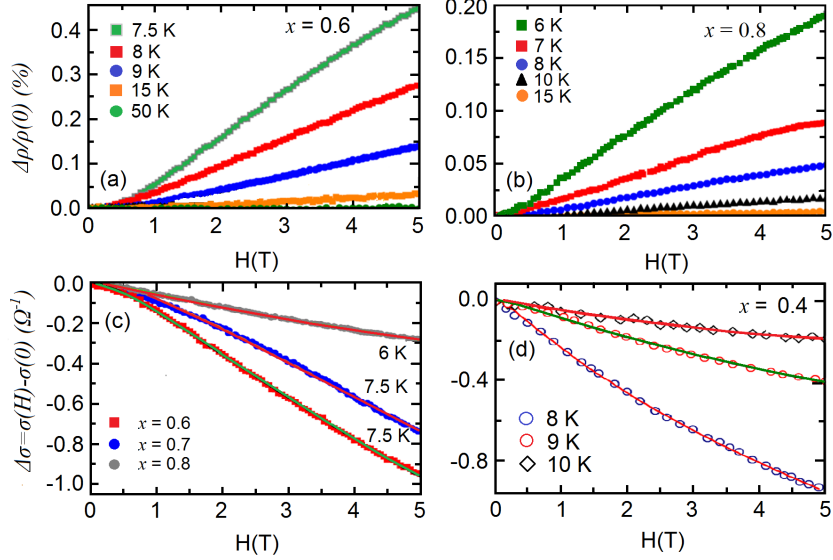


Figure 5.6: (a), (b) Magneto-resistance of the $\text{Ti}_x\text{V}_{1-x}$ alloys having compositions $x=0.6$ and 0.8 at various constant temperatures above T_C . Finite positive magneto-resistance is observed in these alloys at temperatures below $\sim 2T_C$. (c), (d) Magneto-conductivity of the $\text{Ti}_x\text{V}_{1-x}$ alloys at different constant temperatures (open and solid symbols). The solid line denotes the fitting to the magneto-conductivity data based on Eqn. (5.8).

5.2.4 Magneto-resistance of the Ti-V alloys

The magnetic field dependence of magneto-resistance $\Delta\rho/\rho(H=0) = [\rho(H) - \rho(H=0)]/\rho(H=0)$ at various constant temperatures above T_C is shown in the Figs. 5.6(a) and (b) for two compositions of the Ti-V alloys. These Ti-V alloys exhibit strong positive magneto-resistance which increases steadily with increasing magnetic field in the present range of applied magnetic field.

However, the magneto-resistance becomes gradually weaker as the temperature is increased, and becomes vanishingly small for $T > 2T_C$. Very similar behaviour is also observed for other two compositions of the Ti-V alloys (these results are not shown here for the sake of conciseness). Since both the rounding-off behaviour of the $\rho(T)$ curve and the strong positive magneto-resistance are observed in present the Ti-V alloys in the same temperature regime, there is a possibility that these observed phenomena are the manifestations of the same physical phenomenon. The magneto-conductivity $\Delta\sigma(H)[= \sigma(H) - \sigma(H = 0)]$ associated with the AL contribution to the excess conductivity for bulk materials has the form [159]

$$\Delta\sigma(H, T) = \frac{e^2}{4\hbar} \left[\frac{2k_B T}{\pi\hbar\mu} \right]^{\frac{1}{2}} \sum_{n=0}^{\infty} (n+1) [(\varepsilon' + pn)^{-\frac{1}{2}} + (\varepsilon' + pn + p)^{-\frac{1}{2}} - 2(\varepsilon' + pn + \frac{p}{2})^{-\frac{1}{2}}] \quad (5.8)$$

where, $\varepsilon' = \ln(T/T_C) + p/2$, $p = \pi\mu e\hbar/2k_B T$, and μ is the electronic diffusion coefficient. The above equation nicely describes the magneto-conductivity data of the present Ti-V alloys at temperatures above T_C . This is illustrated in Figs 5.6(c) and (d). In order to check the consistency of these fittings we compare the values of μ obtained as fitting parameter with the values available in the literature. A reasonably good agreement is observed between these values. For an example, the fitting procedure gives $\mu \sim 0.5$ m²/sec for the Ti_{0.4}V_{0.6} alloy. Isino [148] had estimated $\mu \sim 0.4$ m²/sec for the Ti_{0.4}V_{0.6} alloy, which is close to the value obtained here. Hence, the present results

clearly indicate that the strong positive magneto-resistance exhibited by the Ti-V alloys is resulted from the quenching of the superconducting fluctuations by the application of magnetic field.

5.3 Summary and conclusions

The temperature dependence of resistivity and the magnetic field dependence of magneto-resistance in the temperature regime above the superconducting transition temperature T_C is studied in four bulk $\text{Ti}_x\text{V}_{1-x}$ alloys having compositions $x = 0.8, 0.7, 0.6$ and 0.4 . These Ti-V alloys show a clear rounding-off behaviour in the temperature dependence of resistivity curve in the temperature regime above T_C , and the trace of this effect persists up to the temperature $\sim 2T_C$. In association with this, the Ti-V alloys exhibit strong positive magneto-resistance in the temperature regime where the rounding-off behaviour in the temperature dependence of resistivity curve is observed. The existing theoretical models for the superconducting fluctuations induced conductivity consistently describe both the temperature dependence of the excess conductivity as well as the magnetic field dependence of magneto-resistance observed in the present Ti-V alloys. These results suggest that the superconducting fluctuations are responsible for the observed rounding-off behaviour of the temperature dependence of the resistivity curve in the present Ti-V alloys. We, therefore, discard the spin fluctuation scenario which was introduced previously for explaining the observed phenomenon.

—This page is intentionally kept blank—

Chapter 6

The normal state properties of the Ti-V alloys

6.1 Introduction

In the chapter 4, we have observed that for the $\text{Ti}_x\text{V}_{1-x}$ alloys with concentrations $x = 0.4, 0.6$ and 0.7 , the experimentally determined superconducting transition temperature T_C is significantly lower than that estimated using McMillan formula [19]. We have also pointed out that the presence of soft-phonon modes and/or spin fluctuations in a material may lead to such a disagreement between the experimental and theoretical values of T_C . In this chapter, we present the results of our study on the various normal state properties of these Ti-V alloys to understand the possible reasons behind this difference between the experimental and theoretical values of T_C . Our studies on the temperature dependence of heat capacity, dc magnetic susceptibility and electrical resistivity indicate the presence of spin fluctuations in the Ti-V alloys, particularly in those having higher V concentration. This is

further supported by the observed enhanced Stoner factor and the validity of the Kadowaki-Woods scaling relation [180] for these Ti-V alloys. Based on these experimental observations we infer that lower value of the experimentally observed T_C as compared to that estimated using McMillan formula is due to the strong pair-breaking effect of the spin fluctuations. On the basis of their theoretical study [93], Pictet *et al.* had also made a similar inference. Our study reveals that the presence of spin fluctuations in Ti-V alloys not only explains the difference between the experimental and theoretical values of T_C , but also accounts for the non-monotonic variation of T_C as a function of x in the $\text{Ti}_x\text{V}_{1-x}$ alloys.

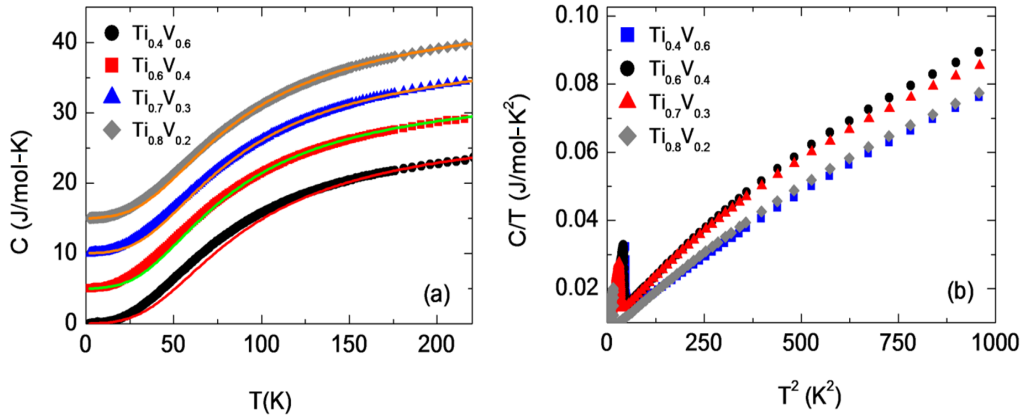


Figure 6.1: (a) The temperature dependence of heat capacity in the temperature range 2-225 K for the Ti-V alloys. The solid lines are the best-fit curves based on the relation $C(T) = \gamma T + C_L$ (see text for details). (b) The temperature dependence of heat capacity of the Ti-V alloys presented in C/T versus T^2 fashion in the temperature range 2-35 K. The non linearity in the C/T versus T^2 plots observed in this temperature range indicates the presence of soft-phonon modes or spin fluctuations in these Ti-V alloys.

6.2 Results and discussion

6.2.1 The temperature dependence of heat capacity of the Ti-V alloys

In Fig. 6.1(a) we show the temperature dependence of heat capacity for the Ti-V alloys in the temperature range 2-225 K. In this figure, the scale on the y-axis actually corresponds to the heat capacity of the $\text{Ti}_{0.4}\text{V}_{0.6}$ alloy only. The rest of the curves are shifted upwards (so as to create a difference of 5 J/mole-K between any two of the curves at the lowest temperature of measurement) for better clarity. In this figure the solid lines are the fits to the experimental data based on the relation $C(T) = \gamma T + C_L$, where C_L represents the Debye lattice heat capacity which is given by

$$C_L(T) = 9R \left(\frac{T}{\theta_D} \right)^3 \int_0^{\theta_D/T} \frac{x^4 e^x}{(e^x - 1)^2} dx. \quad (6.1)$$

Here, R is the universal gas constant and θ_D is the Debye temperature. For performing the fitting, we take θ_D and the Sommerfeld coefficient γ as the fitting parameters. It is evident from Fig. 6.1(a) that the fitting degrades at low temperatures, and the observed disagreement between the experiment data and the theory becomes more prominent as the V concentration in these Ti-V alloys is increased. Such a disagreement between the experimental $C(T)$ data and the theory may arise from using of a single value of θ_D to fit the $C(T)$ data in a large temperature range. However, our thermal expansion measurement on the $\text{Ti}_{0.6}\text{V}_{0.4}$ alloy indicates that the variation of θ_D in the

temperature range from 4.2 K to 300 K is less than 10 % (the experimental data are not shown here). We have found that the observed disagreement between the experimental $C(T)$ data and the theory cannot be accounted by such a small variation in θ_D . In Fig. 6.1(b) we show the plots of C/T as a function of T^2 for the present Ti-V alloys in the temperature range 2-35 K. A non-linearity with a negative curvature is observed in these plots, indicating the presence of low energy excitations such as soft-phonons [118, 120, 181] or spin fluctuations [119, 120] in the Ti-V alloys. In the case of soft-phonons or spin fluctuations, a simplified model has been used in the literature, in which the phonon density of states $F(\omega)$ are represented by a set of Einstein modes (with frequency ω) having constant spacing in the logarithmic frequency scale [118]. This simplified model does not give the detailed map of the phonon density of states that is generally obtained through the neutron scattering experiments but rather produces a smooth phonon distribution function $F(\omega)$. It is reported in literature that certain functional of the lattice heat capacity may be used to represent the form of such phonon spectrum [118]. One such functional $(5/4)R\pi^4C_L T^3$ is an image of the spectrum $\omega^{-2}F(\omega)$ for $\omega = 4.928T$, where ω is expressed in Kelvin. In this model, $F(\omega)$ is given by [118]

$$F(\omega) = \sum_k F_k \delta(\omega - \omega_k). \quad (6.2)$$

Using this representation, the lattice heat capacity C_L is then given by [118]

$$C_L = 3R \sum_k F_k(z_k)^2 e^{z_k} / [e^{z_k} - 1]^2. \quad (6.3)$$

Where, $z_k = \omega_k/T$ and F_k is the weight factor for the ω_k . The value of k is so chosen that the least number of terms is sufficient to fit the experimental heat capacity data. Then F_k is determined by the least square fit with a condition $\sum_k F_k = 1$. We adopt this model to understand the temperature dependence of heat capacity in the normal state of the present Ti-V alloys.

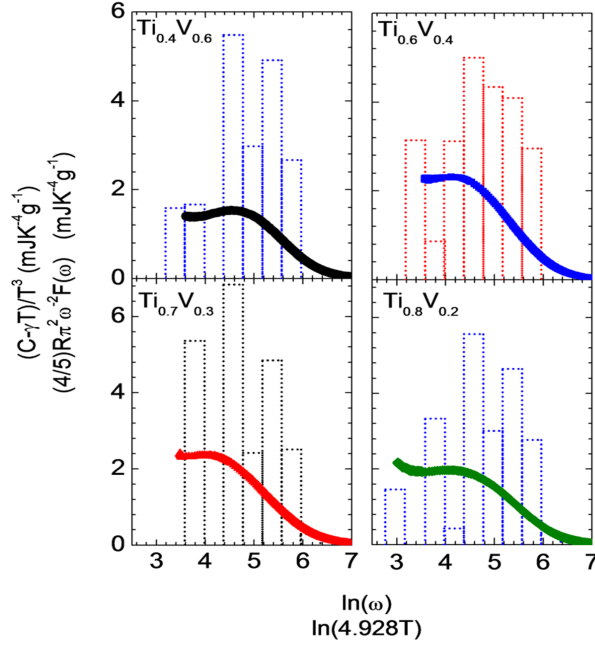


Figure 6.2: The plots of $C_L T^{-3}$ as a function of $\ln(4.928T)$ (indicated by the open symbols with a large density of points) and $(4/5)R\pi^2\omega^{-2}F(\omega)$ as a function of $\ln(\omega)$ (dotted bar curves) for the Ti-V alloys.

Fig. 6.2 shows the plots of $C_L T^{-3} = (C - \gamma T)/T^3$ as a function of $\ln(4.928T)$ for the present Ti-V alloys. The presence of soft-phonon or spin

fluctuations in these alloys is indicated by the increase in $C_L T^{-3}$ at low values of $\ln(4.928T)$. The temperature dependence of C_L is fitted with the above equation by considering 10 Einstein frequencies ($k=10$). The correspondence between the fit and the data is shown by plotting $(4/5)R\pi^2\omega^{-2}F(\omega)$ as a function of $\ln(\omega)$ along with the plot of $C_L T^{-3}$ against $\ln(4.928T)$. Then the characteristic phonon scaling frequency $\bar{\omega}_{log}$ is estimated as [119]:

$$\bar{\omega}_{log} = \exp \left[\frac{\int d(\ln\omega) F(\omega) \ln(\omega)}{\int d(\ln\omega) F(\omega)} \right]. \quad (6.4)$$

The obtained value of $\bar{\omega}_{log}$ can be used to estimate T_C from the Allen-Dynes form [6.8] of the McMillan formula [19] as

$$T_C = \frac{\bar{\omega}_{log}}{1.2} \exp \left[\frac{-1.04(1 + \lambda_{ep})}{\lambda_{ep} - \mu^*(1 + 0.62\lambda_{ep})} \right]. \quad (6.5)$$

In Table 6.1, we present the values of $\bar{\omega}_{log}$ and the corresponding T_C values for all the present Ti-V alloys estimated using $\mu^* = 0.12$ and λ_{ep} values obtained from the heat capacity data (given in Table 4.1). In chapter 4, we have shown that the value of μ^* is about 0.12 for the Ti-V alloys, and such a value of μ^* is commonly used for all the transition metals and their alloys. We find that for the $\text{Ti}_x\text{V}_{1-x}$ alloys having concentrations $x = 0.4$, 0.6 and 0.7, the value of T_C estimated using expression (6.5) is still higher than that obtained experimentally. Hence, the existence of soft-phonons in these Ti-V alloys cannot explain the observed low value of the experimentally T_C of these alloys. We therefore explore the possibility of the existence of

spin fluctuations [92, 183] in these Ti-V alloys, which also could lead to a suppression of T_C . In this direction, we now present the results of our studies on the temperature dependence of dc magnetic susceptibility and electrical resistivity in the normal state of these alloys.

Table 6.1: T_C of the Ti-V alloys estimated with the help of the Allen-Dynes form of the McMillan formula using $\mu^*=0.12$ and, $\bar{\omega}_{log}$ and λ_{ep} obtained from the heat capacity data. The values of $\bar{\omega}_{log}$ obtained from the analysis of the heat capacity data are also given.

	Ti _{0.4} V _{0.6}	Ti _{0.6} V _{0.4}	Ti _{0.7} V _{0.3}	Ti _{0.8} V _{0.2}
$\bar{\omega}_{log}$ (K)	226.3	221.3	235.8	243.5
T_C (K)	18.9	11.8	10.7	4.2

6.2.2 The temperature dependence of magnetic susceptibility of the Ti-V alloys

Fig. 6.3 shows the temperature dependence of dc magnetic susceptibility $\chi = M/H$ for the Ti-V alloys in the temperature range 10-300 K. The magnetization (M) was measured in the presence of 1 T magnetic field using a SQUID magnetometer. The data were corrected for the background signal. For doing this, the SQUID profiles were measured first for the bare sample holder (empty straw) at the temperatures and magnetic fields where the measurements were to be performed on the sample. Then the sample was inserted into the straw keeping the configuration of the straw same, and then the SQUID profiles were obtained at the same temperatures and

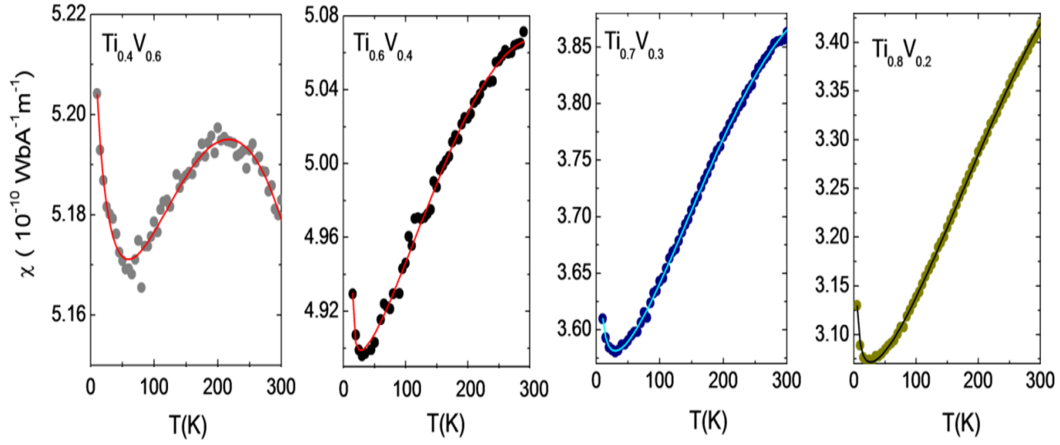


Figure 6.3: Temperature dependence of dc magnetic susceptibility χ for the Ti-V alloys in the temperature range 10-300 K. A peak in the $\chi(T)$ curve is observed at $T \sim 200$ K for $\text{Ti}_{0.4}\text{V}_{0.6}$ alloy. The peak shifts to higher temperatures and the magnitude of χ decreases with increasing Ti concentration. The solid lines represent the fitting based on the Eqn. 1.7.

magnetic fields where the profiles of the empty straw were recorded. The SQUID profiles for the empty straw were then subtracted from the SQUID profiles for the sample plus straw configuration, before fitting the profiles for the estimation of the magnetic moment. Magnetic susceptibility in all the present Ti-V alloys increases with the increase in temperature. Such behaviour is termed as “temperature induced magnetism” which is unlike that of a paramagnet where the susceptibility decreases with increasing temperature. The temperature induced magnetism observed in various transition metals is reported to occur due to the temperature dependence of the Pauli paramagnetism [184]. The temperature dependence of Pauli paramagnetism

can be expressed within the Fermi liquid picture as [185]:

$$\chi(T) = \chi_P \left[1 + \frac{1}{6} \pi^2 (k_B T)^2 \left(\frac{1}{n} \frac{\delta^2 n}{\delta E^2} \right)_{E_F} - \left(\frac{1}{n} \frac{\delta n}{\delta E} \right)_{E_F}^2 \right]. \quad (6.6)$$

Here, $n = N(0)$ is the bare electron density of states (DOS) at the Fermi energy E_F , which has been estimated for the present Ti-V alloys using the band structure calculations (refer to chapter 4). The plots of the bare electronic density of state of the Ti-V alloys as a function of energy (Fig. 4.3 of chapter 4) are used to estimate the quantities $(\delta^2 n / \delta E^2)$ and $(\delta n / \delta E)$ at E_F . The results of these estimations indicate that the coefficient of the T^2 term in the above equation is negative for the $\text{Ti}_x\text{V}_{1-x}$ alloys having compositions $x = 0.4$ and 0.6 . This will lead to a decrease in χ with the increase in temperature, which is not observed experimentally. However, our studies on electronic structure show that the bare electron density of states at the Fermi energy is very large and are dominated by $3d$ electrons. In such case, the Pauli susceptibility is enhanced due to the spin fluctuations, and the temperature dependence of χ follows the relation [186, 187]

$$\chi(T) = \chi(0) - bT^2 \ln \left(\frac{T}{T'} \right), \quad (6.7)$$

where, $\chi(0)$, b , and T' are constants. The characteristic temperature T' is related to the characteristic temperature T_P at which a peak in the temperature dependence of susceptibility occurs, as: $T_P = T'/e^{\frac{1}{2}}$ [186, 187]. The

above equation nicely fits the $\chi(T)$ data of the present Ti-V alloys (Fig. 6.3). The values of $\chi(0)$, b , and T' obtained as the fitting parameters are presented in Table 6.2. It is observed that $\chi(0)$ decreases with the increase in Ti concentration x in the $\text{Ti}_x\text{V}_{1-x}$ alloys, whereas T' increases as x increases. It is also observed that the temperature dependence of susceptibility approaches T^2 behaviour as x increases. This can be interpreted as an indication that the system approaches toward Fermi liquid behaviour with increasing x . A small Curie tail is observed at low temperatures, which may be related to a small amount paramagnetic impurities (not detectable in the XRD measurements) present in these alloys. The isothermal field dependence of magnetization at various constant temperatures above 10 K does not show any indication of saturation even in 8 T applied magnetic field, and thereby ruling out any appreciable contribution from ferromagnetic impurities.

We estimate Pauli spin susceptibility χ^P from the bare electronic density of states at the Fermi energy using the relation $\chi^P = \mu_0\mu_B^2N(0)$, where μ_B is the Bohr magneton and μ_0 is the permeability of the free space. This estimate is almost an order of magnitude lower than the experimental magnetic susceptibility $\chi_{exp} [= \chi(0)/\mu_0]$, indicating that these Ti-V alloys are enhanced Pauli paramagnets. In such cases, the Stoner enhancement factor S can be estimated as

$$S = \frac{\chi_{exp}^P}{\chi^P}. \quad (6.8)$$

Here χ_{exp}^P is the experimentally obtained Pauli spin susceptibility. In order

Table 6.2: Various parameters estimated from the temperature dependence of dc magnetic susceptibility of the Ti-V alloys in their normal state. The parameter T_{sf} is obtained from the temperature dependence of resistivity of the Ti-V alloys in their normal state.

	Ti _{0.4} V _{0.6}	Ti _{0.6} V _{0.4}	Ti _{0.7} V _{0.3}	Ti _{0.8} V _{0.2}
$\chi(0)$ (10^{-10} Wb/A)	5.13±0.03	4.88±0.003	3.55±0.007	3.04±0.003
b (10^{-16} Wb/A-K ²)	2.27±0.6	3.85±0.17	4.91±0.28	4.51±0.06
T' (K)	372±15	512±12	616±19	757±9
χ_{exp} (10^{-4} unit less)	4.08±0.026	3.88±0.0024	2.82±0.005	2.42±0.002
χ_{exp}^P (10^{-4} unit less)	1.81±0.01	1.99±0.001	1.12±0.002	9.08±0.001
Stoner factor S	~2.04	~2.28	~1.40	~1.18
Wilson's coefficient R_W	~1.2	~1.5	~0.94	~0.93
T_{sf} (K)	~155	~90	~70	...

to estimate χ_{exp}^P from χ_{exp} , one needs to know the orbital susceptibility χ_{exp}^O . However, the estimation of χ_{exp}^O from the experimental data is rather difficult. We have taken the values of χ_{exp}^O of the end members of the Ti-V system from the literature. These values are reported to be $\chi_{exp}^O \sim 1.14 \times 10^{-4}$ for β -Ti and $\chi_{exp}^O \sim 3.02 \times 10^{-4}$ for β -V [117]. Linear interpolation between these two end-values is used to estimate χ_{exp}^O for the present alloy compositions. Then χ_{exp}^P values for the present Ti-V alloys are obtained by subtracting χ_{exp}^O from χ_{exp} , and these values are given in Table 6.2. The estimated value of S is ~ 2 (Table 6.2) for the V-rich Ti-V alloys, indicating the relevance of spin fluctuations in these alloys. On the other hand, $S \sim 1$ for Ti_{0.8}V_{0.2} alloy, indicating that the spin fluctuations are suppressed in Ti-rich Ti-V alloys. We have also estimated the Wilson's coefficient R_W for the present Ti-V alloys using the

relation: $R_W = \left(\frac{\pi^2 k_B^2}{3\mu_B^2} \right) \frac{\chi_{exp}^P}{\gamma}$ [188]. The values of the Wilson's coefficient R_W for the present Ti-V alloys are also given in Table 6.2. We observe that $R_W > 1$ for the Ti_xV_{1-x} alloys having concentration $x=0.4$ and 0.6, indicating that these alloys are strongly correlated systems where spin fluctuations are enhanced [188].

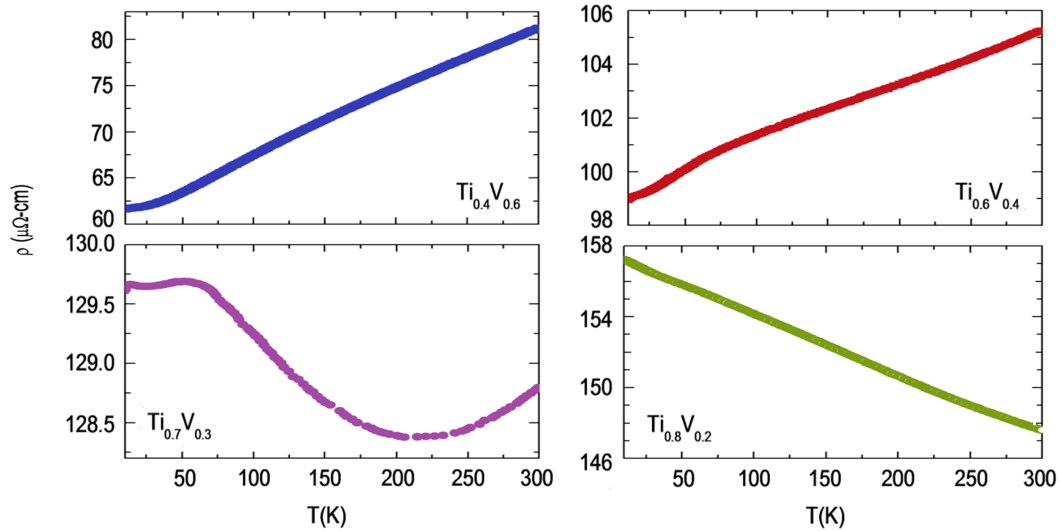


Figure 6.4: Temperature dependence of resistivity of the Ti-V alloys measured in zero applied magnetic field and in temperature range 10-300 K.

6.2.3 Electrical resistivity of the Ti-V alloys

The temperature dependence of electrical resistivity (ρ) for the present Ti-V alloys in the temperature range 10-300 K is shown in Fig. 6.4. The magnitude as well as the temperature dependence of resistivity of these Ti-V alloys is

observed to depend strongly on the alloy composition. For the $\text{Ti}_x\text{V}_{1-x}$ alloys having concentrations $x = 0.4$ and 0.6 , resistivity increases with the increase in temperature in the entire temperature range of measurement. For both these alloys, resistivity shows linear temperature dependence at high temperatures, and a deviation from this linear behaviour is observed at low temperatures. In the main panel of Fig. 6.5(a), the observed linearity of the plot of $(\rho - \rho_0)$ against T^2 for the $\text{Ti}_x\text{V}_{1-x}$ alloys with $x = 0.4$ and 0.6 indicates a quadratic temperature dependence of resistivity of these alloys at low temperatures. Such a quadratic temperature dependence of resistivity at low temperature is commonly exhibited by the materials where the strong presence of spin fluctuations is observed.

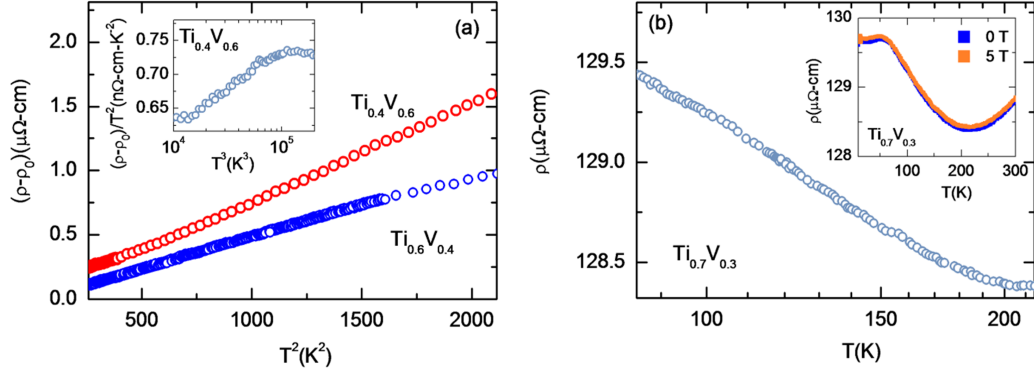


Figure 6.5: (a) Resistivity ρ versus T^2 plots for the $\text{Ti}_{0.4}\text{V}_{0.6}$ and $\text{Ti}_{0.6}\text{V}_{0.4}$ alloys showing the T^2 dependence of resistivity at low temperatures (20-45 K). The inset of (a) show the plot of $(\rho - \rho_0)/T^2$ against T^3 for the $\text{Ti}_{0.4}\text{V}_{0.6}$ alloy to illustrate the relevance of the T^5 term in the $\rho(T)$ data. (b) The plot of the temperature dependence of resistivity for the $\text{Ti}_{0.7}\text{V}_{0.3}$ alloy, where temperature is plotted in \log scale. Its inset shows that the $\rho(T)$ of this alloy remains unaffected on the application of magnetic field.

Although the function $\rho(T) = \rho_0 + AT^2$ well describes the temperature dependence of resistivity of the $\text{Ti}_x\text{V}_{1-x}$ alloys having concentrations $x = 0.4$ and 0.6 at low temperatures, the fitting improves significantly when an additional T^5 term is considered in the fitted function. The T^5 dependence of resistivity at low temperatures is known to arise from the electron-phonon scattering mechanism. The plot of $(\rho - \rho_0)/T^2$ as a function of T^3 is shown in the inset to Fig. 6.5(a) for the $\text{Ti}_{0.4}\text{V}_{0.6}$ alloy. The observed weak slope of this plot indicates that the T^5 term has some relevance in the temperature dependence of resistivity of this alloy at low temperatures, though the coefficient of the T^5 term is very small ($\sim 10^{-9} \mu\Omega\text{-cm-K}^{-5}$) for this alloy. The coefficient of the T^5 term is also found to be very small but negative for the $\text{Ti}_{0.6}\text{V}_{0.4}$ alloy. The negative as well as the small value of the coefficient of T^5 term can be explained within the theoretical models of electrical resistivity which consider the contribution arises from the scattering mechanism between the conduction electrons and the spin fluctuations [189, 190]. The temperature dependence of resistivity arising from the scattering of the conduction electrons by spin fluctuations can be expressed as [189, 190]

$$\rho_{sf}(T) = a \left(\frac{T}{T_{sf}} \right)^2 \left[J_2 \left(\frac{T_{sf}}{T} \right) - \left(\frac{T}{T_{sf}} \right)^3 J_5 \left(\frac{T_{sf}}{T} \right) \right]. \quad (6.9)$$

Here, a is an arbitrary constant, T_{sf} is the characteristic spin-fluctuations temperature and J_n 's are the standard Bloch-Gruneisen scattering integrals. On the other hand, the contribution to the resistivity at low temperatures,

arising from the electron-phonon interactions, is given by [189, 190]

$$\rho_{ph}(T) = b \left(\frac{T}{\theta_D} \right)^5 J_5 \left(\frac{\theta_D}{T} \right), \quad (6.10)$$

where, b is some constant and θ_D is the Debye temperature. Then the total ideal resistivity at low temperatures will be obtained by combining the above two contributions, and is given as

$$\begin{aligned} \rho(T) = \rho_{sf}(T) + \rho_{ph}(T) = & \left(\frac{a}{T_{sf}^2} \right) J_2 \left(\frac{T_{sf}}{T} \right) T^2 + \\ & \left[\left(\frac{b}{\theta_D^5} \right) J_5 \left(\frac{\theta_D}{T} \right) - \left(\frac{a}{T_{sf}^5} \right) J_5 \left(\frac{T_{sf}}{T} \right) \right] T^5. \end{aligned} \quad (6.11)$$

It is evident from Eqn. (6.11) that the electron-spin fluctuations interactions not only give rise to the quadratic temperature dependence of resistivity at low temperatures but also attenuates the usual Bloch-Gruneisen T^5 term. Furthermore, the coefficient of the T^5 term may be even negative if the contribution arises from the electron-spin fluctuations scatterings is greater than that from the electron-phonon scatterings. Thus, we find that all the characteristic features observed in the temperature dependence of resistivity of the $\text{Ti}_{0.4}\text{V}_{0.6}$ and $\text{Ti}_{0.6}\text{V}_{0.4}$ alloys at low temperatures can be explained by considering the presence of spin fluctuations in these alloys. The coefficient A of the T^2 term in the temperature dependence of resistivity is found to decrease with the increase in x , which indicates that the role of spin fluctuations diminishes with the increase in Ti concentration in the Ti-V alloys. The tem-

perature at which resistivity exhibits a deviation from the linear temperature dependence at high temperature regime can be taken as the characteristic spin-fluctuation temperature T_{sf} . The values of T_{sf} for the $\text{Ti}_x\text{V}_{1-x}$ alloys with compositions $x = 0.4$ and 0.6 are given in Table 6.2. It then seems reasonable to assume that the observed deviation of the experimental $C(T)$ data from the curve fitted by considering the contributions from electrons and the lattice may be due to increasing importance of spin fluctuations in these Ti-V alloys at temperatures below T_{sf} , and therefore, the temperature for observing such deviation can be considered as T_{sf} . Accordingly, we have estimated T_{sf} values for the $\text{Ti}_x\text{V}_{1-x}$ alloys with $x = 0.4$ and 0.6 from the heat capacity data, which are found to be very similar to those obtained from the resistivity data. On the other hand, Frings and Franse had shown that the T_{sf} may be identified from the $\chi(T)$ data as the temperature at which the second derivative of χ with respect to temperature goes to zero [191]. For an example, the second derivative of χ goes to zero at temperature $T \sim 120$ K for the $\text{Ti}_{0.6}\text{V}_{0.4}$ alloy, which is slightly higher than the T_{sf} value obtained from the temperature dependence of resistivity and heat capacity data.

The temperature coefficient of resistivity (TCR) $\alpha (= d\rho/dT)$ is negative for the $\text{Ti}_{0.7}\text{V}_{0.3}$ and $\text{Ti}_{0.8}\text{V}_{0.2}$ alloys over a considerably large temperature range. These results are consistent with the previous studies, where a negative TCR was reported for the $\text{Ti}_x\text{V}_{1-x}$ alloys having concentrations in the range $0.6 < x < 0.85$ [42-44]. For the $\text{Ti}_{0.7}\text{V}_{0.3}$ alloy, the resistivity initially decreases as the temperature is decreased from 300 K, and reaches to the

minimum value near to 210 K. Resistivity then starts to increase with further lowering of the temperature from 210 K down to 65 K. For temperatures below 65 K, $\rho(T)$ curve exhibits another weak minimum at temperature close to 30 K, which is visible in the inset of the Fig. 6.5(b). The main panel of Fig. 6.5(b) shows the temperature dependence of resistivity for the $\text{Ti}_{0.7}\text{V}_{0.3}$ alloy, where temperature is plotted in *log* scale. In the temperature range 70-170 K, $\rho(T)$ curve is linear with a negative slope which indicates a $-\ln T$ dependence of resistivity of this alloy in the said temperature regime. The $-\ln T$ dependence of resistivity is known to arise due to either the spin-Kondo effect [192] or TLS (Two-level-system)-Kondo effect [72]. The spin-Kondo effect arises due to the screening of the magnetic moments by conduction electrons in very dilute magnetic alloys, and the effect is known to depend strongly on the applied magnetic field [72]. However, in the present case, it is observed that the $\rho(T)$ curve of the $\text{Ti}_{0.7}\text{V}_{0.3}$ alloy remains unaffected by the application of magnetic fields. This is shown in the inset of Fig. 6.5(b), where the temperature dependence of resistivity measured in zero and 5 T applied magnetic fields is shown for this alloy in the temperature range 10-300 K. On the basis of this observation we argue that the observed $-\ln T$ dependence of resistivity of the $\text{Ti}_{0.7}\text{V}_{0.3}$ alloy cannot be of magnetic origin. The observed behaviour of $\rho(T)$ is therefore attributed to the TLS-Kondo effect. The TLS-Kondo model has been used previously in order to explain the negative TCR of the Ti-V [47] as well as Nb-Ti alloys [46, 47, 193]. The previous studies suggest that the TLS-Kondo effect is related to the formation

of the submicroscopic ω phase precipitations within the main β phase matrix of these disordered transition metal alloys. The ω phase precipitations are known to be formed due the lattice instability associated with the main β phase matrix. In fact, the TLS-Kondo effect becomes the dominant mechanism for the electron scattering process in transition metal alloys, which are at the verge of the β to ω structural phase transformation [194]. Previously, C. C. Tsuei had suggested that the formation of the submicroscopic ω phase can lead to structural indeterminacy in the atomic arrangements in these disordered transition metal alloys [194]. Consequently, there exist a number of local atomic arrangements which are energetically equivalent. As a possible consequence of this fact, a significant number of atoms or group of atoms can tunnel between the states of equivalent energies, i.e., the atoms or group of atoms constitute the two-level-systems (TLS) [194]. The TLS model due to Cochrane *et al.* [72] explains that the two-level state can scatter the conduction electrons in a way analogous to the spin-Kondo type exchange interactions giving rise to the negative TCR with a characteristic $-\ln T$ dependence of resistivity in many disordered materials. The present $\text{Ti}_{0.7}\text{V}_{0.3}$ alloy contains ω phase within the main β phase matrix of this alloy, which clearly indicates the instability of the main β phase matrix of this alloy. In such case, the exhibition of the TLS-Kondo effect is indeed expected.

We have already stated above that a weak dip-like feature is observed in the $\rho(T)$ curve of the $\text{Ti}_{0.7}\text{V}_{0.3}$ alloy at temperatures below 65 K. Such a resistivity dip indicates the interplay of at least two kinds of resistivity con-

tributions with opposite signs of TCR, e.g., a negative TCR due to the TLS-Kondo effect, and a positive TCR that may arise due to various mechanisms including electron-phonon, electron-magnon, and the electron-spin fluctuations scattering. However, the phononic contribution is generally observed to be negligible in materials where the TLS-Kondo scattering is a dominant electron scattering process [194]. Moreover, the role of the electron-phonon scattering is expected to be much reduced at low temperatures. We have already ruled out the presence of any appreciable magnetic impurities in the present Ti-V alloys. Hence, the possibility of a contribution towards the positive TCR due to the electron-magnon scattering can also be ruled out for the $\text{Ti}_{0.7}\text{V}_{0.3}$ alloy. However, a quadratic temperature dependence of resistivity is observed at low temperatures in the case of $\text{Ti}_{0.4}\text{V}_{0.6}$ and $\text{Ti}_{0.6}\text{V}_{0.4}$ alloys, which has been inferred to arise due to the scattering of the conduction electrons by spin fluctuations. Hence, we infer that the dip-like feature observed in the $\rho(T)$ curve of the $\text{Ti}_{0.7}\text{V}_{0.3}$ alloy at low temperatures arises due to the contributions from the TLS-Kondo scattering mechanism and most probably the electron-spin fluctuations scattering mechanism, which becomes effective only below the spin fluctuation temperature T_{sf} . In such a case, we can estimate T_{sf} for this alloy by finding the temperature below which resistivity exhibits a deviation from showing a $-\ln T$ behaviour at low temperatures. A value of $T_{sf} \sim 65$ K is obtained for the $\text{Ti}_{0.7}\text{V}_{0.3}$ alloy, which is lower as compared to the T_{sf} of both $\text{Ti}_{0.4}\text{V}_{0.6}$ and $\text{Ti}_{0.6}\text{V}_{0.4}$ alloys. Moreover, we observe that the characteristic spin fluctuation temperature T_{sf} gradually decreases

with the increase in Ti concentration in the Ti-V alloys. This result again implies that the role of spin fluctuations in the Ti-V alloys becomes suppressed as the Ti concentration is increased in these alloys.

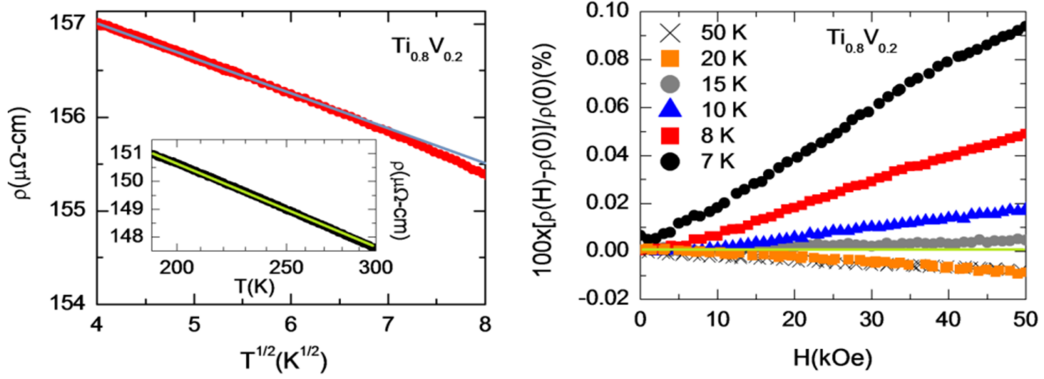


Figure 6.6: (a) Resistivity versus \sqrt{T} plot for the $\text{Ti}_{0.8}\text{V}_{0.2}$ alloy to show the $-\sqrt{T}$ dependence of resistivity at low temperatures (16-50 K). Its inset show the plot of the temperature dependence of resistivity of the $\text{Ti}_{0.8}\text{V}_{0.2}$ alloy, where temperature is plotted in \log scale. (b) The magneto-resistance of the $\text{Ti}_{0.8}\text{V}_{0.2}$ alloy at various constant temperatures.

The TCR is negative for the $\text{Ti}_{0.8}\text{V}_{0.2}$ alloy in the entire temperature range of the present measurements [Fig. 6.4(d)]. The main panel of Fig. 6.6(a) shows the plot of resistivity against \sqrt{T} in the temperature range 15-60 K for the $\text{Ti}_{0.8}\text{V}_{0.2}$ alloy. The observed linearity of this plot with a negative slope suggests that the resistivity in this alloy varies with temperature as $\rho(T) \propto -\sqrt{T}$ in the said temperature range. At higher temperatures, $\rho(T)$ curve deviates from showing the $-\sqrt{T}$ behaviour, and follows the $-\ln T$ dependence for temperatures above 200 K [shown in the inset of Fig. 6.6(a)]. In Fig. 6.6(b), we show the field dependence of magneto-resistance

of the $\text{Ti}_{0.8}\text{V}_{0.2}$ alloy at few selected constant temperatures. Superconducting fluctuation induced conductivity gives rise to the strong positive magneto-resistance in this alloy at temperatures up to about 15 K (refer to chapter 5). For still higher temperatures, a weak negative magneto-resistance is observed for this alloy. However, the magneto-resistance becomes vanishingly small at temperatures $T=80$ K and above (these data are not shown here). The negative magneto-resistance along with the $-\sqrt{T}$ dependence of resistivity implies that the electron conduction mechanism in the $\text{Ti}_{0.8}\text{V}_{0.2}$ alloy is governed by the weak-localization effect [195]. In fact, weak-localization effect is known to become important particularly in highly disordered materials. Among all the present Ti-V alloys, $\text{Ti}_{0.8}\text{V}_{0.2}$ alloy has the highest value of normal state resistivity. This indicates that the degree of disorder is the highest in the $\text{Ti}_{0.8}\text{V}_{0.2}$ alloy among the present T-V alloys. The mean free path for the conduction electrons ℓ_e is estimated for this alloy using the free electron model, which comes out to be almost comparable to the inter-atomic distance. Such a small value of ℓ_e is generally considered to be a pre-requisite for observing the weak-localization effect. However, the weak-localization is known to be a low-temperature phenomenon, and generally becomes less significant at higher temperatures. Consequently, the TLS-Kondo effect becomes the dominant electron scattering mechanism to govern the electrical resistivity of the $\text{Ti}_{0.8}\text{V}_{0.2}$ alloy at high temperature regime. This is indicated by the observed $-\ln T$ dependence of resistivity and almost zero magneto-resistance of this alloy at high temperature regime.

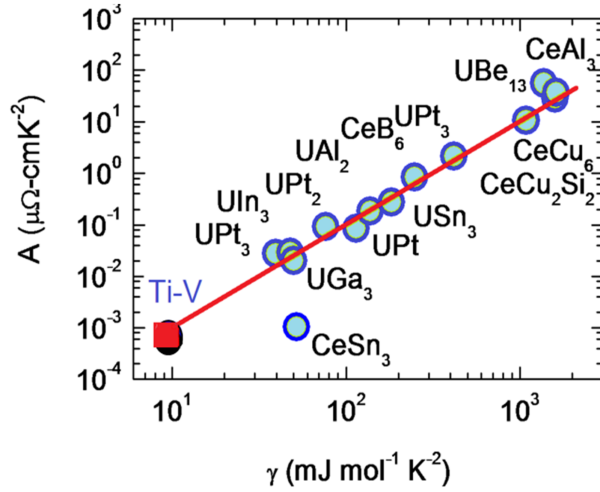


Figure 6.7: Kadowaki-Woods scaling for the $\text{Ti}_{0.4}\text{V}_{0.6}$ (black solid circle) and $\text{Ti}_{0.6}\text{V}_{0.4}$ (red solid square) alloys along with various heavy Fermion and spin fluctuation systems. The solid line represents the function $A/\gamma^2 = 1.0 \times 10^{-4} \mu\Omega\text{-cm}(\text{mole}/\text{mJ})^2$.

6.2.4 Validity of the Kadowaki-Woods scaling relation for the Ti-V alloys

For the heavy Fermion and Spin fluctuation systems, the coefficient A of the quadratic term in the temperature dependence of resistivity and the Sommerfeld coefficient of the electronic heat capacity γ scale according to the Kadowaki-Woods relation [180] given as: $A/\gamma^2 = 1.0 \times 10^{-4} \mu\Omega\text{-cm}^2(\text{mole}/\text{mJ})^2$. The plots of the coefficient A against γ for the $\text{Ti}_x\text{V}_{1-x}$ alloys with compositions $x = 0.4$ and 0.6 along with various heavy Fermion and spin fluctuation systems are shown in Fig. 6.7 in *log-log* scales. The Kadowaki-Woods scaling relation is found to be valid for both these Ti-V alloys, which further supports the presence of spin fluctuations in the Ti-V alloys.

6.2.5 Suppression of T_C due to spin fluctuations in the Ti-V alloys

The influence of spin fluctuations on the suppression of T_C of a superconductor is known to be non-trivial. The strong suppression of T_C in the elemental superconductors such as V and Nb [92, 196, 197], and the absence of superconductivity in Pd and Pt [89, 198] are known to be due to the strong presence of spin fluctuations in these materials. We therefore revisit the problem of T_C in the Ti-V alloys with the inclusion of the effect of spin fluctuations in these alloys. In such case, T_C can be estimated using the modified McMillan formula which takes into account the effect of spin fluctuations, and is given by [199]

$$T_C = \frac{\theta_D}{1.45} \exp \left[\frac{-1.04(1 + \lambda_{eff})}{\lambda_{eff} - \mu_{eff}^*(1 + 0.62\lambda_{eff})} \right]. \quad (6.12)$$

In the above expression, λ_{eff} and μ_{eff}^* are the normalized parameters which are expressed as $\lambda_{eff} = \lambda_{ep}/(1 + \lambda_{sf})$ and $\mu_{eff}^* = (\mu^* + \lambda_{sf})/(1 + \lambda_{sf})$, where λ_{sf} being the electron-spin fluctuations coupling constant [199]. In the previous chapter as well as in Sec. 6.2 of the present chapter, the considerations for the spin fluctuations were not taken into account for the estimation of T_C using McMillan formula. Considering the additional re-normalization due to the electron-spin fluctuation interactions the Sommerfeld coefficient of the electronic heat capacity can be expressed as

$$\gamma = \frac{1}{3} \pi^2 k_B^2 N(0) (1 + \lambda_{ep} + \lambda_{sf}). \quad (6.13)$$

Using the value of $N(0)$ obtained from the band structure calculations and the experimentally measured T_C , θ_D and γ values in Eqns. (6.12) and (6.13), we can estimate the values of λ_{ep} and λ_{sf} without any ambiguity. The values of λ_{ep} and λ_{sf} thus estimated for the present $\text{Ti}_x\text{V}_{1-x}$ alloys are given in Table 6.3. We observe that in the $\text{Ti}_x\text{V}_{1-x}$ alloys, both λ_{ep} and λ_{sf} increase with the decrease in the Ti concentration x . This implies that the initial increase in the experimental T_C with decreasing x down to 0.4 is due to the increase in electron-phonon coupling constant. With further decrease in x below 0.4, the experimental T_C decreases and reaches a value of about 5.4 K for pure V [see Fig. 1.13 (a)]. For the β phase $\text{Ti}_x\text{V}_{1-x}$ alloy system, the residual resistivity ρ_0 decreases progressively as x is decreased [70]. Accordingly, $d\rho/dT$ is expected to increase progressively as x is decreased in these β phase $\text{Ti}_x\text{V}_{1-x}$ alloys. Since $\lambda_{ep} \propto d\rho/dT$ [196], then λ_{ep} is also expected to increase with the decrease in x in the $\text{Ti}_x\text{V}_{1-x}$ alloys. For the present Ti-V alloys, the observed trend of the variation of λ_{ep} with the alloy concentration is consistent with this prediction. Moreover, a relatively higher value of $\lambda_{ep} \sim 1.3$ for the elemental V [91, 92] is also commensurate with the above prediction. Since both λ_{ep} and θ_D [see Fig. 1.12(a)] increases with the decrease in Ti concentration x in the $\text{Ti}_x\text{V}_{1-x}$ alloys with $x \leq 0.4$, then if we disregard the influences of the spin fluctuations, T_C should increase as x is decreased in these Ti-V alloys. In spite of this, the experimental T_C is found to decrease as x is lowered below 0.4. We attribute this to the much stronger influence of the spin fluctuations on T_C of the V-rich Ti-V alloys.

Table 6.3: The electron-phonon coupling constant λ_{ep} and the electron-spin fluctuation coupling constant λ_{sf} for the Ti-V alloys.

	Ti _{0.4} V _{0.6}	Ti _{0.6} V _{0.4}	Ti _{0.7} V _{0.3}	Ti _{0.8} V _{0.2}
λ_{sf}	0.12±0.001	0.042±0.002	0.04±0.002	0
λ_{ep}	1.068±0.005	0.86±0.005	0.84±0.002	0.59±0.001

6.3 Summary and conclusions

We have studied the normal state properties of the Ti-V alloys by measuring the temperature dependence of heat capacity, dc magnetic susceptibility and electrical resistivity. We have estimated the Stoner enhancement factor S and also test the validity of the Kadowaki-Woods scaling relation in order to ascertain the presence of spin fluctuations in the Ti-V alloys. The outcome of the study on the normal states properties of the Ti-V alloys is then used to explain the observed disagreement of the experimental T_C with the theory. The following conclusions are made in this chapter.

- (i) The presence of spin fluctuations in the Ti-V alloys rich enough in V concentration is inferred from: (a) the observed deviation of the experimental heat capacity data from the fitted curve based on the relation $C(T) = \gamma T + C_L(T)$ at low temperatures, where $C_L(T)$ represents the Debye lattice heat capacity; (b) the non-linearity and the negative

curvature in C/T versus T^2 plots at low temperatures; (c) $-T^2 \ln(T)$ dependence of the dc magnetic susceptibility; (d) the enhancement of the Stoner factor S ; (e) a higher value of the Wilson's coefficient R_W than unity; (f) T^2 dependence of resistivity at low temperatures; and (g) the validity of the Kadowaki-Woods scaling relation. The role of spin fluctuations is diminished with the increase in Ti concentration in the Ti-V alloys.

- (ii) The presence of spin fluctuations gives rise to a strong suppression of T_C in the $\text{Ti}_x\text{V}_{1-x}$ alloys having concentrations $x = 0.4, 0.6$ and 0.7 .
- (iii) Similar to λ_{ep} and θ_D , λ_{sf} is also found to increase with the decrease in Ti concentration x in the $\text{Ti}_x\text{V}_{1-x}$ alloys. We suggest that the initial increasing trend of T_C of the $\text{Ti}_x\text{V}_{1-x}$ alloys with the decrease in x down to 0.4 is due to the increase of both λ_{ep} and θ_D with the decrease in x . In spite of increase of both λ_{ep} and θ_D with increasing x in the $\text{Ti}_x\text{V}_{1-x}$ alloys, T_C exhibit a decreasing trend with further lowering of x below 0.4 and reaches a value of about 5.4 K for elemental V. We have attributed this to the increasing role of the spin fluctuations with the decrease in x in the V rich end of the Ti-V alloy system.

Chapter 7

Critical current and flux-line pinning in the Ti-V alloys

7.1 Introduction

In chapter 3 we have seen that the present Ti-V alloys contain various kinds of lattice defects. These are the grain boundaries, edge dislocations, and the secondary phases such as the hexagonal ω phase, hcp α phase, and the stress induced orthorhombic α' phase. These lattice defects are expected to act as flux-line pinning centres, and hence their presence is likely to influence the critical current density of the Ti-V alloys. In this chapter we study the flux-line pinning properties in the Ti-V alloys through dc magnetization measurements. We estimate the critical current density of these alloys from the isothermal magnetic field dependence of magnetization. The magnetic field dependence of the pinning force density is analysed to find out the roles of these metallurgical factors on the critical current density in the Ti-V alloys.

7.2 Results and discussion

7.2.1 Magnetic field dependence of magnetization

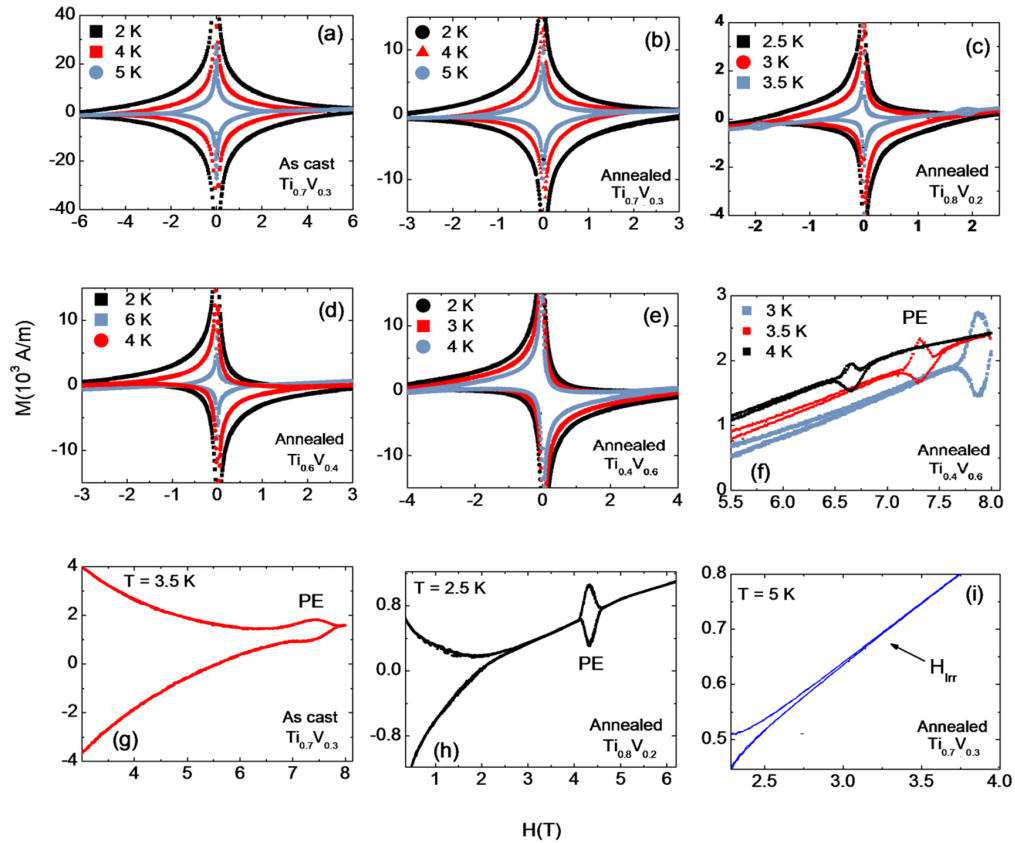


Figure 7.1: $M(H)$ curves for few selected Ti-V alloys at various constant temperatures below T_C . (f)-(g) $M(H)$ curves highlighting the peak-effect in the Ti-V alloys. (i) Illustration of the determination of H_{Irr} from the $M(H)$ curve closure.

Fig. 7.1 present the magnetic field dependence of magnetization (M) of few selected Ti-V alloys at various constant temperatures below their

respective T_C . The $M(H)$ curves are distinctly irreversible over a certain magnetic field regime. Except in the annealed $\text{Ti}_{0.7}\text{V}_{0.3}$ alloy, all the as cast and annealed Ti-V alloys exhibit a clear signature of the peak-effect in the magnetic field dependence of magnetization [Fig. 7.1(f)-(h)]. The upper critical field H_{C2} and the irreversibility field H_{Irr} for these Ti-V alloys at various temperatures are estimated from the $M(H)$ curves. The method of estimation of the H_{C2} has been discussed in chapter 4, and H_{Irr} is taken as the magnetic field value at which irreversible magnetization ΔM goes to zero within the limit of the resolution of the present experimental set-up.

The temperature dependencies of H_{C2} and H_{Irr} for the annealed Ti-V alloys are shown in Fig. 7.2. Unlike in typical low- T_C superconductors, in the present Ti-V alloys particularly in those having higher Ti concentration, $H_{Irr}(T)$ -line is noticeably depressed below the $H_{C2}(T)$ -line. For an example, at 5 K temperature, the H_{Irr} value for annealed $\text{Ti}_{0.7}\text{V}_{0.3}$ alloy is almost 1.5 T lower than the H_{C2} value. The lower value of the H_{Irr} than the H_{C2} is common in high- T_C cuprate superconductors [200, 201], Chevrel phase superconductors [202-206], and MgB_2 superconductor [207-209], where solid flux-line system undergoes a transition into vortex-liquid at magnetic field much below the H_{C2} due to the increasing importance of thermal fluctuations in these superconductors. The Ginzburg number G_i was estimated to be $\sim 10^{-5}$ for the Ti-rich Ti-V alloys (see chapter 4), which indicates that the thermal fluctuation is indeed important in these bulk Ti-V alloys. This

is further confirmed by the magnetic relaxation experiments, the results of which will be discussed in detail in chapter 9. On the basis of these facts, we suggest that in the Ti-rich Ti-V alloys, thermal fluctuations lower the H_{Irr} to a magnetic field value much lower than the H_{C2} , though this observed effect is not as strong as is observed in the high- T_C superconductors.

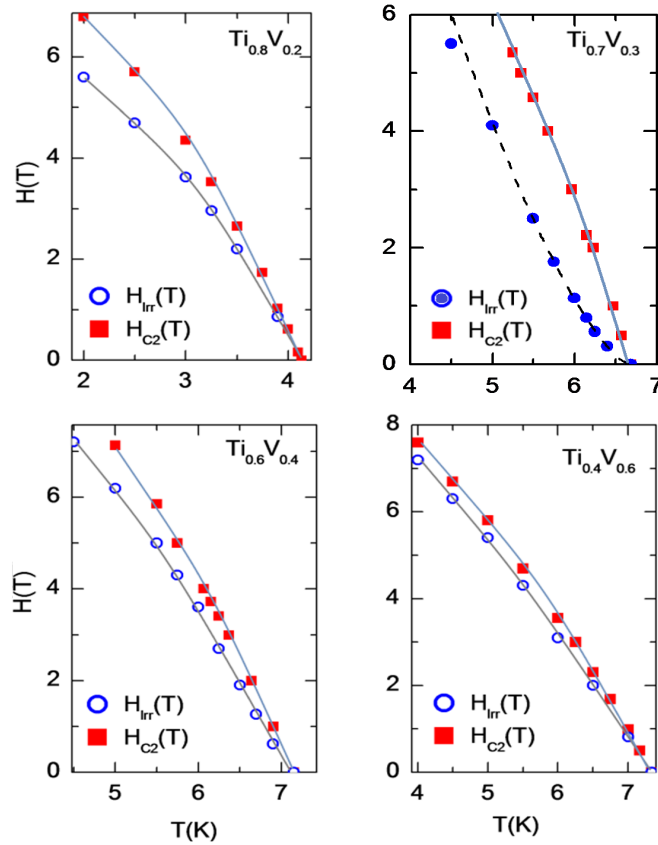


Figure 7.2: Temperature dependence of the characteristic fields H_{C2} and H_{Irr} for the annealed Ti-V alloys (in solid symbols). The solid lines are the guide to the eyes. The dotted line is the fit to the $H_{Irr}(T)$ data of the $Ti_{0.7}V_{0.3}$ alloy based on the relation $H_{Irr}(T) \propto (1 - T/T_C)^n$.

As evident from Fig. 7.2, the temperature dependence of H_{Irr} of the $\text{Ti}_{0.7}\text{V}_{0.3}$ alloy is distinctly different from that of the other Ti-V alloys studied here. In order to understand the distinct feature of the $H_{Irr}(T)$ data of the $\text{Ti}_{0.7}\text{V}_{0.3}$ alloy, we fit the $H_{Irr}(T)$ data using the power law relation: $H_{Irr}(T) \propto (1 - T/T_C)^n$. The best fitting of the experimental data points is obtained for $n=1.43$ (the fitting is shown by the dotted curve in Fig. 7.2). This is very close to the $(1 - T/T_C)^{1.5}$ -dependence of H_{Irr} , which is theoretically predicted for both the phase transition from vortex-glass to vortex-liquid state [38] as well as for the de-pinning of the flux lines due to the thermal fluctuation effect [210]. The superconducting mixed state properties of the $\text{Ti}_{0.7}\text{V}_{0.3}$ alloy will be studied in detail in chapter 8, where we shall attempt to find out whether the $H_{Irr}(T)$ -line of this alloy is a de-pinning line or a glass-transition line.

7.2.2 Magnetic field dependence of the critical current densities in the Ti-V alloys

The irreversible magnetization of a superconductor is related to the critical current density J_C . The critical current density J_C for the present Ti-V alloys is estimated from the irreversible magnetization using Bean's critical state model [27]. According to this model, J_C for a rectangular sample is given by [211]

$$J_C = 20\Delta M \left[\frac{b}{(1 - a/3b)} \right]. \quad (7.1)$$

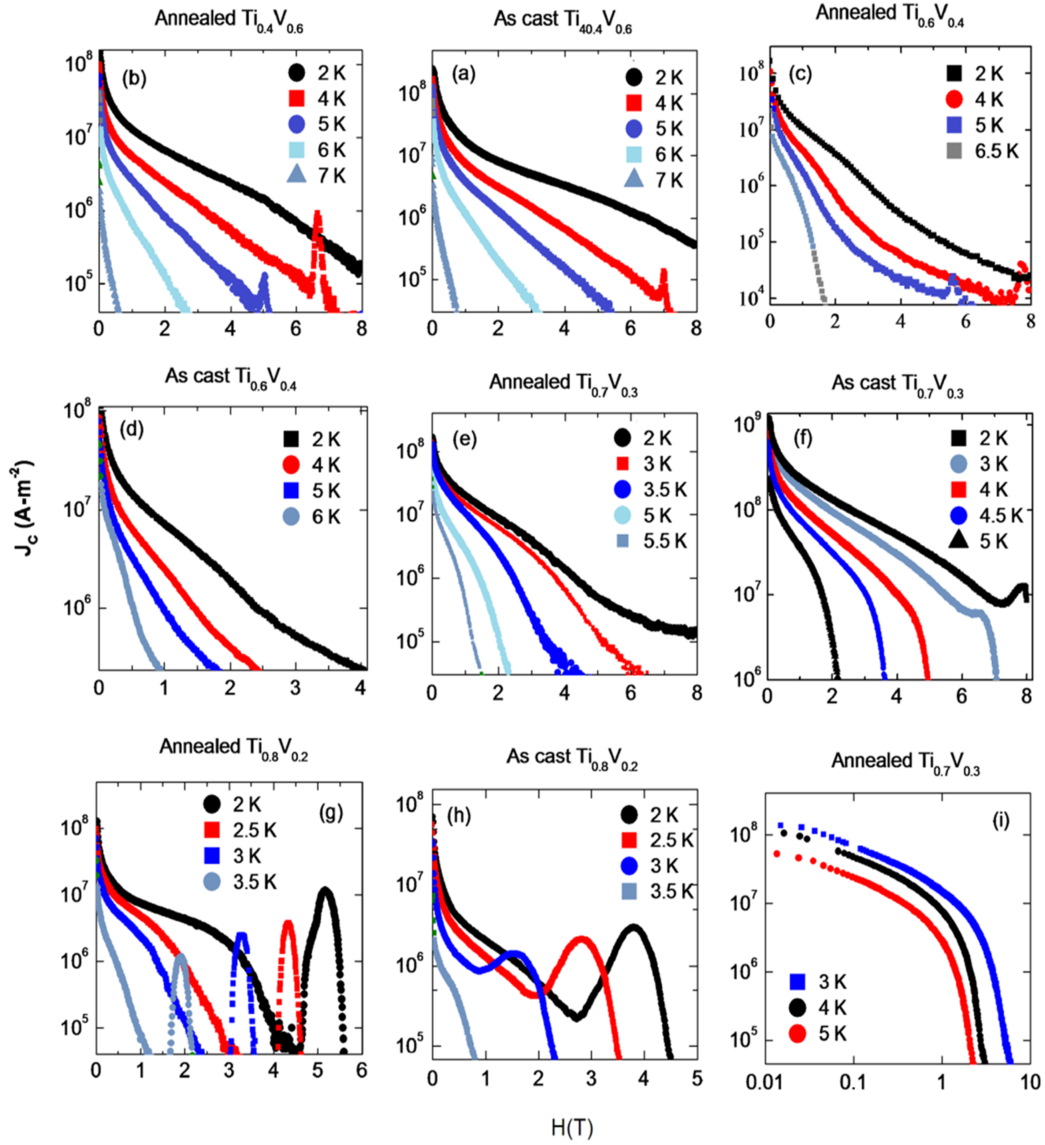


Figure 7.3: (a)-(h) Magnetic field dependence of critical current density J_C for the as cast and annealed Ti-V alloys at various constant temperatures below their respective T_C (J_C is plotted in \log scale). (i) $J_C(H)$ curves for the annealed $\text{Ti}_{0.7}\text{V}_{0.3}$ alloy plotted in \log - \log scales to illustrate the sharp drop-off of J_C in high magnetic field regime.

Here ΔM is the difference in magnetization between the H -decreasing and the subsequent H -increasing branch. The parameters $2a$ and $2b$ ($a > b$) are the dimensions of the sample in the directions normal to the direction of the applied magnetic field. The field dependence of J_C estimated for the annealed and as cast Ti-V alloys at various constant temperatures below their respective T_C is shown in Fig. 7.3. As cast $\text{Ti}_{0.7}\text{V}_{0.3}$ alloy has the highest J_C value among all the present Ti-V alloys. At 2 K temperature and in 2 T magnetic field, J_C for this alloy is $\sim 10^8$ A/m². In the annealed and as cast $\text{Ti}_{0.4}\text{V}_{0.6}$ alloys, J_C exhibits moderate field dependence up to H_{Irr} . On the other hand, J_C in the Ti-rich Ti-V alloys exhibits moderate field dependence only in low magnetic field regime while it drops with increasing magnetic field at an unusually faster rate in high magnetic field regime near to H_{Irr} . These features are more clearly visible in Fig. 7.3 (i), where $J_C(H)$ curves for the annealed $\text{Ti}_{0.7}\text{V}_{0.3}$ alloy are plotted in *log-log* scales. Since thermal fluctuations are important in the magnetic field regime close to H_{Irr} , the observed sharp drop in high-field J_C seems to be related to the de-pinning of the flux lines due to thermal fluctuations effect. Similar high-field J_C behaviour is also observed in MgB_2 superconductor, where the observed behaviour is ascribed to the increased role of thermal fluctuations in this superconductor [207, 212]. On the basis of the results of our estimations of the superconducting parameters of the Ti-V alloys, we have suggested in chapter 4 that the V-rich Ti-V alloys are expected to be superior than the Ti-rich Ti-V alloys from J_C point of view because the line tension energy $E_L [= (\Phi_0/4\pi\lambda)^2 l n \kappa]$

of the flux line is higher for the V-rich Ti-V alloys. A higher value of the line tension energy in the V-rich Ti-V alloys implies that these alloys are capable to compete with the thermal fluctuations effect, and thereby could sustain dissipation-less current to flow up to higher magnetic fields. In agreement with this, the drop-off in the high-field J_C is less severely observed in the case of $\text{Ti}_{0.4}\text{V}_{0.6}$ alloy, and also the H_{Irr} lies very close to the H_{C2} for this alloy.

In order to understand the pinning mechanisms prevalent in the present Ti-V alloys, we estimate the pinning force density F_P for these alloys using the relation: $F_P = J_C \times H$. In Fig. 7.4, we show the magnetic field dependence of the estimated F_P for the present Ti-V alloys at various constant temperatures. A detailed analysis of the field dependence of pinning force density in terms of the size, spacing and nature of the pinning centres, and the nature of their interaction with the flux-lines has been done by Dew-Hughes [213]. It is normally expected that the pinning force density for a type-II superconductor follows the general form [7.16]: $f_P \propto h^p(1-h)^q$, with $f_P = F_P/F_{P,max}$ and $h = H/H_{C2}$. Here, $F_{P,max}$ is the maximum value of F_P at a particular temperature, and the values of p and q depend on the details of the pinning mechanism. According to the model of Dew-Hughes [213], if both the size and spacing of the pinning centres are larger than the magnetic field penetration depth of the superconductor then H can adjust everywhere to its equilibrium value, which is different within the pinning centres from that in the superconducting matrix. The flux-line pinning resulted from this

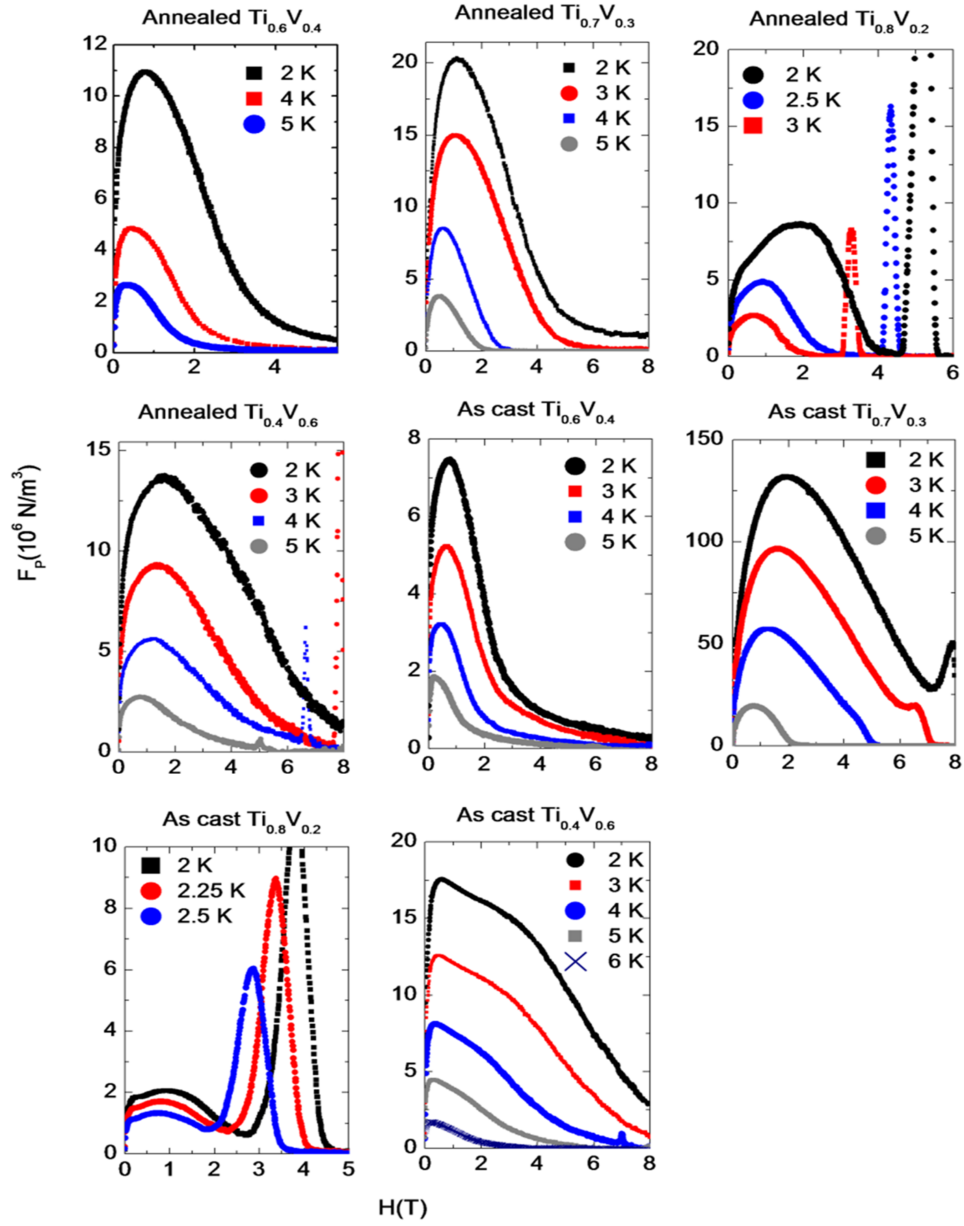


Figure 7.4: Magnetic field dependence of pinning force density F_P for the as cast and annealed Ti-V alloys at various constant temperatures below their respective T_C .

difference is said to originate from the magnetic interaction [213]. If the size or the spacing of the pinning centres is less than the magnetic field penetration depth, then H cannot adjust to its local equilibrium value and adjusts to some other suitable value. Then the flux-line pinning originates from the difference in the superconducting properties, and is said to originate from core interaction [213]. On the basis of these two types of interactions, the following functional forms for the field dependence of pinning force density are available in Dew-Hughes model:

- (i) **Normalized function F_1 :** $f_P \propto h^{\frac{1}{2}}(1 - h)$, for magnetic interaction with the normal volume pins;
- (ii) **Normalized function F_2 :** $f_P \propto h^{\frac{1}{2}}(1 - 2h)$, for magnetic interaction leading to the $\Delta\kappa$ pinning (also called ΔT_C pinning) by the volume pins, where κ is the Ginzburg-Landau parameter;
- (iii) **Normalized function F_3 :** $f_P \propto (1 - h)^2$, for core interaction with the normal volume pins;
- (iv) **Normalized function F_4 :** $f_P \propto h(1 - h)$, for core interaction leading to the $\Delta\kappa$ pinning by the volume pins;
- (v) **Normalized function F_5 :** $f_P \propto h^{\frac{1}{2}}(1 - h)^2$, for core interaction with the normal surface pins;
- (vi) **Normalized function F_6 :** $f_P \propto h^{\frac{3}{2}}(1 - h)$, for core interaction leading to the $\Delta\kappa$ pinning by the surface pins;

- (vii) **Normalized function F_7** : $f_P \propto h(1-h)^2$, for core interaction with the normal point pins; and
- (viii) **Normalized function F_8** : $f_P \propto h^2(1-h)$, for core interaction leading to the $\Delta\kappa$ pinning by the point pins.

We have already observed that H_{Irr} is considerably lower than H_{C2} for the present Ti-V alloys. In such case, it is necessary to replace the scaling field H_{C2} with the H_{Irr} because J_C is almost zero above H_{Irr} . This is also the case for the high- T_C cuprate, Chevrel phase, and MgB₂ superconductors. Moreover, it is well known that the magnetic irreversibility associated with the peak-effect phenomenon has origin(s) different from that of the main irreversible magnetization observed in the low magnetic field regime [214]. Hence, for the present Ti-V alloys, a correct determination of the irreversibility field associated with the main region of irreversible magnetization is not possible because of the presence of the peak-effect in the field dependence of magnetization of these alloys. We shall call the irreversibility field associated with the main irreversible magnetization observed in low magnetic fields as the H^* to distinguish it from the H_{Irr} . Thermal fluctuations can also influence the F_P in high magnetic field regime, which may also lead to some uncertainty in the determination of H^* . In such situations, the irreversibility field associated with the main irreversible magnetization can be alternatively determined from the linear extrapolation of the $F_P(H)$ curve (immediately after the main peak) to $F_P = 0$ by completely disregarding the zone affected by peak-effect and/or thermal fluctuations [215]. However,

Dew-Hughes model suggests that the $F_P(H)$ curves are in general not expected to be linear except in the close vicinity of the reduced field $h = 1$, and this is also evident from the experimental $F_P(H)$ curves shown in Fig. 7.5. Therefore, the straightforward method described above will provide an erroneous determination of H^* . However, with simple mathematical manipulation of the functional form $f_P \propto h^p(1 - h)^q$, we can get the functions $J_C^{1/q} H^{(1-p)/q}$ which are linear in H . Following this, we plot the experimental $J_C(H)$ data in $J_C^{1/q} H^{(1-p)/q}$ versus H fashion for different sets of values of p and q suggested in the Dew-Hughes model. For a certain set of p and q values, the plot of $J_C^{1/q} H^{(1-p)/q}$ against H will be linear, and the linear extrapolation of these plots to $J_C^{1/q} H^{(1-p)/q} = 0$ will provide an accurate estimation of H^* . This is illustrated in Fig. 7.5. We have used this method to find out H^* , and these values are used to interpret the pinning mechanism(s) prevailing in the main region of irreversible magnetization with the help of Dew-Hughes model.

Fig. 7.6-7.10 shows the normalized pinning force density f_P as functions of reduced field $h = H/H^*$ for the as cast and annealed Ti-V alloys at different constant temperatures below their respective T_C . As shown in Fig. 7.6(a), the $f_P(h)$ curves for the annealed $\text{Ti}_{0.8}\text{V}_{0.2}$ alloy at various constant temperatures below T_C do not exhibit scaling behaviour. Moreover, at low temperatures, the $f_P(h)$ curves exhibit a hump like feature in low reduced magnetic field regime. This is more clearly visible in Fig. 7.6(b). These observations indicate that more than one kind of pinning mechanisms is op-

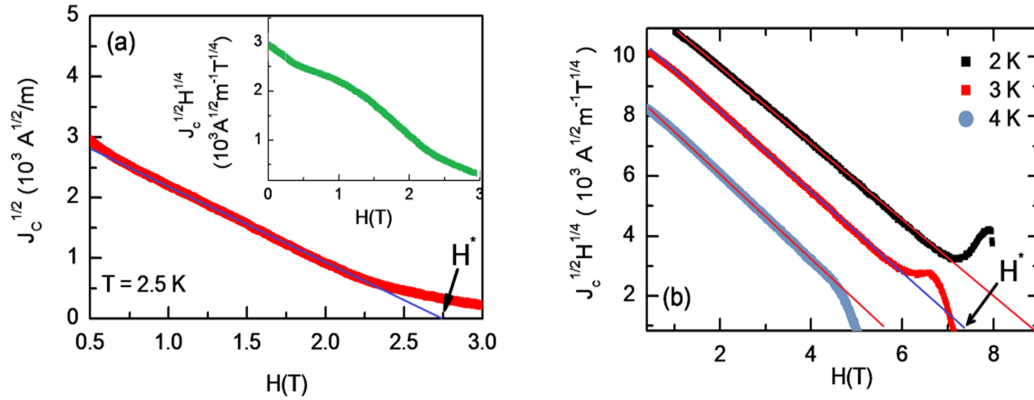


Figure 7.5: (a) $J_C^{1/2} H^{(1-p)/q}$ versus H plots for the annealed $\text{Ti}_{0.8}\text{V}_{0.2}$ alloy. The plot is linear for $p = 1$ and $q = 2$ (main panel), whereas it becomes non-linear for other sets of p and q values available in the Dew-Hughes model. For an illustration $J_C^{1/2} H^{(1-p)/q}$ versus H plot for $p = 0.5$ and $q = 2$ is shown in the inset. (b) $J_C^{1/2} H^{(1-p)/q}$ versus H plots for the as cast $\text{Ti}_{0.7}\text{V}_{0.3}$ alloy for $p = 0.5$ and $q = 2$. The characteristic field H^* is determined from the linear extrapolation of these plots to $J_C^{1/2} H^{(1-p)/q} = 0$.

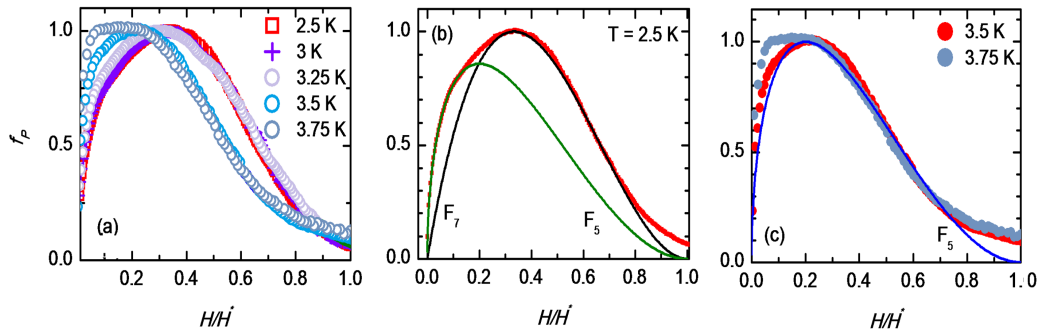


Figure 7.6: Normalized pinning force density f_P against the reduced magnetic field $h = H/H^*$ for the annealed $\text{Ti}_{0.8}\text{V}_{0.2}$ alloy at different constant temperatures below T_C . The open symbols represent the experimental data while the solid lines represent the fittings based on normalized functions F_5 and F_7 available in the Dew-Hughes model.

erating in this alloy. However, in the temperature range 2.5-3.25 K, the $f_P(h)$ curves for the annealed $\text{Ti}_{0.8}\text{V}_{0.2}$ alloy exhibit marginal scaling behaviour in high reduced magnetic field regime above $h > 0.3$. The $f_P(h)$ curves in this reduced magnetic field regime are observed to be well explained with the normalized function F_7 [Fig. 7.6(b), where only the $f_P(h)$ at 2.5 K is shown for clarity], indicating that the normal point pins are the major source of flux-line pinning mechanism in this magnetic field regime. In Fig. 7.6(b), we also observe that the low-field hump in the $f_P(h)$ curve can be fitted with the normalized function F_5 , which suggests that the flux-line pinning at the normal surface pins becomes important in such low magnetic field regime. Accordingly, at relatively higher temperature (say 3.5 K), where pinning force is limited only in low magnetic field regime, $f_P(h)$ curve follows the normalized function F_5 [Fig. 7.6(c)]. As the temperature approaches towards T_C , an additional shoulder-like feature becomes apparent in the $f_P(h)$ curve in very low magnetic field regime, and this becomes more prominent with increasing temperature [Fig. 7.6(c)]. This additional shoulder-like feature cannot be explained with the help of any of the functional forms of $f_P(h)$ available in the Dew-Hughes model.

As shown in Fig. 7.7(a), a major portion of the main peak of the $f_P(h)$ curves of the as cast $\text{Ti}_{0.8}\text{V}_{0.2}$ alloy is masked by the occurrence of the peak-effect, and thereby a limited reduced magnetic field regime is available where the analysis of the field dependence of F_P by using Dew-Hughes model is possible. However, these $f_P(h)$ curves exhibit scaling behaviour in the reduced

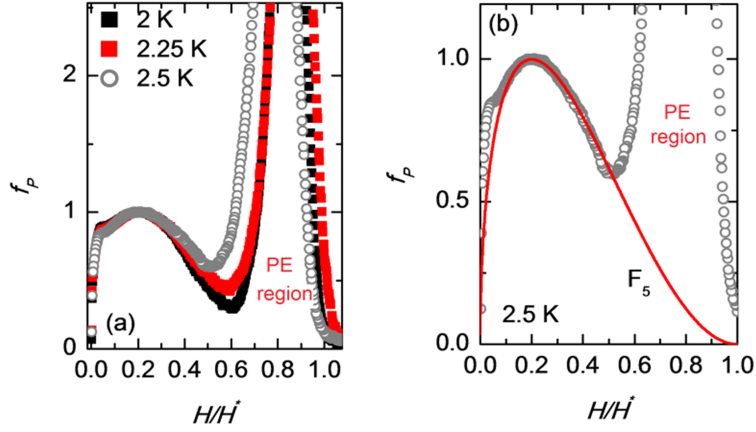


Figure 7.7: Normalized pinning force density f_P as functions of reduced magnetic field $h = H/H^*$ for the as cast $\text{Ti}_{0.8}\text{V}_{0.2}$ alloy at different constant temperatures below T_C . The open symbols represent the experimental data while the solid line represents the fit based on normalized function F_5 .

magnetic field regime except near to the peak-effect regime [Fig. 7.7(a)], and the scaled $f_P(h)$ curves follow the normalized function F_5 [Fig. 7.7(b), where only the $f_P(h)$ at 2.5 K is shown for clarity]. This implies that the normal surface pins have the major contribution in the flux-line pinning mechanism in the as cast $\text{Ti}_{0.8}\text{V}_{0.2}$ alloy. An additional narrow peak becomes clearly visible in the $f_P(h)$ curves of the as cast $\text{Ti}_{0.8}\text{V}_{0.2}$ alloy in very low reduced magnetic field regime below $h < 0.08$, and this peak can be correlated to the shoulder-like feature observed in the $f_P(h)$ curves of the annealed $\text{Ti}_{0.8}\text{V}_{0.2}$ alloy in exceedingly low magnetic field regime.

Fig. 7.8(a) and (c) show that when the temperatures is not very close to T_C , the $f_P(h)$ curves of both the annealed and as cast $\text{Ti}_{0.7}\text{V}_{0.3}$ alloys exhibit scaling behaviour in the entire reduced magnetic field region except in the

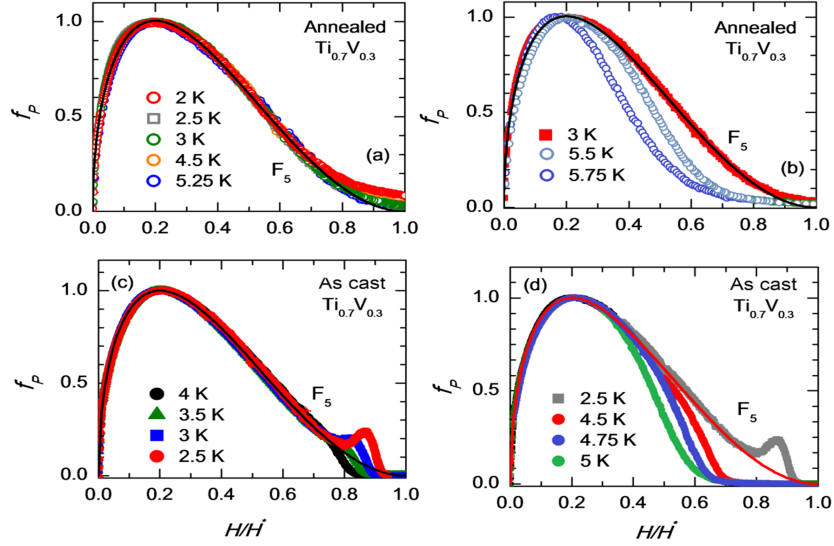


Figure 7.8: $f_P(h)$ curves for the annealed and as cast $\text{Ti}_{0.7}\text{V}_{0.3}$ alloys. The open symbols represent the experimental data while the solid lines represent the fits based on normalized function F_5 .

peak-effect region in the case of as cast $\text{Ti}_{0.7}\text{V}_{0.3}$ alloy. Such a scaling behaviour of the $f_P(h)$ curves indicates that the pinning force in these alloys is mainly limited by only one type of pinning mechanism. These scaled $f_P(h)$ curves follow the normalized function F_5 [Fig. 7.8(a) and (c)], suggesting that the flux-line pinning occurs mainly at the normal surface pins. At relatively higher temperatures ($T \geq 5.25$ K for the annealed $\text{Ti}_{0.7}\text{V}_{0.3}$ alloy and $T \geq 4.5$ K for the as cast $\text{Ti}_{0.7}\text{V}_{0.3}$ alloy), the high-field F_P diminishes with the increase in magnetic field more rapidly than does the low-field F_P . As temperature is increased, this rapid drop in high-field F_P occurs at lower reduced magnetic field. At high temperatures close to T_C , thermal fluctuations effect becomes very robust to diminish the flux-line pinning particularly in

the high magnetic field regime where the elastic energy of the flux-line system is low. Therefore, the observed rapid drop in high-field F_P can be correlated to the de-pinning of the flux lines due to thermal fluctuations.

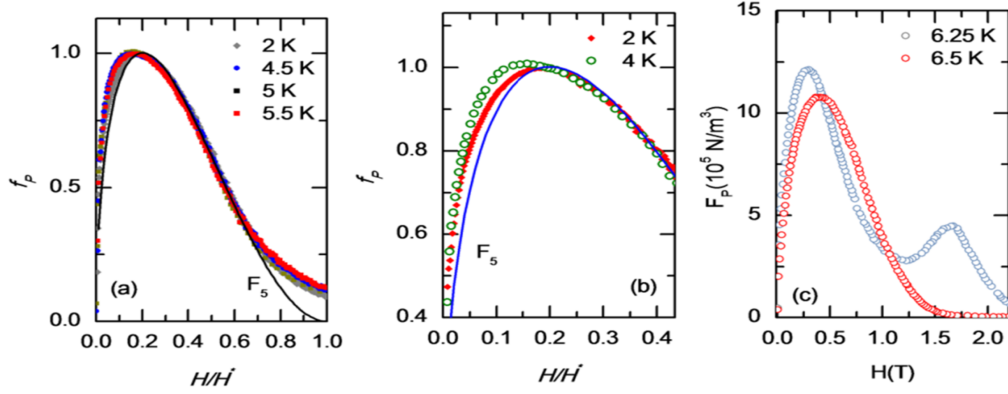


Figure 7.9: (a) Normalized pinning force density f_P against the reduced magnetic field $h = H/H^*$ for the annealed $\text{Ti}_{0.6}\text{V}_{0.4}$ alloy. The solid lines represent the fittings of the experimental data based on normalized function F_5 . (b) $f_P(h)$ curves in low reduced magnetic field region to show that the experimental $f_P(h)$ curves deviate from the fitted curve. (c) $F_P(H)$ for the annealed $\text{Ti}_{0.6}\text{V}_{0.4}$ alloy to illustrate the peak-effect in this alloy.

The $f_P(h)$ curves of annealed $\text{Ti}_{0.6}\text{V}_{0.4}$ alloy are shown in Fig. 7.9(a) for $T \leq 5.5 \text{ K}$. These curves show reasonably good scaling behaviour in the entire reduced magnetic field regime except in very low reduced magnetic field regime. The observed scaling behaviour indicates that the pinning force in the annealed $\text{Ti}_{0.6}\text{V}_{0.4}$ alloy is mainly limited by only one type of pinning mechanism in the concerned temperature and magnetic field regime. These scaled $f_P(h)$ curves follow the normalized function F_5 [Fig. 7.9(a)], suggesting that the flux-line pinning occurs mainly at the normal surface pins. The

$f_P(h)$ curves, however, exhibit an additional source of magnetic irreversibility in very low reduced magnetic field regime, which is indicated by the upward shift of the $f_P(h)$ curves above the normalized function F_5 [Fig. 7.9(b)]. Similar behaviour has also been observed in the case of annealed and as cast $\text{Ti}_{0.8}\text{V}_{0.2}$ alloys. We will address this issue later in this chapter. As shown in Fig. 7.9(c), the second peak in the $f_P(h)$ curve occurring in the high magnetic field regime (due to the peak-effect phenomenon) appears to coalesce with the main peak of the $f_P(h)$ curve for temperatures $T = 6.25$ K. For $T = 6.5$ K and above, the high-field second peak in the $f_P(h)$ curve is concealed within the main peak of the $f_P(h)$ curve. This is inferred from the observed higher value of F_P at 6.5 K than at 6.25 K in certain magnetic field region within the main region of irreversible magnetization [Fig. 7.9(c)]. Due to the occurrence of the peak-effect phenomenon within and around the main peak of the $f_P(h)$ curves, it is not possible to find out H^* for temperatures $T > 6$ K. Consequently, we are prevented to carry out the scaling analysis of the $f_P(h)$ curves of the annealed $\text{Ti}_{0.6}\text{V}_{0.4}$ alloy in the said temperatures regime.

Qualitatively, very similar results are also obtained for the as cast $\text{Ti}_{0.6}\text{V}_{0.4}$ alloy. These results are summarized in Fig. 7.10. Normal surface pins act as the major pinning centres in this alloy for temperatures $T \leq 4$ K, which is indicated by the observed scaling behaviour of the $f_P(h)$ curves, and the agreement of these scaled $f_P(h)$ curves with the normalized function F_5 [Fig. 7.10(a)]. The additional magnetic irreversibility observed in very low reduced

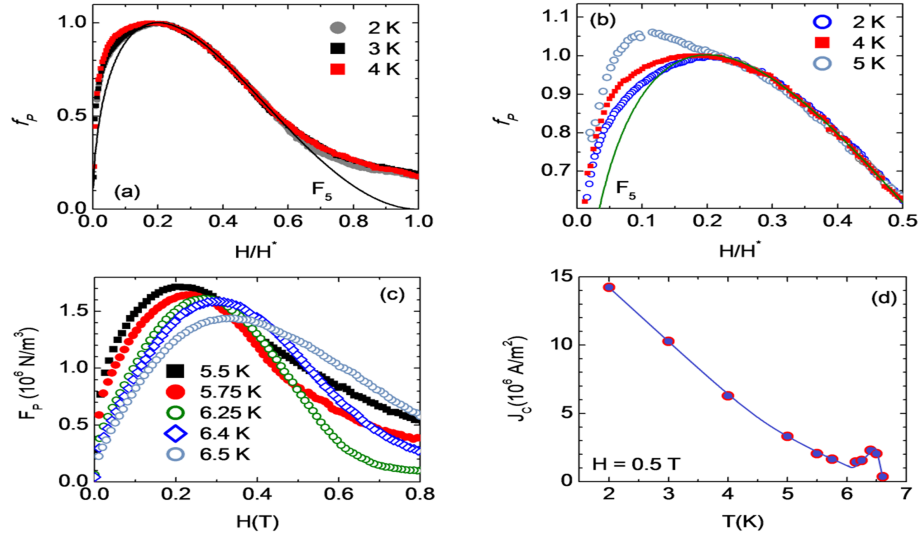


Figure 7.10: (a) $f_P(h)$ curves for the as cast $\text{Ti}_{0.6}\text{V}_{0.4}$ alloy. The solid lines represent the fitting of the experimental data based on normalized function F_5 . (b) $f_P(h)$ curves in low reduced field regime to show that the experimental $f_P(h)$ curves deviate from the fitted curve. (c) $F_P(H)$ curves for the as cast $\text{Ti}_{0.6}\text{V}_{0.4}$ alloy to illustrate the peak-effect in this alloy. (d) Temperature dependence of J_C for the same alloy to illustrate the peak-effect.

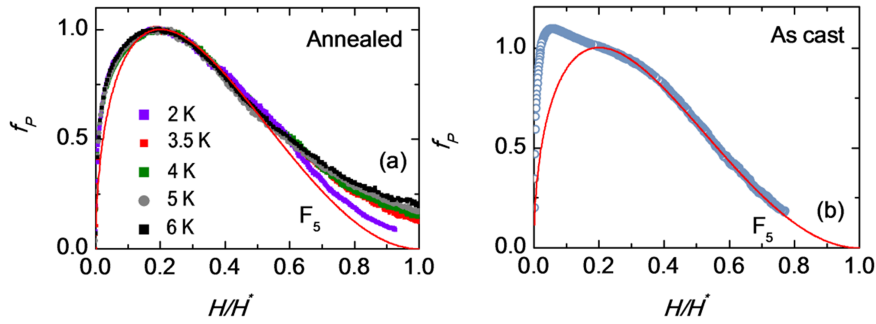


Figure 7.11: (a) Normalized pinning force density f_P against the reduced magnetic field $h = H/H^*$ for annealed $\text{Ti}_{0.4}\text{V}_{0.6}$ alloy. The solid lines represent the fittings of the experimental data based on normalized function F_5 . (b) $f_P(h)$ curve for as cast $\text{Ti}_{0.4}\text{V}_{0.6}$ alloy at 2 K.

magnetic field regime now becomes more prominent in the as cast $\text{Ti}_{0.6}\text{V}_{0.4}$ alloy as compared to its annealed counterpart [Fig. 7.10(b)]. At $T = 5$ K, this additional magnetic irreversibility is strong enough to mask the main peak of the $f_P(h)$ curve, making the determination of $F_{P,max}$ uncertain at this temperature. Because of this, we have arbitrarily chosen $F_{P,max}$ for $T = 5$ K to perform the scaling analysis of the $f_P(h)$ curve. We find that the $f_P(h)$ curve at $T = 5$ K can also be described by the normalized function F_5 [Fig. 7.10(b)]. For temperatures $T > 5$ K, a higher value of F_P is observed at higher temperature than at low temperature in certain magnetic field regime [Fig. 7.10(c)]. This corresponds to a hump in the $J_C(T)$ curve in high temperature regime as is clearly visible in Fig. 7.10(d). Such a hump-like feature in the $J_C(T)$ curve bears evidence for the occurrence of the peak-effect phenomenon in this alloy. The peak-effect in the as cast $\text{Ti}_{0.6}\text{V}_{0.4}$ alloy occurs well inside the main region of magnetic irreversibility for temperatures $T > 5$ K, giving no opportunity to observe the effect separately in $M(H)$ curve and hence in $J_C(H)$ and $F_p(H)$ curves. As the main peak of the $f_P(h)$ curves for $T > 5$ K is significantly influenced by the occurrence of the peak-effect, we do not bother for performing the scaling analysis of the $f_P(h)$ curves in this temperature regime.

Fig. 7.11 shows the $f_P(h)$ curves for the annealed and as cast $\text{Ti}_{0.4}\text{V}_{0.6}$ alloy. For the annealed $\text{Ti}_{0.4}\text{V}_{0.6}$ alloy, $f_P(h)$ curves scale onto each other following the normalized function F_5 up to reduced fields $h \sim 0.6$, indicating that the flux lines are pinned by the normal surface pins in this alloy. Like in

(both the annealed and as cast) $\text{Ti}_{0.8}\text{V}_{0.2}$ and $\text{Ti}_{0.6}\text{V}_{0.4}$ alloys, an additional source of magnetic irreversibility is also observed for this alloy in very low reduced magnetic field regime. On the other hand, in the as cast $\text{Ti}_{0.4}\text{V}_{0.6}$ alloy, this additional low-field magnetic irreversibility becomes very prominent, and the broad peak in the $f_P(h)$ curves in the region of the main magnetic irreversibility reduces to a hump-like structure (Fig. 7.4), as is also the case for the $f_P(h)$ curve of the as cast $\text{Ti}_{0.6}\text{V}_{0.4}$ alloy at $T = 5$ K [Fig. 7.10(b)]. In such case, the uncertainty associated with the determination of $F_{P,max}$ prevents us to carry out a proper scaling analysis of the $f_P(h)$ curves in a wide range of temperature. However, at low temperatures ($T = 2$ K, 2.5 K and 3 K), it is possible to observe the broad peak of the $f_P(h)$ curve separately, and hence the determination of $F_{P,max}$ is possible without uncertainty. We find that the $f_P(h)$ curves of the as cast $\text{Ti}_{0.4}\text{V}_{0.6}$ alloy follow the normalized function F_5 for $T = 2$ K, 2.5 K and 3 K. Hence, similar to the annealed $\text{Ti}_{0.4}\text{V}_{0.6}$ alloy, the normal surface pins act as the major pinning centres in the as cast $\text{Ti}_{0.4}\text{V}_{0.6}$ alloy as well. The result is shown in Fig. 7.11(b) where the $f_P(h)$ curve only at 2 K is shown for clarity.

We now present a detail discussion on the experimental results on the flux-line pinning properties of the currently investigated Ti-V alloys in terms of the microstructural properties of these alloys. The XRD results discussed in chapter 3 indicate that the annealed $\text{Ti}_{0.8}\text{V}_{0.2}$ alloy contain a large amount of ω phase. Since the size of these non-superconducting ω phase precipitates is usually very small ($\sim 0.01 \mu\text{m}$) [62], they act as effective point pinning centre

for the flux lines. Consequently, their presence in the annealed $\text{Ti}_{0.8}\text{V}_{0.2}$ alloy seems to be the major source of point pins in this alloy. However, this alloy also contains extended defect like grain boundaries which are two-dimensional in nature, and thereby can act as normal surface pins. Hence, in the annealed $\text{Ti}_{0.8}\text{V}_{0.2}$ alloy, the dominant contribution of the normal surface pins in low-field F_P , which is inferred from our analysis of the pinning force curves, seems to arise from the flux-line pinning at the grain boundaries. We have observed above that the normal point pins become less effective to contribute towards the pinning force in low magnetic field regime. As compared to the annealed $\text{Ti}_{0.8}\text{V}_{0.2}$ alloy, the pinning force in the as cast $\text{Ti}_{0.8}\text{V}_{0.2}$ alloy is limited within a smaller magnetic field regime [please see the panels (g) and (h) of Fig. 7.3]. Moreover, the as cast $\text{Ti}_{0.8}\text{V}_{0.2}$ alloy contains relatively lesser amount of ω phase as compared to the annealed $\text{Ti}_{0.8}\text{V}_{0.2}$ alloy. Consequently, the contribution of the ω phase towards pinning force becomes reduced, and the grain boundaries play the major role in flux-line pinning mechanism in the as cast $\text{Ti}_{0.8}\text{V}_{0.2}$ alloy.

The role of the normal point pins in the flux-line pinning mechanism is expected to be negligible in the annealed and as cast $\text{Ti}_x\text{V}_{1-x}$ alloys having compositions $x = 0.4, 0.6,$ and 0.7 because the ω phase is almost absent in these alloys (only a very small amount of ω phase is present in the as cast and annealed $\text{Ti}_{0.7}\text{V}_{0.3}$ alloy). The results of the structural investigation also indicate that the defect structures those are present in these alloys are grain boundaries, edge dislocations (most prominently observed in the as

cast $\text{Ti}_{0.7}\text{V}_{0.3}$ alloy and also in the annealed $\text{Ti}_{0.6}\text{V}_{0.4}$ alloy), and α phase (in the annealed $\text{Ti}_{0.7}\text{V}_{0.3}$ alloy and also in the annealed $\text{Ti}_{0.4}\text{V}_{0.6}$ alloy but with very small amount). The presence of the edge dislocations in the present Ti-V alloys is inferred from the observed lining-up tendency of some dotted microstructures within the β phase matrix of these Ti-V alloys [37]. Similar to the grain boundaries, α phase boundaries and the edge dislocations are also two-dimensional in nature, and thereby can act as normal surface pins. In commensurate with the results of these structural investigations we find from our analysis on the field dependence of pinning force curves that the normal surface pins are indeed the major source of flux-line pinning mechanism in these alloys. We also find that the J_C values obtained in these Ti-V alloys have a correlation with the average grain size observed in these alloys. The as cast $\text{Ti}_{0.6}\text{V}_{0.4}$ alloy has the largest grain size. The J_C value in this alloy is also observed to be the lowest among all the as cast and annealed $\text{Ti}_x\text{V}_{1-x}$ alloys ($x = 0.4, 0.6, \text{ and } 0.7$). In the as cast and annealed $\text{Ti}_{0.7}\text{V}_{0.3}$ alloys, grains are observed to be smaller as compared to those in the other Ti-V alloys. The J_C values in the as cast and annealed $\text{Ti}_{0.7}\text{V}_{0.3}$ alloys are also observed to be the higher. However, we observe that the as cast $\text{Ti}_{0.7}\text{V}_{0.3}$ alloy has the highest J_C value though the average grain size in this alloy is observed to be larger than the average grain size of the annealed $\text{Ti}_{0.7}\text{V}_{0.3}$ alloy. This may be due to the presence of additional flux-line pinning mechanism in the as cast $\text{Ti}_{0.7}\text{V}_{0.3}$ alloy, probably provided by the edge dislocations whose presence in this alloy is indicated by the densely distributed dotted microstructures [please

see Fig. 3.3 (f) in chapter 3]. Moreover, the presence of substantial amount of α phase ($\sim 28\%$) in the annealed $\text{Ti}_{0.7}\text{V}_{0.3}$ alloy effectively reduces the volume fraction of the superconducting matrix for super-current flow, and thereby giving rise to a lower value of J_C in the annealed $\text{Ti}_{0.7}\text{V}_{0.3}$ alloy as compared to it as cast counterpart. On the other hand, the annealed and as cast $\text{Ti}_{0.4}\text{V}_{0.6}$ alloys have comparable grain size. Consequently, J_C values are found to be almost comparable in these alloys.

When analysing the experimental $f_P(h)$ curves of the present Ti-V alloys we have tried to fit the maximum possible portions of the $f_P(h)$ curves with the help of Dew-Hughes model. However, we were not successful in very low magnetic field regime where an additional source of magnetic irreversibility is observed. Such an additional hysteresis can appear from the surface barrier effects [26, 216, 217], and the irreversibility contributed by such effects is reported [216] to be quite similar to that contributed by flux-line pinning. We have obtained the evidence of the surface barrier effect in the present Ti-V alloys with the help of the so called minor hysteresis loop (MHL) technique [216]. We find that the MHL initiated from the field-increasing envelope magnetization curve touches the field-decreasing envelope magnetization curve following a nearly-linear path without showing any rounding-off behaviour, as is generally observed in presence of surface barrier effect [216].

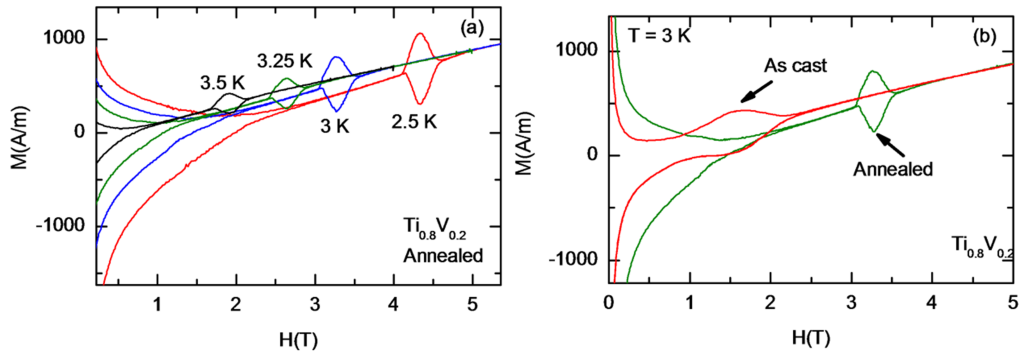


Figure 7.12: (a) The magnetic field dependence of magnetization at different temperatures to show the peak-effect in the annealed $\text{Ti}_{0.8}\text{V}_{0.2}$ alloy. (b) The magnetic field dependence of magnetization for the annealed and as cast $\text{Ti}_{0.8}\text{V}_{0.2}$ alloys, showing that the peak-effect at 3 K occurs in these two samples at different value of magnetic fields.

7.2.3 Peak-effect in the Ti-V alloys

All the annealed and as cast Ti-V alloys except annealed $\text{Ti}_{0.7}\text{V}_{0.3}$ alloy exhibit the peak-effect in the isothermal field dependence of magnetization. The peak-effect observed in the present Ti-V alloys exhibits the following characteristic features:

- (i) Magnetic irreversibility within the peak-effect region becomes larger as the temperature is lowered [Fig. 7.12(a)],
- (ii) The peak-effect shifts to higher magnetic field with decreasing temperature [Fig. 7.12(a)],
- (iii) The onset field for the peak-effect has a correlation with the magnitude of the pinning force density F_P in the region of main magnetic

irreversibility, and it is situated more closer to H_{C2} for the alloys having higher F_P value (in the region of main magnetic irreversibility) [Fig. 7.12(b)], and,

- (iv) The onset field of the peak-effect in the ascending-field cycle is higher than that in the descending-field cycle, as clearly shown in Fig. 7.13.

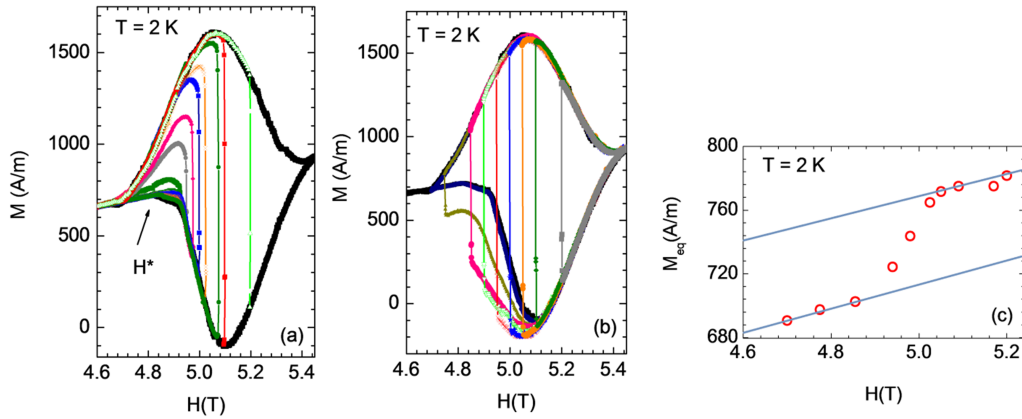


Figure 7.13: Construction of minor hysteresis loops (MHLs) within the peak-effect regime of the annealed $\text{Ti}_{0.8}\text{V}_{0.2}$ alloy. The thick black curves in (a) and (b) are the envelope magnetization curve. (c) The equilibrium magnetization (M_{eq}) of the same alloy at 2 K estimated from the MHLs.

The characteristic feature of the peak-effect outlined in point (iv) is also observed in CeRu_2 [218-224], 2H-NbSe_2 [225], V_3Si [226] superconductors etc., where the peak-effect is thought to be associated with a field-driven first-order phase transition in the flux-line lattice. In the high-field phase of the flux-line lattice, flux lines are pinned to the defect sites more easily, and thereby giving rise to the enhanced irreversible magnetization. In these

superconductors, the behaviour of the minor hysteresis loops (MHLs) within the peak-effect regime are quite anomalous, and are not in accordance with the predictions of Bean's critical state model [218-220, 225-227]. Here, we study the history effect of the magnetic irreversibility within and around the peak-effect regime of the present Ti-V samples. Starting from various points on the envelope $M(H)$ curve within the peak-effect regime, we constructed MHLs by decreasing magnetic field from the lower envelope $M(H)$ curve, and by increasing magnetic field from the upper envelope $M(H)$ curve. These results for annealed $\text{Ti}_{0.8}\text{V}_{0.2}$ sample are shown in Fig. 7.13. We observe that the MHLs initiated from the lower envelope $M(H)$ curve do not reach the upper envelope curve for magnetic fields lower than H_L which corresponds to the minimum observed in the lower envelope $M(H)$ curve in the peak-effect regime [Fig. 7.13(a)]. On the other hand, MHLs initiated from the upper envelope $M(H)$ curve in this field regime undershoot below the lower envelope $M(H)$ curve [Fig. 7.13(b)]. However, MHLs initiated from both the upper and lower envelope $M(H)$ curves in the field regime above H_L reach the opposite envelope $M(H)$ curves without showing any overshooting or undershooting. This observed behaviour of the magnetic hysteresis within the peak-effect regime are very similar to those reported in the references [218, 220, 225, 226, 228,229], and are known to be characteristic features related to the meta-stability (super heating/supercooling) associated with a first-order phase transition in the flux-line lattice [218, 220].

For further study on the first-order phase transition in the flux-line lat-

tice, we have estimated the equilibrium magnetization (M_{eq}) which is a thermodynamic quantity (M is not a proper thermodynamic quantity). M_{eq} is estimated from the end points of the MHLs as prescribed by Roy *et al.* [218]. Fig. 7.13(c) shows that there is a clear jump in the magnetic field dependence of M_{eq} inside the peak-effect regime, which again indicates a first-order nature of the phase transition taking place in the superconducting mixed state. We then estimate the latent heat (L) associate with this phase transition using the Clausius-Clapeyron relation: $L = T\Delta S = T\Delta M_{eq}(dH_{PE}/dT)$, where H_{PE} corresponds to the applied magnetic field for the onset of the peak-effect in increasing field branch [218]. The H_{PE} values at different temperatures were obtained from the experimental $M(H)$ curves, and the slope of the $H_{PE}(T)$ curve at 2 K was used to find L . At 2 K, the value of L for annealed $\text{Ti}_{0.8}\text{V}_{0.2}$ alloy comes out to be $\sim 35 \mu\text{J/g}$. In the annealed $\text{Ti}_{0.4}\text{V}_{0.6}$ alloy, L comes out to be $\sim 70 \mu\text{J/g}$ at 4 K (the related curves are not shown).

Thus, our magnetization measurements show that a first-order phase transition in the flux-line system of the present Ti-V alloys gives rise to the peak-effect in the field dependence of magnetization. Such a first-order phase transition may occur from different origins. Firstly, it is suggested on theoretical ground that a first-order phase transition in the flux-line system may arise due to the formation of the Fulde-Ferrel-Larkin-Ovchinnikov (FFLO) state in the high-field regime [230, 231], and has been considered as the possible explanation for the peak-effect in various superconductors [232-234]. However, the FFLO state is supposed to occur in extremely clean

and strongly Pauli limited type-II superconductors [218]. Although Ti-V alloys are strong Pauli limited superconductors, these alloys are dirty limit superconductors (refer to chapter 4), thereby discarding the possible existence of the FFLO state in the Ti-V alloy superconductors. Moreover, this approach cannot explain the different values of H_{PE} at a given temperature for the annealed and as cast $\text{Ti}_{0.8}\text{V}_{0.2}$ alloys, though the (intrinsic) properties of these samples in their normal state as well as superconducting state are quite similar.

In a second approach, a field-induced transition from the Abrikosov flux-line lattice to a softened flux-line lattice (before the actual melting of the flux-line lattice) is also considered as a first-order phase transition [235]. The softened flux lines at high field are easily pinned even at the weak pinning centres, giving rise to the peak-effect in the field dependence of magnetization curve. However, this approach also cannot explain why does the flux-line system in the annealed and as cast $\text{Ti}_{0.8}\text{V}_{0.2}$ alloys become soft at different values of field though the line tension energy $\varepsilon_0 = (\Phi_0/4\pi\lambda)^2 \ln\kappa$ is the same for both these alloys.

Finally, quenched disorders may also induce a phase transition in the flux-line system from a quasi-ordered Bragg-glass phase to a highly disordered vortex phase, and the possibility of a first-order nature of such a phase transition has been pointed out previously [236]. The disordered vortex phase is strongly pinned phase, giving rise to the peak-effect in the field dependence of magnetization at the order-disorder transition [226, 237-241]. We

have observed that the onset field for the peak-effect has a correlation with the magnitude of the pinning force density F_P in the region of main magnetic irreversibility at lower magnetic fields. Peak-effect occurs at relatively lower magnetic field for alloy having higher F_P value (in the region of main magnetic irreversibility). This indicates that the disorders have significant influence on the occurrence of the peak-effect in the present Ti-V alloys, and disorder driven order-disorder phase transition in the flux-line system might provide an explanation for the observed peak-effect in these alloys. A disorder driven order-disorder transition occurs when the elementary pinning force f_P becomes of the order of the Labusch force $f_{Lab} = \varepsilon_0 \xi / a_0$, where a_0 is the flux-line lattice constant [242]. Since $a_0 = (\Phi_0 / H)^{1/2}$, the expression of the field value at which the disorder-driven order-disorder transition and hence the peak-effect will occur, can be written as $H_{PE} \sim \Phi_0 (f_P / \varepsilon_0 \xi)^2$. Since the superconducting parameters have same values in the annealed and as cast samples of the $\text{Ti}_{0.8}\text{V}_{0.2}$ alloy, we may write for these samples $H_{PE} \propto f_P^2$, i.e., H_{PE} depends strongly on the elementary pinning force f_P . As compared to the annealed $\text{Ti}_{0.8}\text{V}_{0.2}$ alloy, the as cast $\text{Ti}_{0.8}\text{V}_{0.2}$ alloy is expected to have relatively lower value of f_P due to the lower defect density in this alloy (a relatively smaller amount of ω phase is present in the as cast $\text{Ti}_{0.8}\text{V}_{0.2}$ alloy, refer to chapter 3), and thereby resulting in a relatively lower value of H_{PE} for the as cast $\text{Ti}_{0.8}\text{V}_{0.2}$ alloy. This observation clearly indicates that a disorder-driven phase transition in the flux-line system seems to be a plausible mechanism giving rise to the peak-effect in the present Ti-V alloys.

7.3 Summary and conclusions

- (i) The magnetization in the Ti-V alloys was found to be irreversible with respect to increasing and decreasing magnetic fields below an irreversibility field H_{Irr} which is distinctly different from the upper critical field H_{C2} of these alloys.
- (ii) Analysis of the field dependence of the pinning force density in combination with the XRD and optical metallography studies indicate that both the grain boundaries in the main β phase matrix and dislocation arrays whose presence is indicated by the lining-up of etched pits on the β phase matrix [37], act as surface pins for the flux lines. The surface pins are mainly responsible for the critical current density in the as cast and annealed Ti_xV_{1-x} alloys with $x = 0.4, 0.6,$ and 0.7 and also in the as cast $Ti_{0.8}V_{0.2}$ alloy.
- (iii) The pinning force density in the annealed $Ti_{0.8}V_{0.2}$ alloy originates mainly from the flux-line pinning at normal point pins. The ω phase precipitates present in this alloy act the as normal point pins. However, in lower magnetic field regime, flux-line pinning is provided by the surface pins such as grain boundaries.
- (iv) Except for the annealed $Ti_{0.7}V_{0.3}$ alloy, all the annealed and as cast Ti-V alloys exhibit peak-effect in the field dependence of magnetization. Within the peak-effect regime, irreversible magnetization of these Ti-

V alloys shows history effect, which are known to be characteristic features related to the meta-stability (super heating/supercooling) associated with a first-order phase transition in the flux-line system [218, 220]. Magnetic field dependence of equilibrium magnetization (M_{eq}) estimated from the minor-hysteresis-loops (MHLs), shows a clear jump in the peak-effect regime, which again indicates the first-order nature of the phase transition taking place in the flux-line system. We suggest that a disorders-driven ordered-disordered phase transition in the flux-line system is the origin of the first-order phase transition, which in turn gives rise to the peak-effect in the present Ti-V alloys.

Chapter 8

Bose-glass to vortex-liquid phase transition in the vortex state of the annealed $\text{Ti}_{0.7}\text{V}_{0.3}$ alloy

8.1 Introduction

In type-II superconductors, magnetic field penetrates the bulk of the material in the form of superconducting vortices or flux lines when the applied magnetic field is higher than the lower critical field H_{C1} . In defect free type-II superconductors, the repulsive interaction among the flux lines tend to drive the flux lines to get them arranged in a hexagonal array called the Abrikosov lattice [22]. The existence of such an ordered Abrikosov lattice has been observed in the superconducting mixed state of clean Nb samples through neutron scattering experiment [243, 244]. However, flux-line pinning at quenched disorders can prevent the emergence of the long-range order of the Abrikosov lattice [32]. The weak random pinning of the flux lines perturbs the transla-

tional invariance of the Abrikosov lattice, giving a quasi-ordered Bragg-glass phase which has been observed experimentally in the mixed state of several type-II superconductors [33-37]. On the other hand, strong pinning of the flux lines gives rise to the formation of the disordered vortex-glass [38, 39] or the Bose-glass phase [40, 41] depending on the nature and strength of the quenched disorders present in a sample. Generally, a vortex-glass phase exists in disordered materials involving point disorders while a Bose-glass phase is observed in materials with correlated disorders like grain boundaries and/or twin boundaries, and/or heavy ion-induced columnar tracks [245, 246]. The vortex-glass phase continues to exist up to the glass transition temperature T_G , where it transforms into a vortex-liquid through a second order phase transition [38]. In theoretical ground [38-41], it was predicted that when the temperature is increased toward T_G , electrical resistivity in the vortex-liquid phase vanishes following a power law relation $\rho \propto |T - T_G|^s$, where s is the critical exponent of the glass transition. For high- T_C superconductors, T_G is generally found to be substantially lower than the superconducting transition temperature T_C due to the relatively soft vortex matter and the enhanced role of thermal fluctuations in these materials [38]. Consequently, for high- T_C superconductors, an appreciable temperature regime exists between the $T_G(H)$ - and $T_C(H)$ -line, where the description of the vortex-glass transition in term of vortex-liquid resistivity is possible [39]. Therefore, the study of the resistive transition in the presence of magnetic field continues to be an active experimental method for investigating vortex-glass transition in high- T_C

superconductors.

Generally, thermal fluctuations are less effective in bulk low- T_C superconductors, causing the $T_G(H)$ -line to lie very close to the $T_C(H)$ -line. Consequently, it is not possible to study of the vortex-glass transition in bulk low- T_C superconductors through resistive transition measurements. Ideally, one has to rely on the small-angle neutron scattering (SANS), and/or scanning tunnelling microscopy (STM) and/or Bitter decoration (BD) for observing the vortex-glass phase in bulk low- T_C superconductors. Though the experiment felicities like STM and BD can be useful for the real space imaging of the vortex-glass phase and SANS for mapping of the vortex-glass phase in reciprocal space, the dynamical nature of the vortex-glass phase remains completely unrevealed in these experiments. Experimental study of the vortex-glass phase in bulk low- T_C superconductors through resistive transition measurement is therefore necessary for a comparative study of the vortex-glass phase in low- T_C and high- T_C superconductors, and also in the point of view of the dynamical nature of the vortex-glass phase in a bulk low- T_C superconductor. Dimitriv *et al.* [37] have recently found the existence of the Bragg-glass phase in the mixed state of a disordered $\text{Ti}_{0.21}\text{V}_{0.79}$ superconductor through SANS experiments. In Ti-V alloy system, the amount of disorder is enhanced significantly with increasing Ti concentration because of the formation of the ω phase and the martensite α or α' phase within the major β phase matrix of these alloys [42, 51]. In chapter 3, we have found that the above mentioned secondary phases are indeed present in the

samples of $\text{Ti}_{0.8}\text{V}_{0.2}$ and $\text{Ti}_{0.7}\text{V}_{0.3}$ alloys. Hence, the presence of a highly disordered vortex-glass and/or Bose-glass phase is likely in the Ti-rich Ti-V alloys. Moreover, we have found in the previous chapters that the thermal fluctuations become increasingly important in Ti-rich Ti-V alloys. This gives rise to an appreciable magnetic field-temperature regime between the $H_{C2}(T)$ - and $H_{Irr}(T)$ -line [$T_G(H)$ -line is equivalent to $H_{Irr}(T)$ -line], where a vortex-liquid phase exists with non-ohmic resistivity [39]. We have therefore explored the possibility of such vortex-liquid to vortex-glass phase transition in Ti-rich Ti-V alloys through electrical resistivity measurements, and indeed observed the signatures of the stated phase transition in the sample of annealed $\text{Ti}_{0.7}\text{V}_{0.3}$ alloy. These results are presented in this chapter.

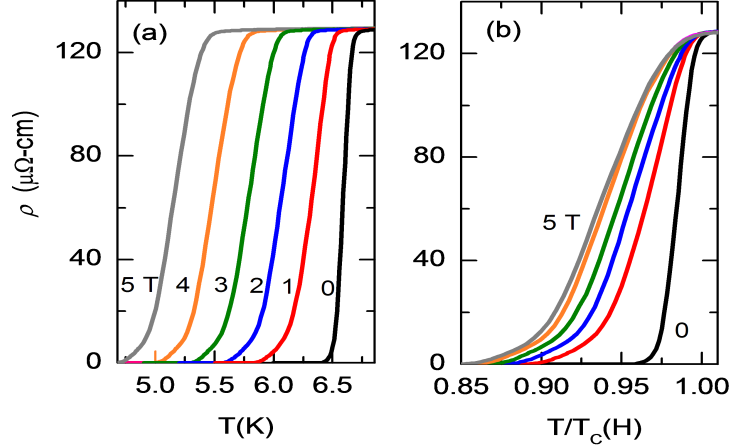


Figure 8.1: (a) Temperature dependence of electrical resistivity of annealed $\text{Ti}_{0.7}\text{V}_{0.3}$ sample measured at low temperatures and in different magnetic fields. (b) The same curves plotted in a reduced temperature scale to highlight the field induced broadening of the superconducting transition.

8.2 Results and discussion

8.2.1 Temperature dependence of electrical resistivity in different constant magnetic fields: Evidence of a glass to liquid phase transition in the flux-line system of the annealed $\text{Ti}_{0.7}\text{V}_{0.3}$ sample

Fig. 8.1 (a) shows the temperature dependence of resistivity ρ measured for the annealed $\text{Ti}_{0.7}\text{V}_{0.3}$ sample at low temperatures and in the presence of various constant applied magnetic fields ranging from zero to 5 T. In zero magnetic field, the sample enters into the superconducting state at the superconducting transition temperature $T_C = 6.69$ K with a transition broadening of $\Delta T_C \sim 0.14$ K. Here, T_C is defined as the temperature at which a steep increase in the temperature derivative of ρ first appears on the higher temperature side. The superconducting transition broadening ΔT_C is defined as the temperature interval where resistivity drops from 90 % to 10 % of its the normal state value across the superconducting transition. In the presence of magnetic field, T_C shifts to lower temperatures and the superconducting transition becomes more broadened. This latter effect is clearly visible in Fig. 8.1 (b), where the resistivity is plotted against the reduced temperature $t = T/T_C(H)$. It is well known that the broadening of the superconducting transition in the presence of magnetic field could be resulted from thermally-activated-flux-flow (TAFF). The temperature dependence of resistivity in such a case is generally analysed with the help of the Arrhenius relation given as [249]

$$\rho(T, H) = \rho_0 \exp \left[-\frac{U(T, H)}{k_B T} \right], \quad (8.1)$$

where, k_B is the Boltzmann constant, ρ_0 is a pre-exponential factor (constant), and $U(T, H)$ is the activation energy associated with the flux-flow. The Arrhenius plots ($\ln \rho$ versus T^{-1} plots) in different applied magnetic fields are shown in Fig. 8.2 (a). It can be seen from this figure that except at temperatures in the close vicinity of T_C , the Arrhenius plots are linear down to a characteristic temperature T^* , indicating that the observed magnetic field-induced broadening of the resistive transition is caused by the TAFF at temperatures above T^* . At temperatures below T^* , the Arrhenius plots deviate from showing the linear behaviour and exhibits a strong downward bend. This suggests that the activation energy for flux motion increases more rapidly at temperatures below T^* than in the TAFF regime. This becomes more evident in Fig. 8.2 (b), where we present the plots of the function $F [= -d(\ln \rho)/dT^{-1}]$ against temperature for different values of the applied magnetic field. According to the Arrhenius relation, the function F is proportional to the activation energy U . It can be seen from this figure that the activation energy tends to diverge as the temperature is decreased below T^* . Such a diverging behaviour of the activation energy at low temperatures has previously been observed in many high- T_C superconductors and is attributed to a crossover to a critical region associated with the vortex-liquid to vortex-glass phase transition [250-253].

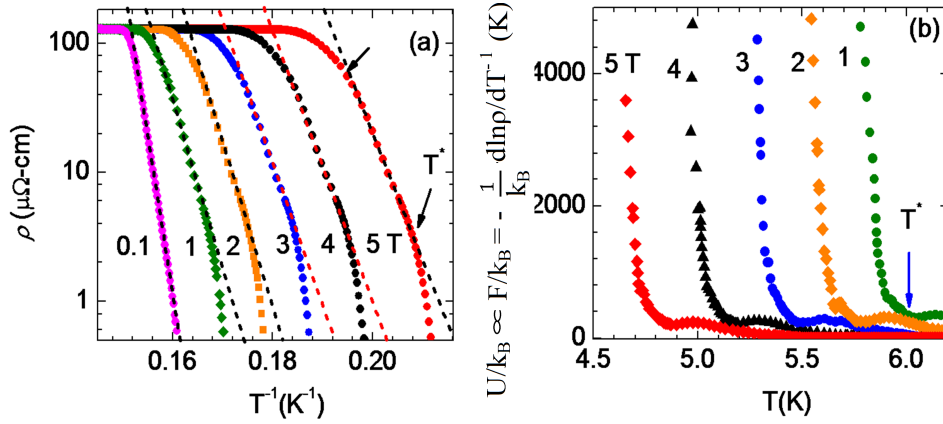


Figure 8.2: (a) The Arrhenius plots obtained for the annealed $\text{Ti}_{0.7}\text{V}_{0.3}$ sample in different magnetic fields. These plots exhibit a change of slope at the characteristic temperature T^* . (b) Temperature dependence of the activation energy U for this sample in various constant magnetic fields.

Following the power law relation $\rho \propto |T - T_G|^s$ for the vortex-liquid resistivity, one can expect the plot of the inverse of the logarithmic derivative of resistivity $[d(\ln\rho)/dT]^{-1}$ against T to be linear in the critical region of the vortex-liquid to vortex-glass transition. In Fig. 8.3, the plots of $[d(\ln\rho)/dT]^{-1}$ against temperature are shown for the annealed $\text{Ti}_{0.7}\text{V}_{0.3}$ sample for 0.5 and 5 T applied magnetic fields. In agreement with the theory, these plots are linear at temperatures below T^* , indicating the existence of a glassy vortex phase in this sample at temperatures below T_G . We then estimate the T_G using the Vogel-Fulcher relation: $[d(\ln\rho)/dT]^{-1} = (T - T_G)/s$ [254-256]. According to this relation, T_G is obtained by finding the temperature where the linear portion of $[d(\ln\rho)/dT]^{-1}$ versus T plot extrapolates to $[d(\ln\rho)/dT]^{-1} = 0$. Additionally, the critical exponent s at different applied

magnetic fields is estimated from the inverse of the slope of the linear section of these plots, and is shown in Fig. 8.4 (a). The value of s is found to be ~ 1.8 , and is almost independent of magnetic field. This value is smaller than the values of $s \sim 6-8$ generally obtained in the vortex-liquid to vortex-glass phase transition in several high- T_C superconductors where point disorders act as the major flux-line pinning centres [254, 257]. However, similar small values of s as estimated for the present sample have been obtained for phase transition from vortex-liquid to Bose-glass in materials involving correlated disorders, such as twined $\text{YBa}_2\text{Cu}_3\text{O}_{7-\delta}$ ($s \sim 2$) [254, 258] and YBCO with columnar defects ($s \sim 2.4$) [259].

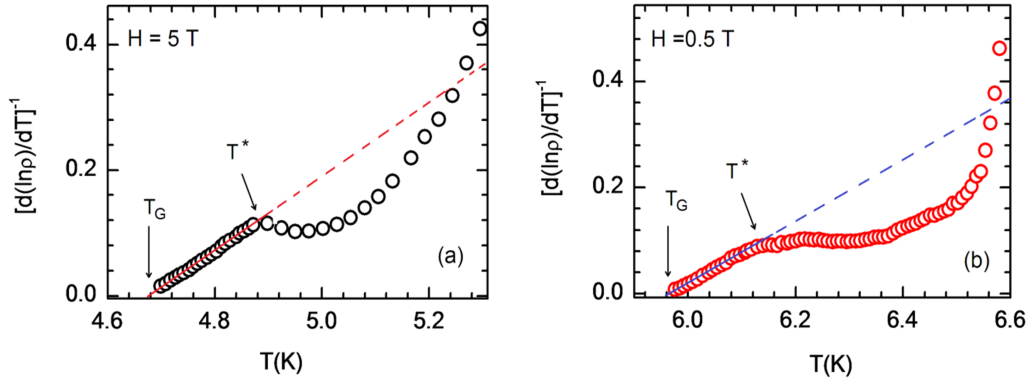


Figure 8.3: The plots of $[d(\ln\rho)/dT]^{-1}$ against temperature for the annealed $\text{Ti}_{0.7}\text{V}_{0.3}$ sample for 5 and 0.5 T magnetic fields.

We present in Fig. 8.4 (b)-(d) few selected micrographs obtained in scanning electron microscopy (SEM) and optical metallography experiments on the annealed samples of the $\text{Ti}_{0.7}\text{V}_{0.3}$ alloy. These micrographs reveal that the crystal disorders which can lead to the flux-line pinning in the present

sample consist of mainly grain boundaries and martensitic α phase. The X-ray diffraction result indicates that the amount of the martensitic α phase in this alloy is about 28 % (refer to chapter 3). These extended disorders are correlated over mesoscopic length scales, and the presence of these correlated disorders gives rise to the Bose-glass phase in the annealed $\text{Ti}_{0.7}\text{V}_{0.3}$ sample, which is consistence with the estimate of the low value of the critical exponent s for this sample.

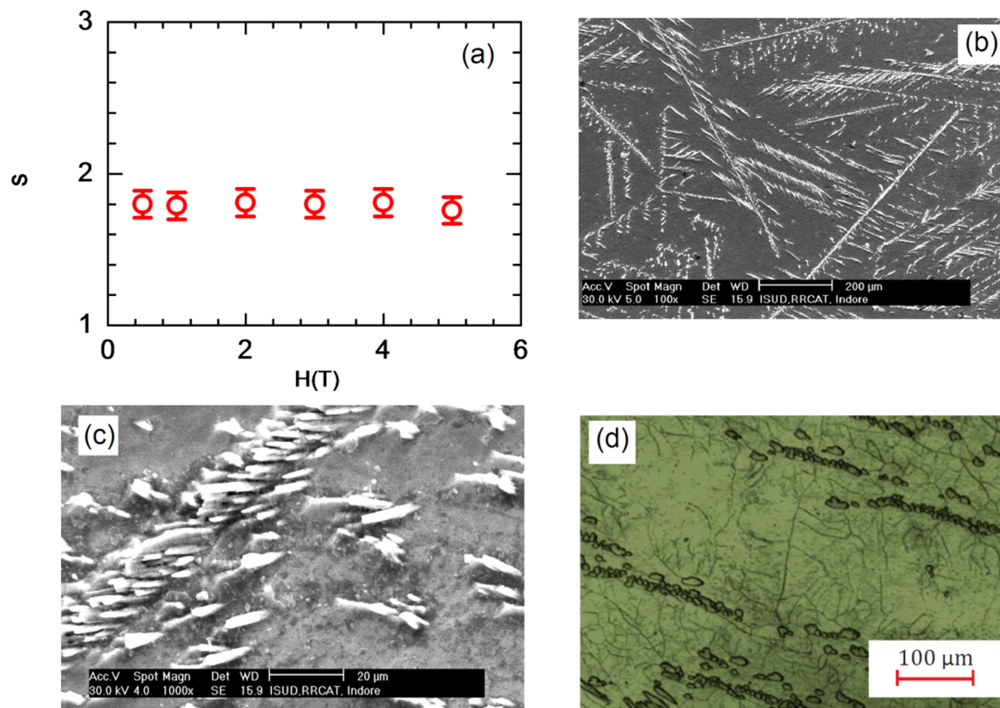


Figure 8.4: (a) Critical exponent s for the annealed $\text{Ti}_{0.7}\text{V}_{0.3}$ sample in various magnetic fields. (b), (c) SEM images of this sample showing the presence of martensite α phase in the main β phase matrix this sample. (d) Optical micrograph showing the grain structures in this sample.

8.2.2 The modified vortex-glass model

In the previous section, we have obtained the experimental evidence for the existence of a glassy vortex phase in the mixed state of annealed $\text{Ti}_{0.7}\text{V}_{0.3}$ sample based on the prediction of the vortex-glass theory [38-41]. Recent works [247, 248] have made modification in the vortex-glass theory to give a consistent description of vortex-liquid resistivity in the critical region of the vortex-liquid to vortex-glass transition in the high- T_C oxide superconductors. This modified vortex-glass model has been extensively used in the recent times to ascertain both the vortex-liquid to vortex-glass as well as the vortex-liquid to Bose-glass transition in various high- T_C oxide and Fe-based superconductors [247, 248, 255, 256, 260-263]. This modified vortex-glass model takes the effective pinning energy U_0 into consideration while analysing the vortex-liquid to vortex-glass transition. This is done by replacing the temperature difference $(T - T_C)$ by an energy difference $(k_B T - U_0)$. In this model the temperature dependence of resistivity in the critical region of vortex-liquid to vortex-glass transition is expressed as: [247, 248]

$$\rho(T) = \rho_n \left| \frac{k_B T}{U_0(H, T)} - 1 \right|^s. \quad (8.2)$$

The modified vortex-glass model assumes an empirical effective pinning energy $U_0(H, T)$ for the high- T_C oxide superconductors, which has the form [247, 248]

$$U_0(H, T) = U_H \left[1 - \frac{T}{T_C} \right]; U_H = k_B T_C H^{-\beta}. \quad (8.3)$$

In the above relation, U_H is a function of field only and β is a constant independent of temperature and magnetic field. The model also assumes that the transition from vortex-liquid to vortex-glass occurs at T_G , where the thermal energy becomes equal to the pinning energy, i.e., $U_0(H, T_G) = k_B T_G$. With this assumption the magnetic field dependent part of $U_0(H, T)$ in Eqn. (8.3) is obtained as a unique function of T_G as

$$U_H(H) = \frac{k_B T_C T_G}{T_C - T_G}. \quad (8.4)$$

Using the above form of $U_H(H)$, the empirical pinning energy given in Eqn. (8.3) is then reformulated as:

$$U_0(H, T) = \frac{k_B T_G \left[1 - \frac{T}{T_C} \right]}{\left[1 - \frac{T_G}{T_C} \right]}. \quad (8.5)$$

When the effective pinning energy given in Eqn. (8.5) is substituted back in Eqn. (8.2), the expression for the temperature dependence of resistivity in the critical region associated with the vortex-liquid to vortex-glass transition is obtained as

$$\rho(H, T) = \rho_n \left| \frac{T(T_C - T_G)}{T_G(T_C - T)} - 1 \right|^s. \quad (8.6)$$

The resistivity given in Eqn. (8.6) depends on the magnetic field explicitly through the field dependence of T_G . Eqn. (8.6) predicts a scaling behaviour between the normalized resistivity ρ/ρ_n and the scaling temperature

$T_S = [T(T_C - T_G)/T_G(T_C - T) - 1]$ in the critical region of the vortex-liquid to vortex-glass transition [247, 248]. Such a scaling behaviour between ρ/ρ_n and T_S has been found to exist in various disordered high- T_C superconductors such as YBCO single crystals [247, 248], Ho-doped (Bi, Pb)-2212 [255], BaFe₂As₂ single crystal [256], Ba_{0.55}K_{0.45}Fe₂As₂ [262], and C⁴⁺-irradiated BaFe_{0.19}Ni_{0.1}As₂ single crystal [263] etc., and this scaling behaviour has been used to estimate the critical exponent s of the vortex-glass phase transition in these materials. Another important aspect of the modified vortex-glass model is that it provides consistent description of the effective pinning energy U_0 in the critical region of the vortex-glass transition. The effective pinning energy U_0 is important for the understanding of the flux-line pinning properties of a superconductor. We shall now use this modified vortex-glass model to study the vortex-liquid to Bose-glass transition in the annealed Ti_{0.7}V_{0.3} sample.

8.2.3 Temperature and field dependence of effective pinning energy

In the modified vortex-glass model, temperature and field dependence of $U_0(H, T)$ may be obtained from Eqn. (8.2) as

$$U_0(H, T) = k_B T \left[1 - \left(\frac{\rho}{\rho_n} \right)^{\frac{1}{s}} \right], \quad (8.7)$$

provided s and ρ_n are known. The values of $U_0(H, T)$ are estimated using Eqn. (8.7) for the annealed Ti_{0.7}V_{0.3} sample. For the estimation of $U_0(H, T)$,

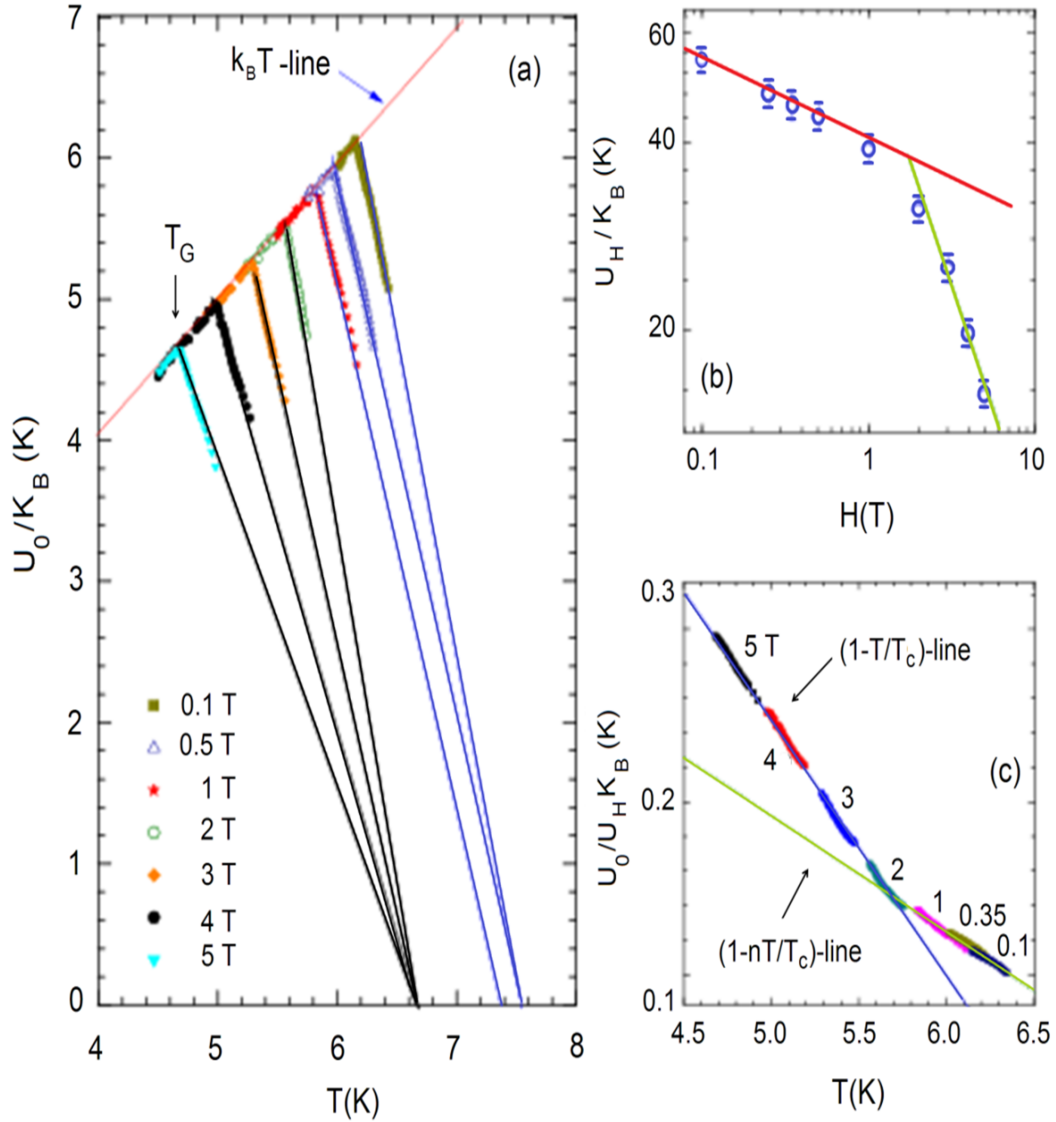


Figure 8.5: Temperature dependence of the effective pinning energy U_0 for the annealed $\text{Ti}_{0.7}\text{V}_{0.3}$ sample in different magnetic fields. (b) The field dependence of U_H of the same sample, which is calculated using Eqn. (8.4). (c) The $U_0(H, T)/U_H$ versus T curves showing the temperature dependent part of the pinning energy.

we have taken ρ_n as the resistivity value measured at 15 K, and we have used the values of s presented in Fig. 8.4 (a). The estimated values of U_0 in different magnetic fields are shown as a function of temperature in Fig. 8.5 (a). Only the data points within the critical region of the vortex-liquid to Bose-glass transition, i.e. in the temperature regime $T_G \leq T \leq T^*$, are shown here for the sake of clarity. In this figure, it is observed that these $U_0(H, T)$ curves exhibit linear temperature dependence. In the modified vortex-glass model, T_G value is determined from the point of intersection between the $U_0(H, T)$ curve and the $k_B T$ -line as indicated in Fig. 8.5 (a) [247, 248, 255, 256]. T_G values determined at various magnetic fields using this procedure match with those determined in the previous section. For $H \geq 2$ T, the straight lines obtained from the extrapolation of these linear $U_0(H, T)$ curves meet at a common point $T = T_C$, where U_0 becomes zero. This confirms that for $H \geq 2$ T, U_0 in the critical region does vary with temperature following $(1 - T/T_C)$ dependence. However, for $H < 1$ T, we find that the straight lines obtained by the extrapolation of these linear $U_0(H, T)$ curves meet at a common point $T \sim 7.56$ K on $U_0(H, T) = 0$ line. On the other hand, for $H = 1$ T, this extrapolated straight line meets $U_0(H, T) = 0$ line at a temperature slightly higher than T_C but lower than 7.56 K. These experimental facts indicate that for $H < 2$ T, U_0 in the critical region varies with temperature following a temperature dependence other than $(1 - T/T_C)$ law.

In order to find out the exact temperature dependence of U_0 in the applied magnetic field regime $H < 2$ T, we compare the experimental $U_0(H, T)$ data

for the present $\text{Ti}_{0.7}\text{V}_{0.3}$ sample with the more general expression of $U_0(H, T)$ given as $U_0(H, T) = U_H(1 - T/T_C)^{n(H)}$, where the values of n depends on the dimensionality of the flux-line system [264]. In the present case, we find that n is unity for $H \geq 2$ T while it assumes some values other than unity for $H < 2$ T. Binomial expansion of the above form of effective pinning energy gives $U_0(H, T) \sim U_H[1 - n(H)T/T_C] + D(T/T_C)$. Here, the term $D(T/T_C)$ represents the deviation from the linear behaviour of $U_0(H, T)$, which arises from the higher order term in (T/T_C) . However, the observed linearity of the $U_0(H, T)$ curves for $H < 2$ T suggests that the term $D(T/T_C)$ can be considered to be negligible in the present case. Therefore, we may write $U_0(H, T) \sim U_H[1 - n(H)T/T_C]$. Then the extrapolated $U_0(H, T)$ curves will give a threshold at $T = T_C/n(H)$. $U_0(H, T)$ curves for $H < 1$ T give a threshold at 7.56 K, which implies $n \sim 0.87$ in this magnetic field regime.

For $H \geq 2$ T, we can estimate the U_H values in different magnetic fields from the slope of the linear $U_0(H, T)$ curves (the slope being $-U_H/T_C$). Alternatively, we can also estimate U_H from Eqn. (8.4) using the experimentally obtained value of T_G . We find that the U_H values estimated using both these procedures nicely agree with each other. On the other hand, for $H < 2$ T, the slope of the linear $U_0(H, T)$ curves is $-nU_H/T_C$. Hence, the values of U_H for $H < 2$ T can be determined from the slope of the linear $U_0(H, T)$ curve and the corresponding n value. The alternative route for finding U_H for $H < 2$ T is obtained from the fact that in the modified vortex-glass model, the glass transition temperature T_G is defined as $k_B T_G = U_0(H, T_G)$.

Since $U_0(H, T_G) = U_H(1 - T_G/T_C)^{n(H)} = k_B T_G$ for $H < 2$ T, we can write $U_H = k_B T_G / (1 - T_G/T_C)^{n(H)}$. Therefore, the values of U_H at different magnetic fields below 2 T can be estimated from the corresponding values of T_G and n using the above relation. A good agreement is obtained between the values of U_H estimated using these two procedures, indicating that the values of $n(H)$ obtained previously are quite reasonable.

In Fig. 8.5 (b), we present the magnetic field dependence of U_H in *log-log* scales covering the magnetic field range $0.1 \leq H \leq 5$ T. In this figure, we observed that $U_H(H)$ exhibits a power law relation $U_H(H) \propto H^{-0.13}$ for $H \leq 1$ T. On the other hand, the field dependence of U_H can be roughly described by another power law relation $U_H(H) \propto H^{-0.8}$ for $H \geq 2$ T. Having obtained the field dependence of U_H from our experimental data, we are now in a position to extract the temperature dependent part of $U_0(H, T)$ as $U_T(T) = U_0(H, T)/U_H$, and is shown in Fig. 8.5 (c). This figure shows a linear relationship in $U_0(H, T)/U_H$ versus T curves. For $H \geq 2$ T, these curves fall onto the $(1 - T/T_C)$ -line. On the other hand, the corresponding curves for $H \leq 1$ T fall onto the $(1 - 0.87T/T_C)$ -line. These observations are consistent with our inferences made above.

8.2.4 Scaling of the vortex-liquid resistivity

We now look into the scaling behaviour of the ρ/ρ_n versus T_S curves for the annealed $\text{Ti}_{0.7}\text{V}_{0.3}$ sample in the light of the above discussion. We have observed that, for $H \geq 2$ T, $U_0(H, T)$ in the critical region of the vortex-

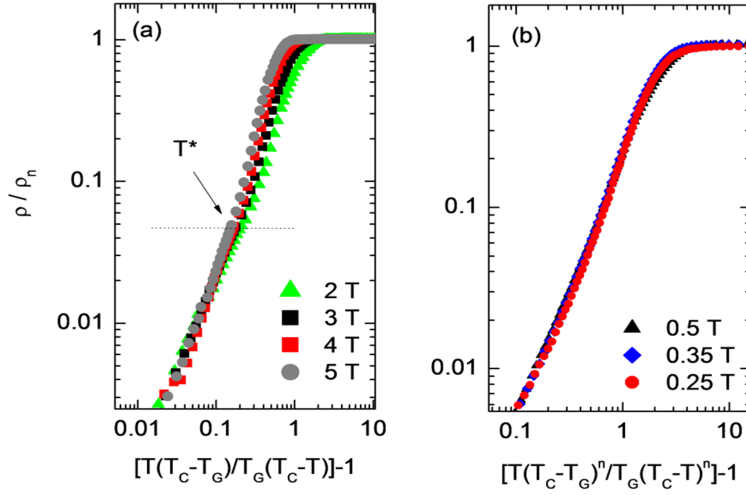


Figure 8.6: The *log-log* plots of normalized resistivity against the scaling temperature for the annealed $\text{Ti}_{0.7}\text{V}_{0.3}$ sample. For $H \geq 2$ T, we use the scaling temperature proposed in Ref. [247] while for low magnetic field regime we use the scaling temperature derived by us (see the relevant text).

liquid to Bose-glass transition follows the empirical relation given in Eqn. (8.3). Consequently, the ρ/ρ_n versus T_S curves for $H \geq 2$ T overlap with each other in the critical region of Bose-glass transition, i.e. in the temperature regime $T_G \leq T \leq T^*$. This is shown in Fig. 8.6 (a). For $H < 2$ T, both the magnetic field and temperature dependence of $U_0(H, T)$ is different from that observed for $H \geq 2$ T. Consequently, the ρ/ρ_n versus T_S curves for $H < 2$ T do not scale with each other and also with the corresponding curves for $H \geq 2$. However, for $H < 1$ T, it is found that U_0 varies with temperature as $U_0(T) \propto (1 - T/T_C)^n$, where $n \sim 0.87$. Moreover, in this magnetic field regime, the magnetic field dependent part of $U_0(H, T)$ can be obtained in term of T_G as: $U_H = k_B T_G / (1 - T_G/T_C)^n$. Hence, the overall effective pinning energy in

this magnetic field regime can be expressed as

$$U_0(H, T) = U_H(H) \left[1 - \frac{T}{T_C}\right]^n = \frac{k_B T_G \left[1 - \frac{T}{T_C}\right]^n}{\left[1 - \frac{T_G}{T_C}\right]^n}. \quad (8.8)$$

This relation for $U_0(H, T)$ is evidently different from one given in Eqn. (8.5), and accordingly, the scaling relation between ρ/ρ_n and the scaling temperature will also be different for $H < 1$ T. Substituting Eqn. (8.8) in Eqn. (8.2), we obtain the temperature and magnetic field dependence of resistivity in the critical region of the Bose-glass transition as

$$\rho(H, T) = \rho_n \left| \frac{T \left[1 - \frac{T_G}{T_C}\right]^n}{T_G \left[1 - \frac{T}{T_C}\right]^n} - 1 \right|^s. \quad (8.9)$$

Eqn. (8.9) predicts a scaling behaviour between the normalized resistivity ρ/ρ_n and a modified scaling temperature $T'_S = [T(T_C - T_G)^n / T_G(T_C - T)^n - 1]$. In agreement with this, a good scaling behaviour between ρ/ρ_n and T'_S is obtained for $H < 1$ T, and these scaled curves are shown in Fig. 8.6 (b). In the modified vortex-glass model, the critical exponent s is determined from the slope of these scaled curves. In this method, the value of s comes out to be ~ 1.7 , which is close to the value obtained in Sec. 8.2. Hence, we have found that the scaling behaviour of the electrical resistivity in the critical region of vortex-liquid to Bose-glass transition remains valid in annealed $\text{Ti}_{0.7}\text{V}_{0.3}$ sample. Since both temperature and magnetic field dependence of $U_0(H, T)$

in the annealed $\text{Ti}_{0.7}\text{V}_{0.3}$ sample are distinctly different in the magnetic field regimes below and above 2 T, the scaling behaviour of the resistivity are also found to be different in these magnetic field regimes.

8.2.5 Vortex matter phase diagram

The field-temperature ($H - T$) phase diagram for the annealed $\text{Ti}_{0.7}\text{V}_{0.3}$ sample is shown in Fig. 8.7. In this phase diagram, $T_G(H)$ -, $T_C(H)$ -, and $H_{Irr}(T)$ -line respectively represent the glass transition line, the upper critical field line and the irreversibility field line. $T_G(H)$ -line and $T_C(H)$ -line [or equivalently $H_{C2}(T)$ -line] are constructed from the $\rho(T)$ curves in various applied magnetic fields, and the procedures employed to determine T_C and T_G have been discussed above. The irreversibility field H_{Irr} is determined from the field dependence of magnetically measured critical current density J_C for this sample using a criterion that J_C falls to zero (within the limit of experimental accuracy) at H_{Irr} . In this phase diagram, both $T_G(H)$ -line and $H_{Irr}(T)$ -line lie distinctly below the $T_C(H)$ -line. Since both $T_G(H)$ -line obtained from resistivity measurements and $H_{Irr}(T)$ -line obtained from magnetic measurements represent the magnetic field limit up to which a superconductor can carry currents without dissipation, they should coincide with each other, and this is indeed observed for $H \geq 2$ T. However, for $H < 2$ T, $T_G(H)$ -line splits strongly away from the $H_{Irr}(T)$ -line towards lower temperatures. Consequently, there exists a finite magnetic field and temperature region between $T_G(H)$ -line and $H_{Irr}(T)$ -line, where finite role of flux-line

pinning still survives. We have also found that both temperature and field dependences of U_0 in this sample undergo a change of behaviour at almost the same magnetic field value where the splitting of the $T_G(H)$ -line from the $H_{Irr}(T)$ -line starts to occur, and thereby suggesting a common origin for all of these observed phenomena. In the following sections we will investigate for the probable origin leading to these observed phenomena.

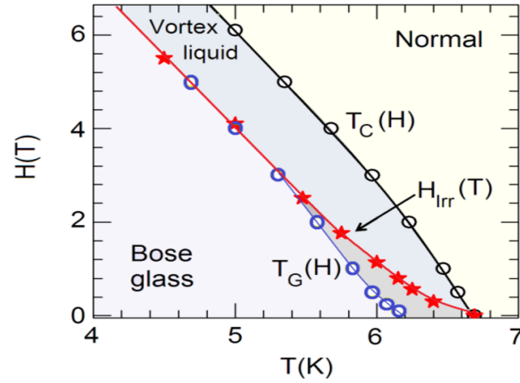


Figure 8.7: The field-temperature ($H - T$) phase diagram for the annealed $\text{Ti}_{0.7}\text{V}_{0.3}$ sample

8.2.6 Crossover from individual flux-line pinning to collective pinning regime and its manifestations

The weak magnetic field dependence of U_0 observed in low magnetic fields suggests that individual pinning of the flux lines co-exists with the collective flux-creep phenomenon in this magnetic field regime [265]. For higher applied magnetic fields, the flux lines are very large in number, and hence, the flux-line spacing becomes significantly smaller than the magnetic field

penetration depth. In such case, we expect, particularly in the high- κ materials like Ti-V alloys, a crossover to a new kind of pinning regime due to collective behaviour of the flux lines, where U_0 becomes strongly dependent on magnetic field [210]. Qualitatively very similar change of behaviour of the field dependences of U_0 is also observed in various superconductors such as BaFe₂As₂ single crystal [256], Fe_{1+y}(Te_{1+x}S_x)_z [266], Nd(O,F-)FeAs single crystal [267] superconductors etc. Due to the collective behaviour of the flux lines in higher magnetic field, the entire flux-line system will undergo a phase transition from Bose-glass to vortex-liquid at T_G . Since flux-line pinning and hence J_C vanishes within the vortex-liquid phase, $T_G(H)$ -line will be identical to $H_{Irr}(T)$ -line, and this is indeed observed for $H \geq 2$ T.

However, in low magnetic field regime, the collective behaviour among the flux lines becomes weak. In such case, when the flux-line system undergoes a phase transition from Bose-glass to vortex-liquid phase, few flux lines may still be remained pinned at some stronger pinning sites available in the sample via the individual flux-line pinning mechanism, which is consistent with the observed slow variation of $U_H(H)$ in this magnetic field regime. Hence, in low magnetic field regime, J_C may not vanish at $T_G(H)$ -line due to the existence of individual pinning of few flux lines at temperatures above T_G . However, the line tension of these pinned flux lines will eventually vanish at $H_{Irr}(T)$ -line [25], and thereby the pinned flux lines above the $T_G(H)$ -line will be capable of escaping from the pinning sites to give rise to a zero pinning state of the sample at and above the $H_{Irr}(T)$ -line. Hence, in the $H - T$ phase

diagram, $T_G(H)$ -line will be located below the $H_{Irr}(T)$ -line in low magnetic field regime. This is what we observe in Fig. 8.7. Based on this argument, we will now explain the change of behaviour of the temperature dependence of U_0 observed below and above a crossover magnetic field $H_D \sim 2$ T.

In the case of the extended defect such as grain boundaries and martensitic α phase, the effective pinning energy U_0 arises from the loss of condensation energy within the generalized pinning volume, and is expressed as $U_0(T, H) \propto H_C(T)^2 \xi(T) 2l_P$ [268]. Here, H_C is the thermodynamic critical field, ξ is the coherence length, and l_P is the length of pinning sites along the direction of the applied magnetic field. Thus, the temperature dependence of H_C and ξ governs the temperature dependence of U_0 . Since $\xi(T) \propto (1 - T/T_C)^{-1/2}$ and $H_C(T) \propto (1 - T/T_C)$ near T_C [269], the temperature dependence of U_0 will be obtained as $U_0(T) \propto (1 - T/T_C)$, which is indeed observed experimentally for $H \geq 2$ T. In annealed $\text{Ti}_{0.7}\text{V}_{0.3}$ sample, different orientations and sizes of the extended disorders like grain boundaries and martensitic α phase lead to a distribution of l_P and hence U_0 over the sample volume. However, in high magnetic field regime, the flux-line system can be described by a single value of U_0 rather than a distribution of U_0 because of the collective behaviour of the flux-line system. On the other hand, in low magnetic field, the single flux-line pinning occurring above $T_G(H)$ -line at some mesoscopic strong pinning sites like α phase may give rise to Bose-glass islands having relatively higher U_0 and hence T_G values within the interstitial vortex-liquid phase [270, 271]. The pinned flux lines within these

Bose-glass islands are then expected to be de-localized and thereby forming the vortex-liquid at a relatively higher temperature [270-272]. Consequently, in low magnetic field regime, when temperature is increased keeping the magnetic field constant, there are two independent ways which govern the temperature dependence of U_0 . Firstly, U_0 decreases following $(1 - T/T_C)$ dependence which arises from the temperature dependence of the intrinsic superconducting parameters. Secondly, an increase in temperature in presence of a constant magnetic field involves the melting transitions of the Bose-glass islands having higher and higher U_0 values. As a result of this, the pre-factor U_H , which was presumed to be independent of temperature in high magnetic field regime, also evolves with temperature in low magnetic field regime. Such a temperature evolution of U_H along with the usual $(1 - T/T_C)$ dependence gives rise to an overall slow variation of U_0 in low magnetic field regime than observed in high magnetic field regime. Hence, we suggest that in $\text{Ti}_{0.7}\text{V}_{0.3}$ sample, the co-existence of the Bose-glass islands within the interstitial vortex-glass slows down the dynamic of the flux lines in low magnetic field regime.

8.3 Summary and conclusions

In summary, we have investigated the resistive transition of $\text{Ti}_{0.7}\text{V}_{0.3}$ sample in presence of magnetic fields up to 5 T. We have found experimental evidences for the existence of a Bose-glass vortex state in the superconducting

mixed state of this sample. In the magnetic field regime $H \geq 2$ T, the vortex-liquid resistivity exhibits a scaling behaviour as predicted for vortex-glass and/or Bose-glass scenario, proving further evidence of a Bose-glass transition in the studied sample. However, the vortex-liquid resistivity does not follow the same scaling relation in the magnetic field regime $H < 2$ T. This is due to the fact that both the temperature as well as magnetic field dependencies of the effective pinning energy U_0 are distinctly different in the magnetic field regimes below and above 2 T. We have formulated a new scaling relation to describe the vortex-liquid resistivity for $H < 2$ T by taking into account the experimental temperature dependence of U_0 in this magnetic field regime. Another important result of this study is that although the Bose-glass transition line [$T_G(H)$ -line] obtained from the resistive transitions overlaps with the magnetically measured irreversibility line [$H_{Irr}(T)$ -line] for $H \geq 2$ T, they strongly split from each other for $H < 2$ T. We have suggested that all observed phenomena i.e. the change of behaviour of both the temperature and magnetic field dependencies of U_0 and the splitting of the $T_G(H)$ -line from the $H_{Irr}(T)$ -line, all occurring at a crossover field $H_D \sim 2$ T, are manifestations of the combined effects of the spatial variation of U_0 over the sample volume and the crossover in the pinning behaviour from individual to collective pinning regime with increasing magnetic field.

Chapter 9

High-field paramagnetic Meissner effect in the multi-phase Ti-V alloy superconductors

9.1 Introduction

When a type-II superconductor is cooled down across the superconducting transition temperature T_C in the presence of magnetic field smaller than the lower critical field H_{C1} , it expels the magnetic flux from its interior. In an ideal defect-free type-II superconductor, the complete expulsion of magnetic flux leads to the perfect diamagnetic state of superconductor, which is characterized by the dc magnetic susceptibility $\chi = M/H = -1$. Conventionally, this behaviour is taken as the hallmark of superconductivity. However, the presence of crystal defects cannot be avoided in real superconductors. The flux expulsion then becomes incomplete due to the pinning of the flux lines at the defect sites. In such case, when the temperature is decreased below

T_C , the field-cooled magnetization decreases from its normal state paramagnetic value and assumes a value $|\chi| < 1$. However, in certain samples of both high- T_C cuprate and conventional low- T_C superconductors, the field-cooled magnetization increases as the temperature is decreased below T_C in the presence of a very low magnetic field of the order of few Oe. The field-cooled magnetization in the superconducting state of these samples even becomes larger than the normal state paramagnetic magnetization. This observed behaviour is in striking contrast to the conventional diamagnetic response of a superconductor, and is known as “paramagnetic Meissner effect” (PME) or “Wohleben effect” [273]. PME was initially observed in high- T_C superconductors [274-278], where it is explained considering the existence of spontaneous super-current in an unconventional pairing state [279, 280]. Later on, PME was also observed in conventional low- T_C superconductor like Nb [281-283], Al [284], Pb nano-wire arrays [285] and multi-phase $\text{Sn}_{90}\text{In}_{10}$ alloy [286] in the presence of low magnetic field. These observations suggest that the PME is not necessarily dependent upon some intrinsic unconventional mechanism unique to the high- T_C superconductors. In conventional low- T_C superconductors, the low-field PME is thought to originate due to the trapping of flux lines and the subsequent compression of these trapped flux lines while cooling the sample below T_C [287, 288]. Such flux compression could be resulted from the inhomogeneous cooling of the sample [287] and/or could also be an intrinsic property originating because of the sample boundaries present in any finite-size superconductor [284, 288].

However, in some recent studies on $\text{YBa}_2\text{Cu}_3\text{O}_{7-\delta}$ [289-292], hetero-structures of $\text{YBa}_2\text{Cu}_3\text{O}_{7-\delta}/\text{La}_{0.67}\text{Sr}_{0.33}\text{MnO}_3$ [293], MgB_2 [294, 295], and thin film Nb [296] samples, PME has been observed in the presence of sufficiently high magnetic field of the order of few Tesla, and thus the effect is termed as high-field PME or HFPME. A non-uniform distribution of flux lines caused by flux-line pinning at the inhomogeneously distributed pinning centres within the superconducting matrix has been argued to be behind the origin of the HFPME [291, 293, 295]. In chapter 3, we have seen that the Ti-rich Ti-V alloys such as $\text{Ti}_{0.8}\text{V}_{0.2}$ and $\text{Ti}_{0.7}\text{V}_{0.3}$ alloys are formed in multi-phase crystallographic structures. The secondary phases like α , α' and ω phases are found to be present in the main β phase matrix of these alloys. The flux-line pinning at these secondary phases may lead to a non-uniform distribution of flux lines over the sample volume, thereby providing an opportunity for studying the HFPME in these alloys. In the present chapter, we present an experimental study on the HFPME in as cast and annealed samples of the $\text{Ti}_{0.8}\text{V}_{0.2}$ alloys and annealed sample of the $\text{Ti}_{0.7}\text{V}_{0.3}$ alloy.

9.2 Results and discussion

9.2.1 Temperature dependence of magnetization

Figs. 9.1(a)-(c) shows the temperature dependence of magnetization measured in zero-field-cooled (ZFC), field-cooled-cooling (FCC) and field-cooled-warming (FCW) protocols in the presence of 10 mT magnetic field for the

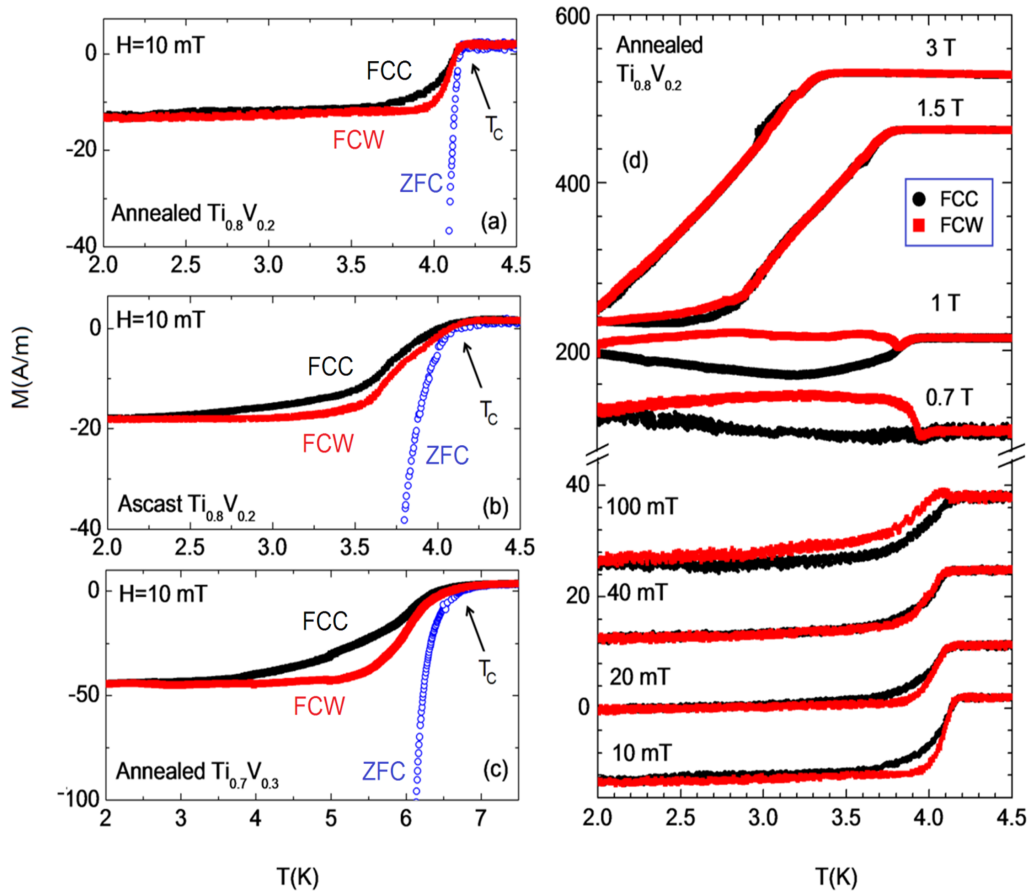


Figure 9.1: (a)-(c). The temperature dependence of magnetization obtained in the ZFC, FCC and FCW protocols for the as cast and annealed $\text{Ti}_{0.8}\text{V}_{0.2}$ samples and annealed $\text{Ti}_{0.7}\text{V}_{0.3}$ sample in the presence of 10 mT magnetic field. The field-cooled magnetization demonstrates a thermal hysteresis, and the magnetization measured in the cooling-down cycle (FCC) is more positive than the magnetization obtained in warming-up cycle (FCW). (d) The evolution of the temperature dependence of the FCC and FCW magnetization with increasing magnetic field up to 3 T for the annealed $\text{Ti}_{0.8}\text{V}_{0.2}$ sample. The temperature dependence of the FCW magnetization curve tends to switch above the corresponding FCC magnetization curve as the magnetic field is increases up to a certain limiting value.

as cast and annealed $\text{Ti}_{0.8}\text{V}_{0.2}$ samples and annealed $\text{Ti}_{0.7}\text{V}_{0.3}$ sample. These samples exhibit diamagnetic behaviour at temperatures below T_C . As can be seen from these figures the ZFC magnetization lies well below the field-cooled magnetization. In type-II superconductors, the flux-line pinning within the bulk of the sample significantly influences the flux expulsion during the field-cooled measurement while the flux exclusion during the ZFC measurement is not affected by the same, thereby leading to a marked difference between the ZFC and the field-cooled magnetization.

The field-cooled magnetization exhibits a thermal hysteresis, and the magnetization measured in the cooling-down cycle (FCC) is more positive than the magnetization obtained in warming-up cycle (FCW). Such a thermal hysteresis of the field-cooled magnetization is a characteristic feature of type-II superconductors where the flux-line pinning at the topological defects is relevant, and is consistent with the theoretical interpretation based on critical-state model calculations [297]. When a bulk superconducting sample is cooled below T_C in the presence of magnetic field higher than the lower critical field H_{C1} , the flux-line pinning at the topological defects causes freezing of the flux lines beyond the flux trapping depth L from the sample surface [297]. During the subsequent warming-up cycle, these frozen-in flux lines relax and move toward the regions of lower flux-line density. The flux-line relaxation process hinders the penetration of flux lines into the sample from the outside during the warming-up cycle. Hence, the number of flux lines penetrating the sample during the warming-up cycle is always lesser than

those expelled during the initial cooling-down cycle, and thereby causing a more positive value of the FCC magnetization than the FCW magnetization.

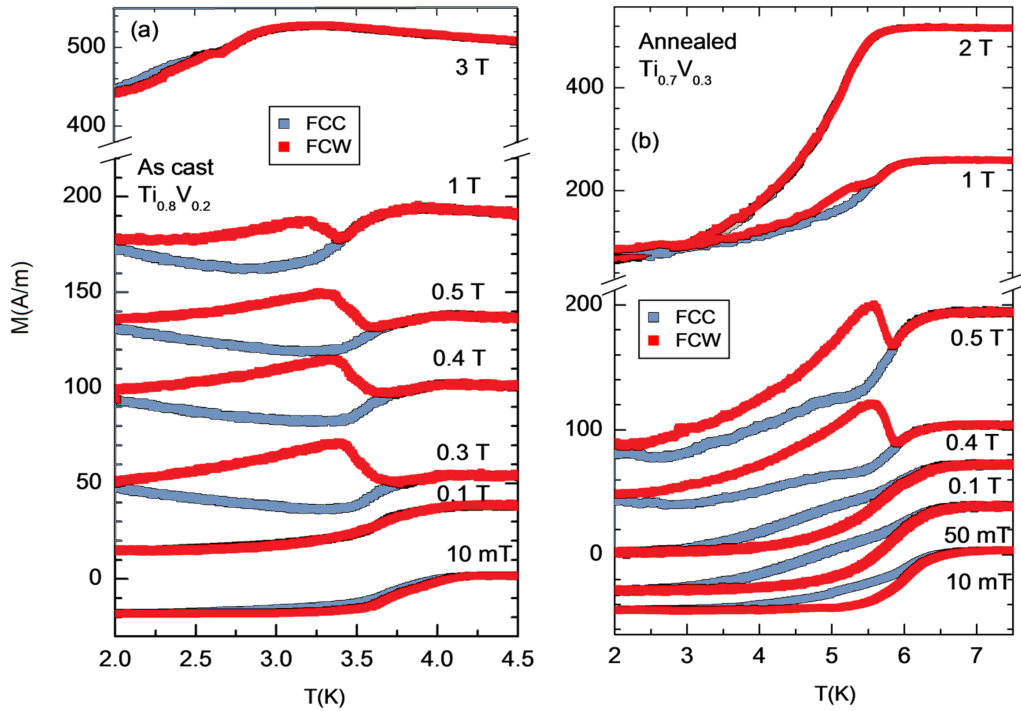


Figure 9.2: The evolution of the temperature dependence of the FCC and FCW magnetization with increasing magnetic field in the (a) as cast $\text{Ti}_{0.8}\text{V}_{0.2}$ sample and (b) annealed $\text{Ti}_{0.7}\text{V}_{0.3}$ sample.

Fig. 9.1(d) shows the evolution of the temperature dependence of the FCC and FCW magnetization for the annealed $\text{Ti}_{0.8}\text{V}_{0.2}$ sample with increasing applied magnetic fields. Few of these curves are shifted vertically for a clear comparison. For magnetic fields up to $H = 20$ mT, FCC magnetization curve lies above the FCW magnetization curve. These curves merge onto one another for $H = 40$ mT. For still higher magnetic field, FCW magneti-

zation curve switches above the FCC magnetization curve, which is opposite to the conventional behaviour of a type-II superconductor. For such high applied magnetic field, thermal hysteretic behaviour between the FCC and FCW magnetization is also observed to be much more pronounced than that observed in low magnetic field regime. Moreover, for $H = 0.7$ and 1 T, FCC magnetization initially decreases from its normal state value when the temperature is decreased below T_C , and then starts to increase with further decrease in temperature. However, FCC magnetization in the superconducting state remains smaller than the normal state magnetization. FCW magnetization, on the other hand, initially increases with increasing temperature, and then drops back to the FCC magnetization in the close vicinity of T_C . FCW magnetization in the superconducting state even becomes larger than the normal state magnetization for $H = 0.7$ T. For $H \geq 1.5$ T, thermal hysteresis between the FCC and FCW magnetization becomes reduced and the sample approaches more towards conventional behaviour. The thermo-magnetic response of the as cast $\text{Ti}_{0.8}\text{V}_{0.2}$ and annealed $\text{Ti}_{0.7}\text{V}_{0.3}$ samples is qualitatively very similar to that observed in the annealed $\text{Ti}_{0.8}\text{V}_{0.2}$ sample, and is shown in Fig. 9.2 (a) and (b). However, in the case of annealed $\text{Ti}_{0.7}\text{V}_{0.3}$ sample, the increase of the FCC magnetization with decreasing temperature is observed to be less prominent and becomes observable only at temperatures below 3 K. The observed thermo-magnetic behaviour of the present set of samples in certain high applied magnetic field regime is distinctly different from conventional behaviour of a type-II superconductor.

As stated in the introduction section, the increase of FCC magnetization with decreasing temperature below T_C may be resulted from the flux compression effect. However, the flux compression is known to give rise to the paramagnetic response of the sample only in the presence of applied magnetic field smaller than H_{C1} , and the superconducting samples are generally found to recover the diamagnetic response in higher applied magnetic field [287, 295, 298]. In the present set of Ti-V samples, HFPME is observed in the presence of applied magnetic fields much larger than H_{C1} , suggesting that the flux compression may not be behind the origin of the observed effect in these samples. The observed characteristic features of the HFPME, such as, the increase of the FCC magnetization with decreasing temperature below T_C , a higher value of the FCW magnetization as compared to the FCC magnetization, and also the time dependence of the FCC magnetization which will be presented below, are unique to the HFPME [291, 292, 294, 296], suggesting that the HFPME might have an origin which is entirely different from that of the low-field PME.

HFPME is observed in the present set of samples only at temperatures below the irreversibility temperature T_{Irr} (which is taken as the temperature at which the temperature dependence of the ZFC curve bifurcates from the FCC magnetization curve), indicating that flux-line pinning might be responsible for the observed effect in these samples. In chapter 3, we have found that both the as cast and annealed $\text{Ti}_{0.8}\text{V}_{0.2}$ samples contain stress induced martensitic α' phase within the main β phase matrix of these sam-

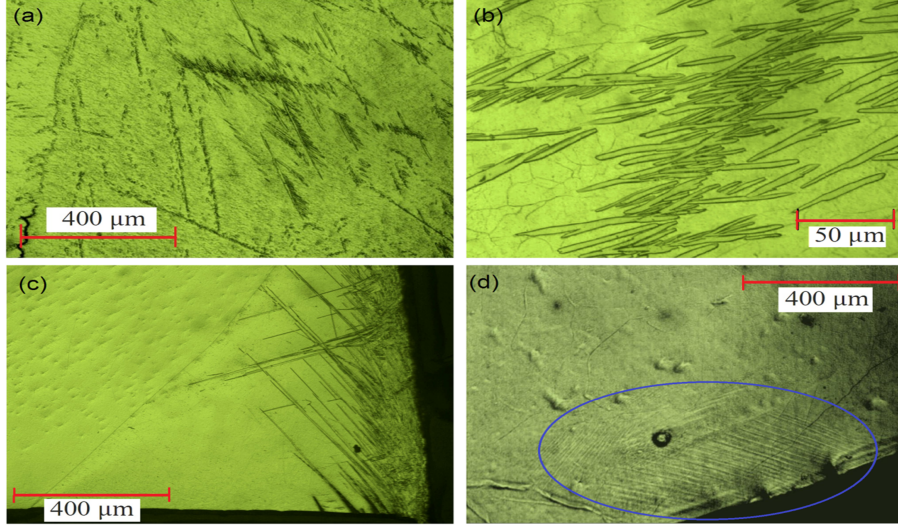


Figure 9.3: Optical micrographs showing the spatial distribution of α phase in the annealed $\text{Ti}_{0.7}\text{V}_{0.3}$ sample (a, b) and α' phase in the annealed (c) and as cast (d) $\text{Ti}_{0.8}\text{V}_{0.2}$ samples.

ples. On the other hand, annealed $\text{Ti}_{0.7}\text{V}_{0.3}$ sample contains martensitic α phase within the main β phase matrix of this sample. As can be seen in Fig. 9.3, the martensitic α' and α phase are inhomogeneously distributed within the main β phase matrix of these Ti-V samples. Reported T_C values of pure α phase Ti-V alloys indicate that these martensitic α^M phases (we will use this common symbol α^M to denote the martensitic α and α' phases) are non-superconducting in the temperature range of present measurement [6, 51]. Hence, the non-superconducting α^M phase regions can act as efficient flux-line pinning sites. Then the flux-line pinning at the α^M phase regions will lead to an inhomogeneous distribution of flux lines over a macroscopic length scale much larger than the magnetic field penetration depth

λ , which is only 2-3 hundreds of nm for the present Ti-V alloys (see Table-4.3 of chapter 4). Such a spatially inhomogeneous distribution of flux lines could result in a net bulk current to flow inside the sample in accordance with the Maxwell's equation $\vec{J} = \vec{\nabla} \times \vec{H}$. The bulk current referred above has a direction opposite to the diamagnetic screening current flowing at the surface of the sample. Hence, a net paramagnetic response of the sample will be obtained when the paramagnetic response resulting from the bulk current exceeds the diamagnetic response from the surface screening current.

As described in chapter 3, α' phase in both the as cast and annealed $\text{Ti}_{0.8}\text{V}_{0.2}$ samples is a stress induced phase, which is formed during mechanical processing of the samples such as cutting of the sample [58, 108, 110]. It is then possible to get rid of this α' phase from these samples by annealing them at some elevated (β -field) temperature. The disappearance of the HFPME in a sample devoid of any α' phase will be a confirmatory test for the viewpoint that the HFPME observed in the present samples is indeed related to the flux-line pinning at the α^M phase regions. Motivated by this, we have performed a second stage annealing of the annealed $\text{Ti}_{0.8}\text{V}_{0.2}$ sample initially used for magnetization measurements. The protocol employed in this second stage annealing is identical to the first stage annealing protocol. The magnetization measurements are then performed again on this re-annealed sample. We present in Fig. 9.4(a) the temperature dependence of the FCC and FCW magnetization of this re-annealed sample in the presence of 1 T magnetic field. For comparison we also show in Fig. 9.4(b), the temperature

dependence of FCC and FCW magnetization of the initially annealed sample in the same applied magnetic field. As can be seen from these figures, the HFPME is not observed in the re-annealed sample. This experimental observation confirms that the flux-line pinning at the α^M phase regions is responsible for the occurrence of the HFPME in the present samples [110].

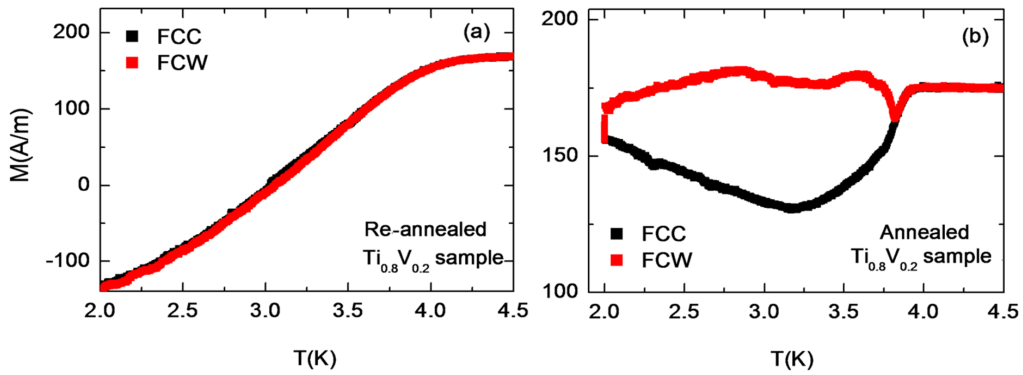


Figure 9.4: Temperature dependence of the FCC and FCW magnetization measured in presence of 1 T magnetic field for the (a) re-annealed and (b) the initially annealed $\text{Ti}_{0.8}\text{V}_{0.2}$ samples.

However, the annealed $\text{Ti}_{0.4}\text{V}_{0.6}$ sample also contains α phase within the main β phase matrix of this sample (refer to chapter 3). The optical micrographs of this sample are shown in Fig. 9.5(a), which clearly show the presence of needle-shaped martensitic α phase within the main β phase matrix. The martensite α phase appears to be inhomogeneously distributed in the main β phase matrix of this sample. In spite of that, no indication of the HFPME is observed in this sample, suggesting that the flux-line pinning at spatially inhomogeneous distribution of non-superconducting phases may not

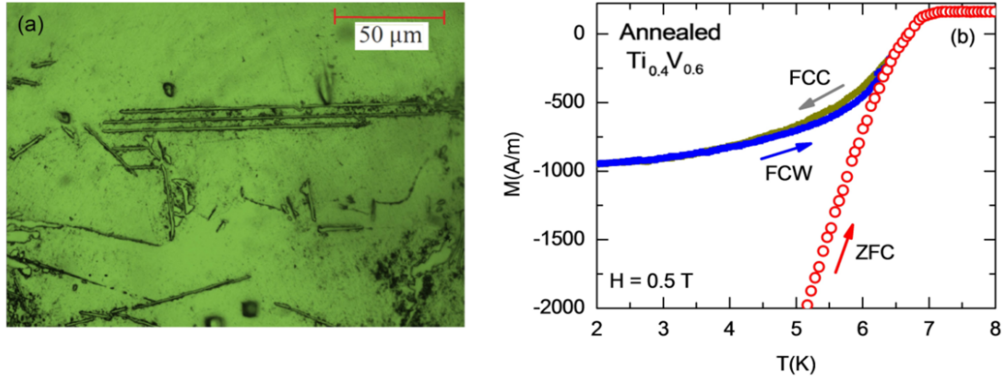


Figure 9.5: (a) Optical micrograph of the annealed $\text{Ti}_{0.4}\text{V}_{0.6}$ sample showing the formation of the needle-shaped martensitic α phase within the main β phase matrix of this sample. (b) Temperature dependence of the ZFC, FCC and FCW magnetization in 0.5 T applied magnetic field for the same sample showing no indication of the HFPME in this sample.

be the only factor leading to the observation of the HFPME in the present samples. Moreover, the common characteristic features associated with the HFPME such as the more positive value of the FCW magnetization than the FCC magnetization, time as well as temperature sweep rate dependence of the FCC magnetization (will be discussed later in this chapter) etc., cannot be explained by assuming only the static metastable distribution of the flux lines driven by flux-line pinning. We therefore suggest that though the metallurgical aspect is essential for the occurrence of the HFPME, there must be some other mechanism(s) which play(s) supplementary role in the occurrence of the effect.

Dias *et al.* [291] have studied the HFPME in a series of melt-textured $\text{YBa}_2\text{C}_3\text{O}_{7-\delta}$ samples. Terentiev *et al.* [296] have also studied this effect in

a thin film Nb sample. Their studies show that the paramagnetic FCC magnetization in their samples relaxes monotonically towards increasing positive value. Based on their experimental results, these authors have interpreted that flux-creep effect has a crucial role to play in the occurrence of the HF-PME [291, 296]. It is notable that all the superconducting samples such as melt-textured $\text{YBa}_2\text{C}_3\text{O}_{7-\delta}$ [289-292], $\text{YBa}_2\text{Cu}_3\text{O}_{7-\delta}/\text{La}_{0.67}\text{Sr}_{0.33}\text{MnO}_3$ heterostructures [293], MgB_2 [294, 295], Nb thin film [296] etc., which are reported so far to exhibit the HFPME, are also susceptible towards strong flux-creep effect. In high- T_C cuprate and MgB_2 superconductors, enhanced flux-creep effect is well documented in the literature. On the other hand, flux-creep effect is enhanced drastically in low- T_C thin film Nb sample because of the small flux-line correlation length L_C in thin film sample [264]. It is then quite genuine to think that the flux-creep effect might have some important role to play in the occurrence of the HFPME. In order to ascertain this viewpoint, we first check the relevance of flux-creep in the present bulk Ti-V alloys through the magnetic relaxation experiments.

9.2.2 Time dependence of magnetization

Fig. 9.6 shows the time dependence of the FCC magnetization for the annealed Ti-V samples. The magnetization is measured after field-cooling the samples at 1 K/min from 10 K to the measuring temperature. For $H = 0.05$ T, FCC magnetization of the annealed $\text{Ti}_{0.7}\text{V}_{0.3}$ sample decreases monotonically with time. This is shown in Fig. 9.6(a). Similar behaviour is also ob-

served in the as cast and annealed $\text{Ti}_{0.8}\text{V}_{0.2}$ samples (not shown here). This kind of diamagnetic relaxation behaviour is quite common in the high- T_C superconductors. The enhanced flux-creep in the high- T_C superconductors assists the flux lines to escape from the interior of the sample, thereby leading to the observation of the diamagnetic relaxation of the FCC magnetization. Hence, we may infer from the present observations that flux-creep effect is indeed important in the Ti-rich Ti-V samples.

The relevance of flux-creep in the Ti-rich Ti-V samples can also be understood in terms of the relatively larger values of the Ginzburg number G_i estimated for them. The G_i numbers is $\sim 10^{-5}$ for the $\text{Ti}_{0.8}\text{V}_{0.2}$ and $\text{Ti}_{0.7}\text{V}_{0.3}$ alloys (see chapter 5). Although this value of G_i number is smaller than the $G_i \sim 10^{-2}$ for the high- T_C cuprate superconductors, it is considerably larger than the $G_i \sim 10^{-8}$ for the typical low- T_C superconductors. This underlines the importance of flux-creep effect in these Ti-rich Ti-V alloys. On the other hand, the G_i number for the $\text{Ti}_{0.4}\text{V}_{0.6}$ alloy is almost one order of magnitude lower than those for the $\text{Ti}_{0.8}\text{V}_{0.2}$ and $\text{Ti}_{0.7}\text{V}_{0.3}$ alloys, implying negligible importance of the flux-creep effect in the $\text{Ti}_{0.4}\text{V}_{0.6}$ alloy (see chapter 5). Accordingly, the FCC magnetization of the annealed $\text{Ti}_{0.4}\text{V}_{0.6}$ sample, measured at 2 K and in presence of 0.05 T magnetic field, does not exhibit any diamagnetic relaxation behaviour [Fig. 9.6(b)]. Interestingly, this sample does not exhibit any signature of the HFPME though it contains the spatially inhomogeneous distribution of α phase within the main β phase matrix of this sample. Hence, the observations of the HFPME in

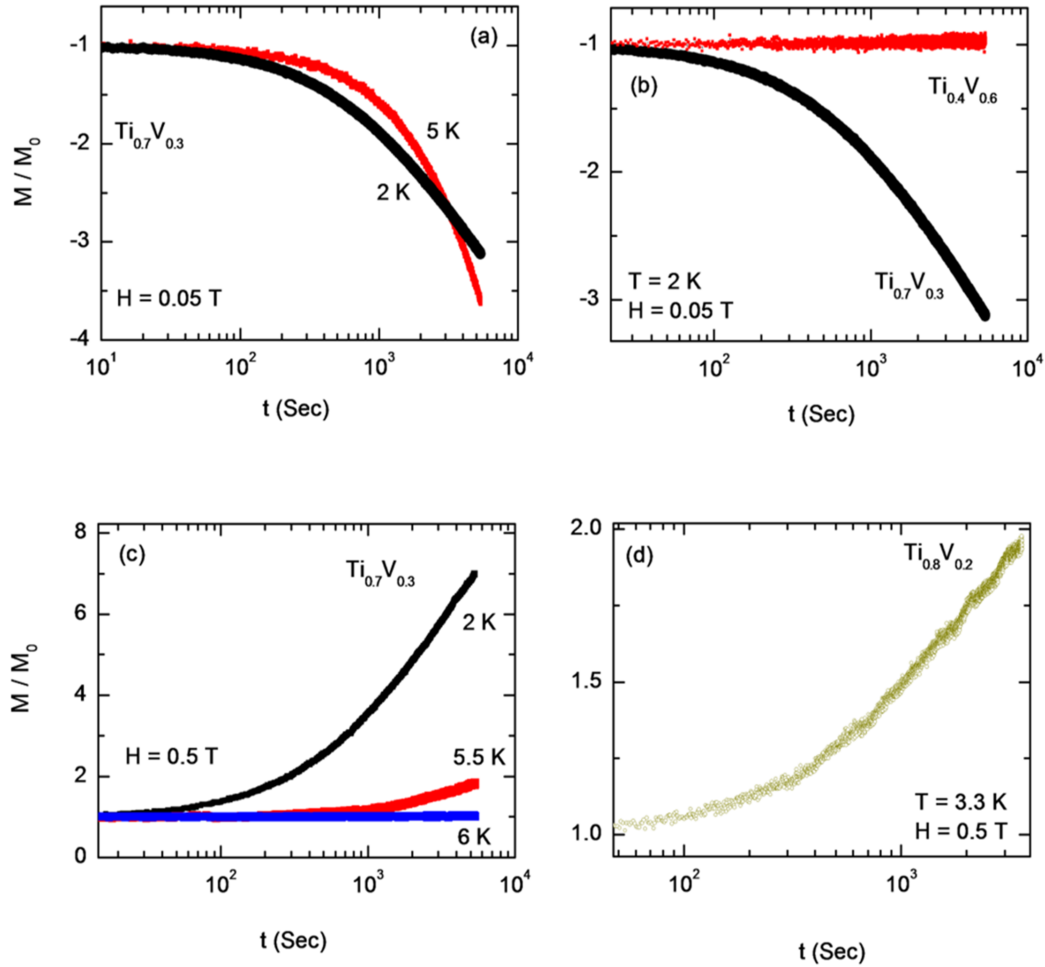


Figure 9.6: Time dependence of the FCC magnetization for the annealed samples of the Ti-V alloys in the presence of different constant applied magnetic field and temperatures. The measurements are performed after field-cooling the samples from 10 K to the measuring temperatures using a temperature sweep rate of 1 K/min. The magnetization is normalized by M_0 which denotes the magnitude of the magnetization at $t = 0$. The Ti-rich Ti-V alloys exhibit diamagnetic relaxation behaviour at low magnetic field regime and paramagnetic relaxation behaviour at relatively higher magnetic field regime.

the $\text{Ti}_{0.8}\text{V}_{0.2}$ and $\text{Ti}_{0.7}\text{V}_{0.3}$ samples and its absence in the $\text{Ti}_{0.4}\text{V}_{0.6}$ sample signify that the flux-creep might be a necessary ingredient for the occurrence of the HFPME. In this context, it is important to mention that all the superconducting samples such as melt-textured $\text{YBa}_2\text{Cu}_3\text{O}_{7-\delta}$ [289-292], $\text{YBa}_2\text{Cu}_3\text{O}_{7-\delta}/\text{La}_{0.67}\text{Sr}_{0.33}\text{MnO}_3$ hetero-structures [293], MgB_2 [294, 295], Nb thin film [296] etc., which are reported so far to exhibit the HFPME, are also susceptible towards strong flux-creep effect.

Figs. 9.6(c) and (d) show that for $H = 0.5$ T, FCC magnetization of the annealed $\text{Ti}_{0.8}\text{V}_{0.2}$ and $\text{Ti}_{0.7}\text{V}_{0.3}$ samples relaxes monotonically towards increasing positive value. This behaviour is opposite to the one expected from the conventional flux-creep scenario described above. This anomalous paramagnetic relaxation of the FCC magnetization depicted in Fig. 9.6(a) has been observed previously in $\text{YBa}_2\text{Cu}_3\text{O}_{7-\delta}$ [291, 292] and thin film Nb [296] superconducting samples exhibiting the HFPME, suggesting that this observed behaviour is a characteristic of the HFPME. The observed time dependence of the HFPME clearly indicates the correlation of the vortex dynamics with the HFPME. In the present Ti-V samples, the size of the needle-shaped α^M phase regions is much larger than the size of the other relevant pinning centres such as the ω phase precipitations and grain boundaries available in the $\text{Ti}_{0.8}\text{V}_{0.2}$ and $\text{Ti}_{0.7}\text{V}_{0.3}$ samples. Consequently, these α^M phase regions are capable of pinning a flux line over longer length scale, and thereby making the flux-line pinning most favourable at these regions. Then it seems reasonable that the flux line could creep preferentially into

the α^M phase regions from other weak pinning centres. When the flux lines creep into the α^M phase regions from the rest of the sample and get pinned there, some parts of the sample get depleted (compared to the equilibrium distribution) of flux lines, and this creates the scope for additional flux lines to enter into the sample from outside. As a possible consequence of this fact, the anomalous paramagnetic relaxation of the FCC magnetization observed in the present samples may occur in two ways. Firstly, the relatively higher density of the flux-lines at the α^M phase regions developed by the flux-creep effect will give rise to the gradually higher paramagnetic response of the sample with elapsed time. Secondly, the entry of additional flux lines into the sample will also contribute to increase the magnetization of the sample with time. We now try to explain all the characteristic features associated with the HFPME based on the interpretations made above.

(i) Temperature sweep rate dependence of the FCC magnetization

Fig 9.7 shows the temperature dependence of the FCC magnetization for the as cast and annealed $\text{Ti}_{0.8}\text{V}_{0.2}$ samples measured using two different temperature sweep rates. This figure shows that the thermo-magnetic behaviour of these samples is highly sensitive to the temperature sweep rate. FCC magnetization is higher for a slower temperature sweep rate. This is also observed for the annealed $\text{Ti}_{0.7}\text{V}_{0.3}$ sample (not shown here). The longer elapsed time during a FCC measurement performed at a relatively slow temperature sweep rate allows relatively large number of flux lines to creep into the α^M phase regions, and thereby produces higher paramagnetic response of the sample.

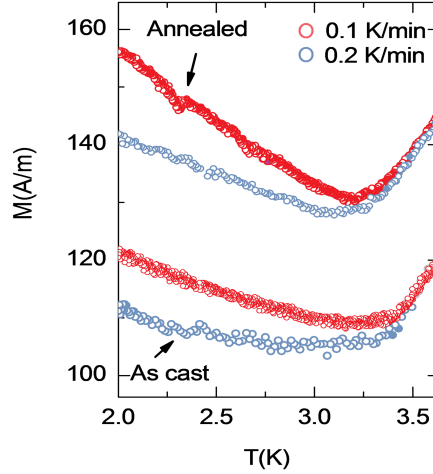


Figure 9.7: Temperature dependence of FCC magnetization for the as cast (in 0.5 T applied magnetic field) and annealed (in 1 T applied magnetic field) samples of $\text{Ti}_{0.8}\text{V}_{0.2}$ alloy in two different temperature sweep rate.

(ii) Thermal hysteresis between the FCC and FCW magnetization

FCC and FCW measurements are performed in temporal sequence, and FCW measurement follows the FCC measurement. While switching the experimental protocol from FCC to FCW, the sample is kept at a constant temperature (2 K in the present case) for a finite period of time. During this elapsed time, flux-creep into the α^M phase regions results in an increase of the paramagnetic response of the sample, which is evident from the steep jump of the FCC magnetization at 2 K in Fig. in 9.4(b). On warming-up the sample above 2 K, flux-creep into the α^M phase regions along with the usual entry of additional flux lines into the sample during the warming-up cycle gives rise to the further enhancement of the paramagnetic response of the sample. Consequently, the FCW magnetization is higher than the FCC magnetiza-

tion. On further increase in temperature the inhomogeneous distribution of flux lines over the sample volume is washed out in the close vicinity of T_C because of decreasing pinning efficiency of the α^M phase regions and the entry of large number of flux lines into the sample in this temperature regime. Consequently, FCW magnetization falls back onto the FCC magnetization before the sample enters into the normal state at T_C .

(iii) Temperature dependence of the paramagnetic relaxation behaviour of FCC magnetization

Fig. 9.6(c) shows that the paramagnetic relaxation behaviour of the annealed $\text{Ti}_{0.7}\text{V}_{0.3}$ sample gradually diminishes as temperature is increased towards T_C . Very similar behaviour is also observed in high- T_C materials exhibiting the HFPME [291, 292]. When a highly dense state of the flux lines at some α^M phase regions is developed by the flux-creep and the subsequent pinning of the flux lines at that region, the flux lines come quite close to each other. However, in a high- κ material like Ti-V alloys (refer to chapter 4), strong vortex-field associated with the flux line exists beyond the normal core of the flux line [147], and thus the overlapping of such strong vortex-field opposes the flux lines to come exceedingly closer to each other in the length scale much lower than the magnetic field penetration depth λ . In such case, the average separation between the flux lines and hence the density of flux lines at some α^M phase regions will be determined by the mutual competition between the pinning energy and repulsive energy due to the interactions between the vortex-field associated with the flux lines. In the previous chapter, we have

found that the resistive transition of the annealed $\text{Ti}_{0.7}\text{V}_{0.3}$ sample in the presence of magnetic field show indications for the existence of a Bose-glass phase in the superconducting mixed state of this sample. This glass phase exists up to the $H_{Irr}(T)$ -line (or equivalently $T_G(H)$ -line) which is, in general, situated in the field-temperature ($H - T$) phase diagram, not far away from the $H_{C2}(T)$ -line for a low- T_C superconductor. Therefore, in the $H - T$ regime near to $H_{Irr}(T)$ -line, the inter-spacing between the flux lines can be assumed to be slightly lower than the normal core diameter of the flux lines, which is just twice the coherence length $\xi(T)$. The exhibition of a glassy vortex phase in $H - T$ regime up to $H_{Irr}(T)$ -line is an indicative of the fact that the pinning energy dominates over the vortex-vortex repulsive energy even when the inter-spacing between the flux lines becomes close to $2\xi(T)$. In other words, we may say that the sufficiently higher pinning strength of the α^M phase regions present in the annealed $\text{Ti}_{0.7}\text{V}_{0.3}$ sample enables pinning of as much as flux lines at these α^M phase regions until the inter-spacing among the flux lines becomes $\sim 2\xi(T)$. This interpretation leads us to conclude that **the density of the flux lines at the α^M phase regions and hence the strength of the HFPME is expected to depend on $\xi(T)$** . Since ξ diverges at T_C as $\xi(T) \sim (1 - T/T_C)^{\frac{1}{2}}$, a given size of a non-superconducting region such as the α^M phase region is capable of accommodating relatively larger number of flux lines at lower temperatures. As a possible consequence of this fact, a relatively larger number of flux lines will be allowed to creep into the α^M phase regions at lower temperatures, producing stronger para-

magnetic relaxation of the sample at lower temperatures. This explains the observed temperature dependence of the paramagnetic relaxation behaviour of the FCC magnetization, and will in general hold for any superconductor whenever the pinning strength of the non-superconducting regions present in the sample is sufficiently high.

(iv) Anisotropic behaviour of the HFPME in high- T_C cuprate superconductors

Another experimental observation which seems to be important in the present context is that the HFPME observed in high- T_C cuprate superconductors exhibits strong anisotropic behaviour, and the effect is more strongly observed when the magnetic field is applied parallel to the ab basal plane [291, 292]. This anisotropic behaviour becomes stronger as the anisotropy parameter is increased. In order to explain this observed anisotropic behaviour of the HFPME in the melt textured $\text{YBa}_2\text{C}_3\text{O}_{7-\delta}$ samples, Dias *et al.* have assumed a preferential orientation of the needle-shaped non-superconducting Y211 precipitates parallel to the ab basal plane [291]. Based on this assumption they have argued that the relatively larger interfacial region between the Y211 precipitate and YBCO matrix along the ab basal plane reinforces the flux-line pinning when the magnetic field is applied parallel to the ab plane [291]. Consequently, HFPME is enhanced when the magnetic field is applied parallel to the ab plane. However, in reality, the needle-shaped Y211 precipitates are found to be randomly distributed within the YBCO matrix in all possible orientations [292, 299]. In our view, the observed anisotropic behaviour

of the HFPME in high- T_C cuprate superconductors arises mainly from the different values of the coherence length in the ab basal plain and along the c direction. In high- T_C cuprate superconductors, the coherence length ξ_{ab} along the ab plain is significantly higher than the coherence length ξ_c along the c direction. For the field orientation $H||ab$, the diameter of the normal core of the flux lines is $\sim 2\xi_c$ while it is $\sim 2\xi_{ab}$ for the field orientation $H||c$. A relatively smaller normal core diameter of the flux lines for the field orientation $H||ab$ allows relatively larger number of flux lines to be pinned at the Y211 precipitates and thereby produces much stronger HFPME in this field orientation.

9.3 Summary and conclusions

The present experimental observations together with few other experimental results available in the literature [291, 293, 295, 296] lead to the following conclusions: The meta-stability of the flux-line system driven by flux-line pinning at the inhomogeneously distributed α^M phase within the superconducting matrix is the essential mechanism leading to the observation of the HFPME in the present Ti-V alloy samples. The flux-creep effect acts as an additional ingredient for the occurrence of the HFPME. The characteristic features of the HFPME observed in the present Ti-V samples are found to be explained consistently when the flux-creep effect (vortex dynamic) is taken into account along with the (static) metastable distribution of the flux lines

resulted from the flux-line pinning at the spatially inhomogeneous distribution of α^M phase. Thus it appears that the HFPME may be considered in general to be a common feature of the type-II superconductors having inhomogeneous distribution of pinning centres within the superconducting matrix and finite role of flux-creep effect. The HFPME is also found to depend on the fundamental superconducting length scale ξ of a superconductor because the density of the flux lines at the non-superconducting regions indirectly depends on this length scale, particularly when the pinning strength is sufficiently high. Based on the present results obtained for the Ti-V samples, we suggest that the superconductors with significant role of flux-creep effect and very small values of ξ are favourable to exhibit strong HFPME. The high- T_C cuprate superconductors, which usually show giant flux-creep effect and have very small values of ξ , are known to exhibit very strong HFPME. Similarly, the very rare observation of the HFPME in low- T_C superconductors can also be understood from the negligible role of flux-creep and very large values of ξ in these superconductors. On the other hand, Ti-V and MgB₂ superconductors lie in-between the high- T_C cuprate and conventional low- T_C superconductors in terms of the strength of flux-creep effect and the value of ξ . Accordingly, HFPME is observed in the Ti-V and MgB₂ superconductors, though the effect is less prominent as compared to that observed in high- T_C cuprate superconductors [291, 293-295].

—This page is intentionally kept blank—

Chapter 10

Summary, conclusions and future outlook of the study

10.1 Summary and conclusions

In this thesis we have presented an experimental study on four $\text{Ti}_x\text{V}_{1-x}$ alloys having concentrations $x = 0.8, 0.7, 0.6$ and 0.4 . This study was focused to understand the structural properties as well as various important superconducting and normal state properties of these Ti-V alloys. The structural properties are studied through X-Ray diffraction (XRD) experiments (using both laboratory based and Synchrotron radiation sources) and optical metallography. The properties of the Ti-V alloys in their normal as well as superconducting state are studied through the measurements of resistivity, magnetization, and the heat capacity as functions of temperature and magnetic field. In this study, we have also attempted to investigate on how the structural and the normal state properties influence the superconducting properties of these Ti-V alloys. In this chapter we present the overall

summary and the conclusions of this study.

The XRD patterns of the Ti-V alloys were analysed using the Rietveld refinement technique to find out the crystal structure as well as the volume fractions of the constituent phases present in the alloys. The analysis of the XRD results indicates that the present Ti-V alloys are formed predominantly in body-centre-cubic (bcc) β phase crystal structure. Apart from the major β phase, the Ti-V alloys also contain hexagonal ω phase as well as martensite α and α' phases. The martensite α phase has a hexagonal closed packed crystal structure. This phase is formed in a considerably large amount ($\sim 28\%$) in annealed $\text{Ti}_{0.7}\text{V}_{0.3}$ alloy while a small amount of this phase ($\sim 2\%$) is also detected in the annealed $\text{Ti}_{0.4}\text{V}_{0.6}$ alloy. On the other hand, the martensite α' phase is present in both the annealed and as cast samples of the $\text{Ti}_{0.8}\text{V}_{0.2}$ alloy. This martensite α' phase has an orthorhombic crystal structure, and is known to be formed due to a stress induced athermal transformation of the β phase [58, 107, 108].

Optical micrographs show that these polycrystalline Ti-V alloys have very large β phase grains with average grain size ranging from few tens to few hundreds of micron. Apart from the signature of grain boundaries, a dotted microstructure is also visible to be densely distributed over the β phase matrix of few samples of the present Ti-V alloys. In some portion of these samples, the dotted microstructures show a tendency to lining-up, which is reported to indicate the presence of edge dislocations and low angle grain boundaries inside the β phase matrix of these sample [37]. Optical micrographs of the

annealed samples of the $\text{Ti}_{0.7}\text{V}_{0.3}$ and $\text{Ti}_{0.4}\text{V}_{0.6}$ alloys show that the martensite α phase mostly formed in needle shaped pattern, is inhomogeneously distributed within the β phase matrix of these alloys. On the other hand, the stress induced martensite α' phase in both annealed and as cast samples of the $\text{Ti}_{0.8}\text{V}_{0.2}$ alloy is formed in the shape of needles near the edges of these samples. It was inferred that the α' phase is formed during the mechanical processing such as cutting of the sample [110].

We have estimated the superconducting transition temperature T_C , various critical fields (the upper critical field H_{C2} , the lower critical field H_{C1} , and the thermodynamic critical field H_C), the coherence length ξ , the magnetic field penetration depth λ , and the Ginzburg-Landau parameter κ to characterize superconducting state properties of the present Ti-V alloys. We have also estimated the Debye temperature θ_D and the electron-phonon coupling constant λ_{ep} from the low temperature heat capacity data, and the bare electronic density of states at the Fermi energy $N(0)$ obtained from the band structure calculation. The estimated values of λ_{ep} have led us to infer that the Ti-rich Ti-V alloys are weak-coupling superconductors. As the Ti concentration is decreased, λ_{ep} increases and becomes ~ 1 for the $\text{Ti}_{0.4}\text{V}_{0.6}$ alloy, indicating the moderate to strong coupling nature of superconductivity in the V-rich Ti-V alloys. Then we have compared the experimentally determined T_C values with those obtained using McMillan formula [19]. The T_C value thus estimated is found to be much higher than the experimentally determined value for the $\text{Ti}_x\text{V}_{1-x}$ alloys with $x = 0.4, 0.6$ and 0.7 .

It was found that Pauli paramagnetic pair-breaking effect [128, 129] imposes limitation on the experimental H_{C2} in the Ti-rich Ti-V alloy superconductors. However, enhanced electron-phonon interaction in the V-rich Ti-V alloys (as indicated by the increased value of λ_{ep} with increasing V concentration in the Ti-V alloys) reduces the role of the Pauli paramagnetic pair-breaking effect, and thereby the experimentally determined H_{C2} in the V-rich Ti-V superconductors agrees well with the prediction of the Ginzburg-Landau-Abrikosov-Gorkov (GLAG) theory [8, 20].

The field dependence of magnetization curve of few samples of the present Ti-V alloys particularly those having relatively low density of defect structures, bears some signature for the presence of Bean-Livingston surface barrier [26]. However, we have found that in the present Ti-V alloy superconductors the existence of the Bean-Livingston surface barrier does not raise the characteristic field for the first flux-line penetration H_P above the lower critical field H_{C1} . The existence of the Bean-Livingston surface barrier only lowers the rate of flux-line penetration in these samples. The Ginzburg-Landau parameter κ was estimated and found to be very high for these Ti-V alloy superconductors, indicating that these superconductors are extreme type-II superconductors. The κ value increases progressively from 32 to 55 as the Ti concentration is increased from $x = 0.4$ to 0.8 in the $\text{Ti}_x\text{V}_{1-x}$ alloys. From the knowledge of the estimated superconducting parameters, we have inferred that the flux-line lattice in the V-rich Ti-V alloys is more rigid as compared to that in the Ti-rich alloys. This is important information has

implications on the current carrying aspect of these superconductors.

Superconducting fluctuations induced conductivity in the annealed Ti-V alloys above the superconducting transition temperature T_C has been studied through the measurements of electrical resistivity as functions of temperature and magnetic field. All the currently investigated Ti-V alloys exhibit a strong rounding-off behaviour in the resistive transition, and the trace of this behaviour persists up to the temperature $\sim 2T_C$. Moreover, these Ti-V alloys exhibit strong positive magneto-resistance in the same temperature regime where the experimental observation of the excess conductivity is possible within the level of experimental accuracy. Aslamazov-Larkin theoretical model [157] and its extended version [158] consistently describe the excess conductivity data of the present Ti-V alloys. In order to explain the strong positive magneto-resistance observed in the temperature range from T_C to $2T_C$, we have invoked the theoretical model of Usadel [159] which considers the magneto-resistance associated with the Aslamazov-Larkin superconducting fluctuations induced conductivity. We have found that this theoretical model consistently describes the magnetic field dependence of the magneto-resistivity of the Ti-V alloys. Based on these observations we have inferred that the rounding-off behaviour of the resistive transition in the Ti-V alloys occurs due to enhanced role of the superconducting fluctuations in these alloys. The Ginzburg number G_i for the Ti-V superconductors is estimated and found to be $\sim 10^{-6}$ - 10^{-5} , which is intermediate between those for high- T_C cuprate superconductors ($G_i \sim 10^{-2}$) and conventional low- T_C superconduct-

tors ($G_i \sim 10^{-8}$). We have suggested that the moderate value of G_i of the Ti-V superconductors makes the superconducting fluctuations significant in the experimentally accessible temperature window in the present bulk low- T_C superconductors. Hence, the outcomes of the present study resolve the debated problem of the observed rounding-off behaviour of the resistive transition in the Ti-V alloys, for which both the superconducting fluctuations [85-87] and the spin fluctuations [44, 88, 94] scenario were independently proposed previously.

Physical properties such as electric resistivity, magnetization, and heat capacity of Ti-V alloys are studied in the normal state of the Ti-V alloys. The important properties of the Ti-V alloys in their normal state are:

- (i) The considerations of only the electronic and the Debye lattice heat capacity cannot explain the experimental temperature dependence of heat capacity data in the wide temperature range 10-225 K. At lower temperature regime, the experimental heat capacity data deviate from the fitting performed by considering only the electronic and the Debye lattice heat capacity.
- (ii) A non-linearity with a negative curvature is observed in the plots of C/T as a function of T^2 at low temperatures.
- (iii) Dc magnetic susceptibility follows $-T^2 \ln T$ dependence on temperature.
- (iv) There is an enhancement of the stoner factor S in $\text{Ti}_x\text{V}_{1-x}$ alloys with $x \leq 0.7$.

- (v) For the $\text{Ti}_{0.4}\text{V}_{0.6}$ and $\text{Ti}_{0.6}\text{V}_{0.4}$ alloys, the electrical resistivity varies with temperature as $\rho(T) = \rho_0 + AT^2 + BT^5$ at low temperatures. The coefficient of the T^5 term in low-temperature resistivity is found to be very small. This coefficient is positive for the $\text{Ti}_{0.4}\text{V}_{0.6}$ alloy and negative for the $\text{Ti}_{0.6}\text{V}_{0.4}$ alloy.
- (vi) For the $\text{Ti}_{0.4}\text{V}_{0.6}$ and $\text{Ti}_{0.6}\text{V}_{0.4}$ alloys, the Sommerfeld coefficient γ and the coefficient A of the T^2 term in the temperature dependence of electrical resistivity at low temperatures follow the KadowakiWoods relation, according to which $A/\gamma^2 = 1.0 \times 10^{-4} \mu\Omega\text{-cm}(\text{mole/mJ})^2$ for the spin fluctuating systems [180].

All the above characteristic features pointed out above uniquely imply that spin fluctuations are important in the Ti-V alloys particularly in those having high V concentration [155, 156]. The outcome of this study was then used to resolve the problem of the observed disagreement between the experimentally measured and the theoretically predicted T_C values of the $\text{Ti}_x\text{V}_{1-x}$ alloys with $x \leq 0.7$. We have suggested that spin fluctuations, whose presence is evident in various normal state properties of the Ti-V alloys, suppress the T_C from a much higher value $\sim 15\text{-}20$ K (as calculated using McMillan formula) to the experimental value which is less than 8 K for the $\text{Ti}_x\text{V}_{1-x}$ alloys with $x \leq 0.7$ [155, 156].

From the point of practical applications, the critical current density J_C in as cast and annealed samples of the Ti-V alloys has been studied in detail. J_C is estimated from the irreversible magnetization using Bean's critical state

model [27]. As cast $\text{Ti}_{0.7}\text{V}_{0.3}$ alloy has the highest J_C value among all the investigated alloys. To understand the flux-line pinning mechanisms operating in the present Ti-V superconducting alloys, a detailed analysis of the field dependence of pinning force density $F_P (= J_C \times H)$ has been performed using Dew-Hughes model [213]. Flux-line pinning at normal surface pins has the major contribution to the pinning force density in all the as cast and annealed Ti-V alloys except in the annealed $\text{Ti}_{0.8}\text{V}_{0.2}$ alloy. The grain boundaries and edge dislocations seem to constitute the sources of such normal surface pinning centres in these alloys. In the annealed $\text{Ti}_{0.8}\text{V}_{0.2}$ alloy, flux-line pinning occurs predominantly at normal point pins while the role of normal surface pins is prevalent at relatively lower magnetic field. Substantial amount of the ω phase available in this sample functions as the normal point pinning centres. In the present Ti-V alloys, the most relevant pinning centres such as grain boundaries have length scales of the order of few tens to few hundreds of micron while inter-spacing between flux lines is of the order of few tens of nm for an applied magnetic field of only 1 T, implying the lack of sufficient pinning centres in these alloys. In spite of this fact, the zero field J_C value obtained in the as cast $\text{Ti}_{0.7}\text{V}_{0.3}$ alloy is only one order of magnitude lower than that obtained in Nb-Ti superconducting wires which is extensively used in the fabrication of high-field magnets (as cast $\text{Ti}_{0.7}\text{V}_{0.3}$ superconductor: $J_C(H = 0 \text{ T}, T = 4.2 \text{ K}) \sim 7 \times 10^8 \text{ A/m}^2$; Nb-Ti superconductor: $J_C(H = 0 \text{ T}, T = 4.2 \text{ K}) \sim 10^{10} \text{ A/m}^2$ [25]). Therefore, there is an ample scope to achieve a sufficiently high level of J_C in the Ti-V alloy superconductors by

artificially introducing disorders in these materials.

We have further investigated on how the intrinsic superconducting properties of the Ti-V alloys govern the flux-line pinning properties in the same. In these Ti-V alloys, J_C drops sharply in high magnetic field regime and vanishes at the irreversibility field H_{Irr} which is distinctly different from H_{C2} in these alloys. The limitation of J_C in high magnetic field regime was inferred to occur due to the thermal fluctuation effect, as is the case for the high- T_C superconductors. As the value of Ginzburg number G_i decreases with decreasing Ti concentration in the Ti-V alloys, thermal fluctuation effect becomes gradually less important in the V-rich Ti-V alloys. Consequently, the V-rich Ti-V alloys exhibit relatively improved high-field J_C behaviour. So our study shows that **from the J_C point of view the V-rich Ti-V alloys are superior than the Ti-rich Ti-V alloys.**

We have also studied the peak-effect observed in all the annealed and as cast Ti-V alloys except the annealed $Ti_{0.7}V_{0.3}$ alloy. The peak-effect is characterized by an abrupt enhancement of the irreversible magnetization (and hence critical current J_C) in high magnetic field regime below H_{C2} . To investigate into the origin of the peak-effect, we have constructed the minor hysteresis loops (MHLs) in and around the peak-effect regime. Magnetic hysteresis of these Ti-V alloys shows history effects within the peak-effect regime, which are known to be characteristic features related to the meta-stability (super heating/supercooling) associated with a first-order phase transition in the flux-line system [218-220]. We have then estimated equilibrium mag-

netization (M_{eq}) at different magnetic field from these MHLs. The magnetic field dependence of M_{eq} shows a clear jump within the peak-effect regime, which again indicates the first-order nature of the stated phase transition. We have suggested that a disorder-driven phase transition in the flux-line system gives rise to the peak-effect in the present Ti-V alloys.

We have presented a study on the vortex-glass to vortex-liquid phase transition in the flux-line system of the annealed $\text{Ti}_{0.7}\text{V}_{0.3}$ alloy. In order to ascertain the existence of such a phase transition in the flux-line system, the superconducting transition in this alloy has been studied through resistivity measurements in the presence of various constant applied magnetic fields, and the results are analyzed based on the theory of vortex-glass [38-41] as well as the modified vortex-glass model [247, 248]. We have estimated the glass transition temperature T_G and the critical exponent s for the vortex-liquid to vortex-glass phase transition. The s value is found to be ~ 1.8 and is almost independent of magnetic field. From both the estimated values of s as well as the nature of the disorders present in this sample, it is inferred that a Bose-glass [40, 41] vortex phase is formed in the mixed state of the annealed $\text{Ti}_{0.7}\text{V}_{0.3}$ alloy. We have estimated the activation energy or the effective pinning energy U_0 for the annealed $\text{Ti}_{0.7}\text{V}_{0.3}$ alloy using the modified vortex-glass model [247, 248]. Both the temperature and magnetic field dependencies of U_0 in the annealed $\text{Ti}_{0.7}\text{V}_{0.3}$ alloy are found to be distinctly different in the magnetic field regimes below and above 2 T, and these features are attributed due to the crossover from individual vortex pinning

regime to the collective pinning regime. For higher magnetic field (above 2 T), the temperature and magnetic field dependencies of U_0 of the annealed $\text{Ti}_{0.7}\text{V}_{0.3}$ alloy were found to be qualitatively very similar to those predicted for the high- T_C superconductors [247, 248]. Consequently, in this magnetic field regime, the vortex-liquid resistivity of the annealed $\text{Ti}_{0.7}\text{V}_{0.3}$ alloy in the critical region of the vortex-liquid to Bose-glass phase transition has been observed to follow the scaling behaviour predicted by the modified vortex-glass model [247, 248]. However, the same scaling law referred above was found to be not valid in low magnetic field regime. We have proposed a new scaling law for the vortex-liquid resistivity for low magnetic field regime. The vortex-liquid resistivity of the annealed $\text{Ti}_{0.7}\text{V}_{0.3}$ alloy in low magnetic field regime has been found to follow this new scaling law. This is the first study showing the scaling behaviour of the vortex-liquid resistivity in a low- T_C superconductor.

We have studied the high-field paramagnetic effect (HFPME) in as cast and annealed samples of $\text{Ti}_{0.8}\text{V}_{0.2}$ alloy and annealed sample of $\text{Ti}_{0.7}\text{V}_{0.3}$ alloy. In presence of relatively higher magnetic field (of the order of 1 Tesla), FCC magnetization of these multiphase Ti-V samples increases when temperature is decreased well below T_C . Moreover, in the superconducting state, FCW magnetization is found to be larger than the FCC magnetization. The FCW magnetization in the superconducting state even becomes larger than the normal state magnetization. These observed magnetic behaviours are distinctly different from the conventional magnetic responses of a type-II su-

perconductor, and are known as characteristics of the HFPME [291-296]. We have suggested that the inhomogeneous distribution of flux lines driven by the flux-line pinning at α (or α') phase regions is the essential mechanism leading to the observed HFPME in these samples. The above interpretation has been tested and confirmed by observing the complete disappearance of the HFPME in a $\text{Ti}_{0.8}\text{V}_{0.2}$ sample from which α' phase is removed by annealing it at an elevated β -field temperature. FCC magnetization exhibits strong dependence on both time as well as the temperature sweep rate of the measurements. Based on these experimental results, we have recognized the flux-creep effect as an important ingredient for the occurrence of the HFPME. We have interpreted that the creep of the flux lines into some stronger pinning centres available in these alloys (α or α' phase in these Ti-rich Ti-V alloys) enhances the flux-line density at these pinning centres, and thereby giving rise to the increase in paramagnetic response of the samples with time. We have also found that the coherence length ξ is another important factor, which governs the strength of the HFPME in a superconductor. These factors referred above successfully explain all the characteristic features associated with the HFPME exhibited by the present Ti-V alloys as well as many other superconducting systems.

10.2 Future outlook

One of the important outcomes of the present study is that the superconducting transition temperature T_C of the Ti-V alloys is significantly reduced due to the presence of spin fluctuations in these alloys. This result provides a way to achieve significantly higher T_C values up to $\sim 15-20$ K for the Ti-V alloys by suppressing the role of spin fluctuations in these alloys. The doping of a third element with negligible influence of spin fluctuations into the Ti-V alloys by not perturbing the electronic band structure remarkably could be a possible technique for the T_C enhancement. However, the malleability, which is known to be one of the important merits of the Ti-V superconductors for being used in technological applications, should not be compromised by such T_C enhancement process. The origin of spin fluctuations in the Ti-V alloys is itself an interesting research problem which is yet to be answered properly.

While investigating on the critical current aspect of the present Ti-V alloys, we have found that there is an ample scope to achieve a sufficiently high level of J_C in the Ti-V superconducting alloys by artificially introducing disorders in these alloys. In this direction, we have planned to introduce disorders in the present Ti-V alloys by heavy ion irradiation technique which is known to be one of the promising techniques for the improvement of the critical current density. Currently, this work is in ongoing stage.

Moreover, in this thesis, a little effort has been put to study the peak-effect phenomenon, which is observed quite often in the Ti-V alloys as well

as many other Ti-based transition metal alloys. To obtain a more complete and comprehensive picture of this phenomenon, we are now studying this phenomenon in detail.

References

- [1] L. C. Woods, in “Theory of Tokamak transport: New aspects for nuclear fission reactor design” (WILEY-VCH Verlag GmbH & Co. KGaA, Weinheim, 2006).
- [2] <http://www.iter.org>.
- [3] <http://www.nndc.bnl.gov/nudat2/>
- [4] G. Audi, O. Bersillon, J. Blachot, and A. H. Wapstra, Nucl. Phys. A **729**, 3 (2003).
- [5] M. Tai, K. Inoue, A. Kikuchi, T. Takeuchi, T. Kiyoshi, and Y. Hishinuma, IEEE Trans. Appl. Supercond. **17**, 2542 (2007).
- [6] J. K. Hulm and R. D. Blaugher, Phys. Rev. **123**, 1569 (1961), *and references therein*.
- [7] T. Takeuchi, H. Takigawa, M. Nakagawa, N. Banno, K. Inoue, Y. Iijima, and A. Kikuchi, Supercond. Sci. Technol. **21**, 025004 (2008).
- [8] P. H. Bellin, H. C. Gatos, and V. Sadagopan, J. Appl. Phys. **41**, 2057 (1970).
- [9] H. Kamerlingh-Onnes, Comm. Phys. Lab. Leiden **122b** (1911), reprinted in Proc. K. Ned. Akad. Wet. **14**, 113 (1911).
- [10] H. Kamerlingh-Onnes, Comm. Phys. Lab. Leiden **133d** (1913), reprinted in Proc. K. Ned. Akad. Wet. **16**, 113 (1911).
- [11] C. Kittel, *Introduction to Solid State Physics* (6th ed.) (John Wiley & Sons, Inc., New York, 1986).
- [12] W. Meissner and R. Ochsenfeld, Naturwissenschaften **21**, 787 (1933).
- [13] F. London and H. London, Proc. Roy. Soc. A **149**, 71 (1935).
- [14] E. Maxwell, Phys. Rev. **78**, 477 (1950).

- [15] C. A. Reynolds, B. Serin, W. H. Wright, and L. B. Nesbitt, Phys. Rev. **78**, 487 (1950).
- [16] J. Bardeen, L. N. Cooper, and J. R. Schrieffer, Phys. Rev. **106**, 162 (1957) and **108**, 1175 (1957).
- [17] H. Frohlich, Phys. Rev. **79**, 845 (1950).
- [18] B. B. Goodman, J. Hillairet, J. J. Veysie, and Weill, Compt. rend. **250**, 542 (1960).
- [19] W. L. McMillan, Phys. Rev. **167**, 331 (1968).
- [20] V. L. Ginzburg and L. D. Landau, Zh. Eksperim. i Teor. Fiz. **20** 1064 (1950).
- [21] J. B. Ketterson and S. N. Song, *Superconductivity* (Cambridge University Press, 1999).
- [22] A. A. Abrikosov, Sov. Phys.-JEPT **5**, 1174 (1957).
- [23] L. Shan, Yong-Lei Wang, B. Shen, B. Zeng, Y. Huang, Ang Li, Da Wang, H. Yang, C. Ren, Qiang-Hua Wang, S. Pan, and Hai-Hu Wen, Nature Physics **7**, 325 (2011).
- [24] I. Fridman, C. Kloc, C. Petrovic, and J. Y. T. Wei, Appl. Phys. Lett. **99**, 192505 (2011).
- [25] Guy Deutscher, *New Superconductors: From Granular to High T_C* (World Scientific Publishing Co. Pte. Ltd., 2006).
- [26] C. P. Bean and J. D. Livingstone, Phys. Rev. Lett. **12**, 14 (1964).
- [27] C. P. Bean, Rev. Mod. Phys. **36**, 31 (1964).
- [28] Y. B. Kim, C. F. Hempstead, and A. R. Strnad, Phys. Rev. Lett. **9**, 306 (1962).
- [29] Y. B. Kim, C. F. Hempstead, and A. R. Strnad, Phys. Rev. Lett. **729**, 528 (1963).
- [30] W. A. Fietz, M. R. Beasley, J. Silcox, and W. W. Webb, Phys. Rev. **136**, A 335 (1964).

- [31] J. H. P. Watson, *J. Appl. Phys.* **39**, 3406 (1968).
- [32] A. I. Larkin, *Sov. Phys. JEPT* **31**, 784 (1970).
- [33] T. Nattermann, *Phys. Rev. Lett.* **64**, 2454 (1990).
- [34] T. Giamarchi and P. Le Doussal, *Phys. Rev. Lett.* **72**, 1530 (1994);
Phys. Rev. B **52**, 1242 (1995).
- [35] X. S. Ling, S. R. Park, B. A. McClain, S. M. Choi, D. C. Dender, and
J. W. Lynn, *Phys. Rev. Lett.* **86**, 712 (2001).
- [36] A. M. Troyanovski, M. van Hecke, N. Saha, J. Aarts, and P. H. Kes,
Phys. Rev. Lett. **89**, 147006 (2002).
- [37] I. K. Dimitrov, N. D. Daniilidis, C. Elbaum, J. W. Lynn, and X. S.
Ling, *Phys. Rev. Lett.* **99**, 047001 (2007).
- [38] M. P. A. Fisher, *Phys. Rev. Lett.* **62**, 1415 (1989).
- [39] D. S. Fisher, M. P. A. Fisher, and D. A. Huse, *Phys. Rev. B* **43**, 130
(1991).
- [40] D. R. Nelson and V. M. Vinokur, *Phys. Rev. Lett.* **68**, 2398 (1992).
- [41] D. R. Nelson and V. M. Vinokur, *Phys. Rev. B* **48**, 13060 (1993).
- [42] E. W. Collings, *Phys. Rev. B* **9**, 3989 (1974).
- [43] E. W. Collings, *AIP Conf. Proc.* **40**, 410 (1978).
- [44] V. A. Rassokhin, N. V. Volkenshtein, E. P. Romanov, and A. F. Prekul,
Sov. Phys.-JETP **39**, 166 (1974) [*Zh. Eksp. Teor. Fiz.* **66**, 348 (1974)].
- [45] A. F. Prekul, V. A. Rassokhin, and N. V. Volkenshtein, *Sov. Phys.-
JETP* **40**, 1134 (1974) [*Zh. Eksp. Teor. Fiz.* **67**, 2286 (1974)].
- [46] T. Sasaki, S. Hanada, and Y. Muto, *Physica* **148B**, 513 (1987).
- [47] T. Sasaki and Y. Muto, *Physica B* **165** & **166**, 291 (1990).
- [48] M. Isino, *J. Phys. Soc. Jpn.* **54**, 3848 (1985).

- [49] C. H. Cheng, C. T. Wei, and P. A. Beck, Phys. Rev. **120**, 426 (1960); *and references therein*.
- [50] C. H. Cheng, K. P. Gupta, E. C. Van Reuth, and Paul A. Beck, Phys. Rev. **126**, 2030 (1962).
- [51] E. W. Collings, P. E. Upton, and J. C. Ho, Journal of the Less-Common Metals **42**, 285 (1975).
- [52] E. W. Collings, previously unpublished research; E. W. Collings; *Applied Superconductivity, Metallurgy, and Physics of Titanium alloys*, Vol. I (Plenum Press, New York, 1986), pp. 296-297.
- [53] H. Okamoto, J. Phase Equilib. **16**, 202 (1995).
- [54] P. Duwez, Trans. Am. Soc. Met. **45**, 934 (1953).
- [55] I. B. Ramsteiner, A. Schöps, F. Phillipp, M. Kelsch, H. Reichert, and H. Dosch, and V. Honkimäki, Phys. Rev. B **73**, 024204 (2006).
- [56] E. W. Collings; *Applied Superconductivity, Metallurgy, and Physics of Titanium alloys*, Vol. I (Plenum Press, New York, 1986).
- [57] M. K. Koul and J. F. Breedis, Acta Metal. **18**, 579 (1970).
- [58] E. S. K. Menon and R. Krishnan, J. Mater. Sci. **18**, 375 (1983).
- [59] K. K. McCabe, *MS thesis*, (Cornell University, Ithaca, New York, 1970) (unpublished).
- [60] K. K. McCabe and S. L. Sass, Phil. Mag. **23**, 957 (1971).
- [61] K. K. McCabe and S. L. Sass, Phil. Mag. **23**, 957 (1971).
- [62] Ch. Leibovitch, A. Rabinkin, and M. Talianker, Metal. Trans. A **12**, 1513 (1981).
- [63] S. K. Sikka, Y. K. Vohra, and R. Chidambaram, Solid State Commun. **42**, 205 (1982).
- [64] S. Hanada and O. Izumi, Metall. Trans. A **17**, 1409 (1986).

- [65] L. -C. Ming, M. H. Manghnani, and R. W. Katahara, *Acta Metal.* **29**, 479 (1981).
- [66] G. Aurelio, A. Fernandez Guillermet, G. J. Cuello, and J. Campo, *Metal. Mater. Trans. A* **33**, 1307 (2002).
- [67] I. A. Bagaryatskii, G. I. Nosova, and T. V. Tagunova, *Dokl. Akad. Nauk SSSR* **105**, 1225 (1955).
- [68] S. L. Sass, *Acta Metal.* **17**, 813 (1969).
- [69] N. Takesue, *Phys. Rev. B* **72**, 174210 (2005).
- [70] T. G. Berlincourt and R. R. Hake, *Phys. Rev.* **131**, 140 (1963).
- [71] J. C. Ho and E. W. Collings, *Phys. Rev. B* **6**, 3727 (1972).
- [72] R. W. Cochrane, R. Harris, J. O. Strom-Olson, and M. J. Zuckermann, *Phys. Rev. Lett.* **35**, 676 (1975).
- [73] E. Abrahams, P. W. Anderson, D. C. Licciardello, and T. V. Ramakrishnan, *Phys. Rev. Lett.* **42**, 673 (1979).
- [74] B. Ya. Sukharevskii, I. S. Shchetkin, and I. I. Fal'ko, *Sov. Phys. -JETP* **33**, 152 (1971), [*Zh. Eksp. Teor. Fiz.* **60**, 277 (1971)].
- [75] S. V. Vonsovsky, Yu A. Izyumov, and E. Z. Kurmaev, *Superconductivity of Transition Metals: Their Alloys and compounds* (Translated by E. H. Brandt and A. P. Zavaritsyn) (Springer Verlag, Berlin, 1982); *and references therein*.
- [76] T. G. Berlincourt and R. R. Hake, *Phys. Rev. Lett.* **9**, 293 (1962).
- [77] W. H. Hackett Jr., E. Maxwell, and Y. B. Kim, *Phys. Letters* **24A**, 663 (1967).
- [78] R. R. Hake, *Phys. Rev.* **158**, 356 (1967).
- [79] R. D. Blaugher, *Phys. Letters* **14**, 181 (1965).
- [80] P. G. de Gennes, *Superconductivity of Metals and Alloys*, (Translated by P. A. Pincus) (W. A. Benjamin Inc., New York, 1966), pp. 24, 225.

- [81] C. Caroli, P. G. de Gennes, and J. Matricon, Physik Kondensierten Materie **1**, 176 (1963); C. Caroli, *ibid.* **3**, 345 (1965).
- [82] L. P. Gorkov, Sov. Phys.-JETP **10**, 998 (1960).
- [83] B. B. Goodman, Phys. Letters **1**, 215 (1962).
- [84] J. B. Vetrano, G. L. Guthrie, H. E. Kissinger, J. L. Brimhall, and B. Mastel, J. Appl. Phys. **39**, 2524 (1968).
- [85] R. R. Hake, Phys. Rev. Lett. **23**, 1105 (1969).
- [86] R. R. Hake, Phys. Letters **32A**, 143 (1970).
- [87] J. W. Lue, A. G. Montgomery, and R. R. Hake, Phys. Rev. B **11**, 3393 (1975).
- [88] A. F. Prekul, V. A. Rassokhin, and N. V. Volkenshtein, JETP Lett. **17**, 252 (1973).
- [89] N. F. Berk and J. R. Schrieffer, Phys. Rev. Lett. **17**, 433 (1966).
- [90] M. J. Zuckermann, J. Phys. C: Solid St. Phys. **3**, 2130 (1970).
- [91] H. Rietschel and H. Winter, Phys. Rev. Lett. **43**, 1256 (1979).
- [92] S. K. Bose, J. Phys.: Condens. Mater **21**, 025602 (2009).
- [93] O. Pictet, T. Jarlborg, and M. Peter, J. Phys. F: Met. Phys. **17**, 221 (1987).
- [94] A. F. Prekul, V. A. Rassokhin, and N. V. Volkenshtein, Sov. Phys.-JETP Lett. **22**, 209 (1975).
- [95] A. F. Prekul, V. A. Rassokhin, and N. V. Volkenshtein, Sov. Phys.-JETP **40**, 1134 (1975).
- [96] B. D. Cullity, *Elements of X-ray Diffraction* (Addison-Wesley, Reading, Massachusetts, 1978).
- [97] B. E. Warren, *X-ray Diffraction* (Dover, 1990).
- [98] J. Als-Nielsen and D. McMorrow, *Element of Modern X-ray Physics* (Wiley & Sons Ltd., 2001).

- [99] <http://www.esrf.eu/computing/scientific/FIT2D/>
- [100] B. D. Cullity and C. D. Graham, *Introduction to Magnetic Materials* (John Wiley & Sons, New Jersey, 2009).
- [101] M. P. Janawadkar, R. Baskaran, R. Saha, K. Gireesan, R. Nagendran, L. S. Vaidhyanathan, J. Jayapandian, and T. S. Radhakrishnan, *Current Science* **77**, 759 (1999).
- [102] S. B. Roy, *Proc. of the Solid State Physics Symposium* **42**, 95 (1999); *and references therein*.
- [103] R. Bachmann, F. J. Di Salvo, T. H. Geballe, R. L. Greene, R. E. Howard, C. N. King, H. C. Kirsch, K. N. Lee, R. E. Schwall, H. U. Thomas, and R. B. Zubeck, *Rev. Sci. Instrum.* **43**, 205 (1972).
- [104] Heat Capacity Option User's Manual, Physical Property Measurement System (PPMS, Quantum Design, USA).
- [105] W. M. Murray and W. R. Miller, *The Bonded Electrical Resistance Strain Gauge* (Oxford University Press, New York, 1992).
- [106] M. Okaji, N. Yamada, H. Kato, and K. Nara, *Cryogenics* **37**, 251 (1997).
- [107] E. W. Collings, *Applied Superconductivity, Metallurgy, and Physics of Titanium Alloys*, Vol. 1 (Plenum Press, New York, 1986); *and references therein*.
- [108] M. K. Koul and J. F. Breedis, *Acta Metall.* **18**, 579 (1970).
- [109] L. -C. Ming, M. H. Manghnani, and R. W. Katahara, *Acta Metall.* **29**, 479 (1981).
- [110] Md. Matin, L. S. Sharath Chandra, M. K. Chattopadhyay, M. N. Singh, A. K. Sinha, and S. B. Roy, *Supercond. Sci. Technol.* **26**, 115005 (2013).
- [111] I. S. Shchetkin and T. N. Kharchenko, *Zh. Eksp. Teor. Fiz.* **64**, 964 (1973) [*Sov. Phys.-JEPT* **37**, 491 (1973)].
- [112] B. I. Verkin, *personal communication*.

- [113] K. Ikeda, K. A. Gschneidner Jr., R. J. Stierman, T.-W. E. Tsang, and O. D. McMasters, *Phys. Rev. B* **29**, 5039 (1984).
- [114] A. LeR. Dawson, D. H. Ryan, and David V. Baxter, *Phys. Rev. B* **54**, 12238 (1996).
- [115] <http://kkr.phys.sci.osaka-u.ac.jp/>
- [116] S. H. Vosko, L. Wilk, and M. Nussair, *Can. J. Phys.* **58**, 1200 (1980).
- [117] I. Bakonyi, H. Ebert, and A. I. Liechtenstein, *Phys. Rev. B* **48**, 7841 (1993).
- [118] R. Lortz, Y. Wang, U. Tutsch, S. Abe, C. Meingast, P. Popovich, W. Knafo, N. Shitsevalova, Yu. B. Paderno, and A. Junod, *Phys. Rev. B* **73**, 024512 (2006).
- [119] K. N. Yang, M. B. Maple, L. E. DeLong, J. G. Huber, and A. Junod, *Phys. Rev. B* **39**, 151 (1989).
- [120] A. Junod, T. Jarlborg, and J. Muller, *Phys. Rev. B* **27**, 1568 (1983).
- [121] T. P. Orlando, E. J. McNiff, Jr. and S. Foner, and M. R. Beasley, *Phys. Rev. B* **19**, 4545 (1979).
- [122] K. M. Ralls, Effects of Metallurgical Structure on the Superconductivity of Nb-Zr and Nb-Ti Alloys, **Ph.D. Thesis**, 1964, Massachusetts Institute of Technology, Cambridge, Massachusetts.
- [123] Henry John Muller, The upper Critical Field of Niobium-Titanium, **Ph.D. Thesis**, 1989, University of Wisconsin-Madison.
- [124] L. P. Gorkov, *Sov. Phys.-JEPT* **7**, 505 (1958).
- [125] L. P. Gorkov, *Sov. Phys.-JEPT* **9**, 1364 (1959).
- [126] G. Bergmann, *Phys. Rev. B* **7**, 4850 (1973).
- [127] D. Saint-James, G. Sarma, and E. J. Thomas, *Type-II Superconductivity* (Pergamon, New York, 1969).
- [128] A. M. Clogston, *Phys. Rev. Lett.* **9**, 266 (1962)

- [129] B. S. Chandrasekher, *Appl. Phys. Lett.* **1**, 7 (1962).
- [130] A. M. Clogston, A. C. Gossard, V. Jaccarino, and Y. Yafet, *Phys. Rev. Lett.* **9**, 262 (1962).
- [131] J. D. Livingston and H. W. Schadler, General Electric Research Laboratory, Report No. **64-RL-3765M**, 25 (1964).
- [132] N. R. Werthamer, E. Helfand, and P. C. Hohenberg, *Phys. Rev.* **147**, 295 (1966).
- [133] D. Rainer and G. Bergmann, *J. Low Temp. Phys.* **14**, 501 (1974).
- [134] N. F. Masharov, *Sov. Phys. Solid State* **16**, 1524 (1975).
- [135] B. T. Geilikman, V. Z. Kresin, and N. F. Masharov, *J. Low Temp. Phys.* **18**, 241 (1975).
- [136] M. Naito, A. Matsuda, K. Kitazawa, S. Kambe, I. Tanaka, and H. Kojima, *Phys. Rev. B* **41**, 4823 (1990).
- [137] R. Liang, P. Dosanjh, D. A. Bonn, and W. N. Hardy, *Phys. Rev. B* **50**, 4212 (1994).
- [138] V. V. Moshchalkov, J. Y. Henry, C. Marin, J. Rossat-Mignod, and J. F. Jacquot, *Physica C* **175**, 407 (1991).
- [139] L. Burlachkov, Y. Yeshurun, M. Konczykowski, and F. Holtzberg, *Phys. Rev. B* **45**, 8193 (1992).
- [140] C. P. Bean, *Phys. Rev. Lett.* **8**, 250 (1962).
- [141] J. C. Martinez, J. J. Prejean, E. Kaldis, and P. Bordet, *Solid State Commun.* **75**, 315 (1990).
- [142] L. Fabrega, B. Martinez, J. Fontcuberta, X. Obradors, and S. Pinol, *Phys. Rev. B* **46**, 5581 (1992).
- [143] S. B. Roy, G. R. Myneni, and V. C. Sahni, *Supercond. Sci. Technol.* **21**, 065002 (2008).
- [144] M. Konczykowski, L. I. Burlachkov, Y. Yeshurun, and F. Holtzberg, *Phys. Rev. B* **43**, 13707 (1991).

- [145] M. Tinkham, *Introduction to superconductivity* (McGraw-Hill, New York, 1975).
- [146] K. J. Song, C. Park, S. S. Oh, Y. K. Kwon, J. R. Thompson, D. G. Mandrus, D. McK. Paul, and C. V. Tomy, *Physica C* **398**, 107 (2003).
- [147] C. P. Poole Jr., H. A. Farach, R. J. Creswick, and R. Prozorov, *Superconductivity*, (Academic Press, London, 2007).
- [148] M. Isino, *Journal of the Physical Society of Jpn.* **54**, 3848 (1985).
- [149] A. L. Fetter, *Phys. Rev.* **147**, 153 (1966).
- [150] V. V. Schmidt, **The Physics of Superconductors: Introduction to Fundamentals and Applications** (Springer-Verlag, Berlin Heidelberg, 1997).
- [151] A. M. Cambell and J. E. Evetts, *Advance in Physics* **21**, 199 (1972).
- [152] B. Bandyopadhyay, P. Watson, Yin Bo, and D. G. Naugle, *J. Phys. F: Met. Phys.* **17**, 433 (1987).
- [153] A. Schmid, *Physik Kondensierten Matere* **5**, 302 (1966).
- [154] E. Abrahams and T. Tsuneto, *Phys. Rev.* **152**, 416 (1966).
- [155] Md. Matin, L. S. Sharath Chandra, R. K. Meena, M. K. Chattopadhyay, A. K. Sinha, M. N. Singh, and S. B. Roy, *Physica B* **436**, 20 (2014).
- [156] Md. Matin, L. S. Sharath Chandra, S. K. Pandey, M. K. Chattopadhyay, and S. B. Roy, *Eur. Phys. J. B* **87**, 131 (2014).
- [157] L. G. Aslamazov and A. I. Larkin, *Phys. Lett. A* **26**, 238 (1968).
- [158] B. Leridon, A. Defossez, J. Dumont, J. Lesueur, and J. P. Contour, *Phys. Rev. Lett.* **87**, 197007 (2001).
- [159] K. D. Usadel, *Z. Phys.* **227**, 260 (1969).
- [160] A. D. Hernandez, B. J. Baelus, D. Dominguez, and F. M. Peeters, *Phys. Rev. B* **71**, 214524 (2005).

- [161] R. Hopfengartner, B. Hensel, and G. Saemann-Ischenko, Phys. Rev. B **44**, 741 (1991).
- [162] W. N. Kang, K. J. Kim, H. J. Kim, E. M. Choi, M. S. Park, M. S. Kim, Z. Du, C. U. Jung, K. H. Kim, S.-I. Lee, and M.-O. Mun, J. Korean Phys. Soc. **40**, 949 (2002).
- [163] Z. Pribulova, T. Klein, J. Kacmarcik, C. Marcenat, M. Konczykowski, S. L. Budko, M. Tillman, and P. C. Canfield, Phys. Rev. B **79**, 020508 (2009).
- [164] Mi-Ock Mun, Sung-Ik Lee, and W. C. Lee, Phys. Rev. B **56**, 14668 (1997).
- [165] A. Lascialfari, T. Mishonov, A. Rigamonti, P. Tedesco, and A. Varlamov, Phys. Rev. B **65**, 180501 (2002).
- [166] E. Bernardi, A. Lascialfari, A. Rigamonti, and L. Romano, Phys. Rev. B **77**, 064502 (2008).
- [167] R. S. Thompson, Phys. Rev. B **1**, 327 (1970).
- [168] W. J. Skocpol and M. Tinkham, Rep. Prog. Phys. **38**, 1049 (1975); *and references therein*.
- [169] K. Maki, Prog. Theor. Phys. **39**, 897 (1968); *and references therein*.
- [170] W. Holm, *Ph.D. thesis*, Royal Institute of Technology (1996).
- [171] W. L. Johnson and C. C. Tsuei, Phys. Rev. B **13**, 4827 (1976).
- [172] W. L. Johnson, C. C. Tsuei, and P. Chaudhari, Phys. Rev. B **17**, 2884 (1978).
- [173] C. Sekirnjak, W. Lang, S. Proyer and P. Schwab, Physica C **243**, 60 (1995).
- [174] W. Lang, W. Kula, and R. Sobolewski, Physica B **194-196**, 1643 (1994).
- [175] D. H. Kim, K. E. Gray, R. T. Kampwirth, and D. M. McKay, Phys. Rev. B **43**, 2910 (1991).

- [176] W. Lang, W. Kula, and R. Sobolewski, *Physica C* **226**, 267 (1994).
- [177] P. P. Freitas, C. C. Tsuei, and T. S. Plaskett, *Phys. Rev. B* **36**, 833 (1987).
- [178] S. L. Liu, G. Longyan, B. Gang, W. Haiyum, and L. Yongtao, *Supercond. Sci. Technol.* **24**, 075005 (2011).
- [179] J. P. Gollub, M. R. Beasley, R. Callarotti, and M. Tinkham, *Phys. Rev. B* **7**, 3039 (1973).
- [180] K. Kadowaki and S. B. Woods, *Solid State Commun.* **58**, 507 (1986).
- [181] Ch. Walti, E. Felder, C. Degen, G. Wigger, R. Monnier, B. Delley, and H. R. Ott, *Phys. Rev. B* **64**, 172515 (2001).
- [182] P. B. Allen and R. C. Dynes, *Phys. Rev. B* **12**, 905 (1975).
- [183] T. P. Orlando and M. R. Beasley, *Phys. Rev. Lett.* **46**, 1981 (1981).
- [184] E. V. Galoshina, *Usp. Fiz. Nauk* **113**, 105 (1974).
- [185] E. W. Collings and J. C. Ho, *Phys. Rev. B* **2**, 235 (1970).
- [186] S. Misawa and K. Kanematsu, *J. Phys. F: Met. Phys.* **6**, 2119 (1976).
- [187] G. Barnea, *J. Phys. C: Solid State Phys.* **8**, L216 (1975).
- [188] X.-W. Guan, X.-G. Yin, A. Foerster, M. T. Batchelor, C.-H. Lee, and H.-Q. Lin, *Phys. Rev. Lett.* **111**, 130401 (2013).
- [189] A. I. Schindler and M. J. Rice, *Phys. Rev.* **164**, 759 (1967).
- [190] A. I. Schindler and B. R. Coles, *J. Appl. Phys.* **39**, 956 (1968).
- [191] P. H. Frings and J. J. M. Franse, *Phys. Rev. B* **31**, 4355 (1985).
- [192] J. Kondo, *Prog. Theor. Phys.* **32**, 37 (1964).
- [193] Y. Hariharan, M. P. Janawadkar and T. S. Radhakrishnan, *Solid State Commun.* **59**, 127 (1986).
- [194] C. C. Tsuei, *Solid State Commun.* **27**, 691 (1978).

- [195] B. Kramer and A. MacKinnon, Rep. Prog. Phys. **56**, 1469 (1993).
- [196] O. Rapp and C. Crafoord, Phys. Stat. Sol. B **64**, 139 (1974).
- [197] M. Wierzbowska, Eur. Phys. J. B **48**, 207 (2005).
- [198] S. Doniach, Phys. Rev. Lett. **18**, 554 (1967).
- [199] J. M. Daams, B. Mitrovic, and J. P. Carbotte, Phys. Rev. Lett. **46**, 65 (1981).
- [200] K. A. Muller, M. Takashige, J. G. Bednorz, Phys. Rev. Lett. **58**, 1143 (1987).
- [201] D. N. Zheng, A. M. Champbell, J. D. Johnson, J. R. Cooper, F. J. Blunt, A. Porch, and P. A. Freeman, Phys. Rev. B **49**, 1417 (1994).
- [202] C. Rossel, E. Sandvold, M. Sergent, R. Chevrel, and M. Potel, Physica C **165**, 223 (1990).
- [203] C. Rossel, O. Pena, H. Schmitt, and M. Sergent, Physica C **181**, 363 (1991).
- [204] M. Suenga, D. O. Welch, and R. Budhani, Supercond. Sci. Technol. **5**, S1 (1992).
- [205] D. N. Zheng, H. D. Ramsbottom, and D. P. Hampshire, Phys. Rev. B **52**, 12931 (1995).
- [206] L. A. Bonney, T. C. Willis, and D. C. Larbalestier, J. Appl. Phys. **77**, 6377 (1995).
- [207] M. J. Qin, X. L. Wang, H. K. Liu, and S. X. Dou, Phys. Rev. B **65**, 132508 (2002).
- [208] C. Hucho, P. Schilbe, and K. Luders, Physica C **377**, 399 (2002).
- [209] D. A. Cardwell, N. Hari Babu, M. Kambara, and A. M. Campbell, Physica C **372**, 1262 (2002).
- [210] Y. Yeshurun and A. P. Malozemoff, Phys. Rev. Lett. **60**, 2202 (1988).

- [211] M. J. Qin, S. Keshavarzi, S. Soltanian, X. L. Wang, H. K. Liu, and S. X. Dou, Phys. Rev. B **69**, 012507 (2004).
- [212] S. R. Ghorbani, X. L. Wang, S. X. Dou, Sung-IK Lee, and M. S. A. Hossain, Phys. Rev. B **78**, 184502 (2008).
- [213] D. Dew-Hughes, Phil. Mag. **30**, 293 (1974).
- [214] S. B. Roy, M. K. Chattopadhyay, and P. Chaddah, J. Phys.: Condens. Matter **18**, 9471 (2006); *and references therein*.
- [215] L. Civale, M. W. McElfresh, A. D. Marwick, F. Holtzberg, C. Field, J. R. Thompson, and D. K. Christen, Phys. Rev. B **43**, 13732 (1991).
- [216] H. Ullmaier, *Irreversible Properties of Type-II Superconductors* (Springer-Verlag, Berlin Heidelberg, 1975).
- [217] L. Burlachkov, M. Konczykowski, Y. Yeshurun, and F. Holtzberg, J. Appl. Phys. **70**, 5759 (1991); L. Burlachkov, Phys. Rev. B **47**, 8056 (1993).
- [218] S. B. Roy and P. Chaddah, J. Phys.: Condens. Matter **9**, L625 (1997); *and references therein*.
- [219] S. B. Roy, P. Chaddah, and S. Chaudhary, J. Phys.: Condens. Matter **10**, 4885 (1998).
- [220] S. B. Roy, P. Chaddah, and S. Chaudhary, Phys. Rev. B **62**, 9191 (2000); *and references therein*.
- [221] R. Modler et al. Phys. Rev. Lett. **76**, 1292 (1996).
- [222] R. Modler, Czech. J. Phys. **46**, 3123 (1996).
- [223] N. R. Dilley, J. Hermann, S. H. Ham, M. B. Maple, S. Spagna, J. Diederichs, and R. E. Sager, Physica C **256**, 140 (1996).
- [224] K. Kadowaki, H. Takeya, and K. Hirata, Phys. Rev. B **54**, 462 (1996).
- [225] G. Ravikumar, P. K. Mishra, V. C. Sahni, S. S. Banerjee, A. K. Grover, S. Ramakrishnan, P. L. Gammel, D. J. Bishop, E. Bucher, M. J. Higgins, and S. Bhattacharya, Phys. Rev. B **61**, 12490 (2000).

- [226] G. Ravikumar, H. Kupfer, A. Will, R. Meier-Hirmer, and Th. Wolf, Phys. Rev. B **65**, 094507 (2002); *and references therein*.
- [227] S. Kokkaliaris, A. A. Zhukov, P. A. J. de Groot, R. Gagnon, L. Taillefer, and T. Wolf, Phys. Rev. B **61**, 3655 (2000).
- [228] A. A. Zhukov, P. A. J. de Groot, S. Kokkaliaris, E. di Nicolo, A. G. M. Jansen, E. Mossang, G. Martinez, P. Wyder, T. Wolf, H. Küpfer, H. Asaoka, R. Gagnon, and L. Taillefer, Phys. Rev. Lett. **87**, 017006 (2001).
- [229] Y. Radzyner, S. B. Roy, D. Giller, Y. Wolfus, A. Shaulov, P. Chaddah, and Y. Yeshurun, Phys. Rev. B **61**, 14362 (2000).
- [230] P. Fulde and R. A. Ferrel, Phys. Rev. **135**, A550 (1964).
- [231] A. I. Larkin and Y. N. Ovchinnikov, Sov. Phys.-JETP **20**, 762 (1965).
- [232] K. Gloss, R. Modler, H. Schimanski, C. D. Bredl, C. Geibel, F. Steglick, A. I. Buzdin, N. Sato, and T. Komatsubara, Phys. Rev. Lett. **70**, 501 (1993).
- [233] K. Tenya, M. Ekedo, T. Tayama, T. Sakakibara, E. Yamamoto K. Maezawa, F. Steglick, N. Kimura, R. Settai, and Y. Onuki, Phys. Rev. Lett. **77**, 3193 (1996).
- [234] J-G. Park, M. Ellerby, K. A. McEwen, and M. de Podesta, J. Magn. Mater. **140+141**, 2057 (1995).
- [235] H. M. Carruzzo and C. Yu, *LANL Archive Preprint cond-mat 9705092* (1997).
- [236] Y. Paltiel, E. Zeldov, Y. Myasoedov, M. L. Rappaport, G. Jung, S. Bhattacharya, M. J. Higgins, Z. L. Xiao, E. Y. Andrei, P. L. Gammel, and D. J. Bishop, Phys. Rev. Lett. **85**, 3712 (2000).
- [237] S. Bhattacharya and M. J. Higgins, Phys. Rev. Lett. **70**, 2617 (1993).
- [238] S. Bhattacharya and M. J. Higgins, Phys. Rev. B **52**, 64 (1995).
- [239] R. Wordenweber, P. H. Kes, and C. C. Tsuei, Phys. Rev. B **33**, 3172 (1986).

- [240] M. Daeumling, J. M. Seuntjens, and D. C. Larbalestier, *Nature* **346**, 332 (1990).
- [241] T. Nishizaki, T. Naito, and N. Kobayashi, *Phys. Rev. B* **58**, 11 169 (1998).
- [242] S. Mohan, J. Sinha, S. S. Banerjee, and Y. Myasoedov, *Phys. Rev. Lett.* **98**, 027003 (2007).
- [243] J. Schelten, H. Ullmaier, and W. Schmatz, *Phys. Status Solidi B* **48**, 619 (1971).
- [244] D. K. Christen, F. Tasset, S. Spooner, and H. A. Mook, *Phys. Rev. B* **15**, 4506 (1977).
- [245] E. R. Nowak, N. E. Israeloff, and A. M. Goldman, *Phys. Rev. B* **49**, 10047 (1994); *and references therein*.
- [246] S. Awaji, M. Namba, K. Watanabe, M. Miura, Y. Yoshida, Y. Ichino, Y. Takai, and K. Matsumoto, *Appl. Phys. Lett.* **90**, 122501 (2007); *and references therein*.
- [247] A. Rydh, O. Rapp, and M. Andersson, *Phys. Rev. Lett.* **83**, 1850 (1999).
- [248] M. Andersson, A. Rydh, and O. Rapp, *Phys. Rev. B* **63**, 184511 (2001).
- [249] P. H. Kes, J. Aarts, J. van den Berg, C. J. van der Beek, and J. A. Mydosh, *Supercond. Sci. Technol.* **1**, 242 (1989).
- [250] H. Safar, P. L. Gammel, D. J. Bishop, D. B. Mitzi, and A. Kapitulnik, *Phys. Rev. Lett.* **68**, 2672 (1992).
- [251] P. Wagner, U. Frey, F. Hillmer, and H. Adrian, *Phys. Rev. B* **51**, 1206 (1995).
- [252] B. Lundqvist, J. Larsson, A. Herting, O. Rapp, M. Andersson, Z. G. Ivanov, and L.-G. Johansson, *Phys. Rev. B* **58**, 6580 (1998).
- [253] S. L. Liu, G. J. Wu, X. B. Xu, J. Wu, H. M. Shao, *Solid State Commun.* **127**, 749 (2003).

- [254] T. Naito, H. Iwasaki, T. Nishizaki, and N. Kobayashi, Phys. Rev. B **70**, 014515 (2004); *and references therein*.
- [255] S. Vinu, P. M. Sarun, R. Shabna, A. Biju, and U. Syamaprasad, J. Appl. Phys. **105**, 123901 (2009).
- [256] S. R. Ghorbani, X. L. Wang, M. Shahbazi, S. X. Dou, K. Y. Choi, and C. T. Lin, Appl. Phys. Lett. **100**, 072603 (2012).
- [257] P. L. Gammel, L. F. Schneemeyer, and D. J. Bishop, Phys. Rev. Lett. **66**, 953 (1991).
- [258] S. A. Grigera, E. Morre, E. Osquiguil, C. Balseiro, G. Nieva, and F. dela Cruz, Phys. Rev. Lett. **81**, 2348 (1998).
- [259] R. J. Olsson, W.-K. Kwok, L. M. Paulius, A. M. Petrean, D. Z. Hofman, and G. W. Crabtree, Phys Rev. B **65**, 104520 (2002).
- [260] B. Lundqvist, O. Rapp, and M. Andersson, Phys. Rev. B **62**, 3542 (2000).
- [261] B. Espinosa-Arronte and M. Andersson, Phys. Rev. B **71**, 024507 (2005).
- [262] H. J. Kim, Y. Liu, Y. S. Oh, S. Khim, I. Kim, G. R. Stewart, and K. H. Kim, Phys. Rev. B **79**, 014514 (2009).
- [263] M. Shahbazi, X. L. Wang, S. R. Ghorbani, M. Ionescu, O. V. Shcherbakova, F. S. Wells, A. V. Pan, S. X. Dou, and K. Y. Choi, Supercond. Sci. Technol. **26**, 095014 (2013).
- [264] T. T. M. Palstra, B. Batlogg, R. B. van Dover, I. F. Schneemeyer, and J. V. Waszczak, Phys. Rev. B **41**, 6621 (1990).
- [265] G. Blatter, M. V. Feigelman, V. B. Geshkenbein, A. I. Larkin, and V. M. Vinokur, Rev. Mod. Phys. **66**, 1125 (1994).
- [266] Hechang Lei, Rongwei Hu, E. S. Choi, and C. Petrovic, Phys. Rev. B **82**, 134525 (2010).
- [267] J. Jaroszynski, F. Hunte, L. Balicas, Y.-J. Jo, I. Raievi, A. Gurevich, D. C. Larbalestier, F. F. Balakirev, L. Fang, P. Cheng, Y. Jia, and H. H. Wen, Phys. Rev. B **78**, 174523 (2008).

- [268] L. Civale, A. D. Marwick, T. K. Worthington, M. A. Kirk, J. R. Thompson, L. Krusin-Elbaum, Y. Sun, J. R. Clem, and F. Holtzberg, *Phys. Rev. Lett.* **67**, 648 (1991).
- [269] E. H. Brandt, *Rep. Prog. Phys.* **58**, 1465 (1995).
- [270] L. Radzihovsky, *Phys. Rev. Lett.* **74**, 4923 (1995).
- [271] A. V. Lopatin and V. M. Vinokur, *Phys. Rev. Lett.* **92**, 067008 (2004).
- [272] S. S. Banerjee, A. Soibel, Y. Myasoedov, M. Rappaport, E. Zeldov, M. Menghini, Y. Fasano, F. de la Cruz, C. J. van der Beek, M. Konczykowski, and T. Tamegai, *Phys. Rev. Lett.* **90**, 087004 (2003).
- [273] M. Sigrist and T.M. Rice, *Rev. Mod. Phys.* **67**, 503 (1995).
- [274] P. Svedlindh, K. Niskanen, P. Norling, P. Nordblad, L. Lundgren, B. Lonnberg, and T. Lundstrom, *Physica C* **162-164**, 1356 (1989).
- [275] W. Braunisch, N. Knauf, V. Kataev, S. Neuhausen, A. Grutz, A. Kock, B. Roden, D. Khomskii, and D. Wohlleben, *Phys. Rev. Lett.* **68**, 1908 (1992).
- [276] Ch. Heinzl, Th. Theiling, and P. Ziemann, *Phys. Rev. B* **48**, 3445 (1993).
- [277] W. Braunisch, N. Knauf, G. Bauer, A. Kock, A. Becker, B. Freitag, A. Grutz, V. Kataev, S. Neuhausen, B. Roden, D. Khomskii, D. Wohlleben, J. Bock, and E. Preisler, *Phys. Rev. B* **48**, 4030 (1993).
- [278] S. Riedling, G. Brauchle, R. Lucht, K. Rohberg, H. V. Lohneysen, H. Claus, A. Erb, and G. Muller-Vogt, *Phys. Rev. B* **49**, 13 283 (1994).
- [279] M. Sigrist and T. M. Rice, *J. Phys. Soc. Jpn.* **61**, 4283 (1992).
- [280] F. V. Kusmartsev, *Phys. Rev. Lett.* **69**, 2268 (1992).
- [281] D. J. Thompson, M. S. M. Minhaj, L. E. Wenger, and J. T. Chen, *Phys. Rev. Lett.* **75**, 529 (1995).
- [282] P. Kostic, B. Veal, A. P. Paulikas, U. Welp, V. R. Todt, C. Gu, U. Geiser, J. M. Williams, K. D. Carlson, and R. A. Klemm, *Phys. Rev. B* **53**, 791 (1996).

- [283] L. Pust, L. E. Wenger, and M. R. Koblischka, *Phys. Rev. B* **58**, 14191 (1998).
- [284] A. K. Geim, S. V. Dubonos, J. G. S. Lok, M. Henini, and J. C. Maan, *Nature* **396**, 144 (1998).
- [285] S. Yuan, L. Ren, and F. Li, *Phys. Rev. B* **69**, 092509 (2004).
- [286] S. Chu, A. J. Schwartz, T. B. Massalski, and D. E. Laughlin, *Appl. Phys. Lett.* **89**, 11903 (2006).
- [287] A. E. Koshelev and A. I. Larkin, *Phys. Rev. B* **52**, 13 559 (1995).
- [288] V. V. Moschalkov, X. G. Qiu, and V. Bruyndoncx, *Phys. Rev. B* **55**, 11795 (1997).
- [289] A. I. Rykov, S. Tajima, and F. V. Kusmartsev, *Phys. Rev. B* **55**, 8557 (1997).
- [290] F. T. Dias, P. Pureur, P. Rodrigues, Jr., and X. Obradors, *Physica C* **354**, 219 (2001).
- [291] F. T. Dias, P. Pureur, P. Rodrigues Jr., and X. Obradors, *Phys. Rev. B* **70**, 224519 (2004).
- [292] Cristol de Paiva Gouvea, F. T. Dias, Valdemar das Neves Vieira, Douglas Langie da Silva, J. Schaf, F. Wolff-Fabris, and J. J. R. Rovira, *Journal of the Korean Physical Society* **62**, 1414 (2013).
- [293] C. Z. Chen, C. B. Cai, L. Peng, Z. Y. Liu, Y. M. Lu, H. W. Wang, and X. M. Xie, *Europhys. Lett.* **89**, 37005 (2010).
- [294] W. A. C. Passos, P. N. Lisboa-Filho, G. L. Fraga, F. W. Fabris, P. Pereur, and W. A. Ortiz, *Brazilian J. Phys.* **32**, 777 (2002).
- [295] V. G. Prokhorov, V. L. Svetchnikov, J. S. Park, G. H. Kim, Y. P. Lee, J-H. Kang, V. A. Khokhlov, and P. Mikheenko, *Supercond. Sci. Technol.* **22**, 045027 (2009).
- [296] A. Terentiev, D. B. Watkins, and L. E. De Long, D. J. Morgan, and J. B. Ketterson, *Phys. Rev. B* **60**, 761 (1999).

- [297] J. R. Clem and Z. Hao, Phys. Rev. B **48**, 13774 (1993).
- [298] G. Li, R. R. Urbano, P. Goswami, C. Tarantini, B. Lv, P. Kuhns, A. P. Reyes, C. W. Chu, and L. Balicas, Phys. Rev. B **87**, 024512 (2013).
- [299] S. Pinol, V. Gomis, B. Martinez, A. Labarta, J. Fontcuberta, and X. Obradors, Journal of Alloys and Compounds **195**, 11 (1993).